AD-A073 766 GENERAL ELECTRIC CO SANTA BARBARA CA TEMPO F/G 19/4
PROCEEDINGS OF THE NUCLEAR BLAST AND SHOCK SIMULATION SYMPOSIUM--ETC(U)
DEC 78 DNA0001-79-C-0081

UNCLASSIFIED DNA-4797P-2 NL

1 OF 4
ADA 073766

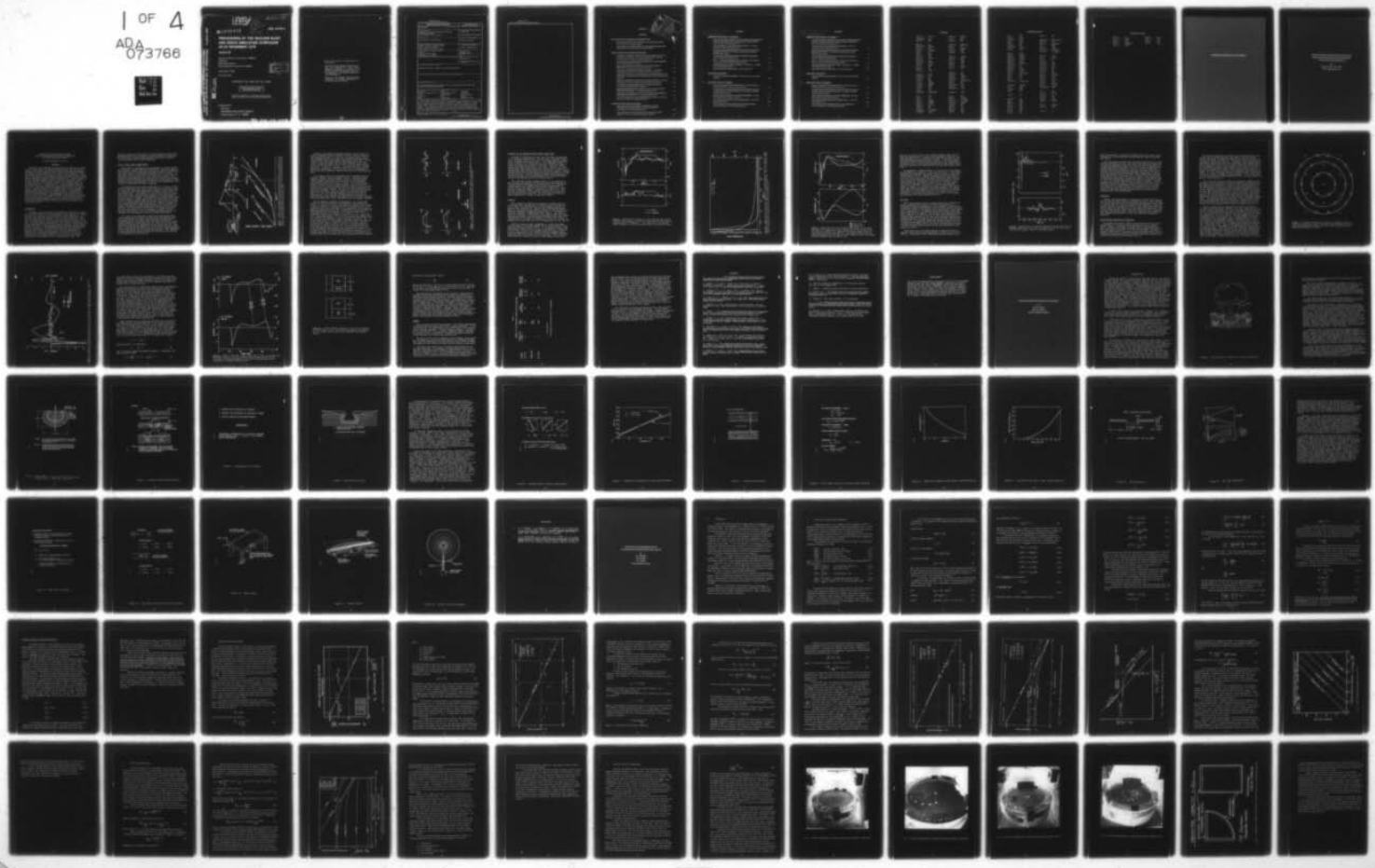

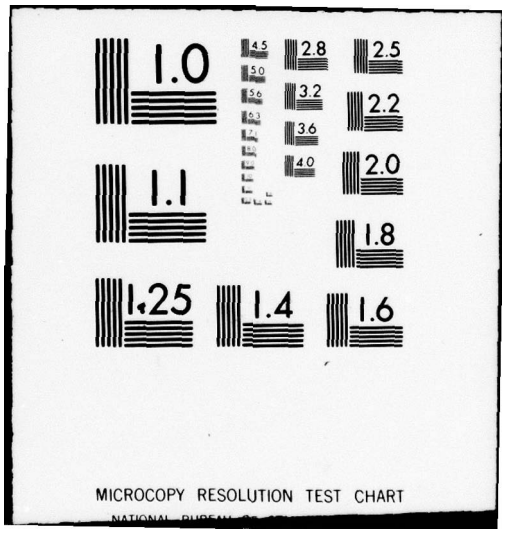
1.0
1.1
1.25
1.4
1.6
1.8
2.0
2.2
2.5
2.8
3.2
3.6
4.0
4.5
5.0
5.6
6.3
MICROCOPY RESOLUTION TEST CHART

LEVEL III
AD-E300 570
10
AD A073766
A073765

DNA 4797P-2

PROCEEDINGS OF THE NUCLEAR BLAST AND SHOCK SIMULATION SYMPOSIUM 28-30 NOVEMBER 1978

Volume II

General Electric Company—TEMPO
DASIAC
816 State Street
Santa Barbara, California 93102

RECEIVED
SEP 13 1979
C

December 1978

Proceedings

CONTRACT No. DNA 001-79-C-0081

APPROVED FOR PUBLIC RELEASE;
DISTRIBUTION UNLIMITED.

THIS WORK SPONSORED BY THE DEFENSE NUCLEAR AGENCY
UNDER RDT&E RMSS CODE B337079464 P99QAXDC00809 H2590D.

DDC FILE COPY

Prepared for
Director
DEFENSE NUCLEAR AGENCY
Washington, D. C. 20305

79 08 28 026

DNA 4797P-2 PROCEEDINGS OF THE NUCLEAR BLAST AND SHOCK SIMULATION SYMPOSIUM 28-30 NOVEMBER 1978

Destroy this report when it is no longer needed. Do not return to sender.

PLEASE NOTIFY THE DEFENSE NUCLEAR AGENCY, ATTN: TISI, WASHINGTON, D.C. 20305, IF YOUR ADDRESS IS INCORRECT, IF YOU WISH TO BE DELETED FROM THE DISTRIBUTION LIST, OR IF THE ADDRESSEE IS NO LONGER EMPLOYED BY YOUR ORGANIZATION.

REVIEW OF THIS MATERIAL DOES NOT IMPLY DEPARTMENT OF DEFENSE INDORSEMENT OF FACTUAL ACCURACY OR OPINION.

DNA PRINTING PLANT

UNCLASSIFIED

SECURITY CLASSIFICATION OF THIS PAGE *(When Data Entered)*

REPORT DOCUMENTATION PAGE		READ INSTRUCTIONS BEFORE COMPLETING FORM
1. REPORT NUMBER DNA 4797P-2	2. GOVT ACCESSION NO.	3. RECIPIENT'S CATALOG NUMBER
4. TITLE *(and Subtitle)* PROCEEDINGS OF THE NUCLEAR BLAST AND SHOCK SIMULATION SYMPOSIUM 28-30 November 1978, Volume II		5. TYPE OF REPORT & PERIOD COVERED Proceedings 6. PERFORMING ORG. REPORT NUMBER
7. AUTHOR*(s)* See individual presentations.		8. CONTRACT OR GRANT NUMBER*(s)* DNA 001-79-C-0081
9. PERFORMING ORGANIZATION NAME AND ADDRESS General Electric Company—TEMPO DASIAC, 816 State Street Santa Barbara, California 93102		10. PROGRAM ELEMENT, PROJECT, TASK AREA & WORK UNIT NUMBERS Subtask P99QAXDC008-09
11. CONTROLLING OFFICE NAME AND ADDRESS Director Defense Nuclear Agency Washington, D.C. 20305		12. REPORT DATE December 1978 13. NUMBER OF PAGES 334
14. MONITORING AGENCY NAME & ADDRESS*(if different from Controlling Office)*		15. SECURITY CLASS *(of this report)* UNCLASSIFIED 15a. DECLASSIFICATION/DOWNGRADING SCHEDULE

16. DISTRIBUTION STATEMENT *(of this Report)*

Approved for public release; distribution unlimited.

17. DISTRIBUTION STATEMENT *(of the abstract entered in Block 20, if different from Report)*

18. SUPPLEMENTARY NOTES

This work sponsored by the Defense Nuclear Agency under RDT&E RMSS Code B337079464 P99QAXDC00809 H2590D.

19. KEY WORDS *(Continue on reverse side if necessary and identify by block number)*

Airblast	DIHEST	Simulation
Ammonium Nitrate Fuel Oil	Environmental Impact	Simulators
BLEST	Ground Shock	Site Selection
Cratering	HEST	Thermal
DABS	Proceedings	Underwater Shock

20. ABSTRACT *(Continue on reverse side if necessary and identify by block number)*

This report contains the papers presented at the Proceedings of the Nuclear Blast and Shock Simulation Symposium held 28-30 November 1978 at the Naval Ocean Systems Center, San Diego, California, under the sponsorship of the Shock Physics Strategic Structures Division (SPSS) of the Defense Nuclear Agency. The symposium provided a forum for the exchange of information on technical approaches and recent accomplishments in the development of nuclear blast and shock simulators. →(cont on p 2)

DD FORM 1 JAN 73 1473 EDITION OF 1 NOV 65 IS OBSOLETE

UNCLASSIFIED

SECURITY CLASSIFICATION OF THIS PAGE *(When Data Entered)*

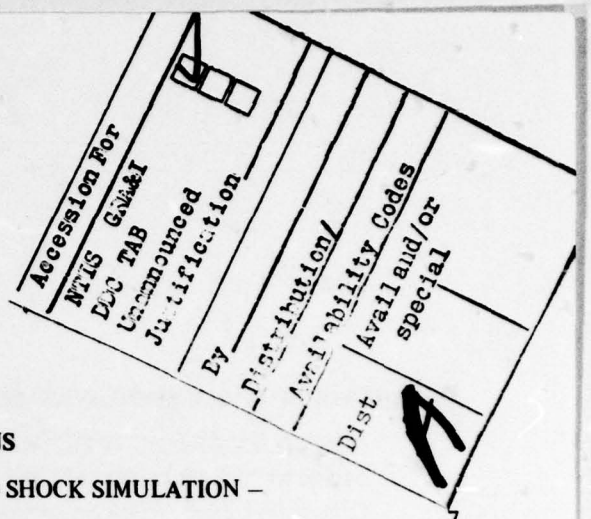

CONTENTS

VOLUME 1

SITE SELECTION AND ENVIRONMENTAL CONSIDERATIONS

TEST SITE SELECTION FOR NUCLEAR BLAST AND SHOCK SIMULATION – LTC J.T. Neal, Air Force Systems Command 7

ENVIRONMENTAL CONSIDERATIONS FOR BLAST AND SHOCK SIMULATION – R.H. Rowland, K.E. Gould, General Electric Company-DASIAC 17

AIRBLAST/THERMAL EFFECTS SIMULATION SESSION

A STATUS AND CAPABILITY REPORT ON NUCLEAR AIRBLAST SIMULATION USING HEST – H.W. Wampler, G.G. Leigh, Civil Engineering Research Facility; Capt. M.E. Furbee, F.E. Seusy, Air Force Weapons Laboratory 27

NUCLEAR AIRBLAST SIMULATION WITH EMPHASIS ON DYNAMIC PRESSURE – Capt. D.P. Martens, DNA Field Command 95

SOME CONSIDERATIONS IN THE DESIGN OF A DYNAMIC AIRBLAST SIMULATOR – J.D. Renick, Air Force Weapons Laboratory 125

NUMERICAL COMPUTATIONS OF SIMULATION TESTS – G.G. Leigh, Civil Engineering Research Facility; C.E. Needham, Air Force Weapons Laboratory 159

FEASIBILITY INVESTIGATION OF A PERMANENT FUEL-AIR EXPLOSIVE BLAST SIMULATOR – R.T. Sedgwick, H.B. Kratz, R.G. Herrmann, T.H. Pierce, Systems, Science and Software 205

THERMAL LAYER SIMULATION BY SOLAR FURNACE RADIATION – T.M. Knasel, M.D. McDonnell, R. Sievers, A. Houghton, Science Applications, Incorporated 253

THE THERMAL RADIATION SIMULATOR DEVELOPMENT PROGRAM – J.F. Dishon III, Science Applications, Incorporated 281

THERMAL/BLAST SIMULATION FACILITIES AT THE U.S. ARMY BALLISTIC RESEARCH LABORATORY – G.Teel, Ballistic Research Laboratory 311

SIMULATION OF TRANSIENT SURFACE LOADS USING PLANE, CYLINDRICAL, AND SPHERICAL BLAST WAVES – H.E. Lindberg, SRI International 327

EFFECTS OF RIBS ON SHOCK WAVE PROPAGATION IN TUBES – T.H. Schiffman, H.F. Korman, TRW Defense and Space Systems Group 365

UNDERWATER SHOCK SIMULATION SESSION

SIMULATION OF THE PULSE FROM AN UNDERWATER NUCLEAR EXPLOSION WITH A PLANAR ARRAY OF EXPLOSIVE SOURCES – A.L. Florence, C.M. Romander, SRI International 387

LOCAL SPHERICITY OF THE ACOUSTIC FIELD GENERATED BY A LINE CHARGE – T.L. Geers, Lockheed Palo Alto Research Laboratory 417

Volume II contains papers from sessions on the following topics:

VOLUME 2

UNDERGROUND SHOCK SIMULATION SESSION

A REVIEW OF PRESENT ESTIMATES OF NEAR SURFACE GROUND MOTIONS FROM NUCLEAR DETONATIONS AT OR NEAR THE EARTH'S SURFACE – Capt. G.W. Ullrich, VELA Seismological Center 7

THE HIGH EXPLOSIVE STANDARD NUCLEAR SOURCE – C.T. Vincent, J.M. Thomsen, Physics International Company 31

GRAVITY-SCALING METHODS APPLIED TO CRATER-INDUCED GROUND MOTIONS AND EFFECTS – K.A. Holsapple, R.M. Schmidt, R.L. Dyrdahl, Boeing Aerospace Company 55

MULTIPLE BURST HE GROUND MOTION GENERATION TECHNIQUES – Capt. R.G. DeRaad, DNA Field Command 93

BLEST – A GROUND SHOCK SIMULATOR – F.E. Seusy, Air Force Weapons Laboratory; H.E. Auld, Civil Engineering Research Facility 123

GROUND SHOCK SIMULATION USING DIHEST – K.B. Simmons, C. J. Higgins, Civil Engineering Research Facility 151

SIMULATION VERSUS STIMULATION – R.J. Port, R&D Associates 177

INSTRUMENTATION SESSION

HE BLAST PRESSURE MEASUREMENTS – Capt. D.J. Ray, Air Force Weapons Laboratory 203

and **HIGH-ENERGY SIMULATION SESSION**

MACH 130 AIR SHOCK ATTENUATION STUDIES – H.D. Glenn, H.R. Kratz, D.D. Keough, R.P. Swift, Lawrence Livermore Laboratory 223

HE SIMULATION OF GROUND SHOCK-INDUCED MX TRENCH COLLAPSE – J.C. Baker, H.R. Kratz, F.I. Peterson, K.D. Pyatt, Jr., L.E. Bailey, J.L. Waddell, Systems, Science and Software 241

COMPUTATIONAL STUDIES OF A VOITENKO COMPRESSOR – P.S. Brown, M.L. Lohman, Lawrence Livermore Laboratory 261

ANFO FOR NUCLEAR WEAPONS EFFECTS SIMULATION – J. Petes, Naval Surface Weapons Center 289

CONVENTIONAL HIGH EXPLOSIVES FOR NUCLEAR SIMULATION – Capt. G.F. Lederman, Jr., Air Force Weapons Laboratory 311

Volume II contains papers from sessions on the following topics:

VOLUME 2

UNDERGROUND SHOCK SIMULATION SESSION

A REVIEW OF PRESENT ESTIMATES OF NEAR SURFACE GROUND MOTIONS FROM NUCLEAR DETONATIONS AT OR NEAR THE EARTH'S SURFACE – Capt. G.W. Ullrich, VELA Seismological Center 7

THE HIGH EXPLOSIVE STANDARD NUCLEAR SOURCE – C.T. Vincent, J.M. Thomsen, Physics International Company 31

GRAVITY-SCALING METHODS APPLIED TO CRATER-INDUCED GROUND MOTIONS AND EFFECTS – K.A. Holsapple, R.M. Schmidt, R.L. Dyrdahl, Boeing Aerospace Company 55

MULTIPLE BURST HE GROUND MOTION GENERATION TECHNIQUES – Capt. R.G. DeRaad, DNA Field Command 93

BLEST – A GROUND SHOCK SIMULATOR – F.E. Seusy, Air Force Weapons Laboratory; H.E. Auld, Civil Engineering Research Facility 123

GROUND SHOCK SIMULATION USING DIHEST – K.B. Simmons, C. J. Higgins, Civil Engineering Research Facility 151

SIMULATION VERSUS STIMULATION – R.J. Port, R&D Associates 177

INSTRUMENTATION SESSION

HE BLAST PRESSURE MEASUREMENTS – Capt. D.J. Ray, Air Force Weapons Laboratory 203

and HIGH-ENERGY SIMULATION SESSION

MACH 130 AIR SHOCK ATTENUATION STUDIES – H.D. Glenn, H.R. Kratz, D.D. Keough, R.P. Swift, Lawrence Livermore Laboratory 223

HE SIMULATION OF GROUND SHOCK-INDUCED MX TRENCH COLLAPSE – J.C. Baker, H.R. Kratz, F.I. Peterson, K.D. Pyatt, Jr., L.E. Bailey, J.L. Waddell, Systems, Science and Software 241

COMPUTATIONAL STUDIES OF A VOITENKO COMPRESSOR – P.S. Brown, M.L. Lohman, Lawrence Livermore Laboratory 261

ANFO FOR NUCLEAR WEAPONS EFFECTS SIMULATION – J. Petes, Naval Surface Weapons Center 289

CONVENTIONAL HIGH EXPLOSIVES FOR NUCLEAR SIMULATION – Capt. G.F. Lederman, Jr., Air Force Weapons Laboratory 311

ATTENDEES

Allen, R.T.	PAC Tech
Armstrong, W.L.	CEL
Auld, H.E.	CERF
Baker, J.C.	SSS
Balachandra, M.	Agbabian
Baron, M.	PWA
Barron, N.	DA/DAMA
Barthel, J.	SSS
Bell, K.	CERF
Bertrand, B.	BRL
Bestgen, R.	FC/DNA
Beyatte, W.	LLL
Bloodgood, V.	NSRDC
Bratton, J.	C/NSC
Brode, H.	RDA
Brown, P.	LLL
Bultmann, E.	C/NSC
Calhoun, D.	CERF
Carpenter, H.	RDA
Coleman, P.	SSS
Colton, J.	SRI
Conley, W.	NSRDC
Conrad, E.	HQ/DNA
Cooper, H.	RDA
Craig, B.	LASL
Craig, J.	SAI
Crenshaw, W.	NARADCOM
Dai, P.	TRW
Davis, H.	MC
Davis, R.	FC/DNA
Deevy, T.	HQ/DNA
Delaar, R.	FC/DNA
Demaris, E.	SSS
Dishon, J.	SAI
Dudash, M.J.	GE–TEMPO
Dyrdahl, R.	Boeing
Edwards, T.Y.	SAMSO
Ernst, C.	MMC
Ethridge, N.	BRL
Fletcher, R.	LB&ERI Inc.
Florence, A.	SRI
Flory, R.	HQ/DNA
Freiberg, R.	NWEF
Furbee, M.	AFWL
Gantick, N.	FC/DNA
Gauthey, R.	NSEC
Geers, T.	LMSC
Giltrud, M.	NSWC
Glenn, H.	LLL
Gordon, J.	NSRDC
Grine, D.	SSS
Hanagud, S.	GIT
Heyman, R.	MMC
Holland, J.	FC/DNA
Holsapple, K.	Boeing
Homes, D.	Aerospace Corp.
Hove, D.	SAI
Huffington, N.	BRL
Hulcher, G.	TRW
Huntington, J.	Acurex
Jaramillo, E.	EG&G
Keefer, J.	BRL
Keller, C.	FC/DNA
Kennedy, L.	GE–TEMPO
Kennedy, T.	HQ/DNA
Kitchens, C.	BRL
Knasel, T.	SAI
Kramer, G.	LLL
Kratz, H.	SSS
Kuhl, A.	RDA

ATTENDEES (Continued)

Lai, J.	TRW
Laupa, A.	Rand
Lederman, G.	AFWL
Leigh, G.	CERF
Lewis, J.	RDA
Lindberg, H.	SRI
Linnerud, H.	JAYCOR
Lipner, N.	TRW
Mackey, J.	EG&G
Malthan, J.	Agbabian
Marlitt, M.	FC/DNA
Martens, D.	FC/DNA
Matalucci, R.	AFWL
McCall, G.	USANACA
McDonnell, M.	SAI
McKay, M.	SAI
McMullan, F.	FC/DNA
Melzer, L.	C/NSC
Merritt, J.	Merritt CASES
Meyer, G.	NOSC
Mills, T.	LLL
Moore, E.	PI
Mortensen, R.	Aerospace Corp.
Nakayama, P.	JAYCOR
Neal, J.	AFSC
Nicholson	NSWC
Noh, W.	LLL
Orphal, D.	CRT
Petersen, C.	SSS
Petes, J.	NSWC
Phillips, J.	CNSC
Pierce, T.	SSS
Pittman, J.	NSWC
Port, R.	RDA
Pusey, H.	NRL
Pyatt, K.	SSS
Quigley, E.	BRL
Radkowski, P.	Radkowski Assoc.
Ranlett, D.	PWA
Ravotto, M.	ARRADCOM
Ray, D.	AFWL
Renick, J.	AFWL
Richmond, D.	LB&ERI Inc.
Rowland, R.	GE–TEMPO
Sachs, D.	Kaman
Safford, F.	Agbabian
Sauer, F.	PI
Schalug, R.	SAI
Schiffman, T.	TRW
Schmidt, R.	Boeing
Schuster, S.	CRT
Sedgwick, R.	SSS
Senseny, P.	SRI
Sevin, E.	HQ/DNA
Shievell, D.	FC/DNA
Shunk, R.	ESI
Stefani, L.	FC/DNA
Strange, J.	WES
Strode, J.	FC/DNA
Sullivan, J.	NAVSEC
Summerfield, M.	PCRL
Teel, G.	BRL
Thomas, J.	FC/DNA
Thomsen, J.	PI
Tillery, R.	NWEF
Triebes, K.	Acurex
Tyler, W.	FC/DNA
Ullrich, G.	HQ/DNA
Ullrich, G.	VELA
Vincent, C.	PI

ATTENDEES (Continued)

Walker, P.E.	LLL	Whitener, J.	RDA
Walker, R.	NSRDC	Williams, J.	AFWL
Wampler, H.	CERF	Wilson, H.	SAI
Waxler, D.	ARRADCOM	Wolf, C.	Acurex
Whang, B.	NSRDC		

UNDERGROUND SHOCK SIMULATION SESSION

A REVIEW OF PRESENT ESTIMATES OF NEAR SURFACE GROUND MOTIONS FROM NUCLEAR DETONATIONS AT OR NEAR THE EARTH'S SURFACE

by

Gilbert W. Ullrich, Capt., USAF

VELA Seismological Center

A Review of Present Estimates of Near Surface Ground Motions From Nuclear Detonations At or Near the Earth's Surface

by Captain Gilbert W. Ullrich

Abstract

Estimates of the ground motion environment are important for design and cost trade studies of land-based weapons systems that may be subjected to the effects from both single and multiple nuclear detonations. In addition, these estimates provide a basis for evaluation of simulation techniques that are designed to replicate this environment. Assessment of the single burst environment estimates indicates that the airslap induced component has been previously characterized. Characterization of the low frequency component, which has been less successful, should be divided into three regions based on range from the detonation point. Characterization of low frequency motions in the close-in range (less than about 900m from a megaton burst) is presently uncertain because of possible significant differences between high explosive and nuclear effects. Characterization of low frequency motions in the far-field region (greater than 1500m from a megaton burst) is improving with understanding developing that the governing physics is Rayleigh Wave effects. Characterization of the transition region (between approximately 900m and 1500m from a megaton burst) is incomplete but the magnitude of motions may be estimated. For sufficiently separated bursts in a multiple burst environment, superposition provides only a baseline with at least enhanced airblast effects and spall contributing to significant variations.

INTRODUCTION

Estimates of the ground motion environment are important for design and cost trade studies of land-based weapons systems that may be subjected to the effects from both single and multiple nuclear detonations. In addition, these estimates provide a basis for the evaluation of simulation techniques that are designed to replicate this environment. Therefore, as a background for the discussion of ground motion simulation, we shall review the present understanding of near-surface ground motions from nuclear detonations on which these estimates are based. In this review, we highlight areas of increased understanding that have developed during research in support of the development of Multiple Launch Point (Ref 1) missile basing systems. We shall first discuss the ground motions expected from a single nuclear detonation and then the effects of multiple, near-simultaneous detonations. We limit our discussion to expectations of near-surface motions resulting within a few seconds from megaton-size detonations within a few kilometers range. The

discussion should, to first order, also be applicable to kiloton size detonations with time and dimensions scaled by cube-root of the yield. The limitations on time and range excludes some possibly important, late-time effects that are poorly understood.

TYPES OF SINGLE BURST GROUND MOTION

Ground motion is produced from the detonation of a nuclear device near the earth's surface through both the initial coupling of radiation from the device (Ref 2) and by the load resulting from the expanding air shock which results from the energy deposited in the air (Fig 1). If the height of burst is sufficient, no radiation will be coupled to the ground and all ground motion will result from the air shock. Thus, airblast-induced ground motion is applicable to a near or above-surface detonation, while radiation-coupled ground motion is applicable to near-surface and buried configurations. We define a buried detonation as one in which no significant air shock is produced.

The expanding air shock can be viewed (Ref 3) as a series of point loads being applied to the surface of the ground as a function of time. At a point just below the ground surface and away from the region below the detonation point, three categories of signals from the series of point loads occurs. One category of signals results from the airblast load directly above the point being considered. The ground motion resulting from this category is designated airslap induced ground motion. A second category of signals results from the transmission through the ground of airblast-induced loads applied closer to, but not at, ground zero. The ground motions resulting from this category of signals will be designated upstream-induced ground motions. The third category of signals, designated as direct-induced ground motions, results at least partially from the airblast loads applied in the ground zero region. The reason for separating this last category of signals from the upstream-induced motion is that the directly coupled energy may also contribute, or even dominate, the direct-induced ground motion.

As a result of the deposition of energy into the ground by both direct coupling and the airblast loading, stress and momentum fields are established which are then either transmitted away by slower propagating waves or dissipated within the region of interest. Transmission mechanisms include shear waves and surface waves; dissipation mechnisms include plastic deformation and work against gravity. Thus, while initial motions are generated as the result of stress wave propagation, additional motion may be the result of either slower propagating waves or insufficient time to dissipate the momentum. This difference is important because cube-root-of-the-yield scaling does not apply to all the mechanisms that stop motion.

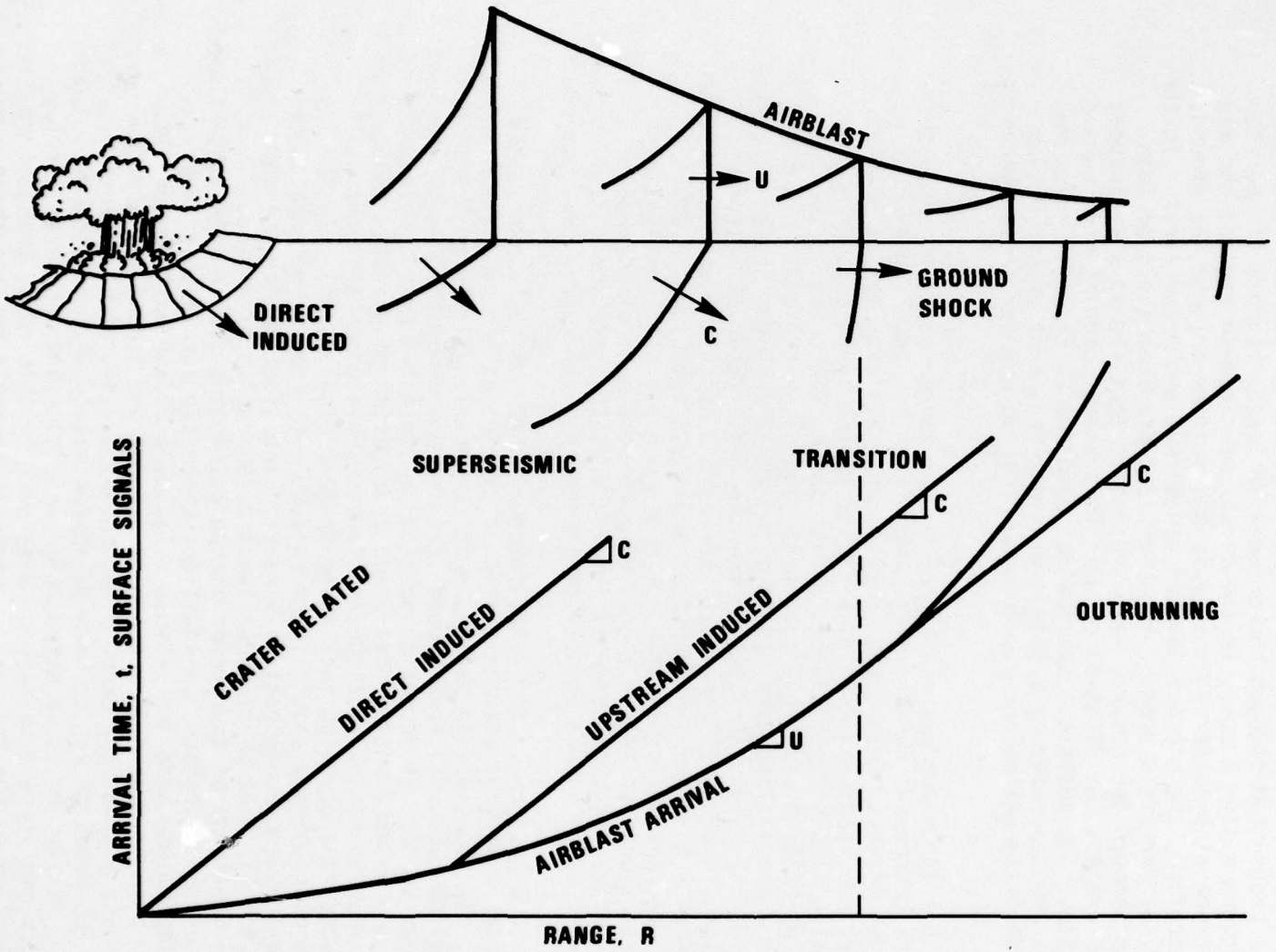

Figure 1. Schematic representation of the ground shock phenomena on a homogeneous site (Ref 4). The top diagram depicts the airblast moving away from the ground zero (crater) region. The lower diagram depicts the arrival times of various ground motions with the airslap motions concurrent with the airblast arrival.

Because of the relative propagation speeds of the air shock and signals propagated through the ground, two major regions of near-surface ground motion occur. In the first, or close-in region, the air shock propagates faster than signals transmitted through the ground, and therefore, the airslap-induced ground motions occur first. In the second, or far-field region, the air blast propagates slower than signals through the ground, with the result that the airslap-induced motions are not the first to occur. This latter condition is termed outrunning. In addition, substantial evidence exists that these two regions are separated by a third, distinct region of ground motion where transitional phenomena, between close-in and far field phenomena, occur.

In all three regions the ground motion may be separated into two distinct components based on frequency (Fig 2). The high frequency component (greater than approximately 5 hertz) is dominated by the airslap induced ground motion, with the timing of this component associated with the arrival of the air shock. The vertical ground motion associated with this component depends on the air shock overpressure, the soil compressibility, and the air shock impulse up to the arrival of the signal reflected from the first material interface with significant impedance increase. The physics of this phenomena has been understood with several successful prediction techniques available (Refs 3, 4, and 5, for example) depending on the desired level of sophistication. While the high frequency component of horizontal ground motion has been somewhat less adequately characterized, important horizontal effects were usually dominated by the low frequency components.

The low frequency components (approximately .5 to 5 hertz) show distinctly different characteristics depending on the ground motion region. In the close-in region, which generally extends to 600 to 900m ($\sim$ 2,000 to 3,000 ft) from ground zero for a one megaton event, the low frequency ground motion was thought to be dominated by a single phase of upward and outward motion that was a combination of upstream induced and direct-induced signals followed by "crater related" motion that attenuated repaidly with increasing range (Refs 3, 4, 5). In the far-field region, beyond about 1,500m ($\sim$ 4,800 ft) from a one megaton event, the low frequency component is a nearly sinusoidal motion, termed "ground roll" (Ref 4), that contains at least a few cycles of motion. The maximum amplitude of the ground motion attenuates slower with range than in the close-in region. In addition, since the airblast is usually traveling slower than the seismic velocities of the earth materials, first motion is upward for points at or near the ground surface, and significant motions may occur prior to, or during, airblast arrival. In the intermediate region between approximately 900 and 1,500m ($\sim$ 3,000 to 4,800 ft), there is no attenuation, and possibly increases, of low frequency amplitude with range. Waveforms in this range change from the close-in type to the far-field type in a presently uncharacterized manner.

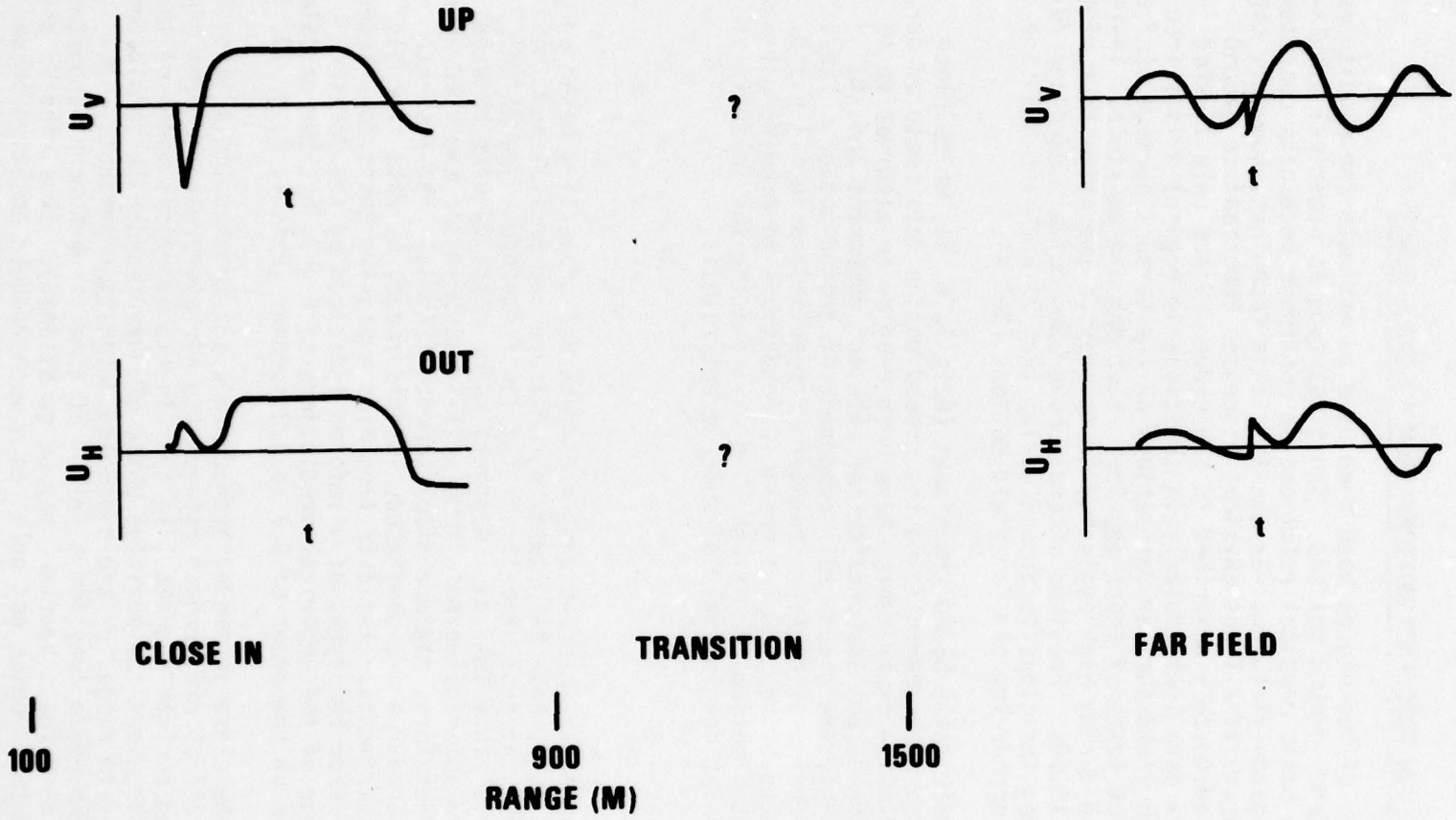

Figure 2. Conceptual velocity histories of ground motions from a one-megaton, near-surface nuclear detonation. Waveforms in the transition region are undefined.

ESTIMATES OF LOW FREQUENCY MOTIONS FROM A SINGLE BURST

Two types of techniques have been used to estimate the magnitudes of low frequency ground motions. The first type is numerical simulations, using basic physical relations in continuum mechanics computer codes, of megaton yield nuclear events. This technique, however, can only be accurate if all the physical processes important to ground motions are adequately described in the codes. Since only limited ground motion data (particularly in the close-in region) exists from previous high yield nuclear detonations on the earth's surface (Ref 6), limited direct tests of those physical relations are possible. Instead, data measured during high explosive tests provide the prime test of the physical relations. Previous attempts have been notably unsuccessful in reproducing the close-in ground motion (Ref 7) but have had some success in reproducing the far-field motions (Ref 4).

Thus, empirically based techniques (Refs 3, 4, 5), which place heavy reliance upon generalizing the ground motion data measured during high explosive experiments, have been used as an alternative to estimating the direct induced/"crater related" component and, to a lesser extent, the ground roll component of ground motion. These empirical techniques, however, require extrapolations in (1) yield, (2) type of explosive, and (3) geologic conditions to provide estimates of ground motion conditions. We will examine the validity of those extrapolations in light of some recent results.

CLOSE-IN

Recent numerical simulations, with material properties based on in-situ test data, have been able to replicate the arrival and, to a lesser extent, the peak velocity of the low frequency component of motion in this range (Ref 8). However, major discrepancies between empirical and numerical predictions still remain in the expected waveforms and, therefore, maximum displacements (Fig 3). The present empirical procedures are dominated, in this range, by data from high explosive experiments. The data from high explosive tests does indeed consistently show the types of waveforms indicated by the "crater related" phase of the empirical predictions of Fig 3, but the unscaled durations are on the order of 0.1 to 0.3 seconds (Refs 4, 7, 9, 10, 11).

Within the close-in range, hydrodynamic air shock calculations indicate essential differences between the air overpressures from high explosive and nuclear sources (Fig 4). In the numerical model of the high explosive event the positive phase of overpressure is terminated, in this close-in range, by the expanding detonation products which sweep the atmosphere away for a period of time (a phenomena supported by measured data that, however, may be questioned). Thus, the HE airblast within this region not only has a much reduced positive phase

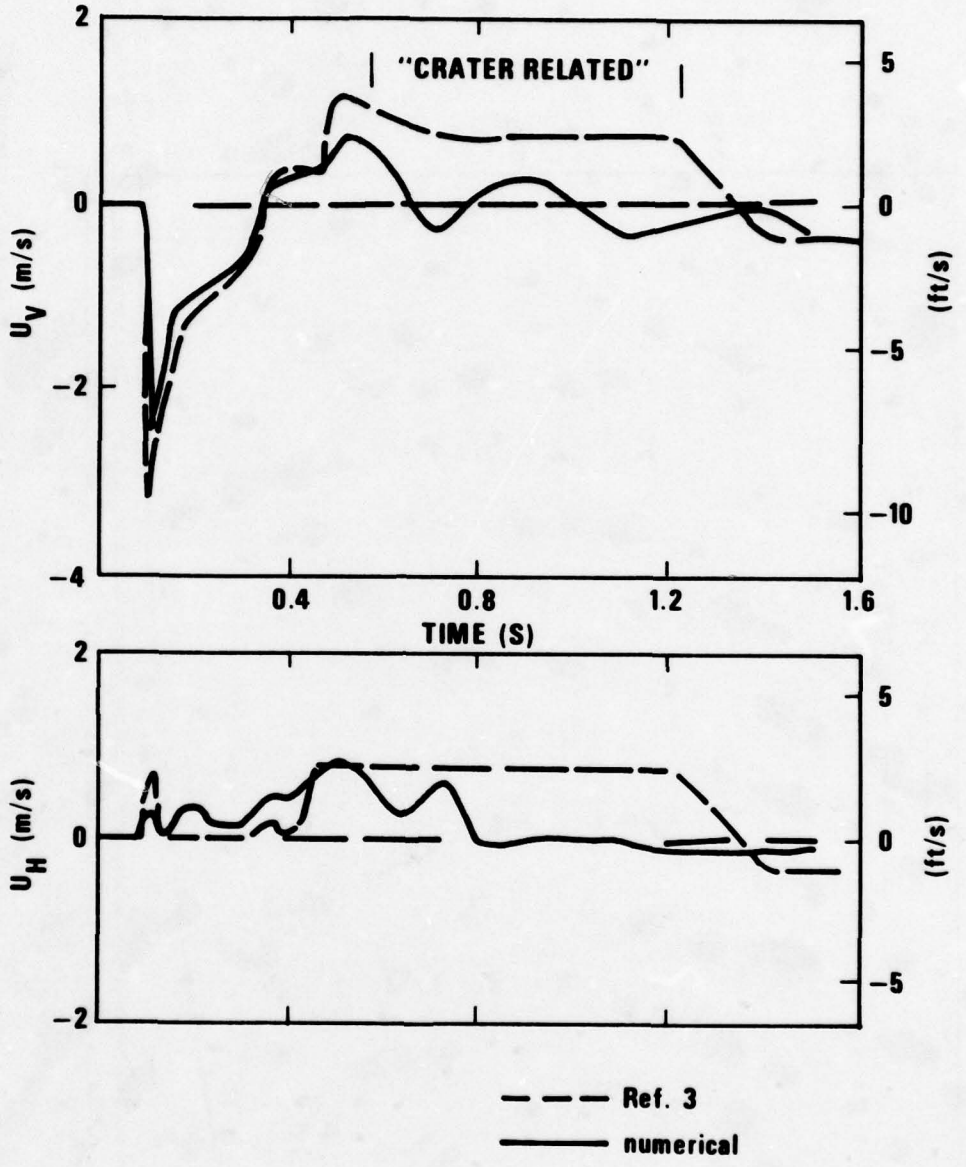

Figure 3. Comparisons of vertical (U_v) and horizontal (U_h) velocity histories from a numerical simulation (solid line) and the prediction using procedures of Reference 3. This comparison is for the 549m (1800 ft) range on a site with a water table at 91.5m (300 ft) depth.

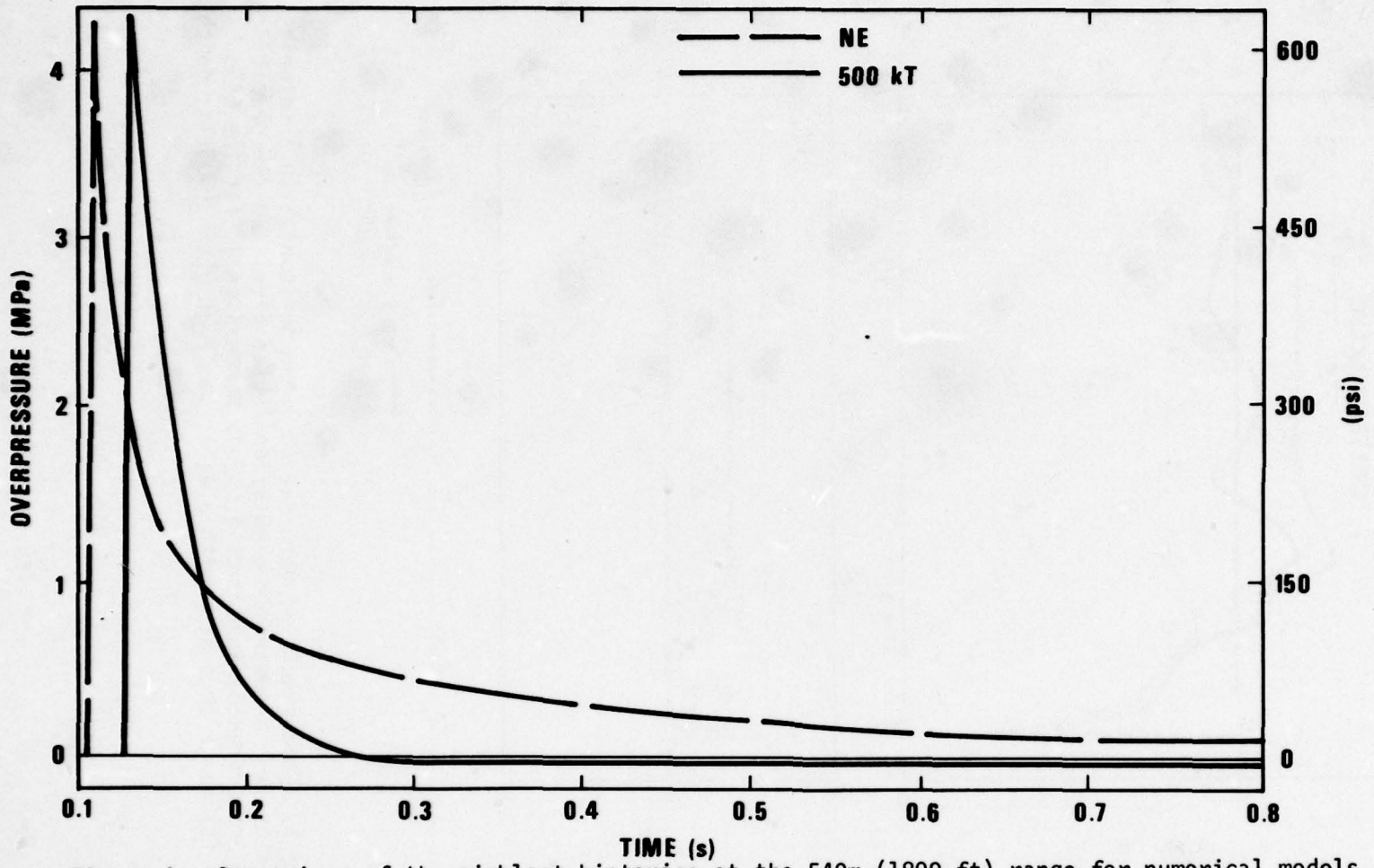

Figure 4. Comparison of the airblast histories at the 549m (1800 ft) range for numerical models of a 1MT nuclear explosion (NE) and a 500KT high explosive detonation. For a 1KT nuclear event (500T high explosive), range and time would be divided by ten.

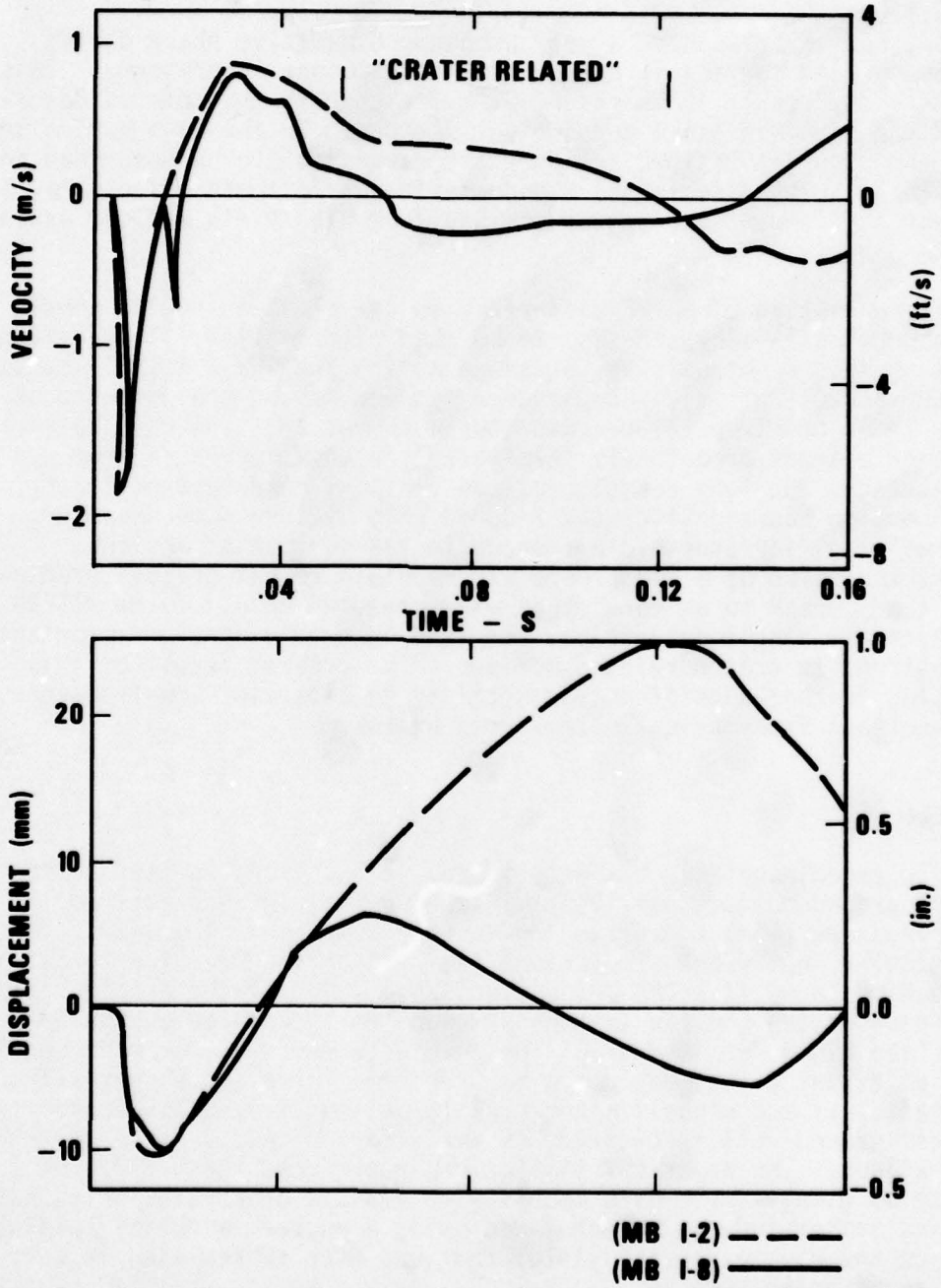

Figure 5. Comparisons of vertical motions at the 0.46m (1.5 ft) depth and 7.6m (25 ft) range from a single charge (MB I-2) with motion at the same depth and 8.0m(26.25 ft) range from the nearest charge interior to a multiple burst charge array (MB I-8). This comparison shows that the upward displacements are inhibited by later airblasts such as that causing the second downward velocity spike on I-8.

duration, but may also have a very pronounced negative phase during which the ground surface is almost free of atmospheric pressure. This difference may result in an essential difference in the mode of deformation from high explosive and nuclear sources. In the high explosive experiments tensile failure and pore air expansion (to be described in the multiple burst discussion) may dominate; while these effects may be much less significant for ground motions from high yield nuclear explosions.

This suggestion of HE/NE difference in the close-in region should be considered only a hypothesis, to be used with caution. Some evidence supporting this hypothesis was obtained during the Phase I experiments of MISERS BLUFF (Ref 12). Comparisons between motion measurements at similar locations from the nearest charge showed that, where airblasts from other charges prematurely terminated the negative phase from the closer charge, the long duration of the vertical component of crater related motion was significantly reduced (Fig 5). We note, however, that similar differences did not occur in the horizontal motions. Further, inclusion of a crude pore air model in recent pretest predictions, that appear to be consistent with measured data, of the MISERS BLUFF Phase II single detonation, resulted in predictions of important contributions to crater related motions. The present result of this discussion is that significant uncertainty in close-in, low-frequency ground motions from nuclear detonations exists.

FAR FIELD

While recent analysis has only increased questions related to the close-in ground motions, analysis of the far-field ground roll is developing a physical understanding of this component of ground motion. In particular, numerical simulations (Ref 13) of the Pre Mine Throw IV-6 and Pre Dice Throw II-1 TNT detonations have demonstrated a good capability of reproducing the low-frequency ground roll measured during both events (see Fig 6 for example). The two tests were conducted on significantly different sites (dry playa for Pre Mine Throw and essentially saturated clays and sands for Pre Dice Throw) and showed substantially different ground-roll frequencies (8 hertz for PMT and 2 hertz for PDT) and durations. The numerical simulations reproduced these differences in spite of using simple site models with elastic properties only, not including crater-induced effects, and using a nuclear airblast loading (of twice the high explosive yield) that was much abbreviated in the ground zero region.

These results led to a further modeling of ground roll using an analytic solution of Rayleigh Surface Waves on layered, elastic sites (Ref 14). The analytic results demonstrated the same capabilities to

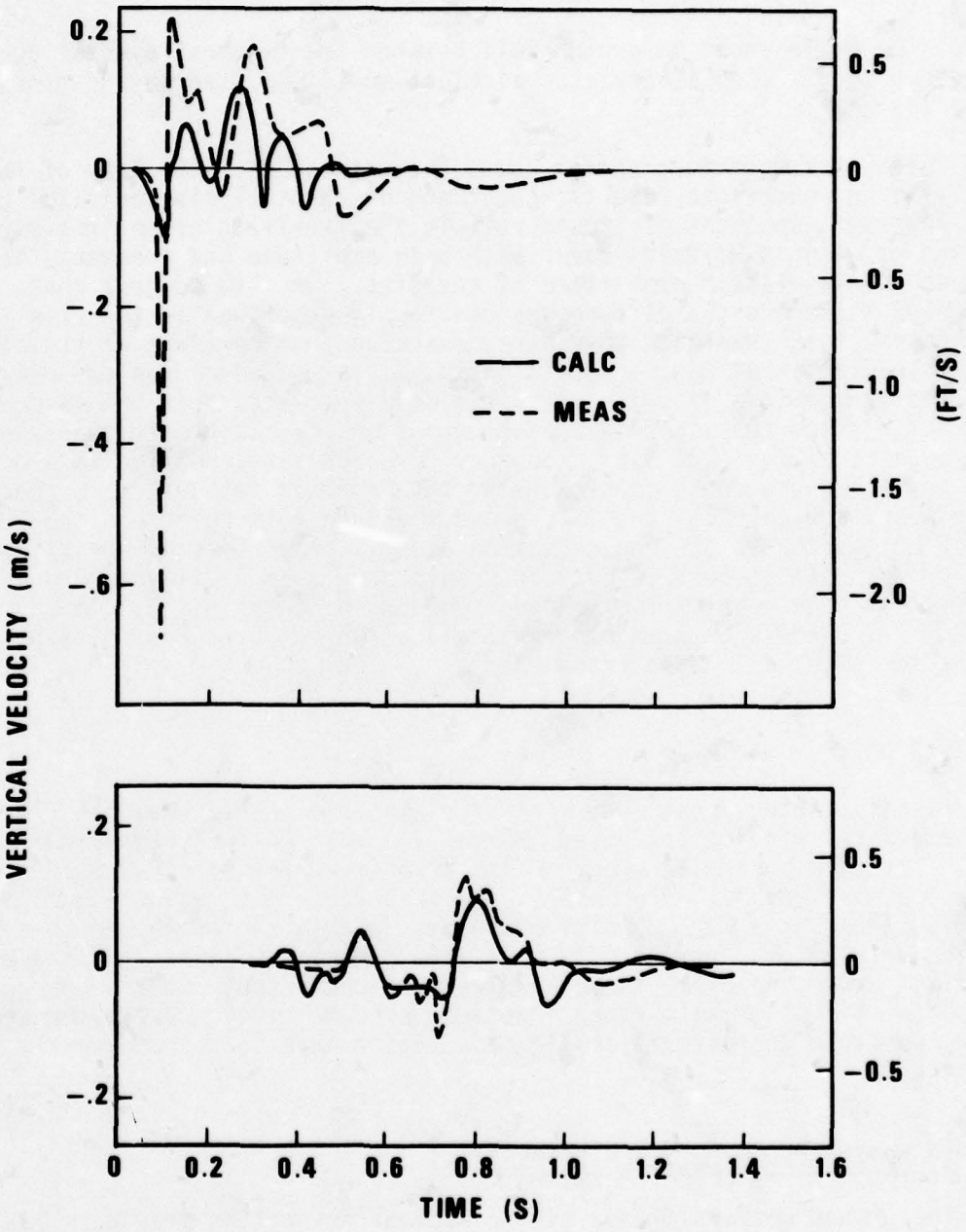

Figure 6. Comparisons of calculated and measured vertical velocities for Pre Mine Throw IV-6 at the 1.5m (5 ft) depth and the 97.6m (320 ft) and 357m (1170 ft) ranges. The top is the nearer range.

model the differences in ground roll between the two test events, again provided that a much abbreviated airblast model was used in the ground zero region.

While some questions remain about the general applicability of these analytic and numerical results, the trend of the analysis indicates that the dominant component of ground roll in the far-field ground motions is a long wavelength Rayleigh Wave, with both amplitude and frequency that depend on the elastic properties of the site. We also suggest that, although there are the differences previously described in the close-in airblasts, these Rayleigh Waves are generated from portions of the airblast loadings that may be sufficiently similar between high explosives and nuclear devices of twice the yield. We speculate that the loading characteristics that control are the gross energy, in the frequency ban of the natural Rayleigh Wave frequency for each site, coupled to a depth of 1/2 to 1/3 the depth comparable to the range of interest. If these hypotheses are correct, then (1) present ground roll relations should be modified to express the dependency on elastic properties of the site, (2) ground roll in surface nuclear events should be similar to ground roll in surface high explosive events of one-half the yield, and (3) ground roll should be simulated by replicating only the controlling characteristics of the upstream load.

TRANSITION

Finally, both recent numerical simulations of nuclear events (Ref 15) and empirical predictions based on measured data (Ref 5), have indicated that a transition region should exist between approximately 900 and 1,500m ($\sim$ 3,000 to 4,800 ft), from a one megaton nuclear detonation. Numerical results that had a high density of output in this region showed that peak motion values were very sensitive to, and sometimes increased with, range. To first order, however, these results were consistent with no change in magnitude of motion with range. Because of complexity and limited attention, waveform characteristics in this region have been inadequately described.

GROUND MOTIONS FROM MULTIPLE DETONATIONS

The ground motions from a single nuclear detonation provide a basic background for all land based systems designed to survive a nuclear attack. However, the emergence of attack vehicles with multiple warheads has resulted in the need to describe the environment from multiple, near simultaneous detonations. As a result of this need, a two phase program of high explosive experiments, designated MISER'S BLUFF, has been conducted to measure the effects of multiple, simultaneous detonations on airblast and ground motion environments (Ref 16).

The principal objective of the Phase I tests was to obtain data from a series small-scale multiple-burst experiments to develop waveform synthesis procedures for predicting ground motions interior and exterior to a multiple charge array (Ref 17). The multiple-burst array design was developed by considering an attack on a hexagonal closely-spaced array of launch points where two-thirds of the launch points were targeted (Fig 7). The unit geometry of such an attack becomes a single ring of 6 charges at the corners of a hexagonal, equally spaced from the center point, with the distance between charges equal to the distance from any charge to the center. The first logical extension of this geometry, which requires 24 charges, is 3 rings of charges, formed by locating charges at the corners of an inner hexagon surrounded by 6 outer hexagons. In this discussion, we shall use data from a single charge event (I-2), a 6 charge event (I-4), and a 24 charge event (I-8).

Since an obvious method of predicting ground motion produced by the detonation of multiple charges is the direct addition (superposition) of the ground motions produced by each charge, the principal questions that were asked during the analysis of Phase I ground motion data were (1) "In what regions of the multiple burst test bed did superposition work?" and (2) "What were the mechanisms that influenced ground motions during the times that superposition failed?" Prior to the Phase I experiments, a review (Ref 17) had indicated that superposition did not always work; however, this conclusion was based on data from multiple charge experiments where there was thought to be strong inelastic interactions between bursts. The charge spacing during the Phase I tests was probably sufficient to preclude these inelastic interactions. Probably as a result, all motions exterior to the charge arrays and at depth interior to the charge arrays were adequately characterized by superposition (Ref 12).

However, superposition was unsuccessful in modeling the motions from near-surface masurements interior to the array. Comparison of the vertical velocity measured at the .46m (1.5 ft) depth near the center of the I-4 array with the band of waveforms constructed by superposition of the single burst data (Fig 8) shows at least four examples of the failure of superposition. The first failure is the peak downward velocity at approximately 25ms (milliseconds) which is underestimated by superposition because of the enhancements, beyond superposition, in air overpressure above the measurement location. The second failure is in the first upward peak at 50ms which is somewhat overestimated by superposition. The third failure is that the downward acceleration following the first upward peak is much greater in the superposed wave than in the multiple burst data. The multiple burst data indicates a gravitational acceleration downward; the single burst data, even before superposition, had a downward acceleration that was greater than could be produced by gravity alone. Apparently, the material in the multiple burst spalled after the rebound; however, the material in the single burst did not spall at this depth. Indeed, tensile failure, if it occurs, will result

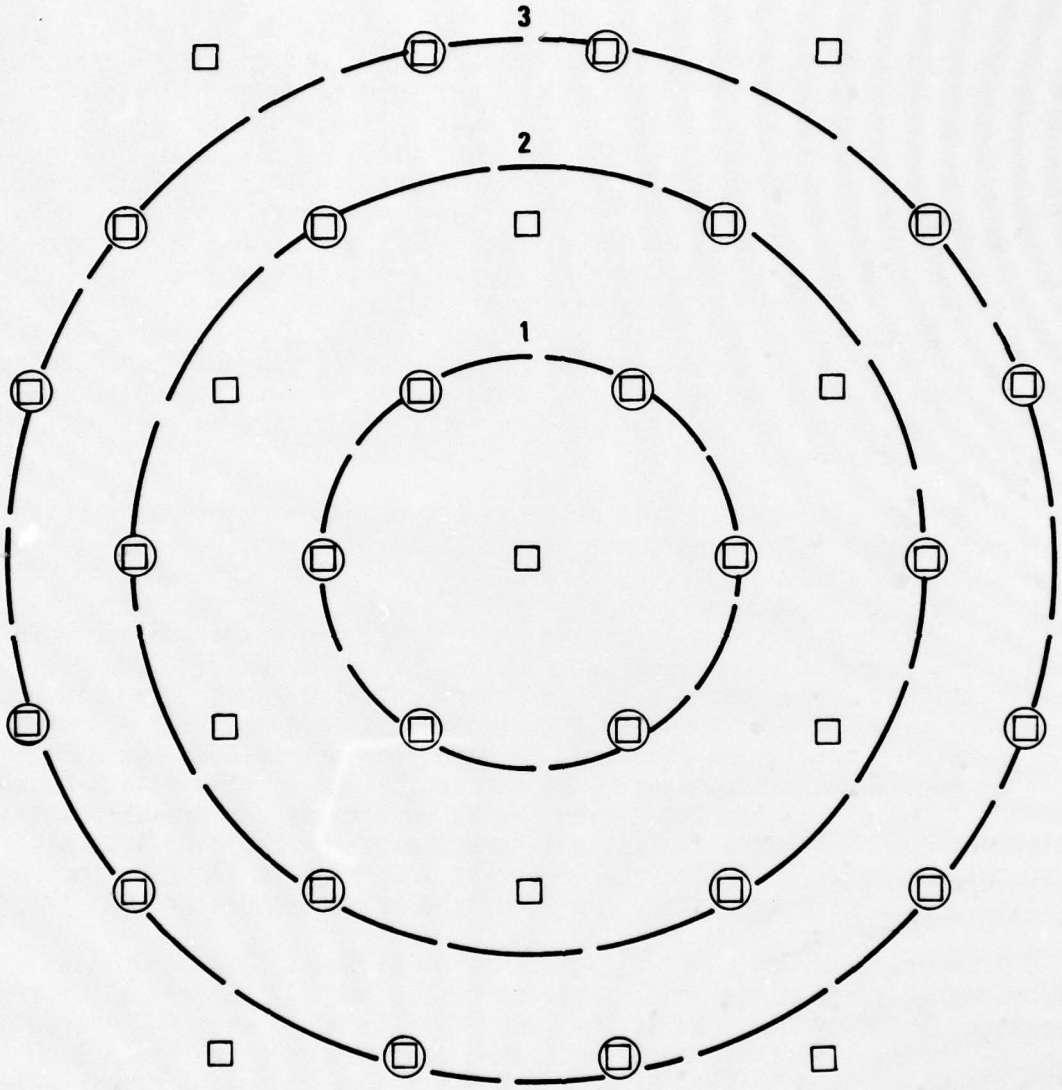

Figure 7. The geometry produced by considering a hexagonal packing of launch points where every third launch point is not targeted. The launch points are represented by squares, and the targeted launch points are represented by squares in circles.

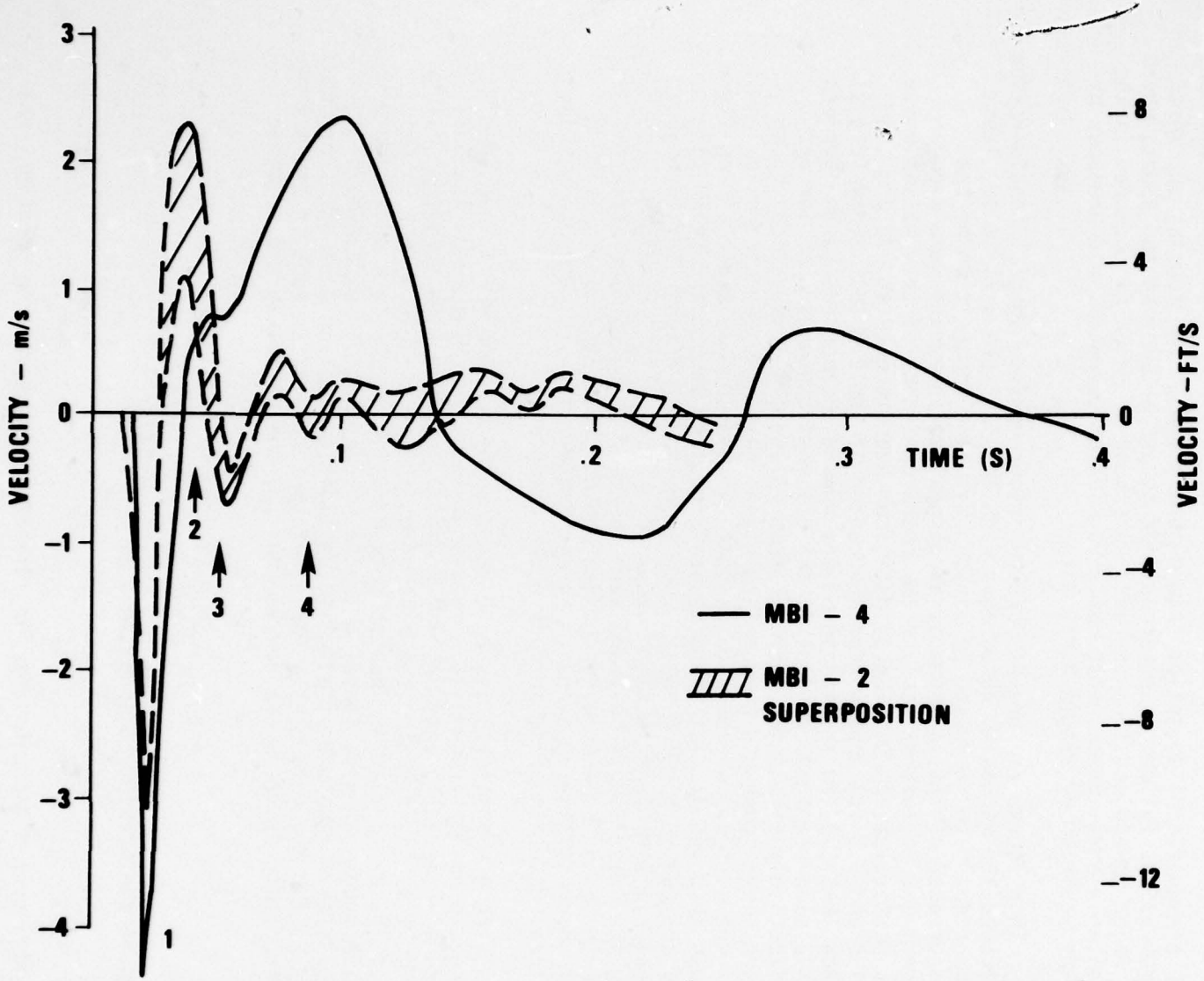

Figure 8. Comparison of measured vertical motion at the .46m (1.5 ft) depth near the center of the MB I-4 array with the band produced by superposition of single burst (MB I-2) measurements (Reference 18).

in a significant deviation from superposition. The fourth, and most impressive, failure of superposition occurs between 60 and 250ms, where a major upward and then downward component of velocity occurred in the multiple burst experiment, while no similar component was produced by superposition of single burst data.

This fourth failure of superposition requires special consideration because the mechanism associated with this failure will become less important with increases of yield. With the recognition of the occurrence of this phenomena, additional measurements were made on event I-8 to further isolate the characteristics of this motion phase. In particular, comparison of data from measurements at .30 and .46m (1.0 and 1.5 ft) depths near the center of the I-8 test array (Fig 9) show that (1) the initiation of the upward motion propagated downward at a slow propagation velocity and (2) that the upward motion was effectively terminated (earlier than in the I-4 observation) by an even slower downward propagating signal that was generated as a result of the airblast arrivals (with peak overpressure an order of magnitude less than the initial overpressure) from the second and third rings of charges in the I-8 array. Additional observations (Ref 12) showed that similar upward motions occurred, at .46m (1.5 ft) depth, elsewhere in the Phase I test beds and were observed 20 to 25 msec after the beginning of an airblast negative phase. Thus, the fourth failure of superposition appeared to be associated with a slowly propagating signal resulting from surface underpressures.

These characteristics have been explained (Ref 12) by considering the expansion stress-strain relationship of the mixture of the soil and air initially entrained in the soil, using a simple piston analogy (Fig 10). By dividing the mass of soil into a rigid piston of mass $\rho_o \ell_o$ (where ρ_o is the in-situ soil density, and ℓ_o is a unit length) with length $(1-\eta)\ell_o$ (where η is the volume fraction of air-filled voids) and a volume of air with negligible mass and an initial pressure of P_o for the volume $\eta\ell_o$; for a constant unit cross section and assuming no air flow, we can derive (Ref 12) the stress-strain relation

$$P = P_o \left\{ \frac{\eta}{\varepsilon + \eta} \right\}^{\gamma} \qquad (1)$$

where the strain, ε, is defined as

$$\varepsilon = \frac{\ell}{\ell_o} - 1 \qquad (2)$$

and γ is the gas constant for adiabatic expansion. In addition, the sonic velocity is then

$$C^2 = \left(\frac{\gamma P_o}{\eta \rho_o}\right) \cdot (\varepsilon + 1)^2 \cdot \left(\frac{\eta}{\varepsilon + \eta}\right)^{\gamma + 1} \qquad (3)$$

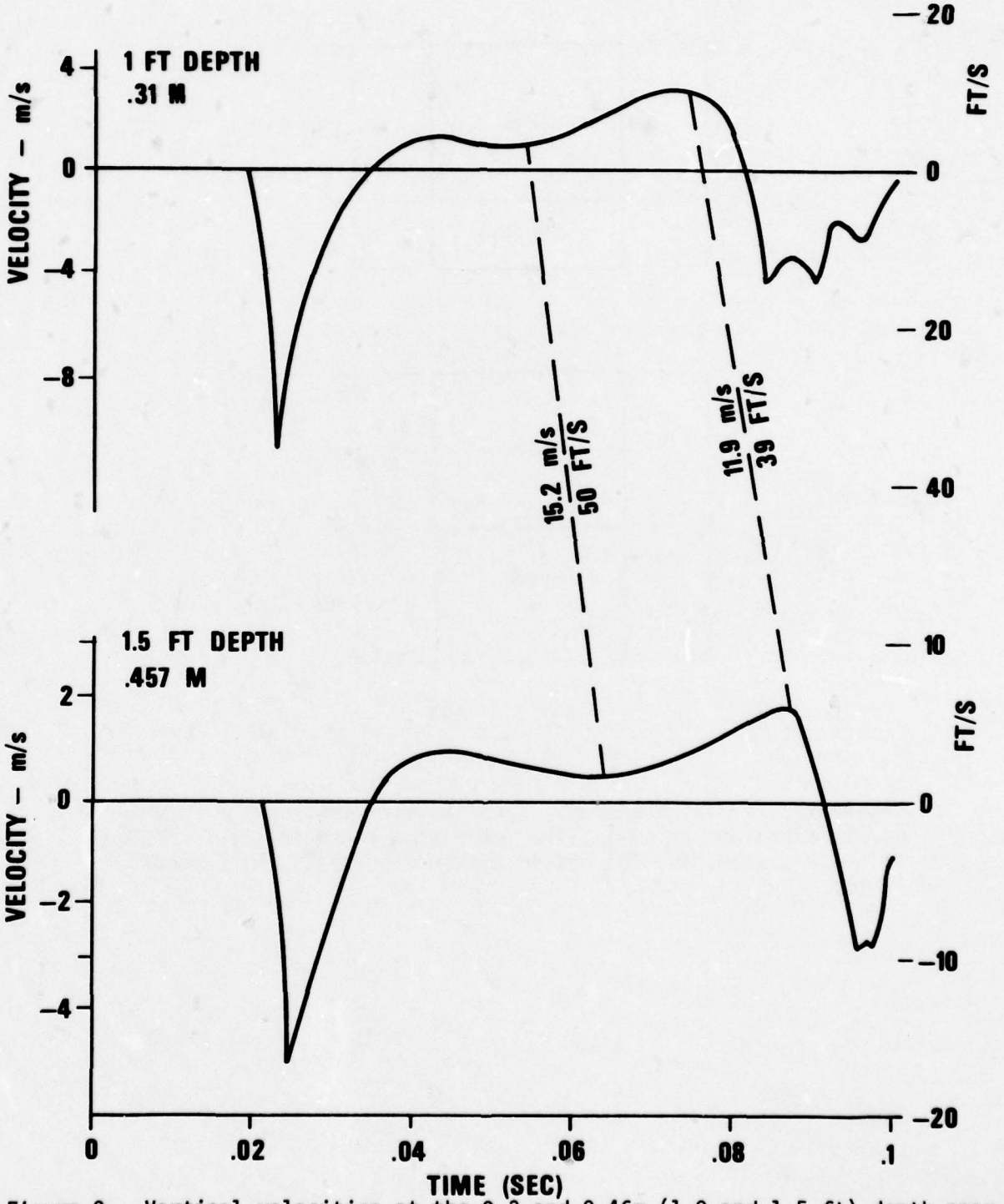

Figure 9. Vertical velocities at the 0.3 and 0.46m (1.0 and 1.5 ft) depth near the center of MB I-8. The data indicate that the upward acceleration was initiated at the shallower gauge 0.01 sec before the deeper gauge and was terminated by a downward propagating wave.

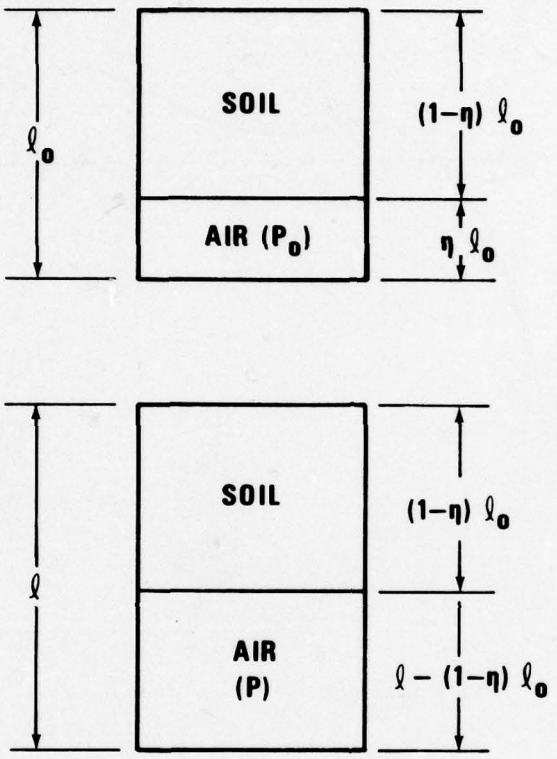

Figure 10. A piston analogy, ignoring air flow, of the expansion of air entrained in soil. The top piston represents the reference soil-air system, and the bottom piston represents the expanded system.

providing an unstrained wave speed of

$$C^2 = \frac{\gamma P_o}{\eta \rho_o} \qquad (4)$$

When we use (Ref 12) a γ for air of 1.4, an initial pressure of 100 kPa ($\sim$ 14.7 psi), an initial density of 1.7 Mg/m^3 and an η of .25, then from (4) we obtain the unstrained wave speed of 18.3 m/s (60 ft/s) which is similar to the wave speeds shown in Fig 9.

Thus the mechanism, designated pore-air expansion, associated with the upward motion that produced the fourth failure of superposition is identified as the expansion, caused by a negative phase of overpressure, of the air originally entrained in the soil. This mechanism is time-dependent and is delicately balanced between overburden weight and magnitude of underpressure. Calculations using models of this process show that it becomes much less significant in megaton size detonations, than in yields associated with high explosives, because of the increased influence of gravitational effects. However, because the process is a response to transient reductions in atmospheric pressure (negative phases of overpressure) and, as discussed earlier, the region where "crater related" motions were measured may be subjected to a pronounced negative phase of overpressure, this process may play a major role in producing motions that have been attributed to cratering effects.

SUMMARY

We thus provide the following assessment of the present understanding of ground motions from single, and multiple, nuclear detonations. In the single burst case the ground motion may be divided into a high frequency and low frequency component. The high frequency component is generated by the local airslap. The low frequency component, however, represents the transmission of, and response to, stresses transmitted through the ground from both local and non-local energy sources.

The physics of the vertical component of high frequency ground motion has been understood, with the horizontal motion less adequately treated. Thus, prediction techniques exist and simulators (such as HEST and DABS) that model the local airblast also model the high frequency ground shock.

The physics that control the low frequency ground motions has not been well understood. The phenomena, and understanding (which is still uncertain) associated with low frequency motions differ as a function of range, as indicated in Table I for a one-megaton nuclear detonation. In the close-in region there are significant differences between the airblast characteristics from nuclear and surface high-explosive detonations.

TABLE I

SUMMARY OF LOW FREQUENCY GROUND MOTION KNOWLEDGE

REGION	OVERPRESSURE (MPa)	RANGE (M)	HE/NE EQUIVALENCE	MAGNITUDE ESTIMATES	WAVEFORM ESTIMATE
CLOSE-IN	1.2	<900	NO	U - YES D - NO	NO
TRANSITION		<900 <1500	?	YES	?
FAR-FIELD	.4	<1500	YES	YES	YES

? - Not defined

Uncertainty associated with all statements

These differences may result in an essential unsimilarity in the duration of motion, with the surface high-explosive source enhancing this duration. Thus, while the maximum velocity associated with the low frequency ground motion can be approximated, the displacement and waveforms are in question. Therefore, simulators (such as MINE THROW and centrifuge tests) should be evaluated for their phenomena definition, and not phenomena replication, potential. In the intermediate region the phenomena is ill-defined, possibly as a result of inadequate study, but the magnitudes of motion can be estimated. Therefore, one may be able to define requirements for motion magnitudes; and stimulation, (possibly by multiple DIHEST lines) as opposed to simulation, may be sufficient. In the far-field region, developing understanding is indicating the governing physics should be similar in high explosive and nuclear detonations. In addition, apparently only limited explosion-characteristics need to be replicated permitting the use of BLEST, DIHEST, or buried charge simulators, with simulation verification and effects replication possible for this region.

The single burst environment definition provides a basic building block for multiple burst environment definition. For sufficiently separated bursts in a multiple burst environment, superposition provides a baseline with at least enhanced airblast effects, tensile failure, and pore air effects (described in the multiple burst discussion) contributing to significant deviations. Of these latter effects, the airblast enhancements and tensile failures prior to airblast arrival are expected to remain important at large yields.

REFERENCES

1. , 1976, MX Weapon System Concept Validation Phase Survivability/Vulnerability Program Plan, Space and Missile Systems Organization, Norton AFB CA 92409.

2. Knowles, C. P. and H. L. Brode, 1977, "The Theory of Cratering Phenomena, an Overview," in Impact and Explosion Cratering (D. J. Roddy, R. O. Pepin, and R. B. Merrill), Pergamon Press, New York, pp 869-895.

3. Crawford, R. E., C. J. Higgins, and E. H. Bultmann, 1974, The Air Force Manual for Design and Analysis of Hardened Structures, AFWL-TR-74-102, The Air Force Weapons Laboratory, Kirtland AFB NM 87117.

4. Lipner, N., D. C. Anderson, and P. K. Dai, 1975, Ground Motion Environments for Generic Site Conditions, 26128-6004-RU-00, TRW Systems Group, Redondo Beach CA 90278.

5. Cooper, H. F., 1978, "Blast and Shock Effects Pertinent to MX (An Annotated Briefing)," RDA-TR-103706-001, R and D Associates, Arlington VA 22209.

6. Stubbs, J., 1977, Redigitization and Superficial Analysis of the Ground Motion Data From Selected Surface Burst Nuclear Experiments, DNA 4088F, Physics International Company, San Leandro CA 94577 (Unpublished).

7. Bratton, J. L., 1973, "Middle Gust-Mixed Company Comparisons," in Proceedings of the Mixed Company/Middle Gust Results Meeting Vol II, DNA 3151P2, General Electric Company - TEMPO (DASIAC), Santa Barbara CA 91302, pp 268-295.

8. Dzwilewski, P. T. and G. W. Ullrich, 1978, Numerical Simulations of the Cratering and Ground Shock from Actual High Explosive and Nuclear Tests, report in preparation, the Air Force Weapons Laboratory, Kirtland AFB NM 87117.

9. Cooper, H. J., and F. M. Sauer, 1977, "Crater-Related Ground Motions and Implications for Crater Scaling," in Impact and Explosion Cratering (D. J. Roddy, R. O. Pepin, and R. B. Merrill, eds) Pergamon Press, New York, pp 1133-1163.

10. Ingram, J. L., 1975, Middle North Series Mixed Company Event: Ground Shock from a 500-ton High Explosive Detonation on Soil over Sandstone, POR 6613, US Army Engineer Waterways Experiment Station, Vicksburg MS 39180

11. Edwards, T. Y. and G. L. Perry, 1976, Middle North Series, Pre Dice Throw II Events, Preliminary Results Report, DNA-POR-6904, Defense Nuclear Agency.

12. Ullrich, G. W., 1978, "Airblast/Ground Motion Effects from Simultaneous Detonations of High Explosive Charges," in Nuclear Technology Digest, AFWL-TR-78-110, Air Force Weapons Laboratory, Kirtland AFB NM 87117, in publication.

13. Auld, H., University of New Mexico Civil Engineering Research Institute, Private Communication.

14. Murphy, J., Computer Sciences Corporation, Private Communication.

15. Ullrich, G. W., 1978, Multiple Aim Point Ground Shock Environment Definition, report in preparation, The Air Force Weapons Laboratory, Kirtland AFB NM 87117.

16. DeRaad, R., 1978, paper presented in this conference.

17. ----, 1977, A Review of High Explosive Testing to Investigate Ground Motions Pertinent to the MX Multiple Aim Point System, unpublished report prepared for the Defense Nuclear Agency/SPSS by the Data Analysis Working Group.

18. Bratton, J. L., 1977, "Fifth Progress Report on the MISERS BLUFF Analysis and Waveform Synthesis Effort," to the Defense Nuclear Agency/SPSS, Science Applications, Inc., Suite 216, 2201 San Pedro NE., Albuquerque NM 87110, December, 1977, Contract DNA 001-77-C-0301.

ACKNOWLEDGMENT

This work was accomplished while the author was at the Air Force Weapons Laboratory under Job Order Number WDNS5801, sponsored by the Defense Nuclear Agency under Subtask Y990AX5B255, Ground Shock Environment Definition. We would like to acknowledge the very helpful comments of Lt Col Matalucci and Mr. Thomas, of the Air Force Weapons Laboratory, and Mr. Lipner, of TRW Systems Group, that much improved this paper. We would also like to acknowledge the guidance provided by Dr. Cooper and Mr. Port, of R&D Associates, Mr. Bratton of SAI, and especially Mr. S. Melzer, of the AFWL, during this study.

THE HIGH EXPLOSIVE STANDARD NUCLEAR SOURCE

by

Coye T. Vincent

Jeffrey M. Thomsen

Physics International Company

INTRODUCTION

Since the advent of the Nuclear Test Ban Treaty, the Defense Nuclear Agency and the Armed Service Laboratories have relied to a large extent on chemical explosive sources for the proof testing of structures and military equipment against the nuclear airblast and ground shock environment. The phenomenological investigation of nuclear effects, especially investigations concerning cratering and ground motion, have relied upon chemical explosive to simulate the nuclear source. In both usages, simulation implies replication of only the nuclear effects of interest. In this study we have limited the simulation objective to the direct- and cratering-induced ground shock, the airblast-induced ground shock and the airblast. This is graphically illustrated in Figure 1. How well high explosive simulation sources replicate the airblast from nuclear weapons can be readily evaluated since considerable data exists for atmospheric nuclear tests made prior to the Nuclear Test Ban Treaty. In addition, the computational aspects of both high explosive and nuclear effects have been studied in considerable detail.

In May, 1970, Physics International Company (PI) proposed a method of using chemical explosives to reproduce the cratering- and direct-induced ground motions of a nuclear surface burst. This method has become known as the MINE THROW technique.

The first test of this technique was the MINE THROW I event. This event had as its objective the reproduction of the directly coupled ground motion produced by the JOHNIE BOY nuclear event which was a 500 ton nuclear explosion buried at 58.5 cm in Area 18 alluvium at the Nevada Test Site. No attempt was made to match the airblast overpressures on MINE THROW I. As the coupled airblast energy did not appear significant, it was postulated that the crater formation for this event was dominated by the directly-induced motion and would not be severely influenced by the difference in airblast between the JOHNIE BOY event and MINE THROW I.

The specific technique for designing the MINE THROW I experiment is as follows. The contour of constant peak stress was obtained from the finite difference calculations of the JOHNIE BOY event, corresponding to the detonation pressure of the explosive used. At each point along that contour, both the pressure as a function of time, P(t), and the time integral of P(t), or specific impulse, were also determined from these calculations. An explosive charge was then shaped in such a way that it reproduced the pressure history and the total specific impulse along this contour. In practice, an iterative series of finite difference calculations were performed, tailoring the high explosive

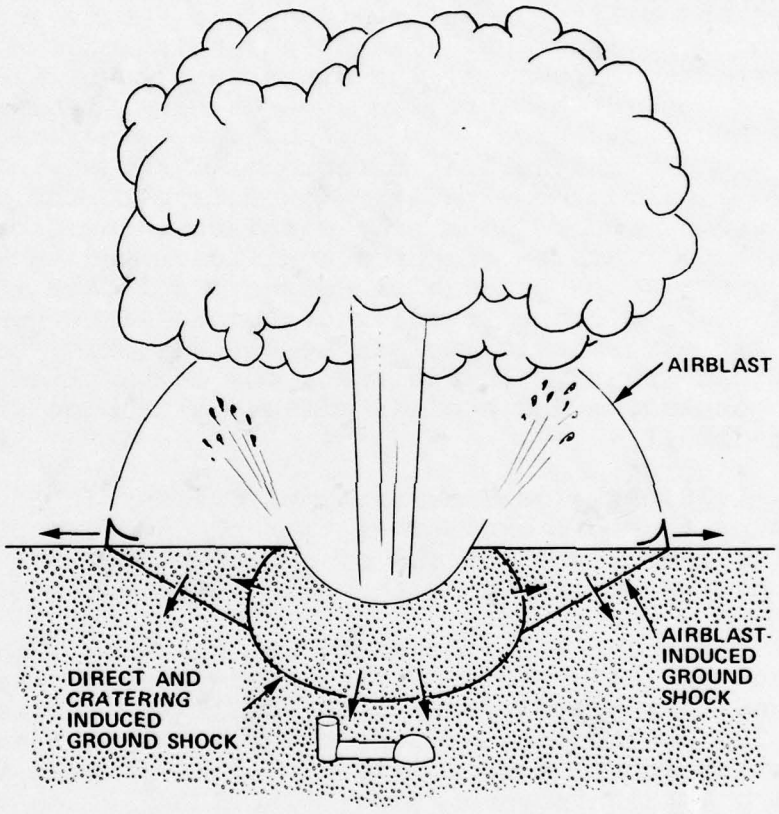

Figure 1 High explosive simulation of nuclear detonation.

to produce the same boundary and initial conditions along the above described contour.

The final charge configuration is shown in Figure 2. A comparison of the final craters for MINE THROW I and JOHNIE BOY showed an agreement in volume and shape within 11 percent. Although JOHNIE BOY had only a few ground motion gages, and these were placed at a large radius from the source, the corresponding gages on MINE THROW I showed very similar displacements and ground motion waveforms. A complete description of the MINE THROW I event is given in Reference 1.

The results show that the MINE THROW technique is a valid technique for reproducing the directly-induced ground motion of a nuclear surface burst of a known degree of coupling.

Subsequent to the MINE THROW I experiment, PI performed calculations (Reference 2), on an explosive configuration which would simulate the directly-induced ground motion of the CACTUS event, a 17 Kt surface nuclear explosion at the Pacific Proving Ground. In this case, the relative airblast-induced motions were much larger than for JOHNIE BOY. It became clear from these calculations that the airblast-induced motions (see Figure 3) on the horizontal plane added a significant impulse that should be included in the simulation technique. Thus, in addition to the target response effects of airblast, and airblast-induced ground motions, there are important phenomenological reasons why a standard cratering simulation technique should include the proper pressure profiles and timing of the airblast. The requirements for this airblast addition is shown in Figure 4.

In March, 1976, Physics International Company proposed a method for applying the required close-in airblast loading to the ground surface in conjunction with the MINE THROW technique to better simulate the cratering-induced and airblast-induced ground motions. This technique is schematically shown in Figure 5. The MINE THROW charge is shown coupled at its edges to a surface charge which extends in a thin sheet above the ground surface to a range of approximately 20 meters. The subsurface charge design is accomplished by using the technology developed for MINE THROW I.

The surface charge design required development of a new technology. This effort has been underway for about two years. During that time a series of one-and two-dimensional calculations were performed to establish the design elements such as the explosive thickness, the standoff distance and initiation pattern for an ANFO surface explosive charge. As a result of that work, a preliminary surface charge design was developed.

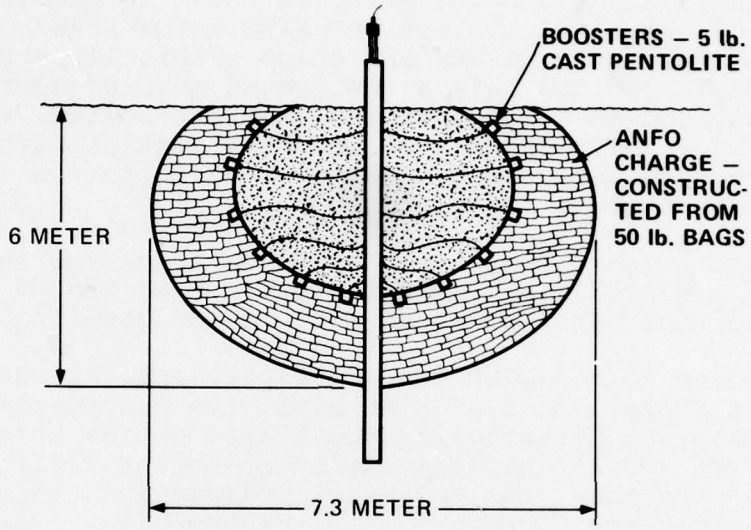

STATUS: FULL SCALE FIELD SIMULATION OF 0.5 kt JOHNIE BOY NUCLEAR EVENT SUCCESSFULLY CONDUCTED ON DECEMBER 15, 1971

RESULTS: JOHNIE BOY DIRECT AND CRATERING-INDUCED GROUND MOTION AND FINAL CRATER WELL SIMULATED. NO ATTEMPT TO SIMULATE AIRBLAST-INDUCED GROUND MOTION

78-11-44

Figure 2 MINE THROW 1-- Direct and cratering-induced ground motion, cratering, and ejecta.

CONCEPT

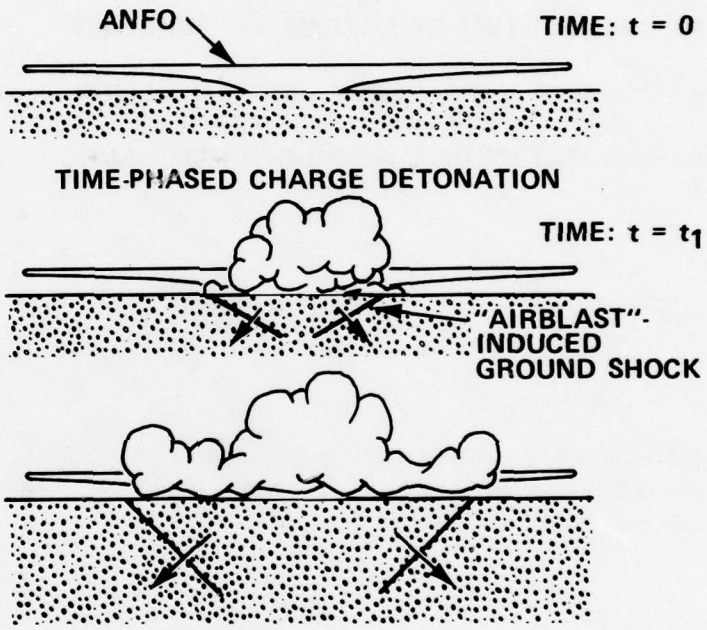

STATUS: CONCEPT DEVELOPMENT AND VALIDATION PROGRAM IN PROGRESS. INITIAL CHARGE GEOMETRIES DESIGNED AND INITIAL COMPUTER CALCULATIONS IN PROGRESS.

78-11-45

Figure 3 Airblast-induced ground motion.

- CORRECT TIME OF ARRIVAL OF "AIRBLAST"
- CORRECT PEAK PRESSURE AS FUNCTION OF RANGE
- CORRECT IMPULSE AS FUNCTION OF RANGE

DESIRABLE

78-11-46

REASONABLE APPROXIMATION TO NUCLEAR SURFACE BURST AIRBLAST FOR $P \lesssim 100$ psi (i.e., AT A RANGE $\gg$ SOURCE DIMENSIONS)

Figure 4 Requirements for airblast.

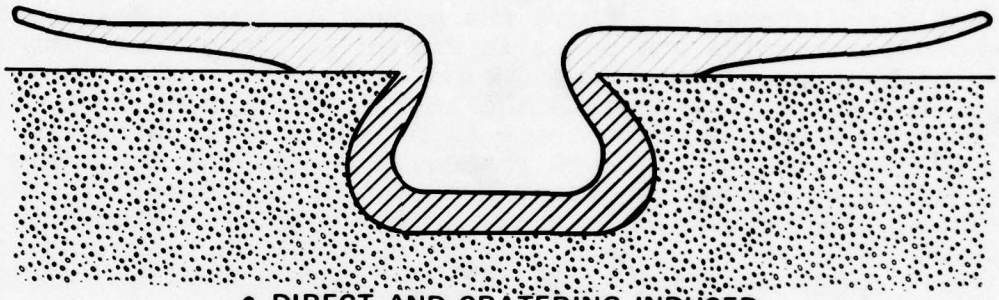

- **DIRECT AND CRATERING INDUCED GROUND MOTION**
- **CRATERING AND EJECTA DYNAMICS**
- AIRBLAST INDUCED GROUND MOTION
- FAR-FIELD AIRBLAST

78-11-47

Figure 5 Charge design concept.

The procedure for performing the surface charge design is shown schematically in Figure 6. The nuclear airblast conditions of peak pressure, P, total impulse, I, and time of arrival, TOA, along the ground surface are well known. In order to simulate these conditions data from both experiments and calculations must be obtained for thin slabs of high explosive of total thickness, A, elevated a distance, V, above the ground surface. The required high explosive results are shown in Figure 6. In general, they relate the peak pressure at the ground surface, P', the total impulse at that point. I', and the corresponding time of arrival, TOA', to both V and A. Once these high explosive results are known, it is a straight forward procedure to develop the basic charge design to accomplish the simulation of the baseline nuclear conditions. The procedure is shown at the bottom of Figure 6. Sufficient information is available to obtain both V and A as a function of range and also the lighting times, LT, of the explosive charge vs range.

An important assumption made in this preliminary design process, was that ANFO in thin sheets acted nearly as an ideal explosive. There was, at that time, some data in existence which indicated the detonation velocities for thin slabs of ANFO might be considerably reduced from the quoted Chapman-Jouget (C-J) value as shown in Figure 7. A number of 1D calculations were performed using the simple geometry shown in Figure 8. First order corrections for small thicknesses of ANFO were used as shown in Figure 9. The assumptions being recognized, a series of experiments were begun at this time, investigating the detonation characteristics of thin slabs of ANFO.

Using this model of an ideal explosive, calculations were performed to determine the thickness of ANFO required as a function of range which is shown in Figure 10, and the times of initiation as a function of range for these thin slabs as shown in Figure 11. These resulted in a preliminary charge design designated 1A which is shown in Figure 12. Recognizing the assumptions used in Charge Design 1A, experiments investigating the detonation characteristics of thin ANFO slabs were performed to check its validity. These experiments consisted of detonating thin slabs of ANFO (17.5 cm to 7.5 cm) thick, 0.6m wide X 1.0m long and with a 50 cm void. Time of arrival pins were installed along two lines to determine velocity of detonation as shown in Figure 13. These results show the presence of a "valley" in the detonation velocity vs range curve for distances within 50 cm of the booster. It appears that ANFO, which is a composite explosive, does not attain its Chapman-Jouget or steady state detonation characteristics immediately upon igniting, but because of the multiplicity of chemical reactions taking place, takes some time to reach the classical C-J conditions. During the transition period between

NUCLEAR CONDITIONS (Brode)

$P = f(R)$ $I = g(R)$ $TOA = h(R)$

HE RESULTS (Experiments and calculations)

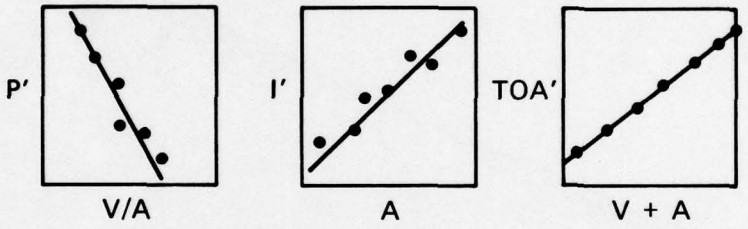

$P' = f'\left(\frac{V}{A}\right)$ $I' = g'(A)$ $TOA' = h'(V + A)$

HE SIMULATION OF NUCLEAR CONDITIONS

$P' = P$ GIVES $\frac{V}{A}$ VERSUS R	$I' = I$ GIVES A VERSUS R	TOA–TOA' GIVES LT VERSUS R FOR A & V DETERMINED

78-10-165

Figure 6 Standard source surface charge design.

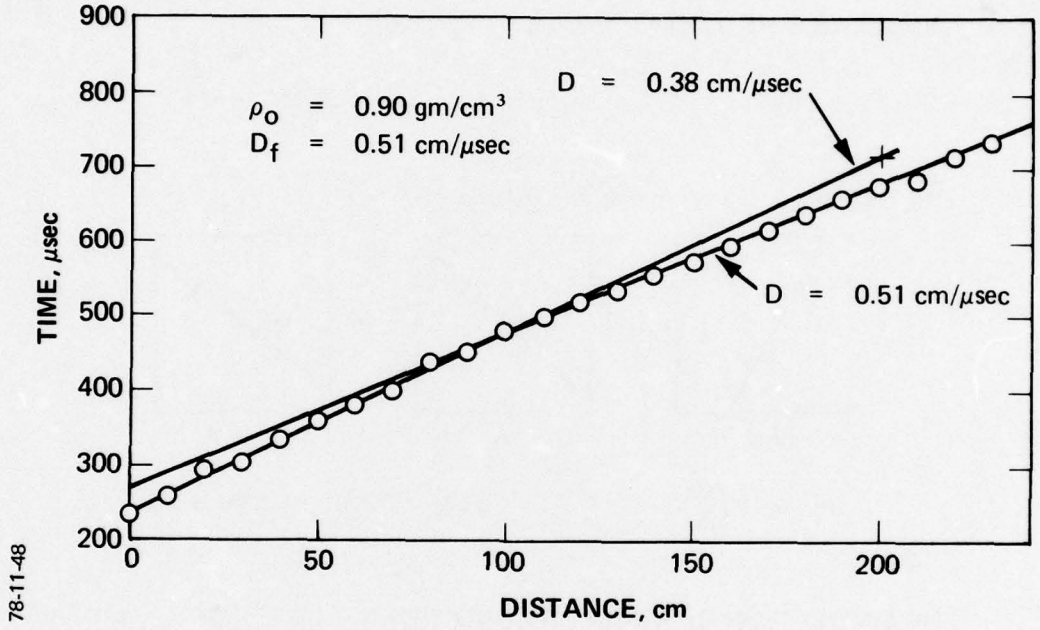

Figure 7 Detonation trajectory for undiluted 94/6 ANFO.

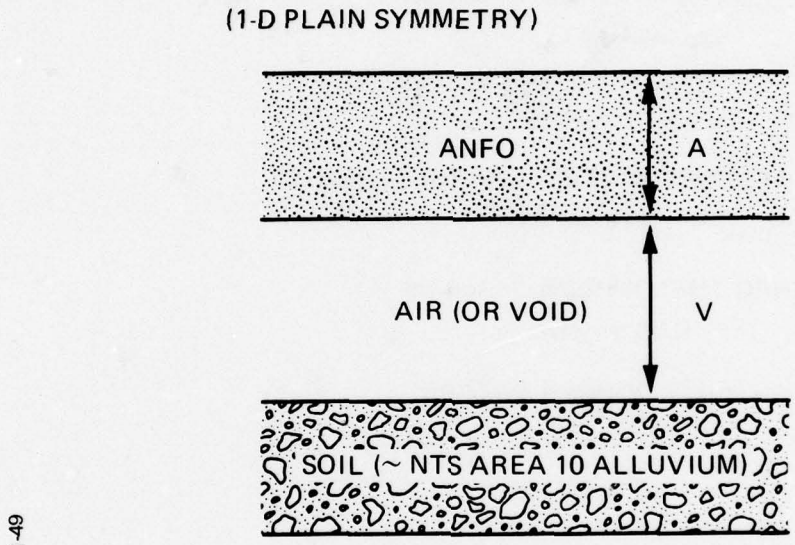

Figure 8 Computational geometry.

FOR ANFO THICKNESSES $>$ 100 cm

$$P_{CJ} \cong 55 \text{ kb}$$
$$D \approx 0.5 \text{ cm}/\mu\text{sec}$$
$$\Gamma_{CJ} = 2.554$$

FOR THESE DETONATION CHARACTERISTICS

$$P_{max} = 7.5\,(V/A)^{-0.685}$$

FOR ANFO THICKNESSES $<$ 100 cm

$$D \approx 0.38 \text{ cm}/\mu\text{sec}$$

FROM CHAPMAN-JOUGET THEORY

$$P_{CJ} = \frac{\rho_o D^2}{\Gamma + 1}$$

ASSUMING Γ = 2.7,

$$P_{det} = 30.5 \text{ kb} \qquad (th < 100 \text{ cm})$$

WE THEN ASSUME

$$P_{max} = \left(\frac{30.5}{5.5}\right) 7.5 \left(\frac{V}{A}\right)^{-0.685}$$

78-11-50

Figure 9 First order correction for small ANFO thickness.

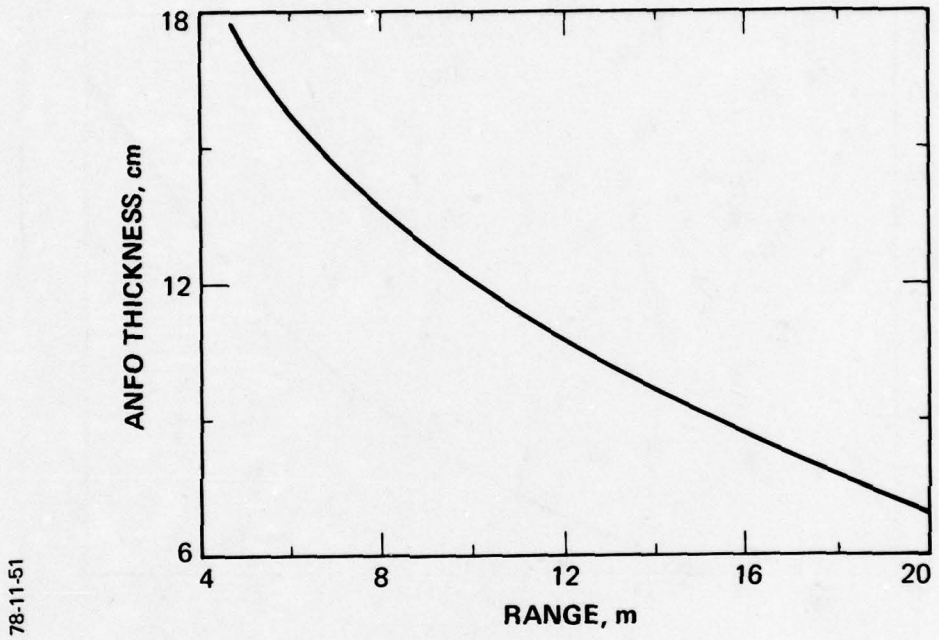

Figure 10 Explosive thickness versus range, charge design 1A.

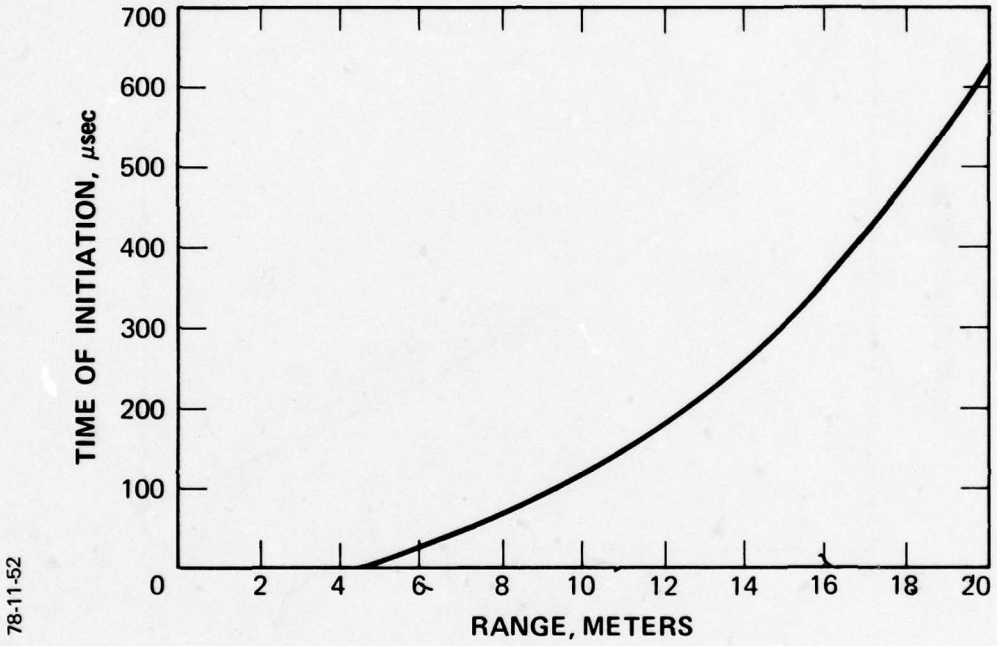

Figure 11 Initiation time versus range, charge design 1A.

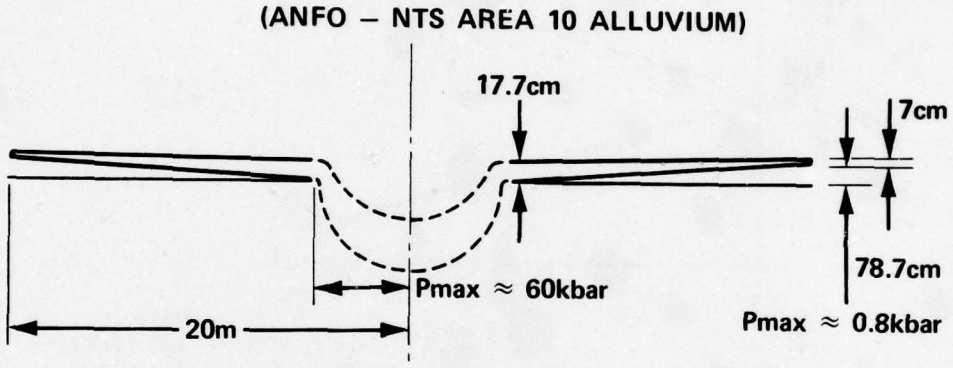

TOTAL EXPLOSIVE WEIGHT: ≈ 103 tons (ANFO)

78-11-53

Figure 12 Charge design 1A.

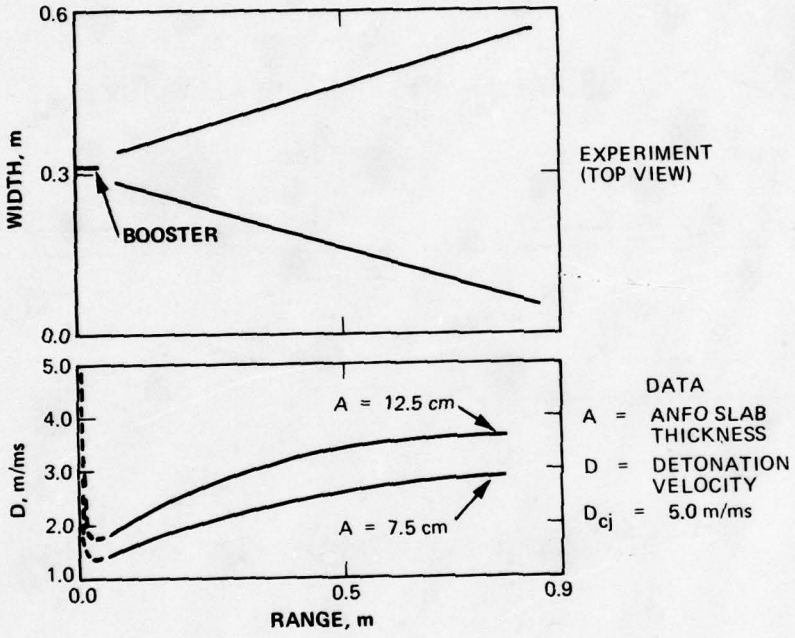

Figure 13 Thin ANFO experiments.

boosting and the C-J conditions, the detonation velocity, D, is substantially lower than the C-J detonation velocity. The velocity slowly increases so that at the end of the valley, D_{cj} for bulk ANFO, is reached. Very little previous work has been performed to examine this phenomena of a non-ideal explosive, yet, this data is crucial to this technique since thin sheets of ANFO must be used to simulate the nuclear airblast-induced ground motion.

Lately, a grain burn model has been implemented in the PISCES computer code to attempt to account for the non-ideal behavior of ANFO. Some initial 1D and 2D calculations have been performed. These calculations have been based on an ANFO grain burn model, shown in Figure 14. The results of these calculations are shown in Figure 15. Much more needs to be done to verify the adequacy of the model. It is felt that the parameters needed for the ANFO grain burn model, must depend only upon the properties of the ANFO itself, thus, 1D spherical and cylindrical calculations, using the grain burn model, should show the presence of the detonation valley if the parameters are to be picked correctly.

A full-scale test, based on charge design 1A, could be constructed by using four foot by eight foot trays as shown in Figure 16. These trays would be made of low mass paper honeycomb supported by low mass styrofoam pillars. The depth of the trays would be adjusted for the correct depth of explosive. The styrofoam pillars would be cut to the proper height above the soil surface. Several hundred of these trays would be required in an arrangement as shown in Figure 17. This shows an artist's concept layout of how the below ground MINE THROW charge is integrated with the above-ground airblast charge. A suitable protective housing must be provided for this entire arrangement, since it would be very susceptible to weather conditions, especially wind loadings and precipitation. Each of the trays could be detonated at the proper time in concentric arrays as shown in Figure 18. Designs have been completed and tested which show the feasibility of these initiation geometries using both electrical timing and pyrotechnic delays.

NON-IDEAL EXPLOSIVES:

- CHEMICAL ENERGY IS RELEASED OVER A FINITE PERIOD OF TIME AFTER THE ARRIVAL OF THE DETONATION WAVE.
- AN ACTIVATION ENERGY IS REQUIRED TO INITIATE THE ENERGY RELEASE.

THUS GRAIN BURN MODEL ASSUMES:

$\frac{dF}{dt} = G(E_a, \tau)$, where

F = FRACTION OF HE CONSUMED AT A POINT

E_a = ACTIVATION ENERGY = αE_o

E_o = TOTAL ENERGY RELEASE/UNIT WEIGHT

τ = TIME OVER WHICH E_o IS COMPLETELY RELEASED AT A POINT

78-10-148

Figure 14 ANFO grain burn model.

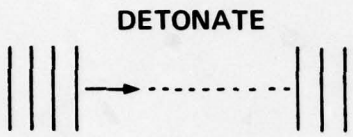

1D CALCULATIONS
(PLANAR SYMMETRY)

TO MATCH DATA

A = 7.5 cm	α = 0.05	τ = 225 μs
A = 12.5 cm	α = 0.05	τ = 100 μs

2D CALCULATIONS
(PLANAR SYMMETRY)

TO MATCH DATA:

A = 7.5 cm	α = 0.15	τ = 50 μs
A = 12.5 cm	α = 0.15	τ = 35 μs

78-10-149

Figure 15 Thin ANFO calculations, grain burn model.

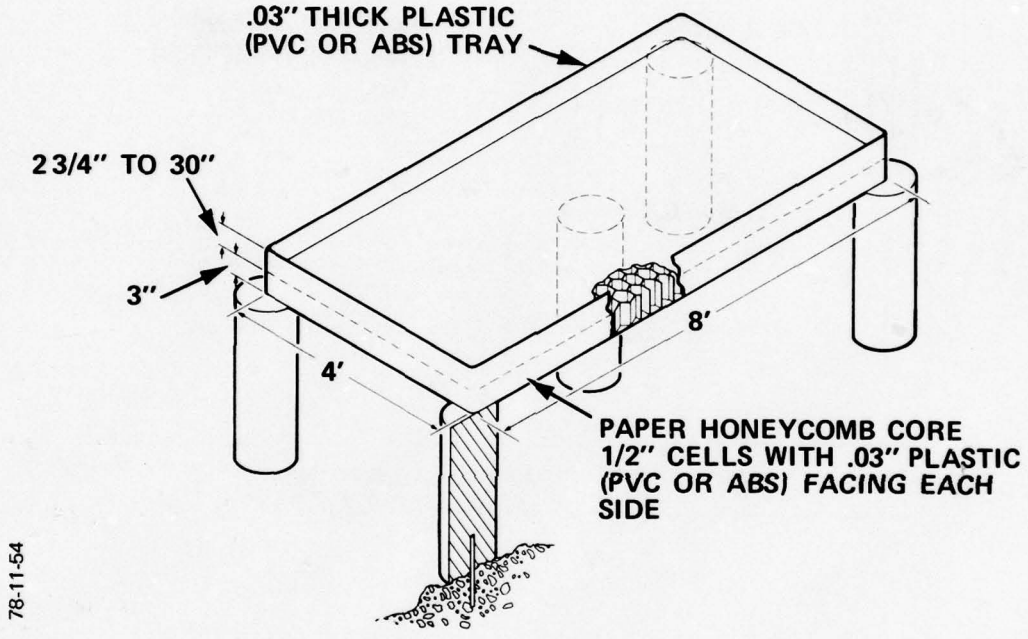

Figure 16 Typical panel.

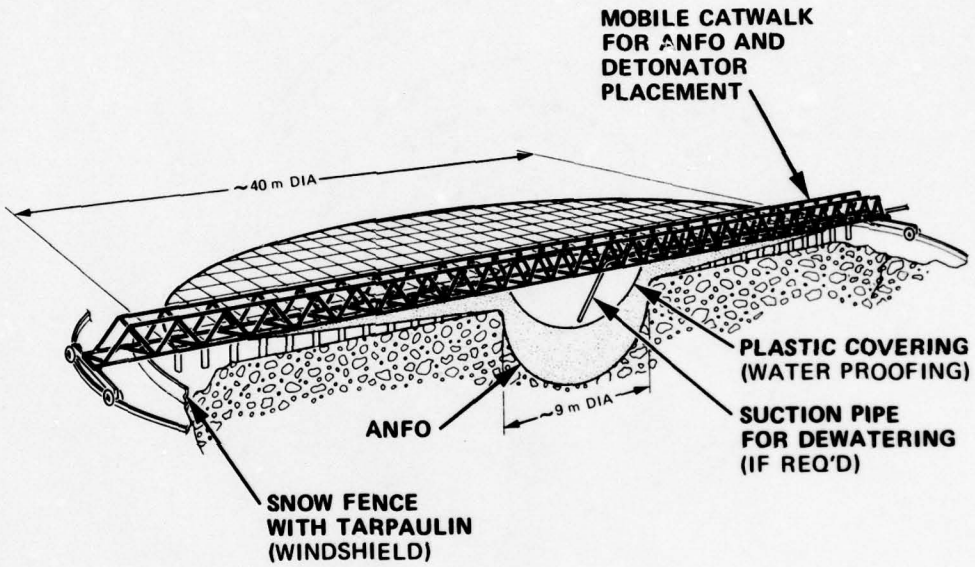

Figure 17 Concept layout.

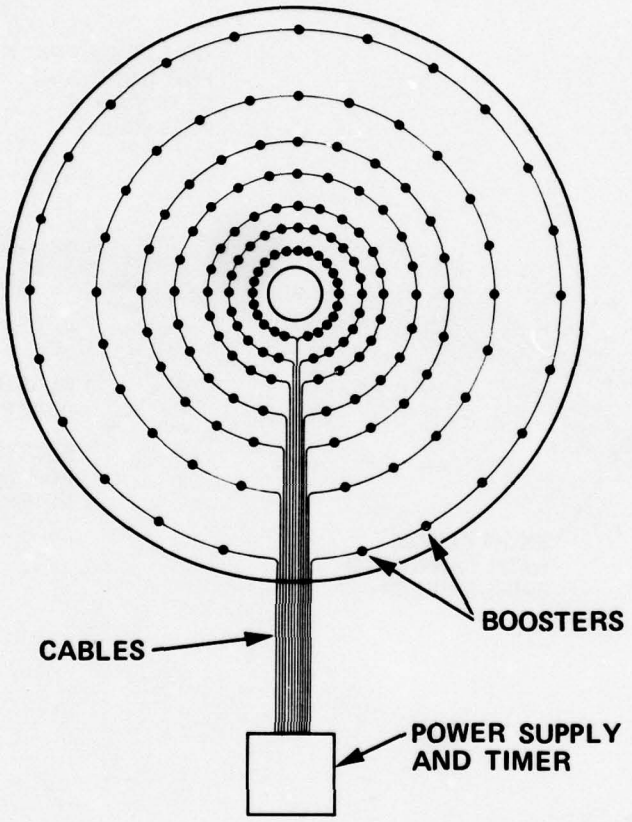

Figure 18 Concept initiation geometry.

REFERENCES

1. T. F. Stubbs, J. A. Kochly, D. S. Randall, F. M. Sauer and C. T. Vincent, MINE THROW I-- A Cratering and Ground Motion Simulation Technique, Defense Nuclear Agency, DNA 3365F, July, 1974, Physics International Company

2. A. C. Buckingham, S. L. Hancock, M. W. McKay, D. L. Orphal, Calculations of CACTUS Ground Motion and Design of the MINE THROW II Charge, Physics International PIFR-383, Volume III, March, 1973, for Defense Nuclear Agency, DNA001-73-C-0052.

GRAVITY-SCALING METHODS APPLIED TO CRATER-INDUCED GROUND MOTIONS AND EFFECTS

by

K.A. Holsapple

R.M. Schmidt

R.L. Dyrdahl

Boeing Aerospace Company

1. Introduction

Cooper (1975) asks the question "Cannot small scale experiments credibly be used to study phenomena (e.g., height-of-burst and layering effects) and scaling rules?" This question is answered and implications on the modeling of ground shock as well as the response of buried structures is addressed.

The approach is based upon performing subscale experiments which are dynamically similar to their full scale prototypes. Two events of different sizes are called similar if each of the pertinent thermomechanical field variables (e.g., stress, velocity, etc.) are equal to within a simple scale factor for the two events. To use this concept, it is necessary to correctly identify the pertinent fields and to control all the test parameters to ensure similarity. The more common practice of extrapolating the results of small scale experiments without due regard to similarity requirements will also be briefly discussed to highlight pitfalls of such a procedure.

Section 2 is a complete similarity analysis for the thermomechanical response of a continuous media. Here the theory is developed and similarity requirements common to all cratering and ground motion applications are derived.

Section 3 gives results demonstrating the applicability to the problem of cratering. In particular, a soil strength model is presented which explains the dependence of apparent crater volume upon charge size and material strength, where the latter is given by a Mohr-Coulomb representation.

Section 4 gives the results of using this same soil strength model to develop a set of non-dimensional parametric curves for the prediction of ground motion. Comparison with limited field data is given and a discussion suggesting refinement of the theory and further verification of its applicability is included.

Section 5 is a discussion of the feasibility of various types of subscale experiments which must be conducted on a centrifuge to achieve the elevated gravity field strength required by similarity. These include ground motion as well as structure-soil interaction.

2. Similarity in Ground Motion Experiments

Ground shock events are of a general class of phenomena involving detonation sources and resulting dynamic stress and deformation fields. It will be shown that a similarity analysis derived for cratering due to near surface bursts is also applicable for ground motion. Schmidt and Holsapple (1978a,1978b) present a general analysis of the requirements of similarity with specific application to cratering. A condensation of that analysis appropriate to the ground shock problem is repeated here.

The parameters and fields used to define and characterize ground shock phenomena include the five fields:

$\vec{x}(\vec{X},t)$ the spatial position vector (1.1)

$\rho(\vec{X},t)$ the mass density per unit volume (1.2)

$\underset{\sim}{T}(\vec{X},t)$ the stress tensor field (1.3)

$\vec{b}(\vec{X},t)$ the body force per unit mass (1.4)

$e(\vec{X},t)$ the internal energy per unit mass (1.5)

where X is the initial position and t is the time. These fields determine the auxiliary fields

$\vec{u}(\vec{X},t) = \vec{x}(\vec{X},t) - \vec{X}$ the displacement vector field (1.6)

$\vec{v}(\vec{X},t) = \frac{d}{dt}\vec{x}(\vec{X},t)$ the velocity field (1.7)

$\vec{a}(\vec{X},t) = \frac{d}{dt}\vec{v}(\vec{X},t)$ the acceleration field (1.8)

$\underset{\sim}{F}(\vec{X},t) = \text{Grad}\ \vec{x}(\vec{X},t)$ the deformation gradient tensor (1.10)

$\underset{\sim}{L}(\vec{X},t) = [\frac{d}{dt}\underset{\sim}{F}(\vec{X},t)][\underset{\sim}{F}(\vec{X},t)]^{-1}$ the velocity gradient tensor (1.11)

The operator d/dt denotes the time derivative at fixed initial position $\vec{X}$, while Grad denotes the gradient with respect to $\vec{X}$ at fixed time t. A superposed arrow denotes a vector and a subposed tilde denotes a tensor. The superscript -1 denotes a tensor inverse, and the superscript T denotes the transpose. The tensor $\underset{\sim}{I}$ is the unit tensor. The symetric part of the tensor $[\underset{\sim}{F}-\underset{\sim}{I}]$ is the infinitesimal strain tensor and the symmetric part of $\underset{\sim}{L}$ is the rate of strain tensor used in fluid mechanics.

The fields are not independent but must satisfy the balance equations of mechanics. In the absence of heat conduction and heat supply, these equations have the form

balance of mass

$$\rho \det(F) = \rho_0 \tag{2}$$

balance of angular momentum

$$\underset{\sim}{T} = \underset{\sim}{T}^T \tag{3}$$

balance of linear momentum

$$\operatorname{div} \underset{\sim}{T} + \rho \vec{b} = \rho \vec{a} \tag{4}$$

and balance of energy

$$\rho \dot{e} = \operatorname{Tr} (\underset{\sim}{T}\,\underset{\sim}{L}). \tag{5}$$

Here ρ_0 is the initial density, div refers to the divergence with respect to $\vec{x}$, and Tr denotes the trace of a tensor. In addition, these fields are related by whichever consitutitive equations describe the response of the media in question and by the initial and boundary conditons.

At surfaces of discontinuity; e.g., detonation fronts, these equations are augmented by jump conditions. For a shock or a detonation wave with local normal $\vec{n}$ moving at speed U into an undeformed and unstressed material, the following equations apply

mass:
$$\rho_0 U = \rho U - \rho(\vec{v}\cdot\vec{n}) \tag{6}$$

momentum:
$$\underset{\sim}{T}\vec{n} + \rho_0 U\vec{v} = 0 \tag{7}$$

energy:
$$\rho_0 U(e-e_0 + \frac{1}{2}\vec{v}\cdot\vec{v} - Q) + \vec{n}\cdot\underset{\sim}{T}\vec{v} = 0 \tag{8}$$

and a compatibility condition

$$U(\underset{\sim}{F}-\underset{\sim}{I})\vec{n} + \vec{v} = 0 \tag{9}$$

where the variables ρ, $\vec{v}$, $\underset{\sim}{I}$, e, $\underset{\sim}{F}$ refer to the properties behind the front, Q is the energy per unit mass added at the jump for a detonation wave, e_o and ρ_o are the energy and the density in the undeformed material ahead of the wave.

Two different solutions corresponding to two different experiments, each satisfying the entire set of eqs. 1 through 9 are to be compared. All of the quantities associated with the second solution will be denoted by primes. These two solutions are said to be <u>similar</u> if the following relationships:

$$\vec{x}'(\vec{X}',t') = \alpha_x \vec{x}(\vec{X},t) \tag{10.1}$$

$$\rho'(\vec{X}',t') = \alpha_\rho \rho(\vec{X},t) \tag{10.2}$$

$$\underset{\sim}{I}'(\vec{X}',t') = \alpha_T \underset{\sim}{I}(\vec{X},t) \tag{10.3}$$

$$\vec{b}'(\vec{X}',t') = \alpha_b \vec{b}(\vec{X},t) \tag{10.4}$$

$$e'(\vec{X}',t') = \alpha_e e(\vec{X},t) \tag{10.5}$$

$$Q'(\vec{X}',t') = \alpha_Q Q(\vec{X},t) \tag{10.6}$$

hold at <u>homologous</u> points defined by

$$\vec{X}' = \alpha_X \vec{X} \tag{10.7}$$

for <u>homologous time</u>

$$t' = \alpha_t t. \tag{10.8}$$

The derived fields are related as a consequence of their definitions by

$$\vec{u}'(\vec{X}', t') = \alpha_x \vec{u}(\vec{X}, t) \tag{11.1}$$

$$\vec{v}'(\vec{X}', t') = \frac{\alpha_x}{\alpha_t} \vec{v}(\vec{X}, t) \tag{11.2}$$

$$\vec{a}'(\vec{X}', t') = \frac{\alpha_x}{(\alpha_t)^2} \vec{a}(\vec{X}, t) \tag{11.3}$$

$$\underset{\sim}{F}'(\vec{X}', t') = \frac{\alpha_x}{\alpha_x} \underset{\sim}{F}(\vec{X}, t) \tag{11.4}$$

$$\underset{\sim}{L}'(\vec{X}', t') = \frac{1}{\alpha_t} \underset{\sim}{L}(\vec{X}, t). \tag{11.5}$$

Here the eight various factors α_i are constants called scale factors. Note that $\alpha_{X_0} = \alpha_x$ if in both solutions, the reference position $\vec{X}$ is the initial position: $\vec{x}(t=0) = \vec{X}$. This is henceforth assumed leaving seven independent scale factors. Thus, in particular, eq.11.4 states that the deformation gradient must be the same at homologous points and therefore the strains are identical also. In more detailed terminology, the two solutions are said to be geometrically, kinematically and dynamically similar (Langhaar, 1951).

The question of the existence of two different experiments related by these similarity requirements is to be investigated. Both sets of fields must satisfy the balance equations given above, regardless of the form of the constitutive equations. This requirement will give certain restrictions relating the seven scale factors. Additional restrictions from specific constitutive equations are derived separately below.

Assume that a primed solution exists, substitute the primed fields into the balance equations 2 through 5 and use the similarity relationships (eqs. 10) to get

$$\alpha_\rho \rho \det F = \alpha_\rho \rho_0 \tag{12.1}$$

$$\alpha_T \underset{\sim}{T} = \alpha_T \underset{\sim}{T}^T \tag{12.2}$$

$$\frac{\alpha_T}{\alpha_x} \operatorname{div} \underset{\sim}{T} + \alpha_\rho \alpha_b \rho \vec{b} = \frac{\alpha_\rho \alpha_x}{\alpha_t^2} \rho \vec{a} \tag{13}$$

$$\frac{\alpha_\rho \alpha_e}{\alpha_t} \rho \dot{e} = \frac{\alpha_T}{\alpha_t} \operatorname{Tr}(\underset{\sim}{T}\,\underset{\sim}{L}) \tag{14}$$

The unprimed fields must also satisfy the balance equations. Hence equations 12.1 and 12.2 are satisfied identically.

For the balance of linear momentum eq. 4 can be used for div T in eq. 13, giving

$$\left[\frac{\alpha_T}{\alpha_x} - \frac{\alpha_\rho \alpha_x}{(\alpha_t)^2}\right] \rho \vec{a} = \left[\frac{\alpha_T}{\alpha_x} - \alpha_\rho \alpha_b\right] \rho \vec{b}. \tag{15}$$

This must hold for all X and t. Thus, unless the acceleration field $\vec{a}$ is itself a scalar multiple of the body force $\vec{b}$ or either $\vec{a}$ or $\vec{b}$ is identically zero, it is necessary that

$$\frac{\alpha_T}{\alpha_x} = \frac{\alpha_\rho \alpha_x}{(\alpha_t)^2} \tag{16}$$

and

$$\frac{\alpha_T}{\alpha_x} = \alpha_\rho \alpha_b. \tag{17}$$

The most common body force per unit mass is a constant vector proportional to a constant gravity, g. In this case, the acceleration field which is a scalar multiple of $\vec{b}$ is at most a rigid body motion. If $\vec{b} = 0$, then eq. 17 is not required. If $\vec{a} = 0$, as in statics, then eq. 16 is not required.

Now substitute $\rho \dot{e}$ from the balance of energy eq. 5 into eq. 14 to get

$$\left[\frac{\alpha_\rho \alpha_e}{\alpha_t} - \frac{\alpha_T}{\alpha_t}\right] \operatorname{Tr}(\underset{\sim}{T}\,\underset{\sim}{L}) = 0 \tag{18}$$

for all $\vec{X}$ and t. Again, assuming the stress and velocity gradient fields are neither identically zero, it is necessary that

$$\alpha_\rho \alpha_e = \alpha_T \ . \tag{19}$$

Lastly, requirements brought about by detonation waves in the explosive can now be included. For this case, both solutions must also satisfy the jump conditions across the wave (eqs. 6-9). An analysis identical to that just given for the balance equations produces only one additional restriction which involves the scale factor α_Q for the energy density of the explosive Q

$$\alpha_Q = \frac{\alpha_T}{\alpha_\rho} \ . \tag{20}$$

Altogether then, the balance equations plus the jump conditions provide four similarity restrictions among the seven scale factors relating the variable fields as defined by eqs. 10.1 through 10.8. Eqs. 16 and 17 are a consequence of the balance of momentum, eq. 19 results from the balance of energy and the energy jump condition supplies the remaining constraint, eq. 20. The balance of mass and the balance of angular momentum provide no restrictions.

It is convenient for the present application to consider α_x, α_t and α_ρ as independent. The four restrictive conditions (eqs. 16-20) can then be used to solve for the remaining scale factors:

$$\alpha_T = \left[\frac{\alpha_x}{\alpha_t}\right]^2 \alpha_\rho \tag{21.1}$$

$$\alpha_b = \alpha_x/(\alpha_t)^2 \tag{21.2}$$

$$\alpha_e = \left[\frac{\alpha_x}{\alpha_t}\right]^2 \tag{21.3}$$

$$\alpha_Q = \left[\frac{\alpha_x}{\alpha_t}\right]^2 \tag{21.4}$$

Therefore it can be seen that, <u>considering only the balance equations and the jump conditions,</u> nontrivial similar solutions with arbitrary scaling of size, time and density are allowed. The four remaining scale factors must then satisfy the four equations, 21.1 through 21.6.

Analysis of Specific Constitutive Equations

The complete solution to the deformation and flow of any continuous medium depends on, in addition to the balance equations and the jump equations given above, the constitutive equations that describe the behavior of that medium. Therefore, while the above similarity requirements (eqs. 21.1 through 21.4) are necessary, the question of their sufficiency must be answered. Note, however, that they are general and apply to all materials.

The nature and type of equations that describe the material behavior for a given medium, and their role in determining similarity requirements is now considered. There are three media in the present problem: the soil, the explosive and the overlying air, at least for near surface bursts. Each of these media is extremely complex. The complete characterization of the soil requires concepts of compressibility, nonlinearity, yield, fracture, porosity, cohesion and others. As disussed by Schmidt and Holsapple (1978a, 1978b), it is not necessary to pick definite constitutive equations for the purposes of a similarity analysis. The complexity of the soil behavior leads one to believe that any scaling or modeling of the soil itself is hopeless, except perhaps in extremely simple problems (Pokrovsky and Fyokorov, 1969). As a consequence, one expects that the same soil medium must be used in two experiments if similarity is to be achieved. For the purposes of this discussion it will be assumed that the same explosive is used in both, and only the size is varied. For this case it is necessary that $\alpha_\rho = 1, \alpha_Q = 1$ and from eq. 21.4, $\alpha_x = \alpha_t$. Hence there remains only one independent scale factor α_x and all others are determined, as follows

$$\alpha_T = 1 \tag{22.1}$$

$$\alpha_b = 1/\alpha_x \tag{22.2}$$

$$\alpha_e = 1 \tag{22.3}$$

$$\alpha_Q = 1. \tag{22.4}$$

In this case, similarity is possible only insofar as the constitutive equations are consistent with this scaling. The stress, the strain, the density, the internal energy and the heat of detonation must be the same at

homologous points. The body force must scale as the reciprocal of the size, and the scale facors for time and distance are equal. Consequently, if α_x = 1/10 so that a 1/10 size scale experiment is to be performed, the body force must be 10 times larger. All events will occur in 1/10 the time over 1/10 the distance, and all velocities will be the same.

Schmidt and Holsapple (1978a, 1978b) have addressed the question of the consistency of material constitutive behavior with the set of eqs. 22.1-22.4. They have proved the statement, "Complete and exact dynamic similarity can be achieved between two different experiments of arbitrary size scale in the same material as long as the constitutive behavior is 1) rate independent and 2) has no inherent size properites." If either of these requirements is not satisfied then the material must also be modeled using the concept of equivalent materials.

Summarizing the above development, the design of a subscale experiment that directly simulates a large full scale event is indeed possible. All dimensions are to be reduced by a common scale factor α_x, which implies the yield of the device is reduced by $(\alpha_x)^3$. The same soil and explosive type is used in both experiments. The body force, i.e., the gravity, must be increased by $1/\alpha_x$. The way that this can be achieved in practice is through the use of a centrifuge.

3. Subscale Cratering Experiments

While the primary interest of this analysis is ground motion phenomena, a closely related problem is that of cratering due to near surface bursts. Recent cratering experiments by Schmidt and Holsapple (1978a, 1978b, 1979) have provided valuable experience in the conduct of explosive testing in the high-G environment of a centrifuge. Furthermore, as will be discussed in the next section, the ground motion due to near surface explosives in various experiments was correlated with the crater parameters in these same experiments (Cooper and Sauer, 1977). Consequently, it is appropriate to summarize recent centrifuge cratering experiments and results here. These subscale explosive cratering experiments were performed in Ottawa sand, desert alluvium, clay, and saturated sand. Two different explosives, PETN and lead azide, in sizes up to four grams, were used. These experiments were conducted using the Boeing geotechnic centrifuge at gravity fields up to 520 G's.

As shown in the previous section, if the body force is increased by a factor of 520, then for this subscale experiment $\alpha_x = 1/520$. The similar full scale experiment is 520 times larger in all linear dimensions. The corresponding charge size is $(520)^3$ times 4 grams, which is a charge size of over 0.6 kilotons of PETN, or an equivalent energy of almost 1 KT of TNT. Therefore the centrifuge experiments have given a direct simulation of relatively large scale field events. This direct simulation technique was demonstrated very successfully with a subscale replication of the JOHNIE BOY 500-ton shallow buried nuclear event conducted at 345 G's (Schmidt, 1978).

The results of centrifuge experiments have been invaluable in understanding both size effects and material strength effects in the various media. The base line experiments in Ottawa sand are shown in Fig. 1 as a plot of the cratering efficiencies

$$\pi_V = V\rho/W \tag{23}$$

versus the gravity-scaled size parameter

$$\pi_2 = \frac{g}{Q}\left[\frac{W}{\delta}\right]^{1/3} \tag{24}$$

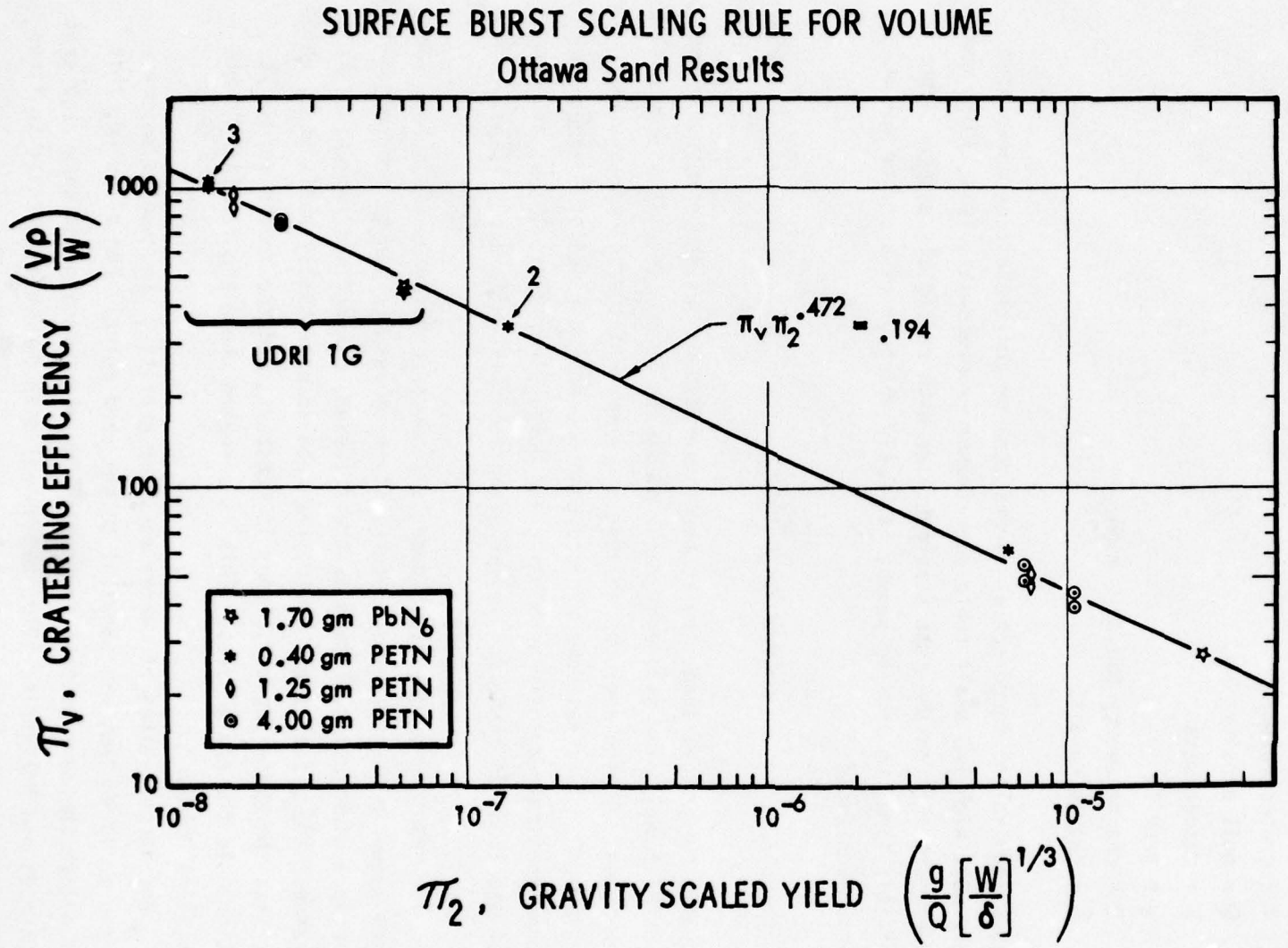

Fig. 1 Cratering efficiency versus scaled size for Ottawa sand.

where

V = crater volume
ρ = soil density
W = charge mass
g = gravity
Q = charge energy per unit mass
δ = charge density

The high-G (equivalent large scale) events done on the centrifuge correlate extremely well with 1-G small scale experiments (Piekutowski, 1974, 1975) and all experiments fall on the same straight line with negligible scatter. The slope of this line, on log-log paper, is -0.472 which gives a crater volume dependence upon yield

$$V \propto W^{0.843} \tag{25}$$

Additionally for Ottawa sand, the crater linear dimensions scale with the energy to the 0.281 power, over an energy range of almost 12 decades. The form of π_2 as given by eq. 24 also includes an adequate representation of the energy density term, Q. This was demonstrated over the entire range of Q encountered for common chemical explosives (Schmidt and Holsapple, 1978a, 1978b) and over an order of magnitude in range for impact experiments (Schmidt and Holsapple, 1978c).

The results for the other materials are superposed on the Ottawa sand curve and shown in Fig. 2. The features of these results can be comprehended by considering a given material such as the alluvium, for a fixed explosive. At small values of π_2, i.e, small yield, the data is essentially horizontal, which implies that the cratering efficiency is constant, and the crater volume is proportional to the charge mass. This is a regime where the familiar "cube-root" scaling holds.

For larger values of charge mass (or gravity), the results become asymptotic to lines that are parallel to the sand curve. For alluvium, this line is almost the same as that for sand. The clay results and saturated sand data (Schmidt and Holsapple, 1979, not shown) both become asymptotic to lines above the sand line, but have approximately the same slope. Thus, in each case

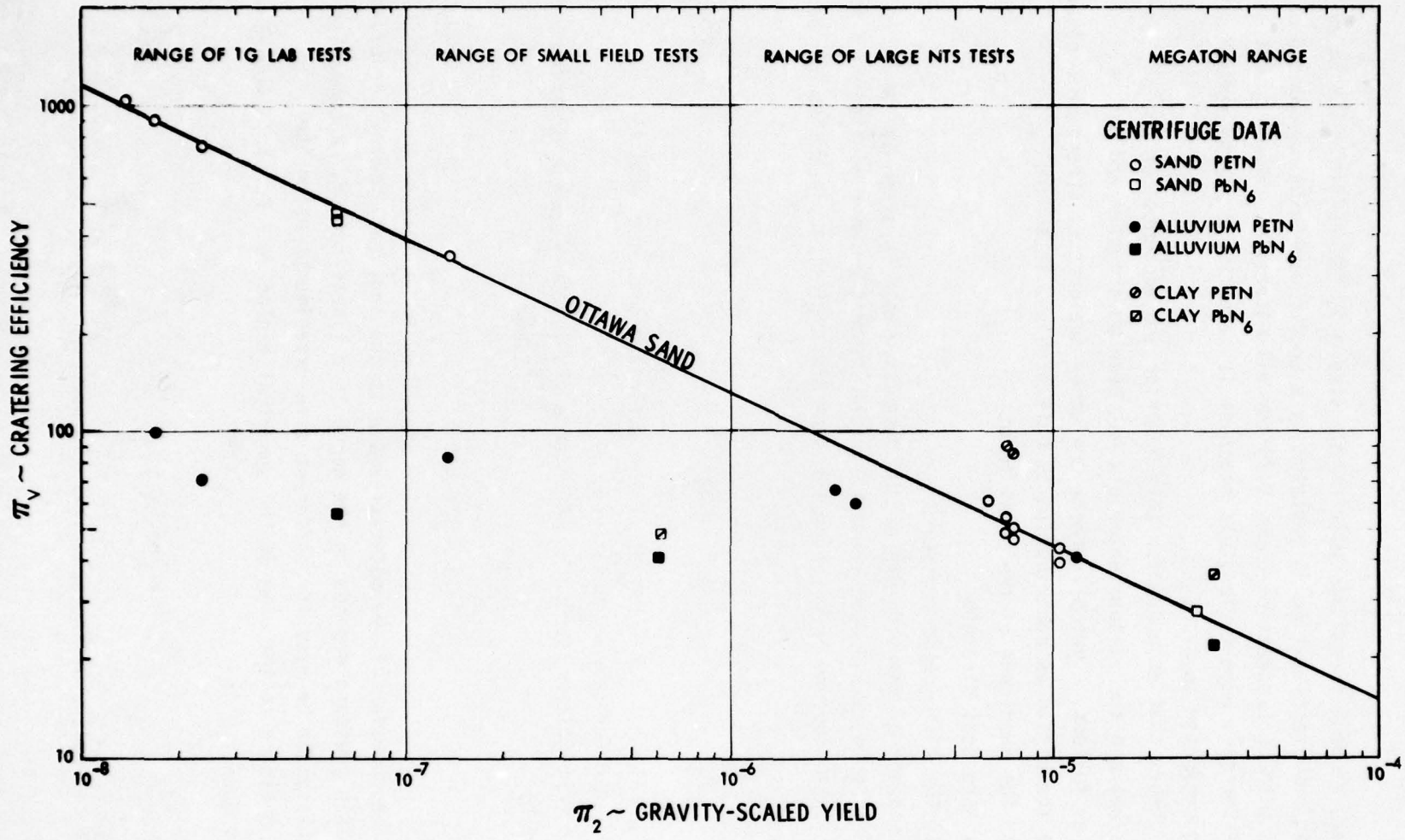

Fig. 2 Cratering efficiency versus scaled size for various media.

there appears to be a transition with charge size and, for sufficiently large experiments, cube root scaling is replaced by a crater dimension dependence on charge mass with an exponent of about 0.28 for all materials. However, the exact value for this asymptotic yield exponent is tentative from the number of experiments conducted to date.

A theory that accounts for this behavior and accounts for the differences between the various materials has been constructed and can be summarized as follows. Typically there are three measures of stress or pressure that can be identified as contributing to this problem. These are

1) the magnitude of the shock front
2) the soil strength
3) the lithostatic pressure.

A measure of the strength of the outgoing shock is given by the magnitude of the Chapman-Jouget pressure in the detonation wave of the explosive. This pressure is given in terms of the explosive properties by the relation

$$P_{cj} = 2(\gamma-1)\,\delta\,Q \tag{26}$$

where γ is the perfect gas constant of the explosive products, and is approximately 2.8 for common explosives.

The Mohr-Coloumb strength model for soils relates the yield strength to the pressure by

$$Y = c + P \tan \phi \tag{27}$$

where c is the cohesion of the material and ϕ is the angle of internal friction. The lithostatic pressure depends on the depth in a linear manner. A comparison of this quantity can be made for different size experiments using the lithostatic pressure at the base of the spherical explosive. For half-buried charges this quantity is

$$P = \rho g a \doteq \rho g \left[\frac{W}{\delta}\right]^{1/3} \tag{28}$$

where, a, is the radius of the spherical explosive.

The relative size and importance of these three pressures can be measured by their ratios. The ratio of lithostatic to C-J pressure is given by

$$P/P_{cj} = \frac{\rho g}{2(\gamma-1)\delta Q}\left[\frac{W}{\delta}\right]^{1/3} \tag{29}$$

which, to within the factor of $2(\gamma-1)\ (\delta/\rho)$ is the gravity-size parameter π_2 defined earlier:

$$\pi_2 = (P/P_{cj})\ 2(\gamma-1)\ \left(\frac{\delta}{\rho}\right). \tag{30}$$

The ratio of the yield strength to the C-J pressure is given by

$$Y/P_{cj} = \frac{c+P\tan\phi}{P_{cj}} = \frac{\rho/\delta}{2(\gamma-1)}\left[\frac{c}{\rho Q} + \pi_2 \tan\phi\right]. \tag{31}$$

The term in square brackets is used to define the dimensionless parameter

$$\pi_Y = \frac{c}{\rho Q} + \pi_2 \tan\phi \tag{32}$$

which depends on the material strength parameters c and ϕ, the explosive property Q and the previous gravity-size parameter π_2. For a cohesionless material such as dry Ottawa sand, this material strength parameters is only a constant factor of tan ϕ different from π_2.

Various measures of cratering, and in particular the resulting crater volume can be expected to depend on these stress ratios. Thus

$$\pi_V = f(\pi_2, \pi_Y) \tag{33}$$

The explicit dependence on π_2 is a measure of the importance of the gravity determined lithostatic pressure relative to the shock strengths. The explicit dependence on π_Y is a measure of the effects of finite material strength compared to the shock strength. This strength term incorporates an additional implicit gravity-size dependence because of the tan ϕ term.

Examination of existing data for granular materials indicates that the explicit dependence on π_2 is not as important as the implicit dependence via the π_Y dependence. Furthermore, π_Y depends linearly on π_2. Consequently, it seems plausible to combine these two dependences, introducing a single parameter incorporating, both π_Y and π_2 in the form

$$\overline{\pi}_2 = \pi_Y + k\pi_2 \tag{34}$$

where k is a universal constant. Written out this gives

$$\overline{\pi}_2 = \frac{c}{\rho Q} + \pi_2 (\tan \phi + k). \tag{35}$$

The constant k is expected to be relatively small compared to the tan ϕ term for materials such as sand. For sand, tan ϕ is about 0.7 so that k should be small compared to 0.7. Only when tan $\phi \doteq 0$ will the exact value of k be significant or determinable.

A plot of π_V versus this combined strength-gravity-size parameter $\overline{\pi}_2$ gives an interesting result, as shown in Fig. 3. All results now superimpose on a single straight line, with equation as shown. If it is assumed that π_V versus $\overline{\pi}_2$ is indeed the same for all materials, then the result when plotted as π_V versus the original gravity-size parameter π_2 is as shown in Fig. 4 for the various combinations of soil media and explosive type. It is seen that these curves reproduce and explain the actual data points extremely well.

From these results, an explanation of the experimental results becomes possible. For small events, π_2 is small, and the cohesion term $c/Q\rho$ dominates in $\overline{\pi}_2$. There is little gravity or size effect and cube root scaling holds. Only for a cohesionless material is this plateau not observed.

The other extreme is for large size events. In this case π_2 is large and the cohesion term can be ignored. The strength of the medium is dominated by the tan ϕ term and by lithostatic pressure. In this extreme, and for a given material and explosive, the parameter $\overline{\pi}_2$ is only a constant factor different from π_2, and a straight line asymptote results on log-log paper. The level of this asymptote, compared to the base line sand data is determined by the magnitude of the tan ϕ of the material compared to that for sand.

Fig. 5 shows a schematic of the nature of the resulting curve for a given material compared to the sand curve. The predicted response is a curve

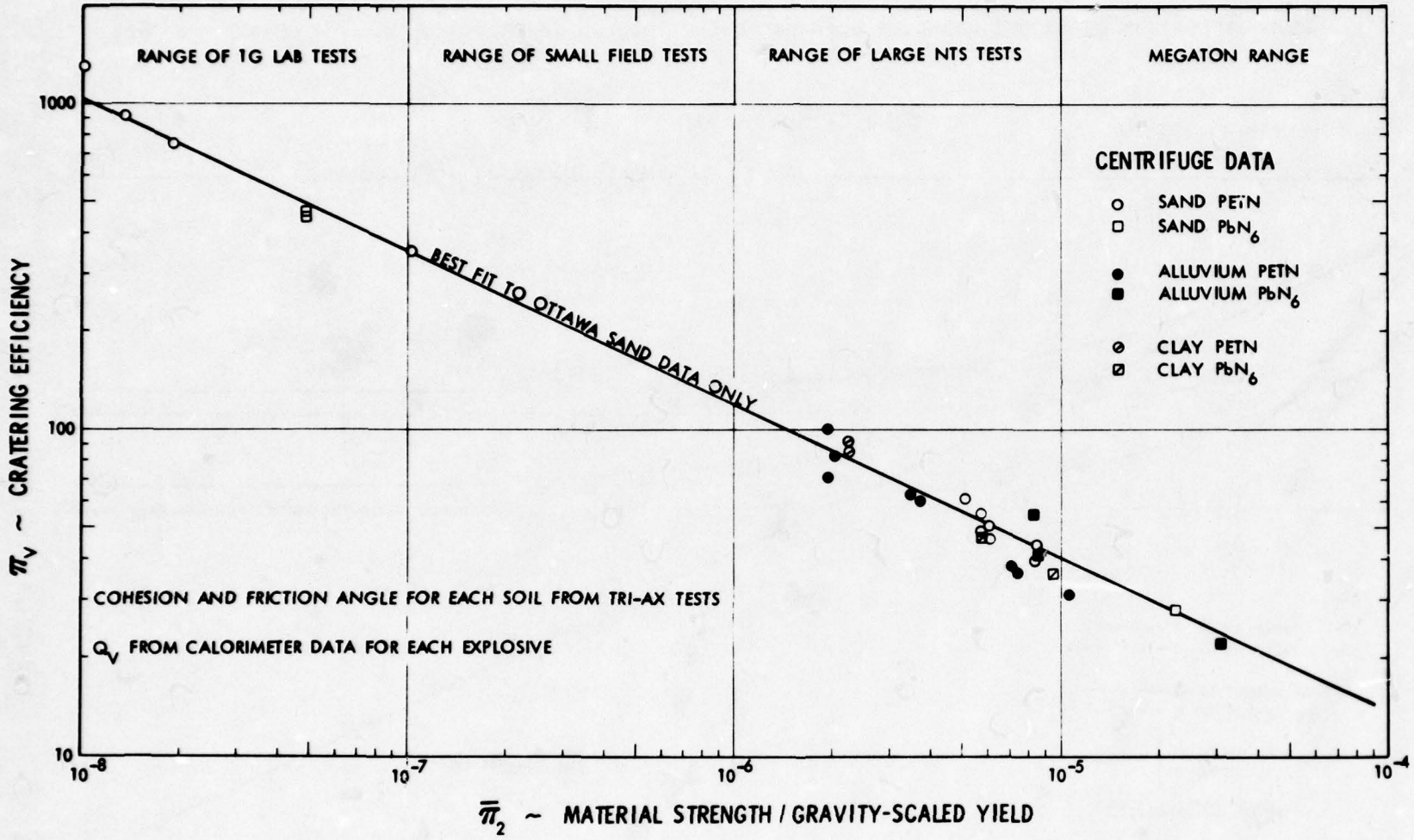

Fig. 3 Cratering efficiency versus combined strength-gravity-size parameter.

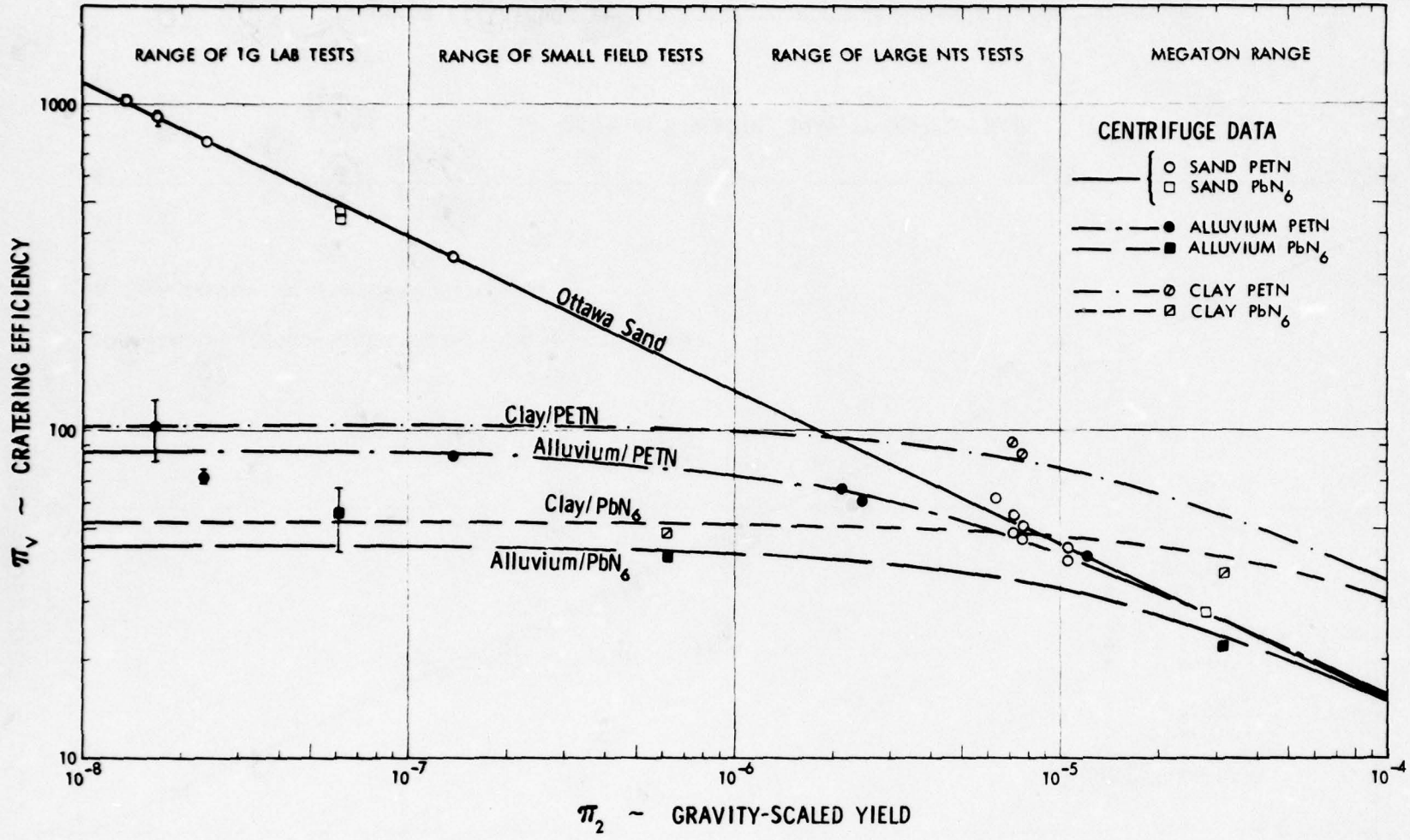

Fig. 4 Comparison in π_2 space of projections based upon strength theory to centrifuge data.

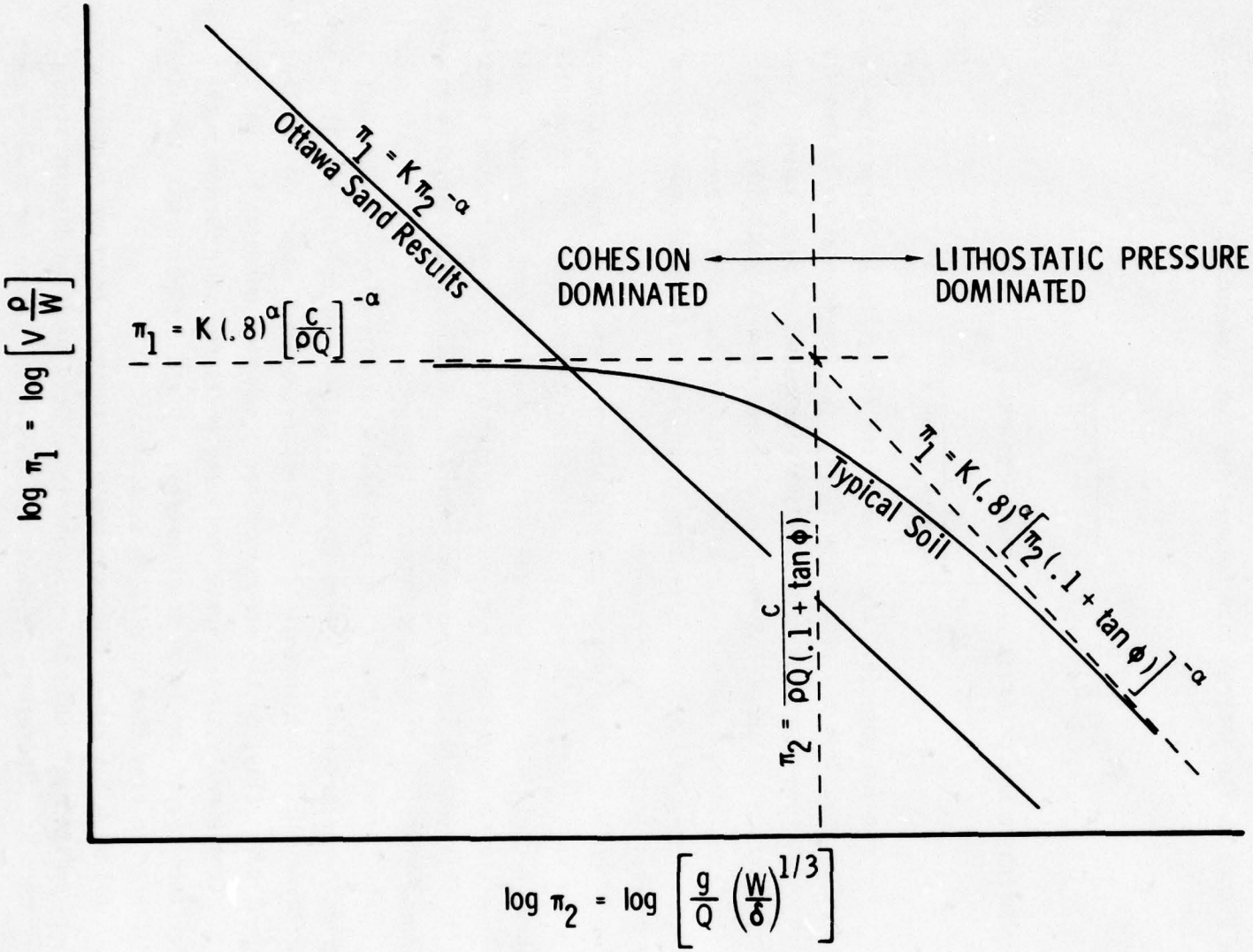

Fig. 5 Strength regimes for material with cohesion and internal friction.

with the two straight line asymptotes as shown. The transition between the cohesion-dominated regime and the lithostatic-pressure dominated regime is shown on the figure as the intersection between the two asymptotes. It is given by the value

$$\pi_2 = \frac{g}{Q}\left[\frac{W}{\delta}\right]^{1/3} = \frac{c}{\rho Q(k + \tan \phi)} \tag{36}$$

corresponding to the critical value of charge mass,

$$W_c = \left[\frac{c\,\delta^{1/3}}{\rho g\,(k + \tan \phi)}\right]^3 \tag{37}$$

For a given material, the value of this transitional charge size can be calculated or read from the plot given in Fig. 6. Representative ranges for the strength parameters of common materials are also shown on this figure. For example, desert alluvium at 1 G requires a charge mass of about 100 tons to reach the transition. The behavior below this critical size is cohesion dominated. Data from tests smaller than this size at 1 G would not extrapolate to the correct large yield behavior.

Prior to the development of this strength theory, it was puzzling to compare the results of cratering in clay as compared to sand. It is usually thought that sand is strengthless and that clay has definite strength. This would lead one to expect that a given explosive would always produce a smaller crater in clay than in sand. However, while the results confirmed this at small π_2 values, large π_2 showed the opposite behavior.

The reason for this is apparent by identifying the two components of the strength parameter model. Sand is essentially cohesionless, but it is not without strength. It has an angle of internal friction of about 35° and thus tan ϕ is about 0.7. Clay, on the other hand has a non-zero cohesion but has very small ϕ. Consequently, under large confining pressure, sand becomes much stronger than clay. For large scale events, a given explosive will produce a larger crater in clay than it will in sand.

Alluvium has almost the same angle of internal friction as does Ottawa sand. In addition, it has non-zero cohesion. This cohesion depends strongly on moisture content. Therefore, it shows the cube-root plateau for small yields, but becomes asymptotic to the sand curve for large yields. This explains why small scale field events cannot be extrapolated to large scale events since they

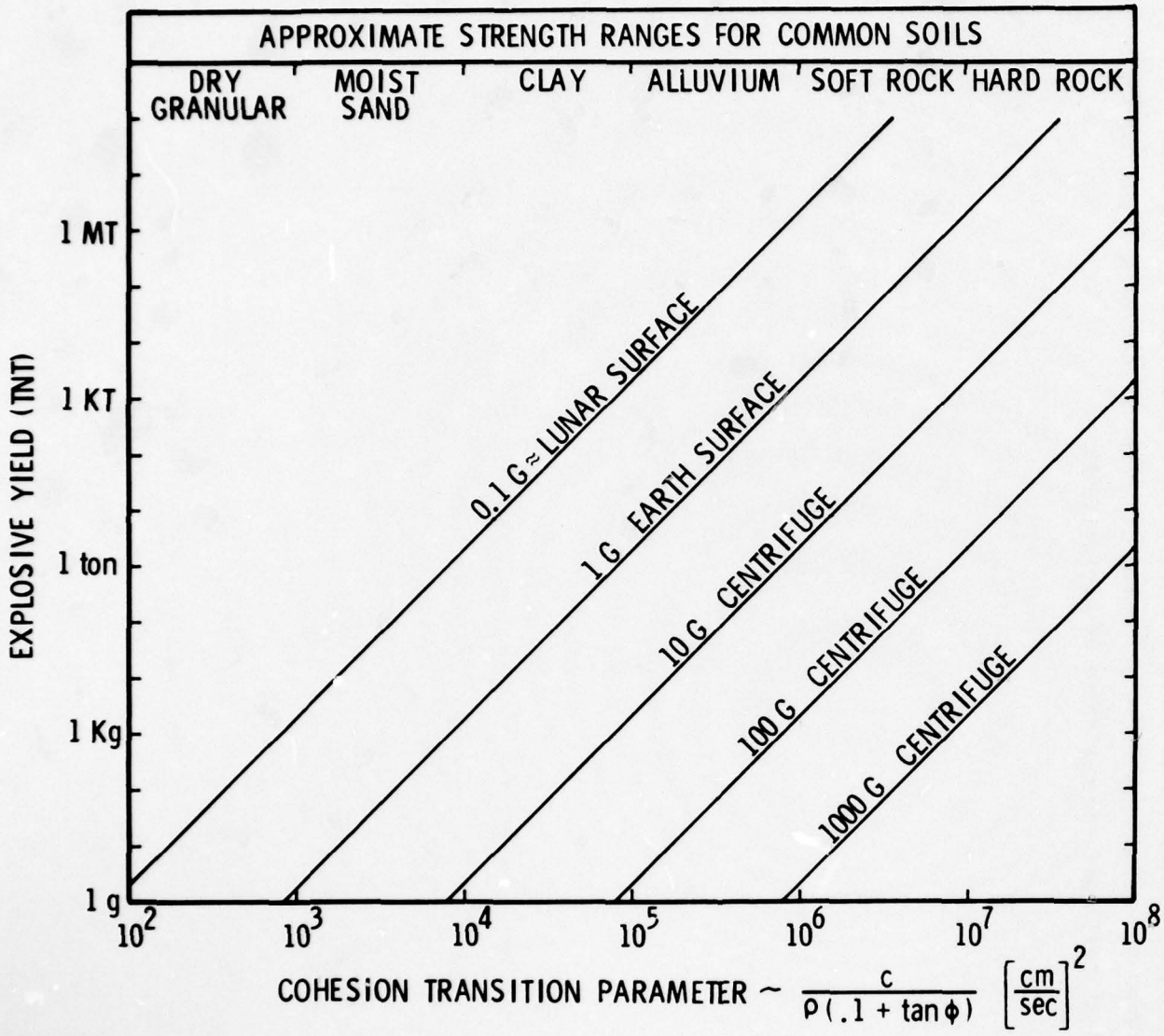

Fig. 6 Transition parameter dependence upon yield of TNT.

do not fit the same scaling law as do the large event data. This fact takes on particular significance when extrapolating to megaton-sized nuclear events.

This soil strength model for crater volume has been applied to various field data using a combined statistical/dimensional-analysis technique (Schmidt, et. al., 1978d). This on-going pilot study has provided a significant improvement in the data correlation for different size events conducted in various soil media over a range of burial depths.

4. Ground Motion Predictions

As discussed above, direct experimental simulation of large scale explosive events is possible, on a centrifuge at greatly reduced scale. This approach has proved to be extremely fruitful for the cratering problem and may also prove to be viable for the near-field ground motion problem. Preliminary feasibility studies verify this hypothesis. In lieu of a direct experimental program, existing field data furnishes the basis for ground shock predictions. Cooper and Sauer (1977) have showed that the apparent crater volume can be used as a measure of the energy imparted to the soil in correlating near-field ground motion measurements. This approach suffers from the fact that the crater volume is itself one of the dependent variables of an explosive event and is probably no easier to predict from existing field data than the ground motion itself. The correlation of ground motion to crater volume is not useful as a predictive tool. However, if one incorporates the crater volume prediction discussed in the previous section with the approach of Cooper and Sauer, then a prediction of the ground motion emanating from a given explosive event can be made.

The crater predictions discussed previously are valid for half-buried charges. In this case the apparent crater volume is predicted by the formula

$$\pi_v = \frac{V\rho}{W} = 0.194\overline{\pi}_2^{-0.472} \tag{38}$$

where, expanding eq. 35 from the previous section

$$\overline{\pi}_2 = \frac{c}{\rho Q} + (\tan\phi + k)\left[\frac{g}{Q}\left[\frac{W}{\delta}\right]^{1/3}\right] \tag{39}$$

and a value for k = 0.1 has been chosen as consistent with existing data.

Cooper and Sauer (1977) give, for near surface bursts, a correlation for peak horizontal displacement d_h as a function of range, r, as follows

$$\frac{d_h}{V^{1/3}} = 0.25\left[\frac{V^{1/3}}{r}\right]^3 \tag{40}$$

supposedly for all materials and explosives.

Equations 38 and 39 can be inserted into eq. 40 to obtain the peak displacement as a function of soil and explosive properties. However, the data used by Cooper and Sauer to obtain the above correlation consisted only of events using TNT. Consequently, using values for the energy density Q and the mass density of TNT, the dependence on material strength and explosive mass in cgs units is

$$d_h = \frac{0.0244}{r^3}\left[\frac{W}{\rho}\right]^{4/3}\left[2.39\ 10^{-11}\frac{c}{\rho} + 1.99\ 10^{-8}\ W^{1/3}\ (\tan\phi + 0.1)\right]^{-0.629} \quad (41)$$

It is convenient to rewrite eq. 41 as

$$d_h\ r^3\left[\frac{\rho}{W}\right]^{4/3} = 0.0244\ \left[2.39\ 10^{-11}\frac{c}{\rho} + 1.99\ 10^{-8}\ W^{1/3}\ (\tan\phi + 0.1)\right]^{-0.629} \quad (42)$$

where the term on the left is a non-dimensional quantity that will henceforth be denoted by the symbol π_{dh}:

$$\pi_{dh} = d_h\ r^3\left[\frac{\rho}{W}\right]^{4/3} \quad (43)$$

The value of π_{dh} is a measure of the peak displacement d_h at a given range and for a given charge size. It is a function of the explosive type and size and the soil material properties as given by eq. 42 for cgs units. A completely non-dimensional form of eq. 42 can be written as follows

$$\pi_{dh} = 0.869\ \left[\ (0.1 + \tan\phi)\pi_2 + \frac{c}{\rho Q}\ \right]^{-0.629} \quad (44)$$

Figure 7 shows the dependence of π_{dh} or charge size W for representative values of material properties. The corresponding general π_2 dependence is also shown.

For a given soil such as desert alluvium, the character of the curve reflects the differing roles of material strength in the different size regimes. At small yields, the cohesion of the alluvium dominates. Consequently the crater volume scales linearly with the charge energy, and the ground shock parameter π_{dh} is independent of charge size. At large yields the confining pressure is much larger and the dominant strength term is due to the angle of internal friction ϕ in the usual Mohr-Coulomb strength criteria. In the latter regime, the relative cratering efficiency, the volume per unit charge energy, decreases

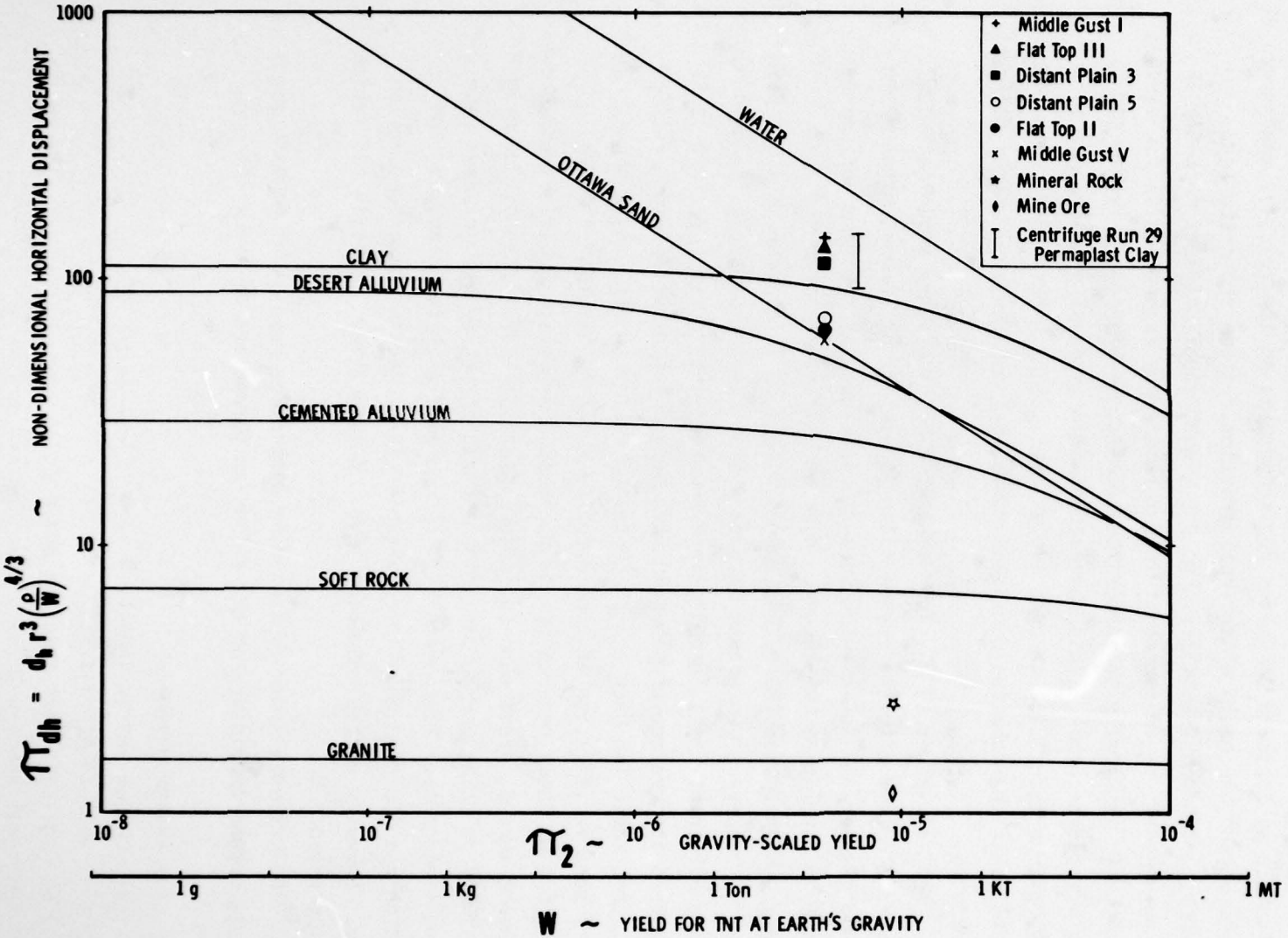

Fig. 7 Non-dimensional range-scaled horizontal displacement parameter as a function of soil type and explosive charge size.

with increasing size and, as a consequence, the predicted ground shock parameter decreases with increasing explosive yield.

For a given material, the transition from the cohesion dominated regime to the confining pressure dominated regime depends on the relative magnitudes of the cohesion and the angle of internal friction. Since the cratering efficiency, and hence presumably also the ground shock, differs markedly in these two regimes, it is important to note where the transition is for various materials. It is clearly inappropriate to measure data in one regime and extrapolate to the other. This observation is of special significance to a material with a transition at relatively large yields, where field data is likely to be in the cohesion dominated range, but results are desired for much larger yields.

Typical values of π_{dh} from several field shots are shown on Fig. 7. They correlate well with the curves. The reason is, of course, because the results of Cooper and Sauer which were an empirical fit to these very events, were used in developing the theory. However, all shots shown for zero d.o.b., with only one exception (Mole 206), were 20 tons of TNT in more-or-less like soil media. However, two events with only small height of burst (tangent above) in a very different media (granite) are shown on this curve also. If it is assumed that the crater volume would have been a factor of 2 larger at zero d.o.b., then these two events also correlate well with the curves shown. Thus there is some verification of the correctness of the strength effects.

Ground shock prediction as determined from Fig. 7 was, as the above development showed, based upon two major ideas. The first that of Cooper and Sauer (1977) relating peak ground displacement to crater volume based upon existing field data. These results, incorporated with the crater volume prediction results of Schmidt and Holsaple (1979) led to the ground motion results. However, at the resulting level of generality, certain limitations should be noted.

The crater volumes predicted by centrifuge results of Schmidt and Holsapple depend explicitly on the following parameters of the event

1) charge mass W
2) charge energy density Q
3) soil cohesion c
4) soil internal friction angle ϕ
5) Soil density ρ.

Their results correlated crater volumes over large ranges of these variables, for the case of half buried charges.

On the other hand, the field data available to Cooper and Sauer for the zero depth of burial case were limited to the range of 20 to 500 tons. Of the eight field events shown in Fig. 7 all were with TNT and six were 20 ton shots, and only relatively small variations in material properties were present. Although the 500-ton data is not shown in Fig. 7, it is only a factor of 3 larger in π_2 and would be just to the right of the 100-ton points shown for Mineral Rock and Mine Ore. These latter two points which represent a limiting soil type had to be adjusted for an h.o.b. effect to be compared with the half buried data. Consequently, the hypothesis of Cooper and Sauer cannot be considered to be verified in large ranges in explosive type, charge mass and media properties. However, some obvious experiments can now be suggested to further verify this type of relationship. These will be discussed in the next section.

5. Subscale Testing of Ground Motion

Pokrovsky and Fyodorov (1969) of the Soviet Union report on ground shock experiments conducted in the centrifuge. These experiments used No. 8 electric detonators buried at 9.5 cm depth in dense sand. At a modeling scale of 65 ($\alpha_x = 65$), this corresponds to 362 kg of TNT buried at 6.2 meters. They sought to measure peak stress isolines using passive identation gauges. These "dynamometers" were 2.5 cm in diameter and 1.8 cm thick giving them a corresponding large size when scaled to the prototype dimensions (1.6 meter x 1.2 meter). Hence they acted as small structures rather than free-field stress gauges. In addition, this type of gauge is not noted for being able to record a peak transient stress amplitude, to say nothing of the reported calibration procedure which was based upon a falling weight scheme.

Nevertheless such a procedure does suggest the possibility of the direct measurement of soil-structure response to the ground shock emanating from an explosive in proximity to the soil. A more sophisticated structure-gauge needs to be devised and could take on various configurations. One of the simplest would be to use a metal tube with either active dynamic instrumentation or to just record the final deformation using a yielding type of structure. The important point is that the similarity relationships derived for the general continuum in Section 2 also apply to the subscale structure. This has not been exploited, but does offer a very attractive approach to subscale testing of structural response to ground motion.

To test the feasibility of such a concept, a simple experiment was devised to examine ground motion scaling on a centrifuge. Using the concept of "modeling of models", two shots were designed to be scaled replicas. Two sizes of explosive were used, 0.49 gms and 4.08 gms of PETN, giving an order of magnitude yield variation. The small charge was fired at a very high value of gravity (504 Gs) corresponding to a very large prototype yield equal to 40 tons of TNT. The larger charge was fired at 294 Gs to give the same value of Π_2 as required by the similarity constraint (eq. 24).

Both shots were half buried spheres placed in "permaplast" oil based modeling clay. This material was chosen for convenience in handling and allowed direct scribing of a grid network on the surface of the sample. Based upon the expected common value for cratering efficiency, Π_V (eq. 23), the scale factor for linear dimensions relating the two shots was

$$\left[\frac{4.08}{0.49}\right]^{1/3} = 2.03. \tag{45}$$

Therefore the two samples were sized accordingly. Two sets of holes were drilled into each sample at increasing scaled radius. The large sample had both a 1/2 inch diameter series and 1/4 inch diameter series. The small one correspondingly had a 1/4 inch diameter series and an 1/8 inch diameter series. The preshot sample configuration can be seen in Figs. 8 and 9. In addition to the holes, various rectangular and radial grids were placed on the samples. A row of nine sand columns was also placed along the radial bisecting the rectangular grid on both specimens. The charges were fired and the resulting crater and residual permanent ground deformation compared. As can be seen in Figs. 10 and 11, the expected similarity in crater size and in the various measures of deformation was achieved. Preliminary analysis of the data for horizontal ground displacement is shown plotted in Fig. 7. The actual measured values at various ranges were multiplied by a factor of two approximating peak values as suggested by Cooper (1971).

The results of this experiment were very encouraging indicating that ground motion experiments can be conducted on a centrifuge. The requirements imposed by boundary conditions for such response will most likely dictate larger sample sizes or the use of a circular segment type sample. Piekutowski (1977) has demonstrated, using a plexiglass boundary, about 20% of the energy is lost based on resulting crater size when comparing a half space results with those from a full space. Using a 90° segment (quarter space) with steel or tungsten alloy walls to minimize the symmetry boundary losses and distortion, sample size could be increased two or three-fold for existing centrifuges (see Fig. 12).

Subscale model testing for ground motion response on a centrifuge also requires the further development of instrumentation techniques. Preliminary tests using carbon piezoresistive gauges to measure free-field stress history were performed (Schmidt and Holsapple, 1979). The results from tests conducted in desert alluvium and in clay demonstrated the feasibility of using miniature gauges on-board a centrifuge. The minor problems encountered with high frequency low level signal transmission across slip rings can be overcome with adequate signal processing. If on-board analog amplification is not sufficient, an analog to digital conversion can be made. A typical scheme would be to use an eight bit parallel transmission employing nine slip rings. A highly noise

Fig. 8 Pre-shot configuration of smaller ground motion specimen, 0.49gm PETN.

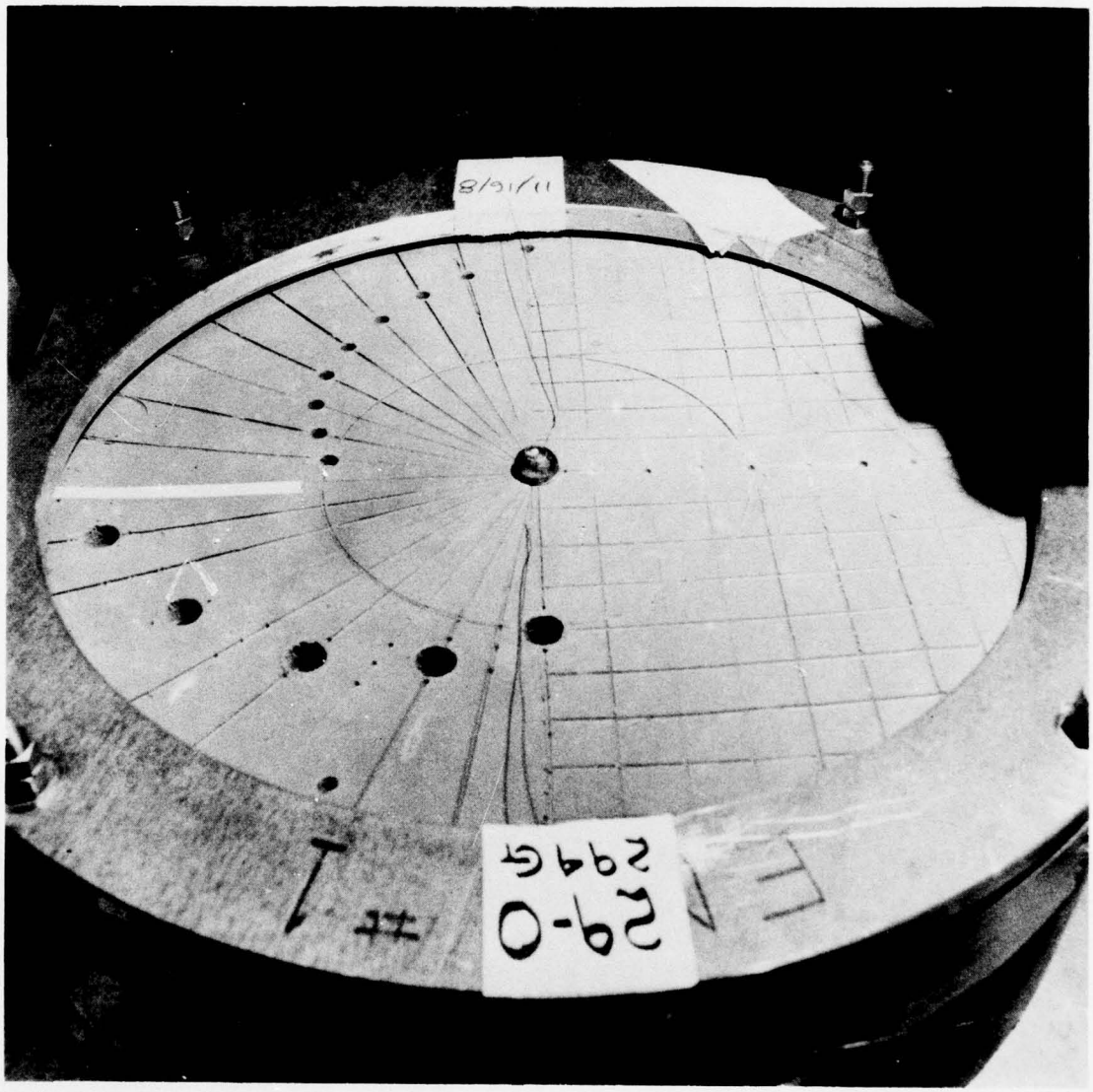

Fig. 9 Pre-shot configuration of larger ground motion specimen, 4.08gm PETN.

Fig. 10 Post-shot configuration of smaller ground motion specimen, 504 Gs.

Fig. 11 Post-shot configuration of larger ground motion specimen, 294 Gs.

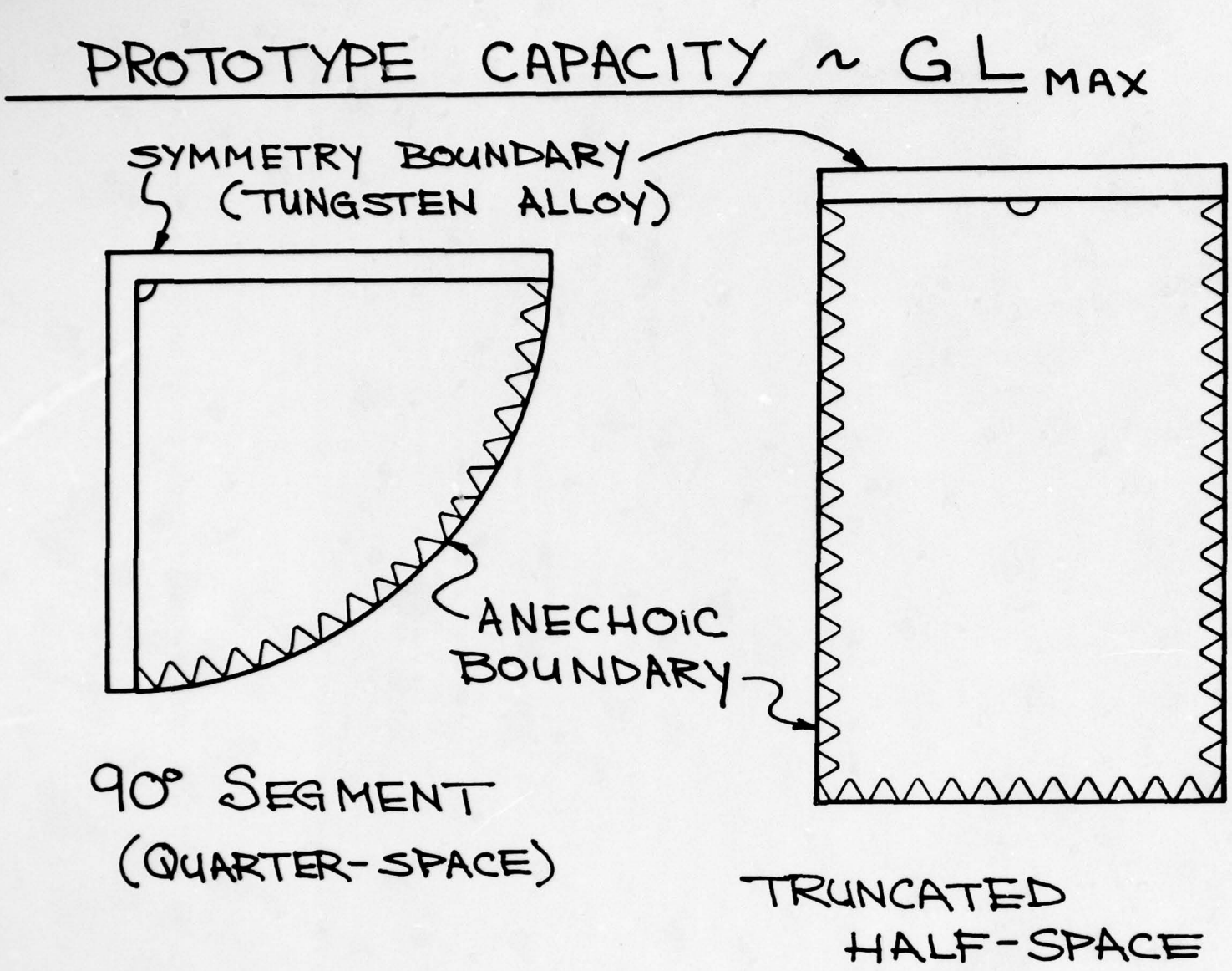

Fig. 12 Candidate soil specimen configurations allowing simulation of increased prototype size.

resistant 20 MHz bandwidth could be achieved with an amplitude sensitivity of one part in 256. The main source of electrial noise is due to the charge firing circuit, which could be circumvented by using on-board capacitors to eliminate the high current signal through the slip rings.

Gauges to measure structural response directly include standard resistive strain gauge applications, variable inductance measurements and others depending on specific structural configuration to be tested. In additon to using standard resistive type strain gauges on structural elements, a recently developed technique using fibre optics could be employed. This is a dynamic displacement gauge using two fibre light paths which can measure surface motions by monitoring the reflected light into the second fibre using a silicon diode or a photo-multiplier tube detector. This scheme is particularly attractive for centrifuge application in that it could all be mounted on-board the rotor and would not be affected by high G forces.

In general, model building techniques need further development. There is first the question of modeling a given site geology. If structural response is to be directly measured, the structure needs to be modeled consistent with the scaling discussed above. Lastly, miniature instrumentation compatible with centrifuge environment and slip ring transmission must be developed. All of these elements are within state-of-the-art techniques and it is only the special application that needs attention.

AD-A073 766 GENERAL ELECTRIC CO SANTA BARBARA CA TEMPO F/G 19/4
PROCEEDINGS OF THE NUCLEAR BLAST AND SHOCK SIMULATION SYMPOSIUM--ETC(U)
DEC 78 DNA0001-79-C-0081

UNCLASSIFIED DNA-4797P-2 NL

2 OF 4
ADA 073766

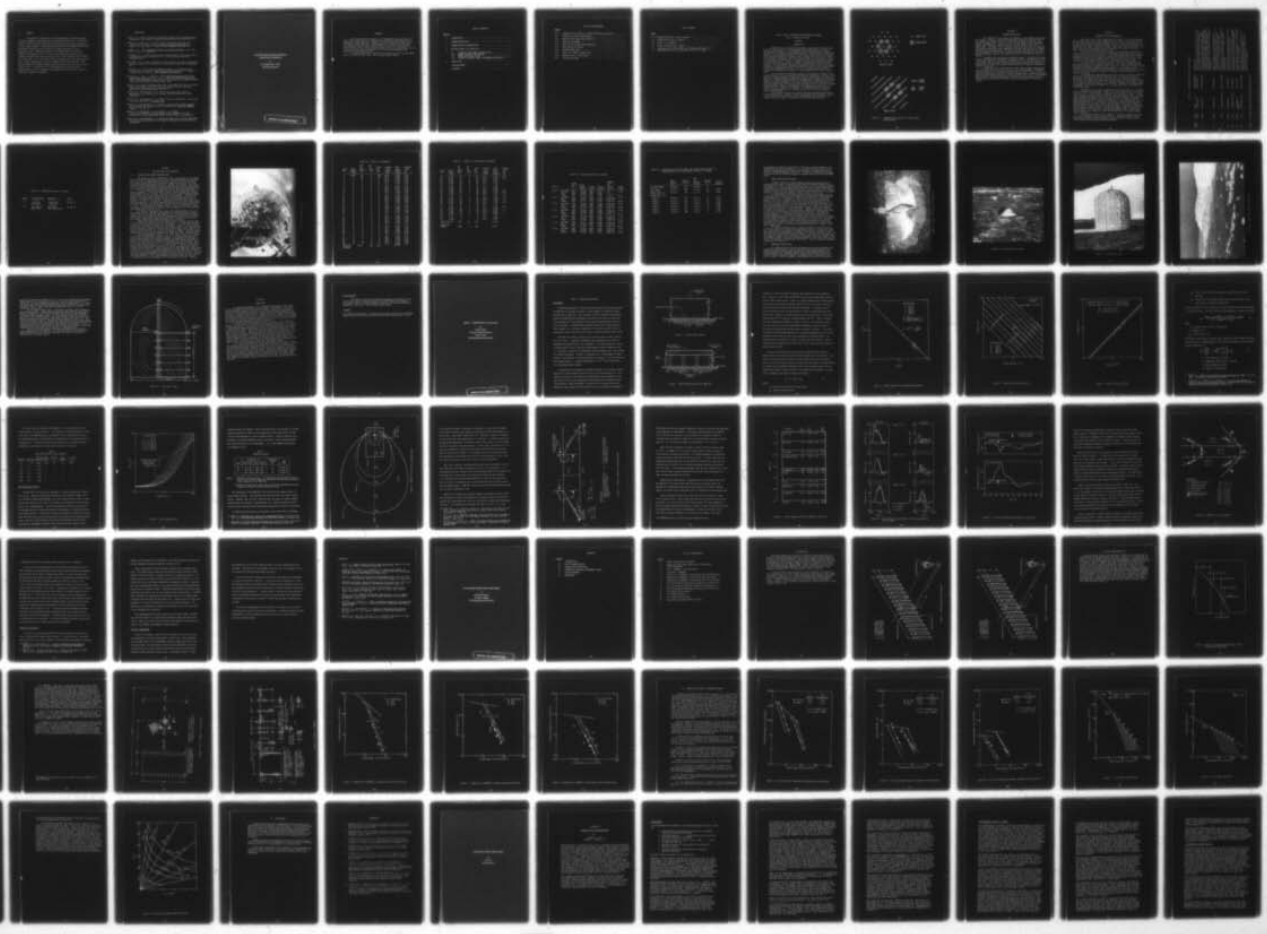

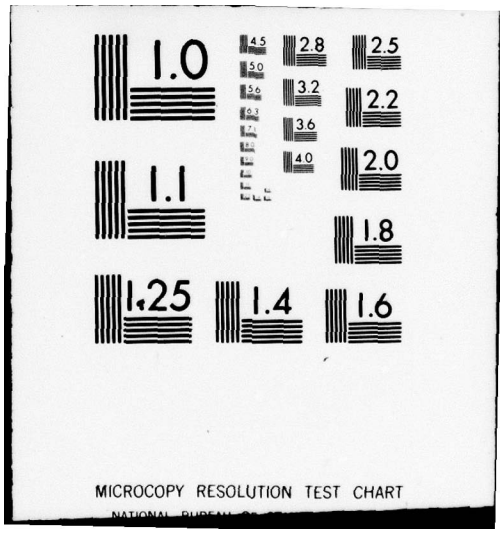
1.0
1.1
1.25
1.4
1.6
1.8
2.0
2.2
2.5
2.8
3.2
3.6
4.0
4.5
5.0
5.6
6.3
MICROCOPY RESOLUTION TEST CHART

6. Summary

The successful application of centrifuge methods to explosive crater formation suggests further application to ground motion studies. A similarity analysis confirms the applicability of previously derived scaling requirements to this latter problem. A non-dimensional horizontal displacement parameter was developed utilizing the earlier results of Cooper and Sauer (1977) in conjunction with a recently developed soil strength theory for cratering (Schmidt and Holsapple, 1979). A plot of this prediction parameter (Fig. 7) compares favorably with limited field data and a simple subscale test performed on a centrifuge. Due to the limited range of explosive yield for existing field data, further experimental studies are suggested using the centrifuge. This gravity-scaled size concept embodies equivalent yields from 1 gm to as large as 1 Mton of TNT. The feasibility of such ground motion studies has been demonstrated and various schemes for instrumentation for free-field as well as structural response are suggested.

7. References

Cooper, H. F. (1975) A review of ground motion from nuclear and high-explosive experiments, DNA Strategic Structures Review Meeting, SRI, Menlo Park, CA.

Cooper, H. F. and Sauer, F. M. (1977) Crater-related ground motions and implications for crater scaling, Impact and Explosion Cratering, (D. J. Roddy, R. O. Pepin and R. B. Merrill, eds.) Pergamon Press, New York.

Langhaar, H. L. (1951) Dimensional analysis and theory of models, p. 68, John Wiley & Sons, Inc., New York.

Piekutowski, A. J., (1974) Laboratory-scale high-explosive cratering and ejecta phenomenology studies, AFWL-TR-72-155, Air Force Weapons Laboratory, Albuquerque, NM.

Piekutowski, A. J. (1975) A Comparison of crater effects for lead azide and PETN explosive charges, AFWL-TR-74-182, Air Force Weapons Laboratory, Albuquerque, NM.

Piekutowski, A.J. (1977) Cratering mechanisms observed in laboratory-scale high-explosive experiments, Impact and Explosion Cratering (D. J. Roddy, R. O. Pepin and R. B. Merrill, eds.) Pergamon Press, New York.

Pokrovsky, G. I. and I. S. Fyokorov, (1969) Centrifugal Model Testing in the Construction Industry, Volumes I and II, "Niedra" Publishing House, Moscow, 1969. (Draft Translation prepared by Building Research Establishment Library Translation Service Great Britain, August 1975).

Schmidt, R. M., (1978) Centrifuge simulation of the JOHNIE BOY 500 ton cratering event, Proceedings of the Ninth Lunar and Planetary Science Conference, Geochimica et Cosmochimica Acta, Supplement 10.

Schmidt, R. M. and Holsapple, K. A. (1978a) Centrifuge crater scaling experiments I: Dry granular soils, Defense Nuclear Agency Report 4568F, Washington D. C.

Schmidt, R. M. and Holsapple, K. A. (1978b) Theory and experiments on centrifuge cratering, submitted to J. Geophys. Res.

Schmidt, R. M. and Holsapple, K. A. (1978c) A gravity-scaled energy parameter relating impact and explosive crater size, (Abstract) Trans. Am. Geophys. Union, Vol. 59, No. 12.

Schmidt, R. M., Holsapple, K. A. and Fisher, L. D. (1978d) Statistical-dimensional analysis applied to the assessment of crater configuration, Final Report, DNA Contract 001-78-C-0326 (in preparation).

Schmidt, R. M. and Holsapple, K. A. (1979) Centrifuge crater scaling experiments II: Material strength effects, Final Report, DNA Contract 001-78-C-0149 (in preparation).

MULTIPLE BURST HE GROUND MOTION GENERATION TECHNIQUES

by

R.G. DeRaad, Capt., USAF

DNA Field Command

PRECEDING PAGE BLANK-NOT FILMED

ABSTRACT

This paper includes a summary of the background issues generating the MISERS BLUFF ground motion test program and a conceptual description of the ground motion experiment plan. Emphasis is placed on describing those methods and support systems which were newly developed in fielding a multiple burst high explosives test program. A description is given of (1) the explosives quality control effort, (2) the charge placement and stacking operations, (3) the firing/initiation system development, and (4) the charge performance and simultaneity measurement program.

The author gratefully acknowledges the support received from the MISERS BLUFF Test Staff and Tech. Reps., Inc. in preparing this paper.

TABLE OF CONTENTS

Section

1 INTRODUCTION- -

2 PROGRAM DESCRIPTION -

3 GROUND MOTION EXPERIMENTATION -

4 MULTIPLE BURST TEST EXECUTION -

4-1 EXPLOSIVES AND CHARGE CHARACTERISTICS - - - - - - - - - - -
4-2 CHARGE PLACEMENT AND STACKING - - - - - - - - - - - - - - -
4-3 ARMING AND FIRING SYSTEM - - - - - - - - - - - - - - - - - -
4-4 SYSTEMS TO MONITOR CHARGE PERFORMANCE/SIMULTANEITY - - - -

5 CONCLUSIONS -

ACKNOWLEDGEMENT -

REFERENCE -

LIST OF ILLUSTRATIONS

Figure

1-1	Hexagonal burst patterns related to MAP basing options	
3-1	Single burst gate layout (MBI-1)	
3-2	Multiple burst gage layout (MBI-4)	
4-1	ANFO bulk placement	
4-2	Photo of TNT charge hole preparation	
4-3	Half-buried TNT charge	
4-4	Complete ANFO stack	
4-5	Event II-2, ANFO 6-charge array	
4-6	Multiple burst firing system	
4-7	Light pipe system	

LIST OF TABLES

Table

3-1 MISERS BLUFF Phase I Event Schedule - - - - - - - - - - - - - - - - - - -

3-2 MISERS BLUFF Phase II Program -

4-1 Stack II-1 parameters -

4-2 Charge characteristics summary -

4-3 Comparison of Pre-DICE THROW, DICE THROW, MISERS BLUFF II-1 and MISERS BLUFF II-2 bag weights and fuel oil content - - - - - - - -

MULTIPLE BURST HE GROUND MOTION GENERATION TECHNIQUES

by R. G. DeRaad, Capt. USAF

SECTION 1

INTRODUCTION

MISERS BLUFF was a Defense Nuclear Agency sponsored series of high explosives (HE) test events to investigate ground motions generated by single and multiple burst detonations. The experimental program was designed to support the USAF Missile X (MX) system development program. The basing mode investigations portion of the development program is vitally concerned with the soil response or ground motion generated by a potential nuclear attack on MX siting bases. The MX system concept incorporates a multiple-aim-point (MAP) basing design which relies on a combination of proliferation of target points and system hardening to achieve a desired survivability. Figure 1-1 presents, schematically, two potential MAP basing concepts, the trench and the shelter, along with the potential targeting concepts. The MISERS BLUFF experimental program consisted of a series of HE events to generate a ground motion data base applicable to the MX nuclear induced ground motion problem emphasized in Figure 1-1, i.e., the problem of multiple burst loading of an unattacked target point from simultaneous attack on nearby target points.

The ground motion experimental program, while designed to support the MX system issues, was built upon previous DNA sponsored ground motion studies; it used charges of explosive weight and type which were well represented in the existing data base. Important DNA tests emphasizing ground motions relatable to MISERS BLUFF single burst events include programs such as MIDDLE GUST, DISTANT PLAIN, Pre-MINE THROW IV, and Pre-DICE THROW II. The Pre-DICE THROW series with the objective of developing comparable trinitrotoluene (TNT) and ammonium nitrate and fuel oil (ANFO) charge explosive response, were conducted at the same site as a portion of the MISERS BLUFF test. However, the uniqueness of the MISERS BLUFF test series is that its primary objective was to develop a data base for multiple detonation induced ground motions.

The following section of this report describes the general MISERS BLUFF program and objectives. Section 3 details the ground motion experiments. Section 4 is concerned with the activities and the problem areas which are felt to be unique to the test program, in particular the multiburst test execution.

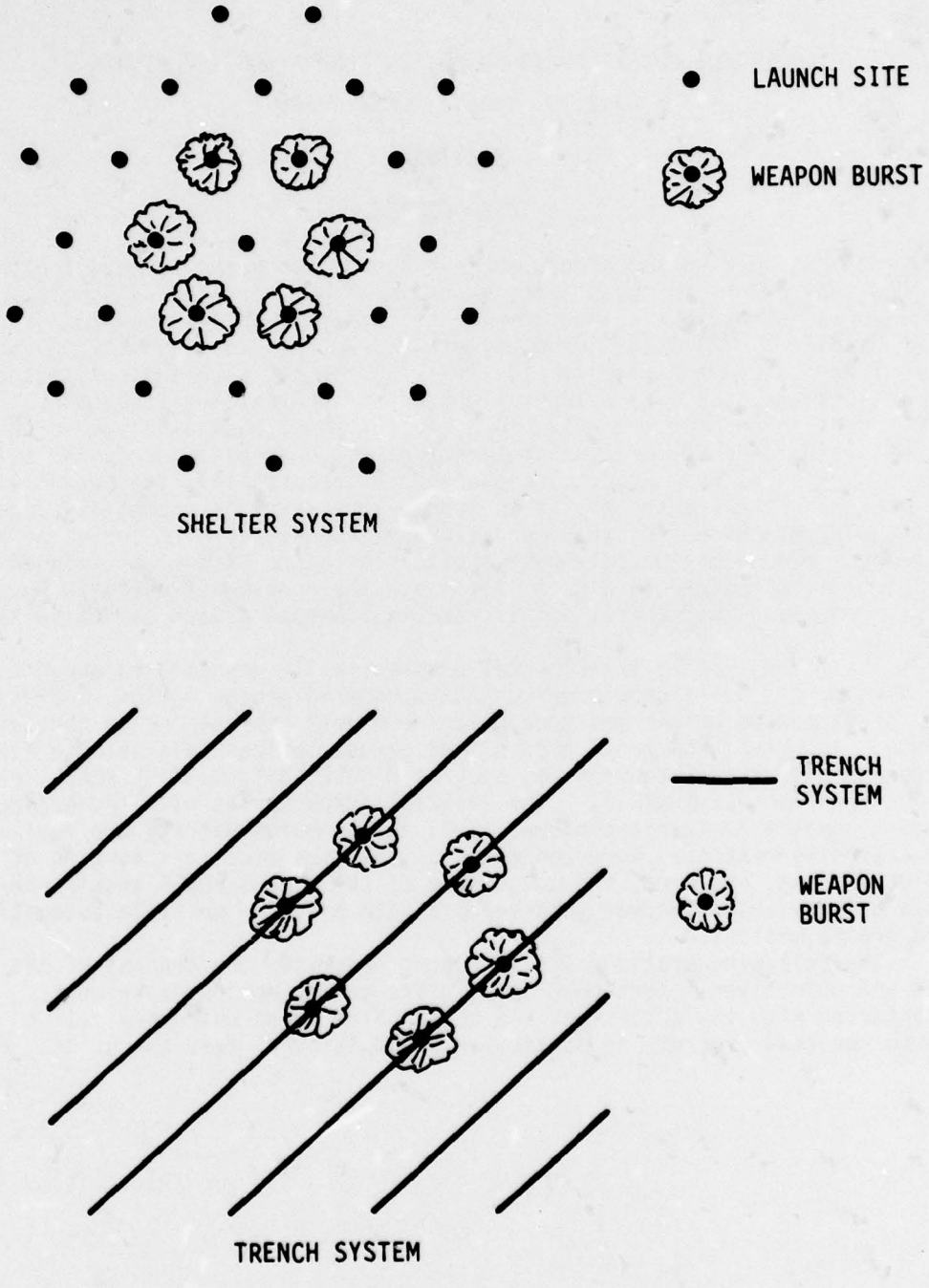

Figure 1-1. Hexagonal burst patterns related to MAP basing options.

SECTION 2

PROGRAM DESCRIPTION

The MISERS BLUFF test program was conducted in two phases and consisted of 10 events. Phase I, a series of eight events using small (256 and 1000 lb) TNT spheres, was fielded at the White Sands Missile Range, New Mexico, from August to December 1977. Phase II, a series of two events using 120-ton ANFO charges, was fielded at the Planet Ranch in Western Arizona, from April to August 1978. The Phase I tests, including three multiburst events of hexagonal array pattern, provided a large quantity of baseline data from which an analytic multiburst model was developed. The Phase II events, consisting of one single and one hexagonal 6-charge array, provided data from which analysts can refine and prove the model both for the larger yield and in a different (MX typical) geology.

Throughout the test program, single burst events in appropriate height-of-burst configurations, preceded the multiburst events. The objective of these single burst events was to serve as a calibration test for the follow-on multiburst events, and to provide a baseline measure for evaluating the adequacy of superposition of single burst ground motion waveforms to represent the measured multiburst waveforms.

Ground motion data measurements for each event included accelerations, particle velocities, soil stress, and soil strain (displacement). Measurements were taken both in the strong motion regions and in the far field or seismic regions surrounding the test bed. Extensive airblast data to support the ground motion data were taken, particularly on the multiple burst events. Approximately 850 channels of the ground motion and the airblast data were obtained in the Phase I testing and similarly 550 data channels were obtained in the Phase II testing.

SECTION 3

GROUND MOTION EXPERIMENTATION

The Phase I test program, conducted at the Queen 15 site on White Sands Missile Range, consisted of eight separate events. Table 3-1 contains a listing of these events along with brief objectives for each. There were essentially two test series within the Phase I program. One, having a half-buried charge configuration, consisted of single burst Events 1 and 3 and multiburst Event 6. The other, having a surface-tangent-above configuration, consisted of the single burst Event 2 and the multiburst Events 4 and 8.

Varying height-of-burst configurations were implemented, including the fully buried Event 5, for the purpose of differentiating and amplifying specific aspects of the ground motion response. The surface tangent events were intended to emphasize the airblast induced ground motions while the half-buried and the fully buried events were to emphasize the crater related motions. Event 7 was included for yield scaling verification in the half-buried configuration.

Explosive charges in the multiple burst test events throughout MISERS BLUFF were configured in a hexagonal pattern(s). This pattern was derived from the MX basing concept arrangements shown in Figure 1-1. The Phase I charge spacing distances for multiburst events were based upon the crater volume scaling ($1/V^{1/3}$) and the anticipated MX spacing distances. The objective being to subject the soil within the hexagonal pattern to environment levels relatable to the problem of interest.

The ground motion measurement plan for the single burst events emphasized the crater volume derived spacing distances and for the multiburst events emphasized the charge array center point which was at a spacing distance from any charge. The center point was emphasized; this point is the location of interest for the MX system application, i.e., the unattacked launch point which could be subjected to multiple, enhanced ground motions. Examples of the ground motion measurement plan are given in Figure 3-1, a single burst event, and Figure 3-2, a multiburst event.

The Phase II test program, conducted at the Planet Ranch site in Western Arizona, consisted of two events. Table 3-2 contains a description, with objectives, for each. These tests were conducted in a miniature or "scaled" alluvial valley typical of western land areas where the MX system may be sited. In addition to providing an opportunity to test the multiburst ground motion predictive model developed from Phase I data, the second event of the Phase II testing generated data which will be used to evaluate the "valley reverberation" problem. Valley reverberation is a term applied to relatively late-time low frequency ground motions which are anticipated to develop under the massive loading of a nuclear attack on a MAP system. In contrast to Phase I, the Phase II multiburst event spacing distance was scaled from the anticipated airblast loading at MX spacing ranges. This resulted in increased environment levels at the center of the charge array relative to either the half-buried or the surface tangent events of Phase I.

The following section of this paper will treat the unique systems and activities essential to the multiburst testing. Included are details of the explosives procurement and the placement, the multicharge initiation system, and the means used to evaluate charge performance.

Table 3-1. MISERS BLUFF Phase I Event Schedule.

Event	Date	Type	Height-of-Burst	Description
I-1	2 Aug	Single burst	Half-buried	Provide single burst baseline data for multi-burst waveform synthesis model development.
I-2	15 Aug	Single burst	Surface Tangent	Identify half-buried versus tangent sphere phenomenological differences in ground shock at outrunning ground ranges (outrunning ranges are those where the crater-induced ground motions precede those induced by overpressure "airslap").
I-3	23 Aug	Single burst	Half-buried	Repeat of Event I-1, but including a more fully instrumented "Plateau" region, i.e., the intermediate distance region where ground motion is little attenuated with range.
I-4	7 Sep	6-charge hex array	Surface Tangent	Provide data for multiburst waveform synthesis prediction model, surface tangent charge configuration.
I-5	22 Sep	Single burst	Fully-buried	Check the effect of depth-of-burial and eliminate airblast-induced ground motions.
I-6	13 Oct	6-charge hex array	Half-buried	Provide data for multiburst waveform synthesis prediction model, half-buried configuration.
I-7	26 Oct	Single burst (256 lb)	Half-buried	Provide data on crater-induced scaling between 1000 lb and 256 lb charges.
I-8	7 Dec	24-charge array	Surface Tangent	Address reproducibility of multiburst data. Correlation with data from Event I-4. Evaluate influence nearest charges versus outer ring of charges.

NOTE: All charges 1000-pound TNT spheres except Event I-7.

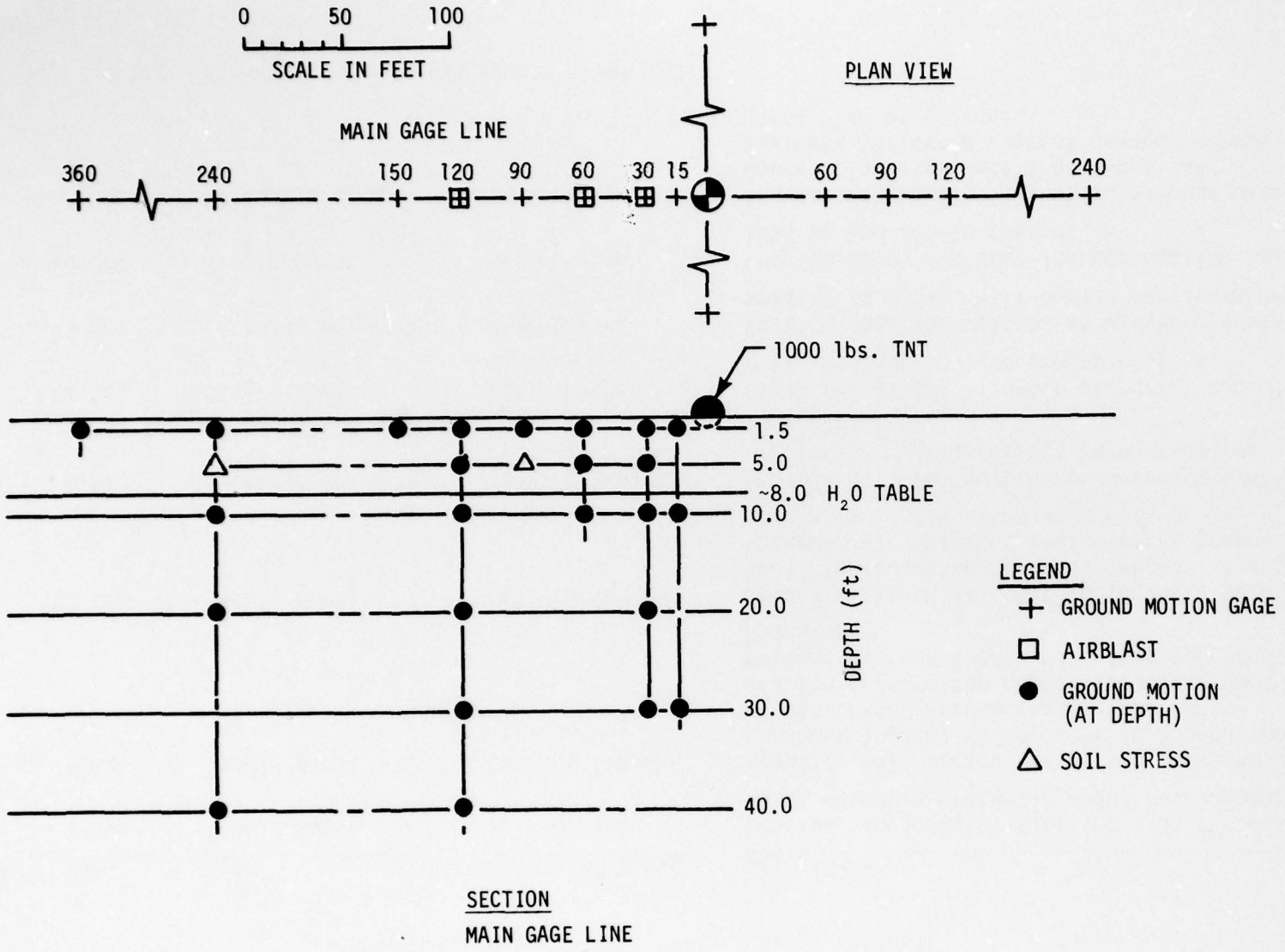

Figure 3-1. Single burst gage layout (MBI-1).

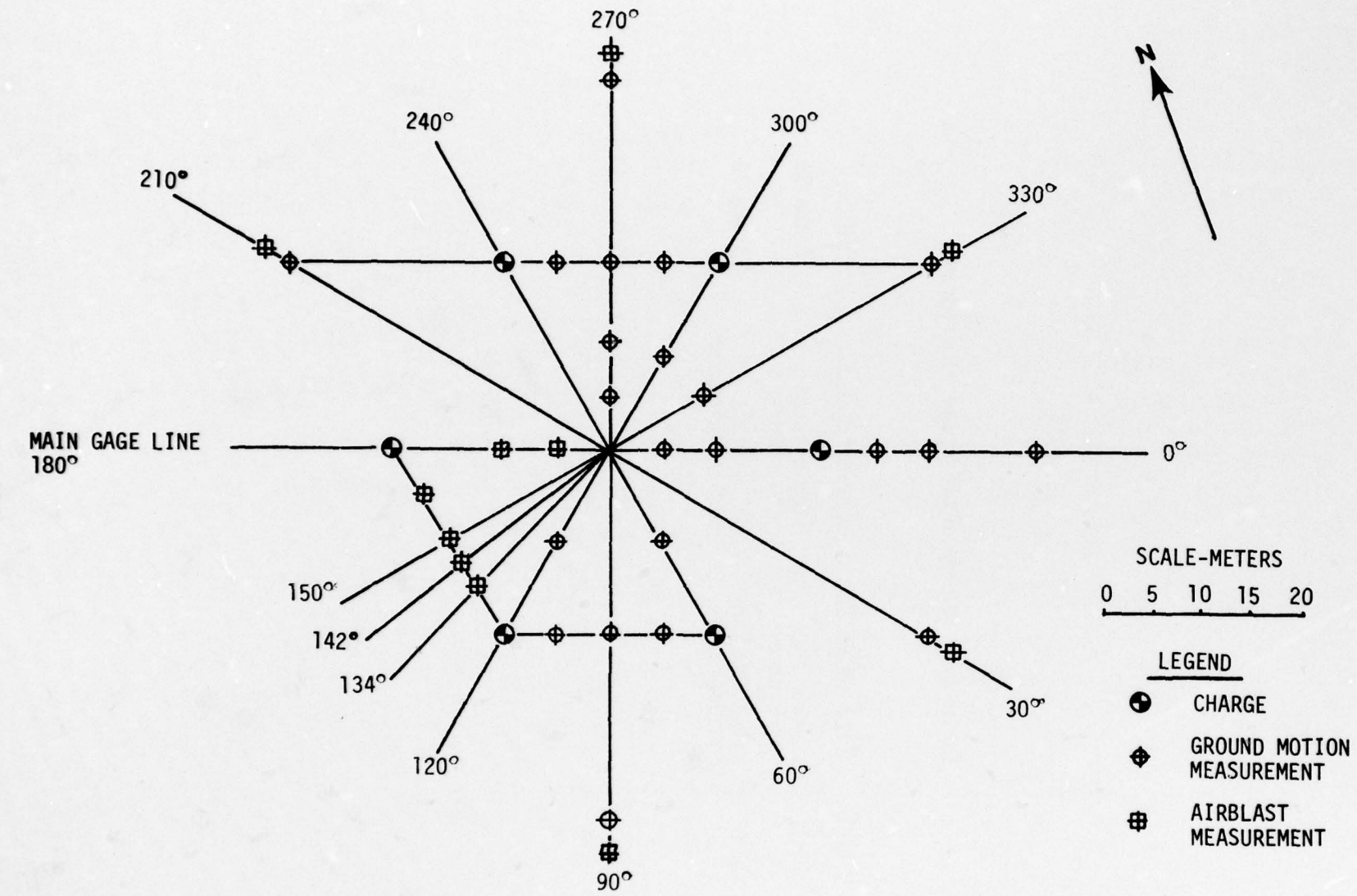

Figure 3-2. Multiple burst gage layout (MBI-4).

Table 3-2. MISERS BLUFF Phase II Program

Event	Configuration	Objective	Date
II-1	120 Ton ANFO Stack	Single burst Baseline	28 Jun 78
II-2	Six, 120 Ton ANFO Stacks	Multiburst Data Acquisition	30 Aug 78

SECTION 4

MULTIPLE BURST TEST EXECUTION

4-1 EXPLOSIVES AND CHARGE CHARACTERISTICS

The explosives used in MISERS BLUFF Phase I testing were all TNT spheres while the Phase II testing employed ANFO right circular cylinders with hemispherical caps. TNT was specified for the Phase I 1000 and 256 lb charges due to the existing ground motion data base for TNT spheres of that size. The large quantity of explosives expended in Phase II dictated use of ANFO for cost reasons. Also, the Pre-DICE THROW testing had established the ground motion comparability for ANFO and the existing data base derived from TNT and nitro-methane explosives.

The TNT spheres were purchased from the U.S. Army Ammunition Depot, Hawthorne, Nevada. A total of 40 nominal 1000 lb spheres and one 256 lb sphere were expended in Phase I testing. Each was cast with a center located pentolite booster which was in direct contact with the firing detonator. Detonators were placed at the sphere center through an access port approximately 3/4 inch in diameter. The detonator and the det cavity were back packed with one and one quarter (1-1/4) lbs of C-4 explosive. Charges were cast from Grade A TNT, using the pelleting method. The central pentolite booster was cast from a 50/50 mixture of TNT and PETN also using the pelleting method. The final charge density was 1.55 g/cc. The specification allowed a ±30 lb variation for the 1000 lb charges. The average charge weight for the nominal 1000 lb charges was 1011 lbs with maximum extremes of +12 lbs and -16 lbs.

The ANFO was obtained by bid purchase from Papago Chemicals, Inc., of Casa Grande, Arizona. The ANFO quality control specifications were the same as those of the Pre-DICE THROW and DICE THROW Events. The specifications included allowable fuel oil content and constraints on ammonium nitrate prill size and on bulk density. ANFO quality checks were performed at the test site by the U.S. Naval Surface Weapons Center under direction of Mr. M. Swisdak.

Samples were taken from the bulk ANFO spread in the voids on each layer of each charge while under construction (see Figure 4-1). Samples were analyzed for both fuel oil content and prill size distribution. Also, the weight of every 20th bag was checked as the charges were constructed. Table 4-1, to quantify and qualify variations, contains a layer-by-layer ANFO parameter record, including the fuel oil content for Stack II-1. Table 4-2 provides a summary of the ANFO stack characteristics for all of the charges of the Phase II testing. Table 4-3 provides a comparison of ANFO parameters from Pre-DICE THROW, DICE THROW, and MISERS BLUFF.

The data presented in Tables 4-1, 2, and 3 indicate some of the problems encountered in the ANFO quality control process. A fluctuating and generally low bag weight necessitated continual assessment and adjustment of the number of bags and the bulk ANFO to be included to obtain the proper charge dimensions and weight. This topic will be treated in the paragraphs on charge stacking. Four of the seven stacks (Stacks II-1, 2, 4, 5) had an average fuel oil content below the specified allowable range of 5.75 to 6.75 percent. In addition, the fuel oil content varied widely within a given stack as can be seen from the oil content variance given in Table 4-2. (Note the comparison to DICE THROW and Pre-DICE THROW in Table 4-3.) The bulk density was generally on the high side of the specification and in some cases exceeded the allowable range of 0.84 to 0.90 g/cc. The prill sizes were adequate although they contained the largest quantity of fines allowed in the specifications. As it became apparent from field checks that the fuel oil content was low, the percentage of oil was boosted at the plant. However,

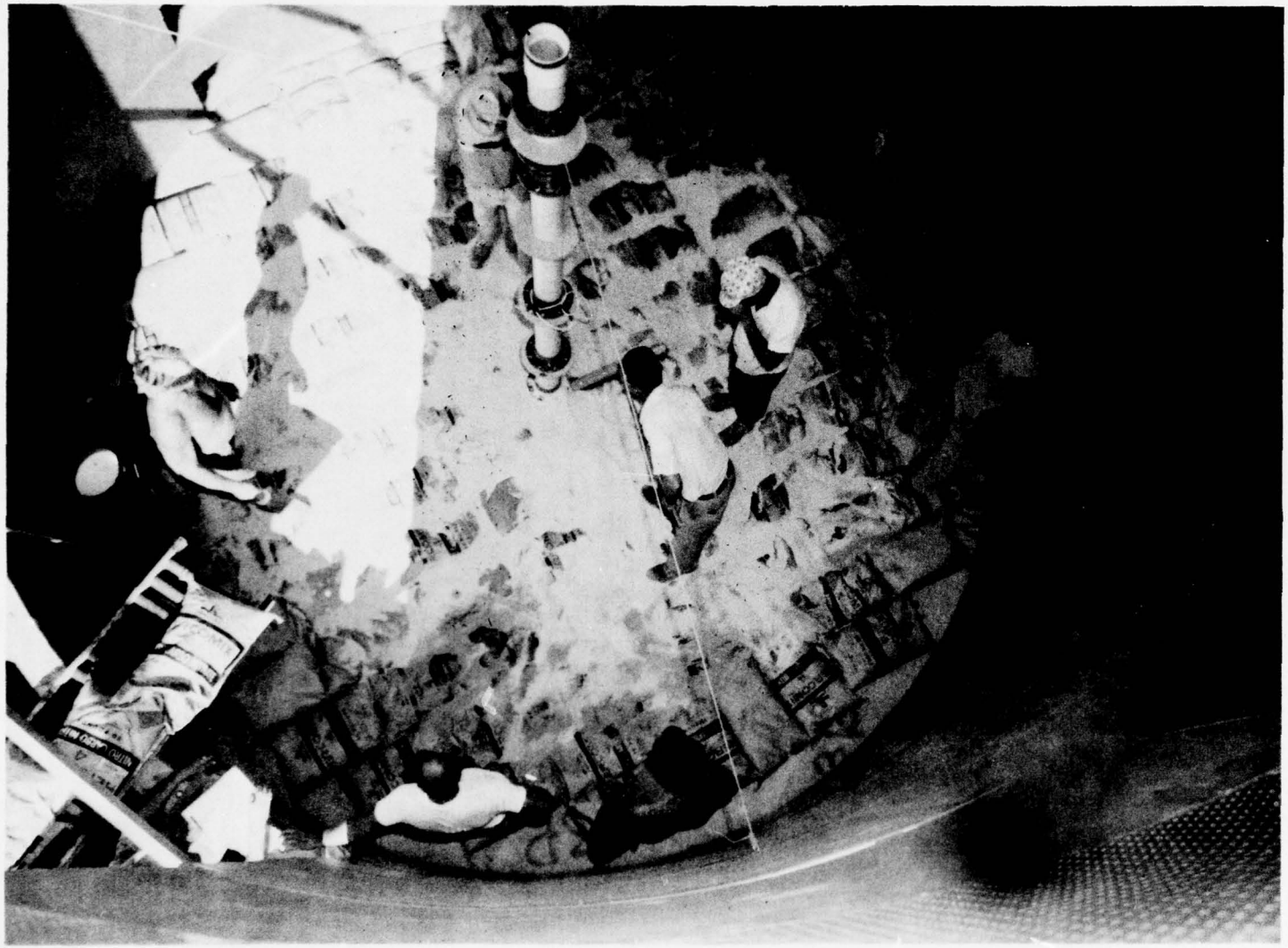

Figure 4-1. ANFO bulk placement.

Table 4-1. Stack II-1 parameters.

Layer No.	Layer Radius (ft)	No. of Whole Bags	No. of Bags Bulk	Total No. Bags	Average Bag Weight (lb)	Total Layer Weight (tons)	Average Fuel Oil (%)
1	8.542	95	8	103	46.8	2.408	4.78
2		94	8	102	46.9	2.392	4.89
3					47.4	2.415	3.93
4					46.6	2.379	5.59
5					47.1	2.402	5.25
6					47.4	2.415	4.54
7					48.4	2.471	4.31
8					48.6	2.481	5.44
9					51.0	2.598	4.09
10					47.0	2.400	6.90
11					46.0	2.369	5.64
12					47.0	2.397	5.48
13					46.4	2.369	4.80
14					45.9	2.341	5.69
15					46.6	2.374	4.02
16					46.6	2.379	3.68
17					48.8	2.488	4.83
18					47.7	2.410	5.25
19					47.4	2.417	3.88
20					47.7	2.433	5.99
21					48.2	2.456	4.59
22					51.0	2.598	5.06
23					49.2	2.512	5.72
24					48.2	2.458	5.45
25					48.4	2.466	5.72
26					47.5	2.422	5.21
27					47.2	2.407	5.20
28					49.1	2.504	5.99
29					49.0	2.501	6.03
30					47.2	2.410	8.88
31					46.2	2.359	6.35
32					46.2	2.356	8.37
33					45.3	2.310	5.54
34					45.4	2.315	5.68
35					44.8	2.338	6.87
TOTAL FOR CYLINDER		3291	280	3571		84.752	

Table 4-1. Stack II-1 parameters (Continued).

Layer No.	Layer Radius (ft)	No. of Whole Bags	No. of Bags Bulk	Total No. Bags	Average Bag Weight (lb)	Total Layer Weight (tons)	Average Fuel Oil (%)
36	8.542	92	9	101	46.2	2.333	5.82
37	8.531	92	9	101	46.4	2.341	5.61
38	8.500	91	8	99	45.8	2.267	-
39	8.458	90	8	98	45.6	2.237	-
40	8.312	88	8	96	45.5	2.184	-
41	8.208	82	9	91	45.4	2.064	-
42	8.104	82	9	91	45.1	2.050	-
43	7.948	82	6	88	45.8	2.016	6.04
44	7.792	79	7	86	45.6	1.962	7.21
45	7.604	73	7	80	46.6	1.862	5.47
46	7.375	68	5	73	46.1	1.684	6.29
47	7.135	64	5	69	44.8	1.546	-
48	6.875	63	5	68	44.4	1.509	7.74
49	6.573	60	5	65	45.3	1.473	4.17
50	6.219	48	5	53	44.1	1.168	-
51	5.802	42	3	45	44.2	0.994	5.45
52	5.375	36	3	39	45.2	0.882	-
53	4.875	35	2	37	44.8	0.828	6.11
54	4.250	26	2	28	46.3	0.649	-
55	3.479	15	2	17	45.3	0.346	-
56	2.417	8	-	8	45.3	0.181	-
57	1.208	4	-	4	45.3	0.090	-
TOTAL FOR CAP		1315	117	1432		32.705	
TOTAL FOR CHARGE		4606	3	5003		117.457	

Table 4-2. Charge characteristics summary.

Charge		Total No. of Bags	Total Weight (tons)	Volume (ft^3)	Density (g/cm^3)	Average Fuel Oil Content (%) (ρ)	Height (ft)
II-1-1	CYLINDER	5390	83.645	2936	0.913	6.5	12.81
	CAP	1413	34.780	1281	0.870	7.4	
	CHARGE	4803	118.425	4217	0.900	6.7±1.3	21.5
II-2-1	CYLINDER	3571	84.962	2985	0.912	5.42±1.12	13.02
	CAP	1432	32.715	1140	0.919	5.99±0.98	
	CHARGE	5003	117.677	4125	0.914	5.55±1.11	20.06
II-2-2	CYLINDER	3468	85.598	2936	0.934	4.07±0.95	13.02
	CAP	1358	33.610	1204	0.894	5.35±1.93	
	CHARGE	4826	119.208	4140	0.923	4.30±1.26	20.80
II-2-3	CYLINDER	3366	82.223	2985	0.882	6.92±1.51	13.02
	CAP	1463	35.897	1288	0.893	4.50±0.73	
	CHARGE	4829	118.120	4273	0.886	6.04±1.73	21.75
II-2-4	CYLINDER	3367	82.120	2985	0.881	5.41±0.74	13.02
	CAP	1507	35.278	1177	0.960	5.48±0.19	
	CHARGE	4874	117.398	4162	0.904	5.42±0.70	19.98
II-2-5	CYLINDER	3468	84.071	2985	0.902	5.22±1.32	13.02
	CAP	1373	33.914	1176	0.924	5.50±0.79	
	CHARGE	4841	117.985	4161	0.908	5.30±1.18	20.32
II-2-6	CYLINDER	3468	83.936	2985	0.901	5.95±0.92	13.02
	CAP	1445	33.734	1157	0.934	6.04±1.63	
	CHARGE	4913	117.670	4142	0.910	5.98±1.21	21.08

Table 4-3. Comparison of Pre-DICE THROW, DICE THROW, MISERS BLUFF II-1 and MISERS BLUFF II-2 bag weights and fuel oil content.

	Bag Weight (lb)	No. of Samples	Fuel Oil Content (%) (ρ)	No. of Samples	Density (g/cm^3)
Pre-DICE THROW	50.8±0.8	203	6.0±0.4	51	
DICE THROW	50.4±1.0	480	6.1±0.4	89	0.914
MISERS BLUFF II-1	49.3±1.1	198	6.7±1.3	50	0.900
MISERS BLUFF II-2					
STACK 1	46.9±1.9	214	5.6±1.1	81	0.914
STACK 2	49.3±2.1	266	4.3±1.3	82	0.923
STACK 3	48.8±2.3	251	6.0±1.7	76	0.886
STACK 4	47.8±2.2	247	5.4±0.7	73	0.904
STACK 5	48.8±1.2	253	5.3±1.2	71	0.908
STACK 6	47.8±2.0	248	6.0±1.2	71	0.910

a discrepancy of from one to two percent of the fuel oil content seemed to exist between plant and field measurements. It is presumed that the high daytime temperatures (approximately 115°F) and the two-day delay, including transit to the test site, caused the apparent loss of oil. In general, the ANFO quality control was much less precise than that achieved in previous tests such as the DICE THROW Events.

4-2 CHARGE PLACEMENT AND STACKING

In Phase I testing, a charge placement technique was developed which allowed intimate contact of the half-buried and the fully buried spheres with an undisturbed soil cavity. A template was used to bore a hole of the proper diameter (see Figure 4-2). The sphere was lowered into place with a lifting device which gripped the interior of the detonator access port. A small amount of soil matching grout was placed in the soil cavity to provide intimate contact at the soil/charge interface. A half-buried TNT charge is shown in place in Figure 4-3.

The ANFO charge stacking process did not involve the placement problems presented by the TNT spheres but was complicated by variations in ANFO bag weight as mentioned earlier. The Event II-1 stack, as the result of an average bag weight of 49.3 lbs, was completed at a weight of 118.2 tons versus the design weight of 119.9 tons. However, it was very close to the design physical size of 21.5 feet high with a radius of 8.5 feet and contained the design 4800 bags. A photo of the completed stack is given in Figure 4-4. For Event II-2, the supplier was requested to provide a similar bag weight in order to obtain six stacks as identical as possible to the first event stack. However, bag weights tended to be lighter and fluctuated. It was necessary to compensate by adjusting the number of bag layers and the amount of bulk ANFO filling the voids. The adjustment approach used was: (1) determine the average bag weight as the cylinder was nearing completion and, (2) adjust the amount of bulk in the cylinder cap to provide the needed compensation. Extra bag layers were required to obtain the desired cylinder height for Stack 1 (2 layers), and Stacks 2, 4, 5, and 6 (1 layer each). This too resulted in weight variations which required compensation by varying the amount of bulk ANFO in the cap. The adjustment process was a dynamic effort which resulted in Event II-2 stacks which deviated from Event II-1 weight by less than 1 percent each.

The stacking process for the six stacks of Event II-2 required 11 days. Stacking was begun on 14 August and was completed 24 August, six days before event day. Each stack was constructed in a wooden shelter as seen in Figure 4-1, which gave protection from the elements and provided a form for the stacking process. Two stacking crews were employed to erect the charges. Charges 2 and 5 were completed on 15 August; charges 1 and 4 on 21 August, and charges 3 and 6 on 24 August. Note that opposite charges in the array were constructed at a given time so that one section of the array was not "aged" more than another. Figure 4-5 shows the completed charge array for Event II-2.

4-3 ARMING AND FIRING SYSTEM

The timing and firing system requirements specified for the MISERS BLUFF program were quite stringent. In the initial phases of program planning, the Data Analysis Working Group (DAWG) sponsored by Hq DNA, determined that simultaneous detonations in a hexagonal pattern would provide the necessary data for the time related ground motion analysis at symmetry points involving two, four, and six charges. Further, nonsymmetric measurement points would allow analyses

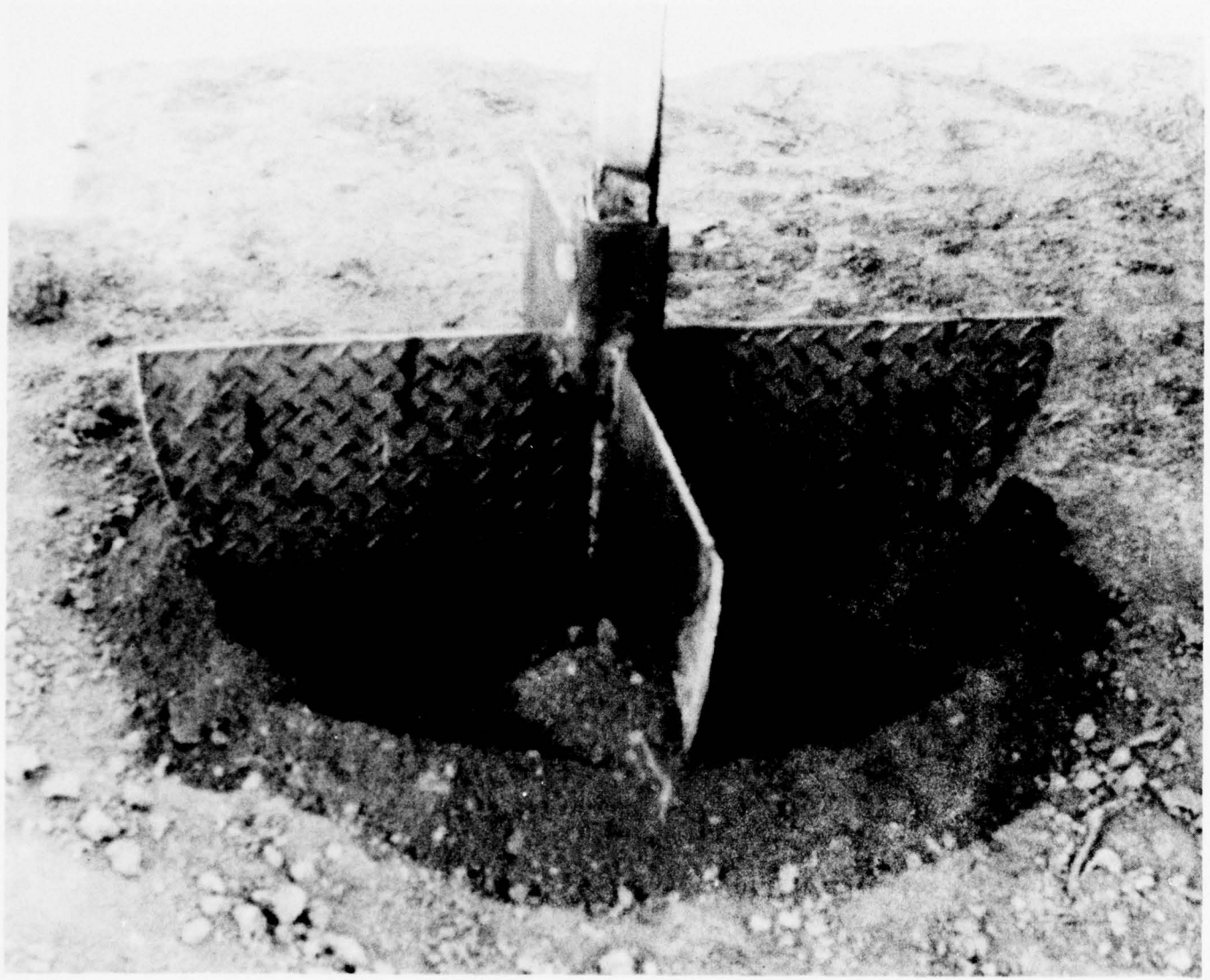

Figure 4-2. Photo of TNT charge hole preparation.

Figure 4-3. Half-buried TNT charge.

Figure 4-4. Complete ANFO stack.

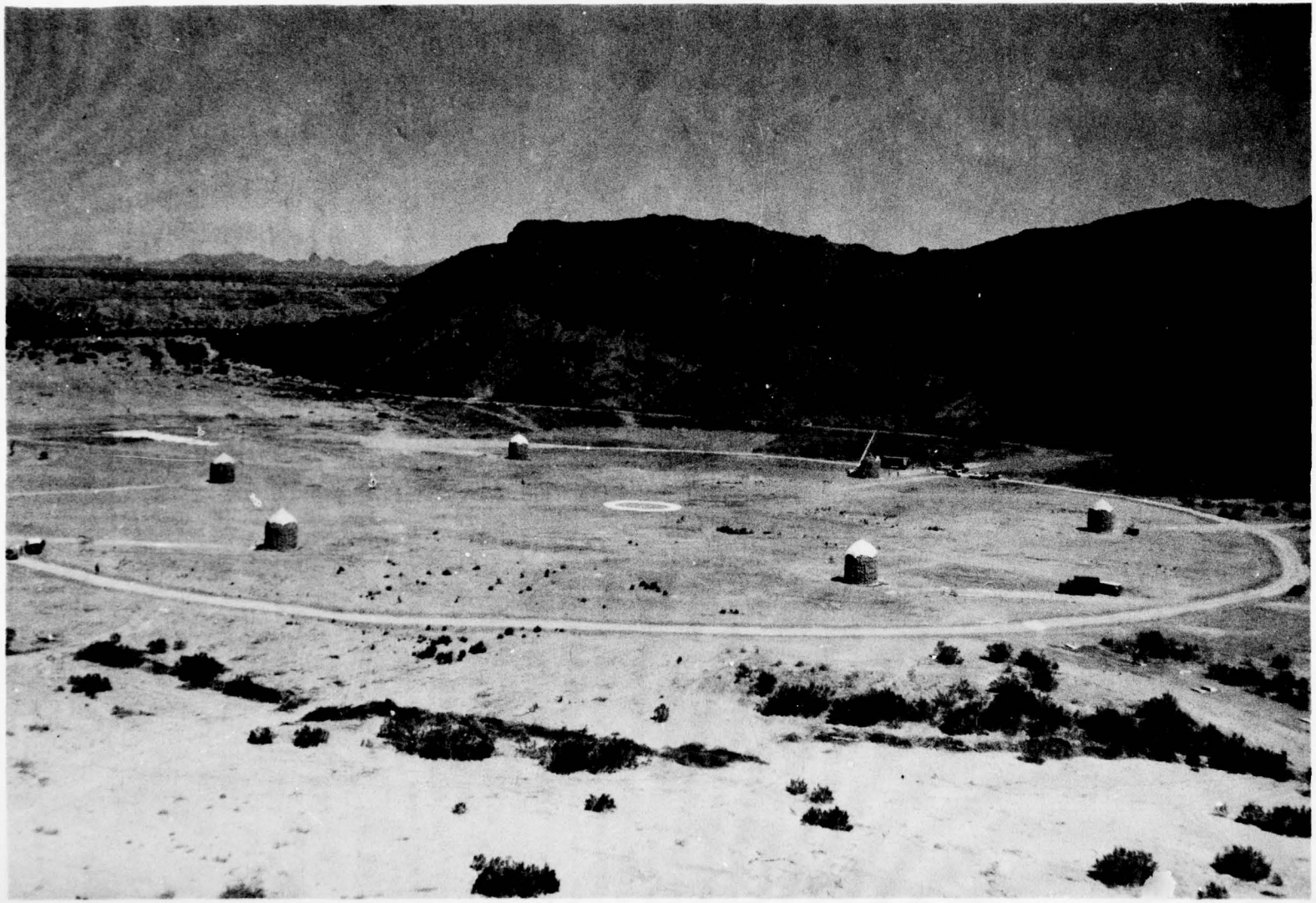

Figure 4-5. Event II-2, ANFO 6-charge array.

simulating non-simultaneous detonations. For these reasons and for simplicity the simultaneous detonation was specified.

For practical, fielding purposes it was necessary to specify an allowable detonator firing time spread for the multiple burst initiation. Studies, reported by the DAWG, indicated that the time-on-target sensitivities for ground motion enhancement in the MX environment could be specified and that a standard deviation in burst timing of 0.1 seconds is essentially simultaneous. Time scaling to the small yield of Phase I would indicate essential simultaneity can be attained from detonation variations on the order of 1.0 to 0.1 ms.

The Sandia Laboratories, Albuquerque (SLA) was selected to provide the arming and firing system for all MISERS BLUFF Events. The system was procured under specification that the maximum allowable time spread for multidetonator firing was not to exceed 10 μs. A schematic of the firing system is shown in Figure 4-6. The schematic is representative of all Phase I Events and, with variations, of Event I-8 (the 24-charge event) and the tests of Phase II. The firing unit, a TC-132 capactive discharge unit designed for nuclear field test applications, is used to fire TC-246 exploding bridgewire detonators. A TC-369 transverter charges the x-unit to 3 kV, which when triggered, discharges through a load ring into the detonator firing cables.

Variations of the basic firing system were used in Event I-8 and in Phase II testing. In Event I-8, the TC-132 x-unit was used as an intermediate trigger to operate four TC-406 x-units. Each TC-406 unit then fired six TC-246 detonators, i.e., six of the TNT spheres. The TC-406 x-unit is identical to the TC-132 except for the triggering circuitry necessary to accommodate the output of the TC-132 when used as a trigger. In Phase II, Event II-1, the TC-132 x-unit was used to fire seven TC-234 detonators which were located on the centerline of the ANFO cylinder. The TC-234 is the same detonator as the TC-246 except that there is an additional three and one-half (3-1/2) gram pellet of RDX explosive on the end of the detonator. The additional boost was desired, as an added safety margin, to initiate the pentolite boosters of the Naval Surface Weapons Center designed booster initiation system. For Event II-2, the TC-132 x-unit was again used as a trigger unit to operate six TC-406 x-units, one for each ANFO stack. Each TC-406 unit, in turn, fired seven TC-234 detonators.

Certification tests were performed by SLA to prove the system design for each configuration prior to fielding. The maximum time spread obtained for any of the system configurations was 49 ns with a simultaneity sigma of 27.1 ns. These results are well within the prescribed allowable 10 μs spread time.

4-4 SYSTEMS TO MONITOR CHARGE PERFORMANCE/SIMULTANEITY

Optical systems were used as the primary means to measure the charge performance and the simultaneity in both phases of the MISERS BLUFF testing. The photographic and photometric diagnostic instrumentation consisted of (1) high-speed Dynafax cameras, (2) Unit Light Radiation (ULR) devices, and (3) streak cameras.

Light breakout at the surface of the charge was used as the measure of simultaneity of detonations in multiburst events. The ULR devices, silicone solar cells with rise time of 1 μs, were used to monitor light breakout at a selected point on each charge in the multiburst events. Data from the ULR devices were recorded by oscilloscope mounted cameras. These measurements were supported with coverage of all detonations by Dynafax cameras operating at 26,000 frames per second, i.e., an interframe time of approximately 40 μs. ULR radiation

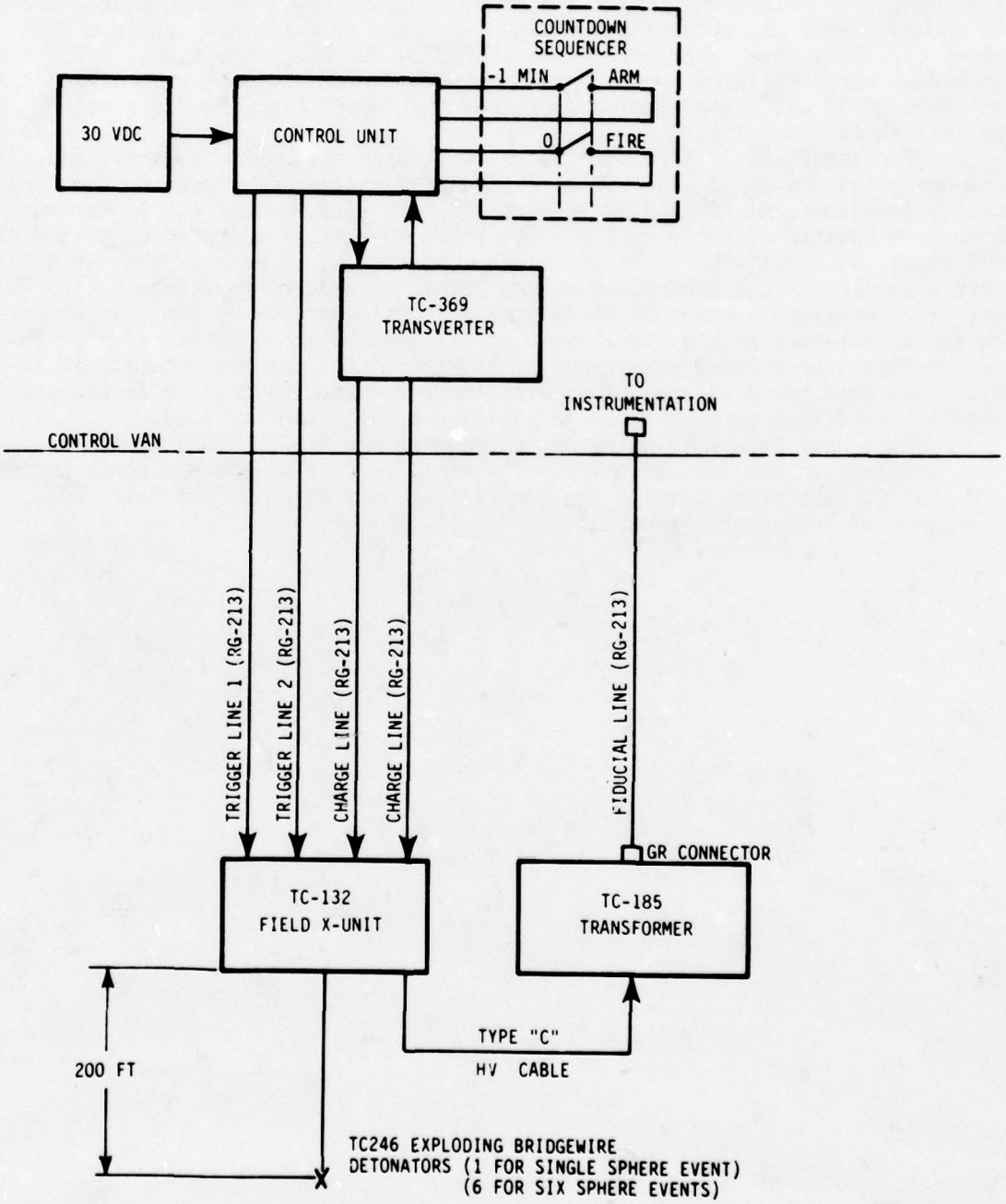

Figure 4-6. Multiple burst firing system.

device data from multiburst Events I-4, I-6, and I-8 show a maximum charge breakout time spread of 6.6 μs, occurring in Event I-4. Due to a limited supply of ULR devices (7), only seven charges were monitored on the 24-charge Event, I-8. Remaining charges were monitored by the Dynafax cameras which could give a maximum time resolution of 40 μs. Final timing data from multiburst Event II-2 are not available at this writing.

For the Phase II ANFO events, an additional diagnostic tool was added to those described above. A light transmission pipe system, developed by the Denver Research Institute, was installed in each ANFO stack to monitor the performance of the main booster assembly system. The light transmission system consisted of metal pipes, with polished interior, which were abutted to each of the seven octol boosters located on the centerline of the charge cylinder (See Figure 4-7). The light pipes provided a means of transmitting light generated by the booster detonation to the exterior of the stack where streak cameras (at a distance) were employed to record the time related appearance of light from the seven boosters. It is anticipated that these records along with the ULR data will provide an average ANFO detonation velocity for each stack in addition to simultaneity data.

Much data have been gathered to document the MISERS BLUFF explosive charge preparation and the execution. The final evaluation of the charge performance characteristics must await the compilation and review of the data and preparation of the several reports.

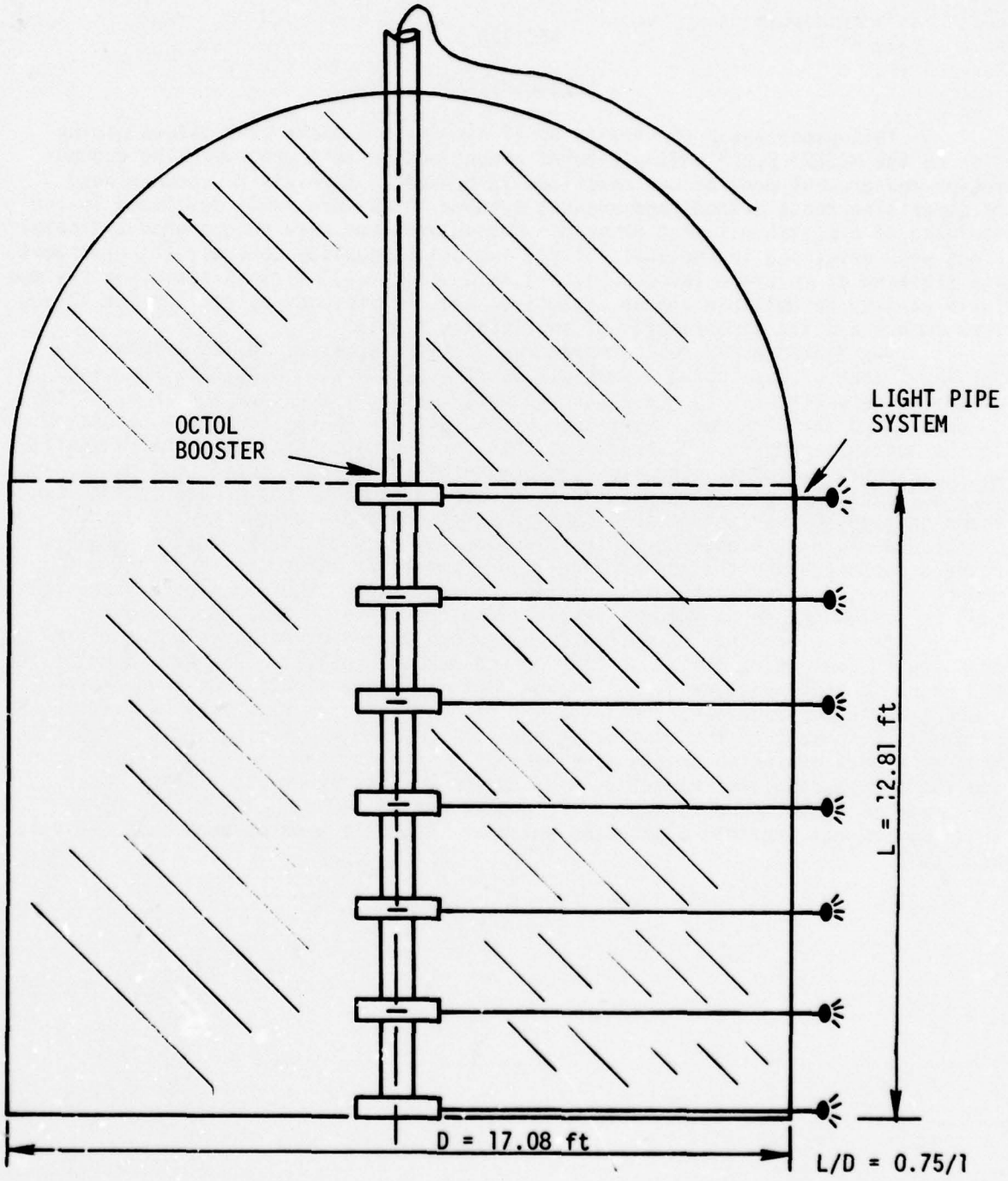

Figure 4-7. Light pipe system.

SECTION 5

CONCLUSIONS

This paper has presented in brief summary the background issues giving rise to the MISERS BLUFF multiple burst ground motion test program. The ground motion measurement program was described in concept. Emphasis has been placed on describing those methods and support systems which were newly developed in the fielding of a multiburst test program. Unique problems were encountered and solutions were developed in the areas of (1) explosives quality control, (2) placement and stacking of multiple TNT charges and ANFO stacks, (3) firing/initiation systems for a variety of multiple charge explosives and, (4) methods to monitor the charge performance and the simultaneity of multicharge events.

The MISERS BLUFF test program was highly successful in its primary objective: that of developing a multiple burst ground motion data base for high explosive detonations. The data are currently undergoing evaluation in an attempt to understand the phenomena generated by the multiple energy sources interacting in the nonlinear regime. Observations thus far indicate that additional investigation may prove useful. They may include specialized small scale testing, i.e., 1000 lb tests, designed to emphasize particular aspects of the ground motion waveforms through the variations in height-of-burst coupled with the variations in charge spacing distances. Laboratory testing may provide useful data on spall related phenomena and the convergence of horizontal waves at the center of multisource arrays. In addition, the information from MISERS BLUFF has emphasized the need to review and to reevaluate results from the previous testing.

It is clear that HE multiple charge ground motion data are but a first step toward evaluating the MX nuclear ground motion problem. The need to establish the nigh explosive nuclear ground motion link is a very significant problem requiring further evaluation. Analytic evaluations and the comparison of existing data will be a part of the continuing effort. Additional testing and the development of a high explosive charge more nearly duplicating the energy partitioning and the energy coupling characteristics of the nuclear event are likely. Much work remains to be accomplished on the ground motion issues. The MISERS BLUFF test program has provided a baseline which may be built upon through both analysis and test.

ACKNOWLEDGEMENT

This paper has drawn upon information contained in proposals and preliminary data reports from participants in the MISERS BLUFF Test Program, particularly those of the Denver Research Institute, the Sandia Laboratories, Albuquerque, and the U.S. Naval Surface Weapons Center.

REFERENCE

Data Analysis Working Group, "A Review of High Explosive Testing to Investigate Ground Motions Pertinent to the MX Multiple Aim Point Systems," May 13, 1977.

BLEST – A GROUND SHOCK SIMULATOR

by

Frank E. Seusy

Air Force Weapons Laboratory

Harry E. Auld

Civil Engineering Research Facility

PRECEDING PAGE BLANK-NOT FILMED

BLEST - A Ground Shock Simulator

DEVELOPMENT

The Berm-Loaded Explosive Simulation Technique (BLEST) was developed during the HARD PAN Test Program to provide a low-cost method of simulating airblast loadings over a large area. The requirement to load a large area was generated because the HARD PAN Test Site geology consisted of rock layers at relatively shallow depths and it was predicted that the ground shock would outrun the airblast environment. The BLEST design approach assumes that at large distances from a target, it is relatively unimportant if the correct pressure history is simulated so long as the correct total impulse is applied with the proper timing.

The BLEST was initially conceived as an explosive weave or sheet overlaid with soil (fig. 1). Feasibility experiments were conducted using a weave of detonating cord overlaid with a soil overburden. The second concept was a matrix of charges placed in drill holes which approximated a plane of explosives (fig. 2). There were substantial cost advantages with this approach and it was selected for further development. In order to standardize on a limited number of charge weights, it was decided to vary charge spacing as a means of varying the effective areal charge density. A standard charge depth of $1.8\ W^{1/3}$ was selected where W is the charge weight in pounds.

Calibration tests are required to determine impulse as a function of charge spacing for a given explosive and for the soil at a particular test site. The impulse delivered to a test plane can be determined by using photopoles to map the vertical velocity of the overburden around charges and by knowing the overburden density. Active instruments, including soil stress gages and accelerometers, are more expensive and are thought to be less reliable than photopoles.

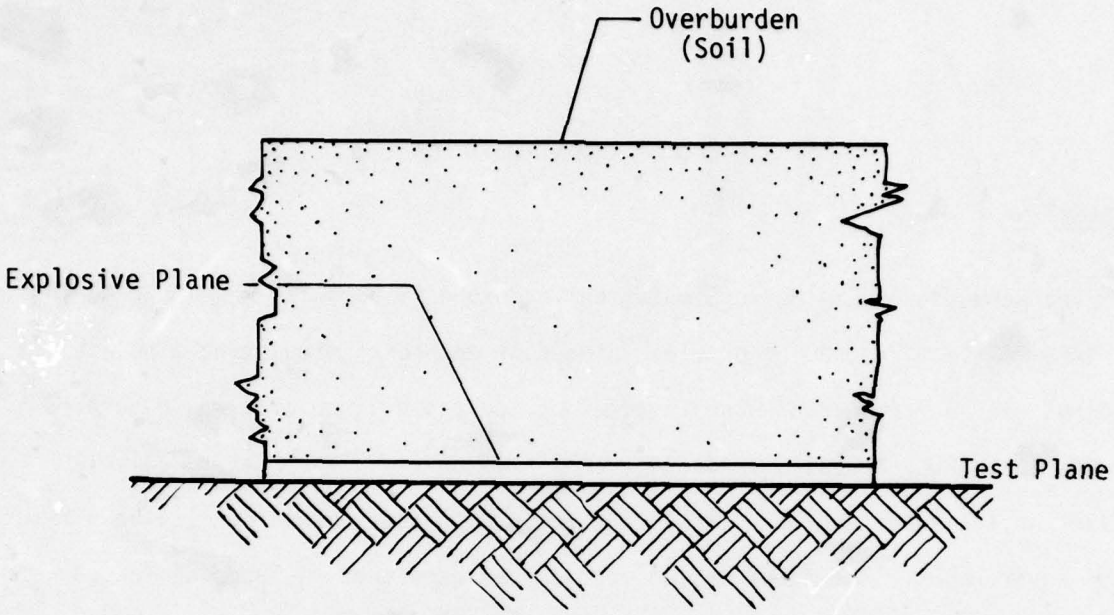

Figure 1. Initial BLEST Concept

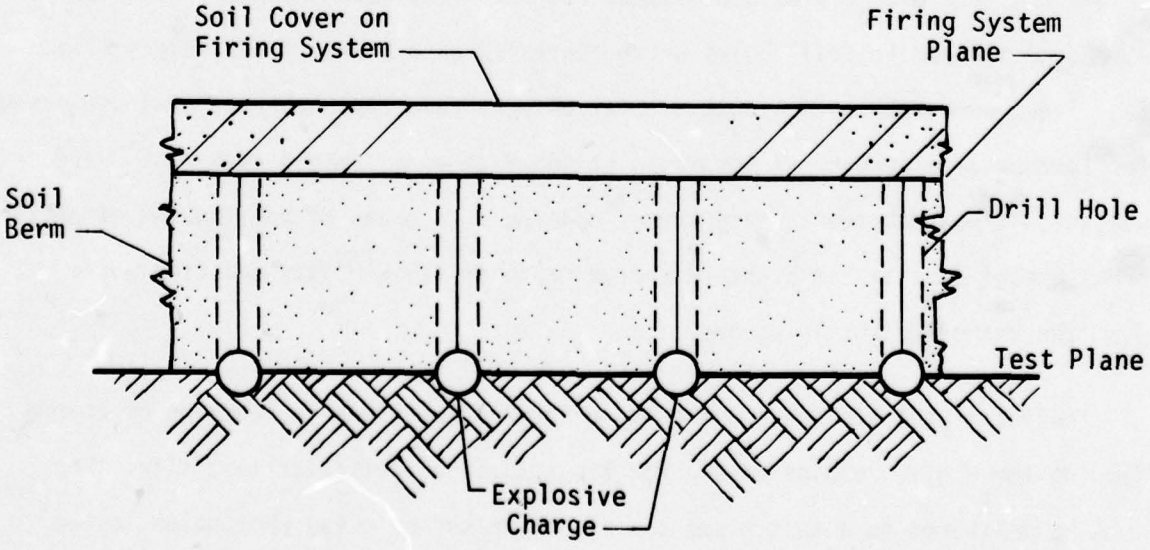

Figure 2. BLEST Concept Utilized for HARD PAN

Figures 3, 4, and 5 are BLEST calibration data presented in three different ways. Figure 3 is data from the HARD PAN Test Site with scaled impulse plotted versus scaled charge spacing. Figure 4 is impulse plotted versus charge spacing. The solid lines are derived from the straight line fit to the data in figure 3, with individual data points from HARD PAN overplotted. The dashed lines on figure 4 show the limits of charge spacing in terms of charge depth that have been tested. Figure 5 is impulse plotted versus the square root of the average charge weight per ft^2 times the overburden weight per ft^2. Figure 5 includes data from experiments configured as shown in figure 1 at the McCormick Ranch test area as well as data from experiments configured as shown in figure 2. No explosive energy corrections were made to the data in figure 5. The explosive used on the HARD PAN experiments was an aluminized ammonium nitrate slurry. Detonating cord (PETN) was used on the experiments at McCormick Ranch. The important point to recognize in figure 4 is that very low impulses (<7 psi-s) require discrete charges of less than 25 lbs, which is near the lower bound for many low-cost slurries.

The need for loading large surface areas was identified by studies of ground shock arrival times on vertical buried structures in layered media. The design of load areas and the design of impulse levels within the load area requires data on the seismic profile of the test bed, the location of target points of interest and the required simulation times at those target points, and the ground zero, height of burst and yield of the weapon to be simulated. The load area is bounded by the locus of points described by:

$$T_T + T_S = T_{AS} + T_{GS} \qquad (1)$$

where,

T_T = Time of first arrival at target point

T_S = Desired simulation time

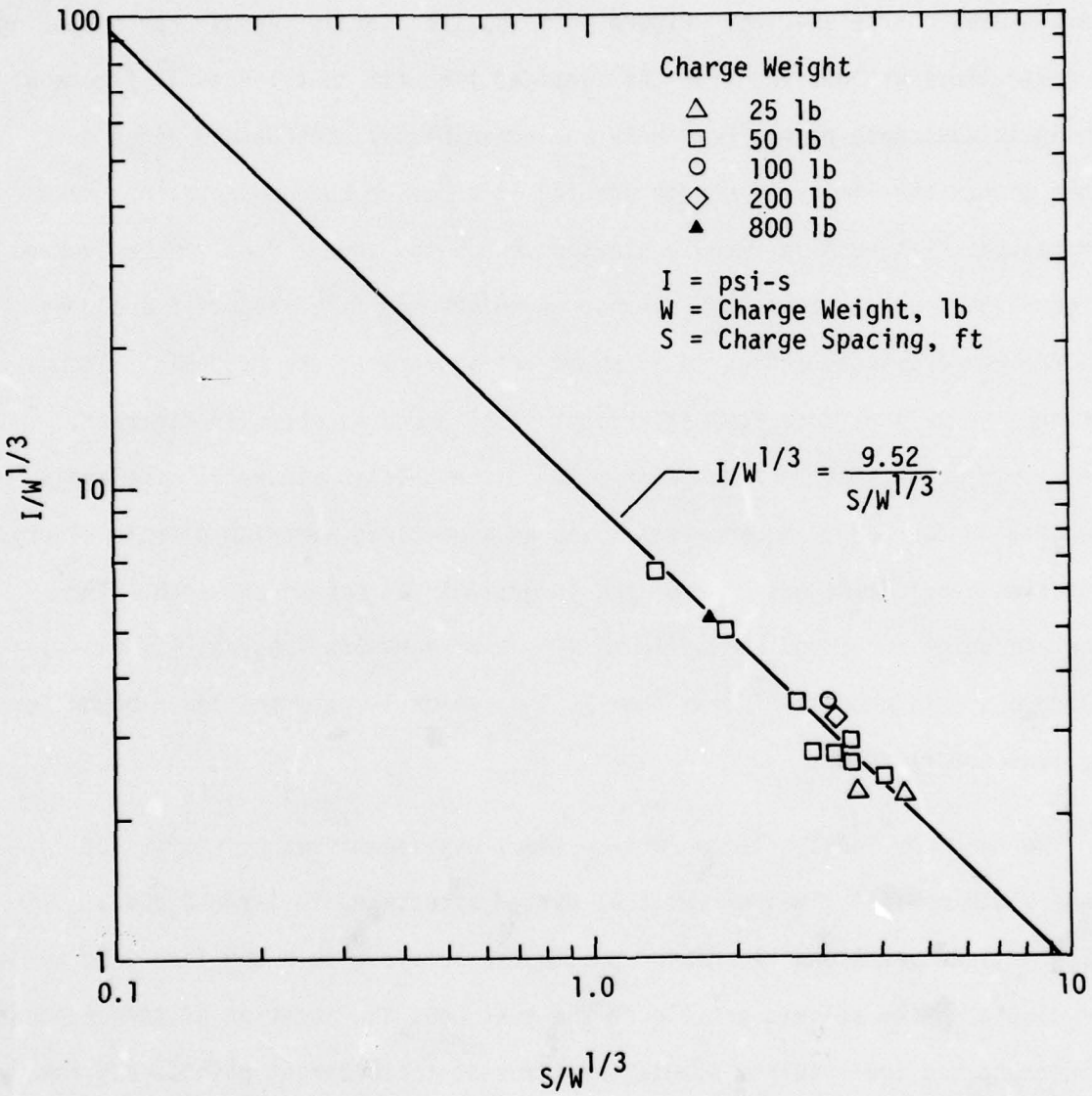

Figure 3. Scaled Impulse Versus Scaled Charge Spacing

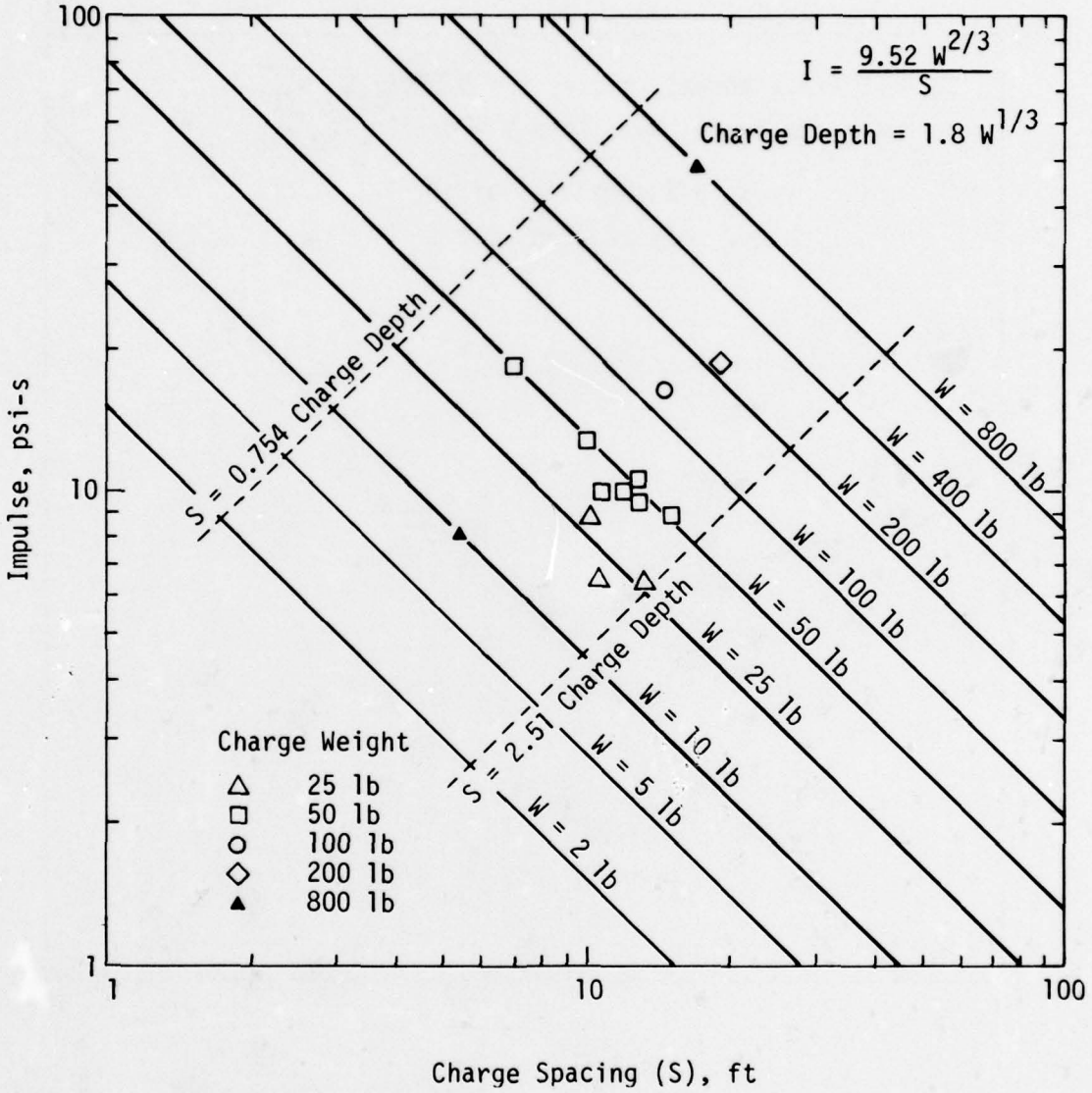

Figure 4. Impulse Versus Charge Spacing

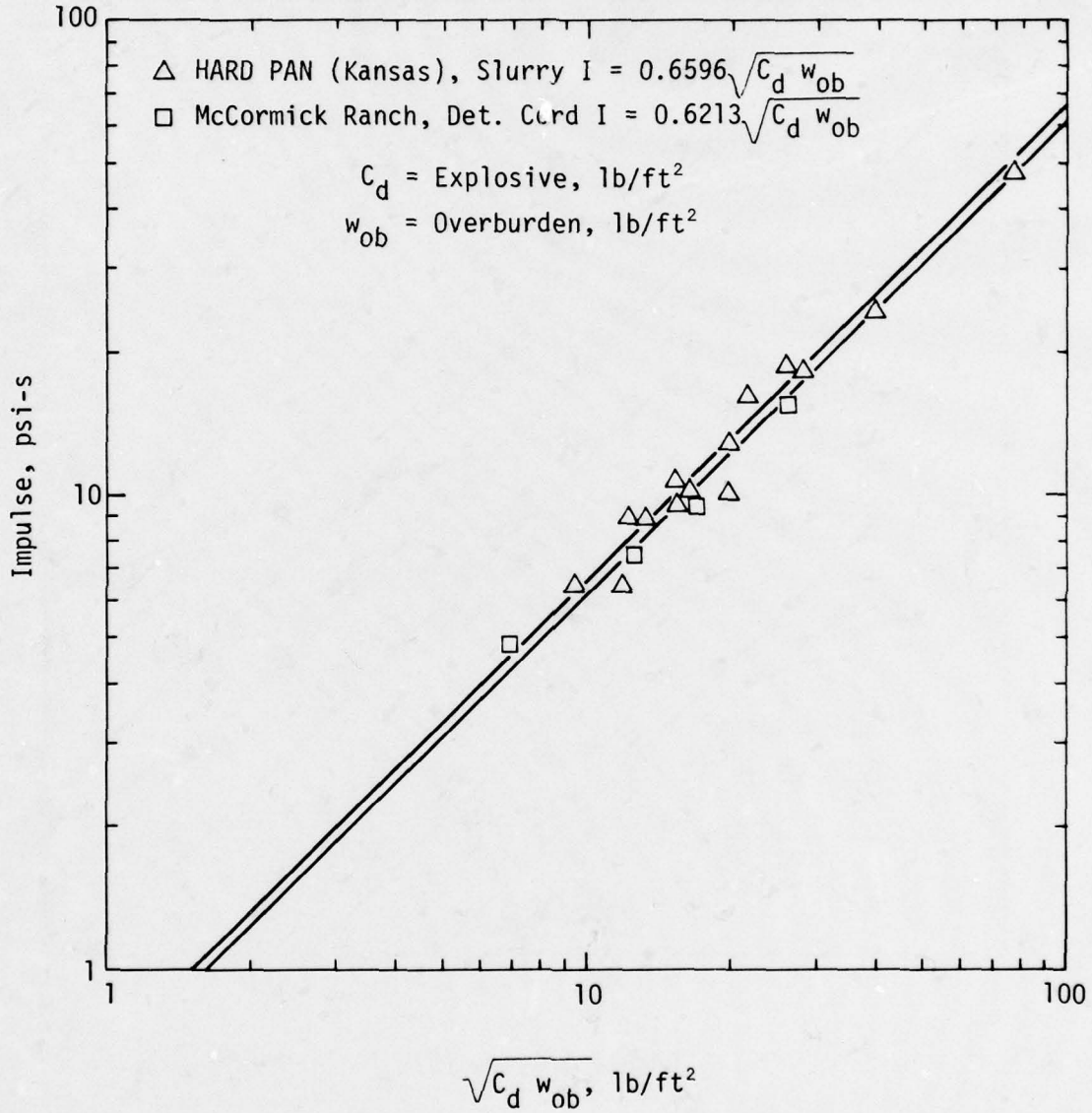

Figure 5. Impulse Versus $\sqrt{C_d\ w_{ob}}$

T_{AS} = Time of arrival of the air shock at a specified point in the test bed

T_{GS} = Travel time of the ground shock from the specified point in the test bed to the specified target point.

The time of arrival of the air shock from nuclear detonations has been documented in a variety of forms. One which has been used extensively is given by reference 1.

$$T_{AS} = \frac{.5429W - 21.185RW^{2/3} + 361.8R^2 W^{1/3} + 2383R^3}{W^{2/3} + 2.048RW^{1/3} + 2.687R^2} \qquad (2)$$

where,

W = 2x weapon yield in KT for surface burst

R = Range in K ft

T_{AS} = Arrival time in ms

The minimum travel time of the ground shock (compression wave) between two points on the surface of a layered geology is determined by evaluation of the following relation (reference 2):

$$T_{GS}^{N} = \left(\sum_{i=1}^{N} 2 H_i \sqrt{\frac{1}{C_i^2} - \frac{1}{C_{N+1}^2}} \right) + \frac{x}{C_{N+1}} \qquad (3)$$

H_i = Layer thickness, ith layer

C_i = Compression wave velocity, ith layer

x = Range between two points

N = Number of possible paths

---

1. Brode, H.L., Height of Burst Effects at High Overpressures, RM6301, The Rand Corps., Santa Monica, California, July 1970.

2. Crawford, R.E., Higgins, C.J., Bultmann, E.H., The Air Force Manual for Design and Analysis of Hardened Structures, AFWL-TR-74-102, Air Force Weapons Laboratory, Kirtland AFB, New Mexico, October 1974.

With definitions of the time of arrival of the air shock and of the travel time of the ground shock, the minimum value of the sum of the two for a given target range is the value for T_T, the time of the first arrival at the target point. The load area for a hypothetical case might appear as shown in figure 6 for load points A, B, and C.

At the boundary of the load area, the load is applied for zero time; i.e., there is no excess time for a portion of the pressure time history to reach the target point. Interior to the load boundary there is excess time, T_L, for the load to be transmitted to the target point. Interior to the load area boundary, equation (1) becomes:

$$T_T + T_S + T_L = T_{AS} + T_{GS} \qquad (4)$$

The interpretation of T_L used in the HARD PAN series is illustrated in figure 7. If the pressure and impulse time histories shown in figure 7 are the ideal nuclear overpressure waveforms, and if the ground shock traveled at a constant velocity C, the target point could only receive the portion of the signal sent during T_L. On this basis, I_1 would be the design impulse at that point. Programs have been written for the HP9820 to draw contours of constant impulse for design of a BLEST. The inputs to these programs are polynomial or segmented fits to the air shock time of arrival, ground shock transit time, and nuclear impulse as a function of range and time.

There are non-simulation effects associated with overburden fallback from the BLEST. Essentially the same impulse is delivered to the test bed by the fallback as was initially imparted to the test bed and overburden. The use of discrete charges and relatively high overburden velocities tends to scatter the overburden in space, and delay the return in time. Therefore, overburden fallback cause little concern in most test applications.

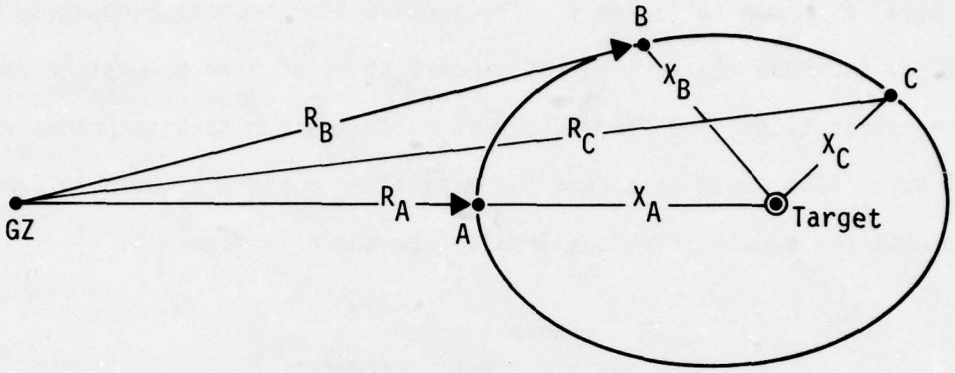

Figure 6. Load Area for Hypothetical Case

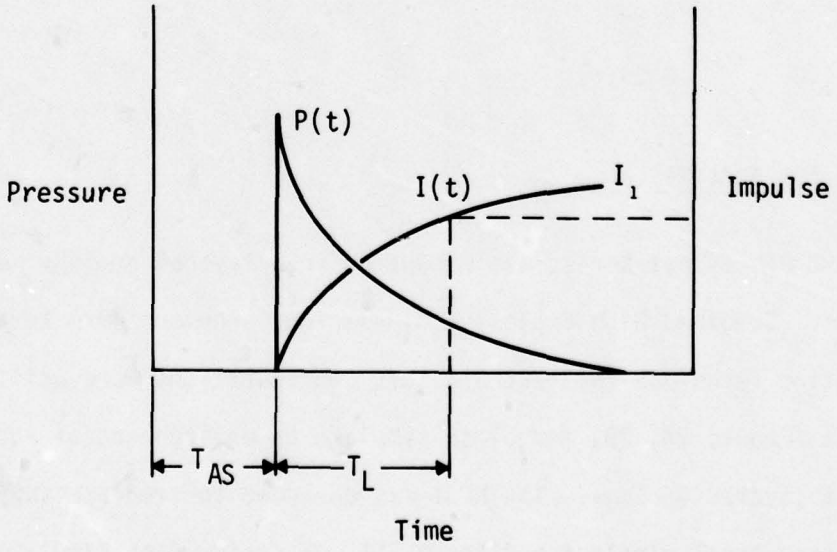

Figure 7. Interpretation of T_L

For small areas of relatively low impulse, it is less expensive to construct a BLEST as shown in figure 1. The construction technique shown in figure 2 was used in the HARD PAN series, and appears to be of more general interest for future applications, and therefore cost estimates for that technique will be presented here. The basic data used for estimating costs are shown in table 1. Estimated cost per square ft versus impulse are shown in figure 8.

Table 1
BASIC DATA FOR BLEST COST ESTIMATES

Chg Wght	Hole Diam	Drilling Hole Cost/ft	Survey	Chg Cost lb	Over Burden D	O.B. Cost yd^3
25	1.0 ft	$5.00	3.60	.50	2 ft	$2.00
50	1.0	5.00	"	"	"	"
100	1.5	5.40	"	"	"	"
200	2.0	5.70	"	"	"	"
400	3.0	6.20	"	"	"	"
800	4.0	6.69	"	"	"	"

APPLICATION AND ANALYSIS

The HARD PAN I Test Series was conducted in a layered geology near Trading Post, Kansas. Combined High Explosive Simulation Technique/Berm Loaded Explosive Simulation Technique (HEST/BLEST) test configurations were utilized in three of the tests (Events 2A, 2B, and 3) to simulate an environment of nuclear ground motions in a layered geology. The HEST was designed to simulate the effects of the propagating local airblast and the BLEST was designed to simulate the effect of upstream airblast. A scaled test structure was buried at a specified location under each HEST cavity and this structure was the target of the simulated nuclear blast. Both the scaled structure and the free-field beneath the HEST cavity were heavily instrumented to measure their motion and stress response to the

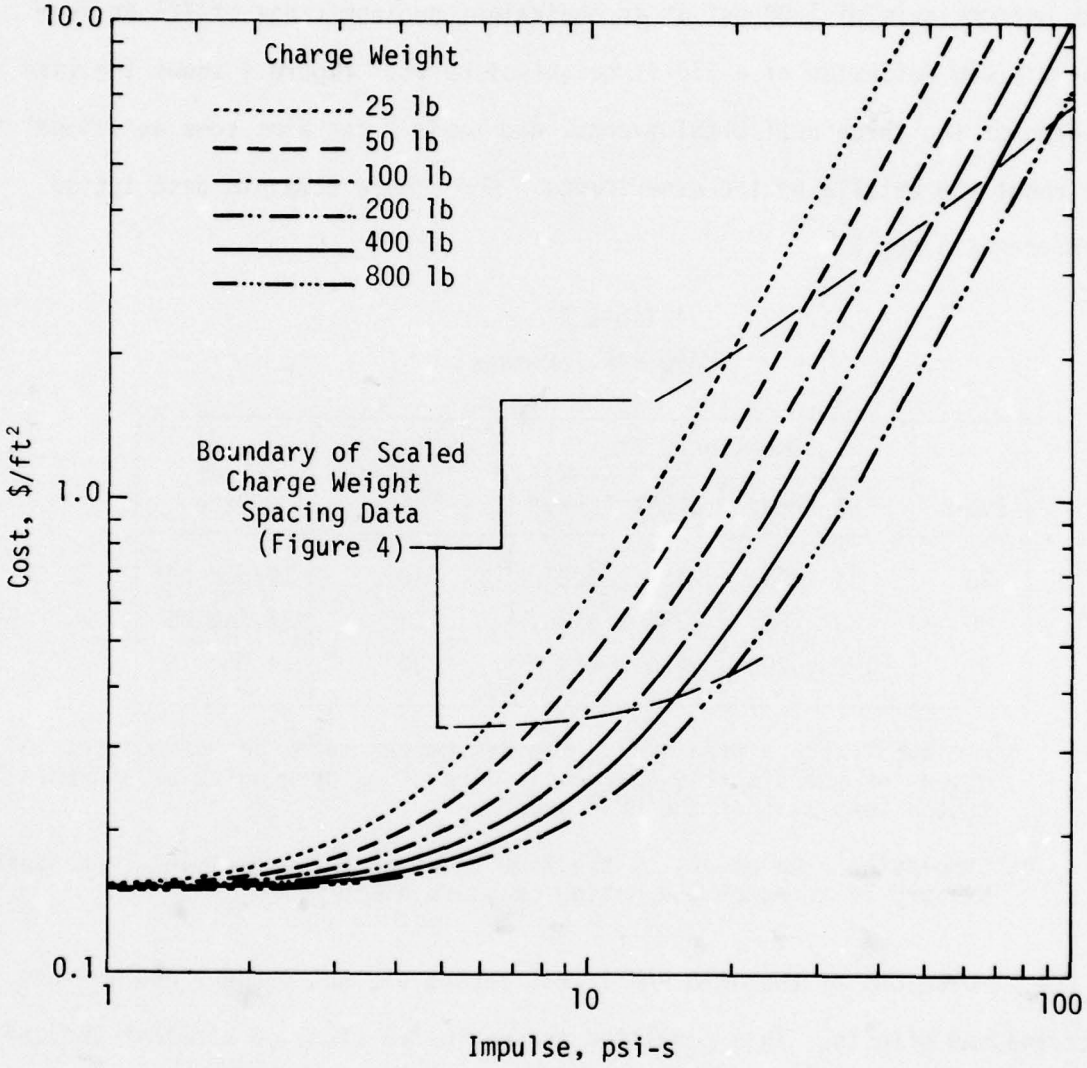

Figure 8. BLEST Estimated Cost

simulated nuclear environment. Each of the three events was designed to simulate a peak overpressure of 1200 psi at an equivalent nuclear range of 725 ft from a 125-kt yield detonated at a 210-ft height-of-burst. Figure 9 shows the size and shape of the three HEST/BLEST events, and table 2 contains some additional facts about the details of the experiments. For a more complete description, see reference 3 and 4.

Table 2
HARD PAN I Events

Event	Dimensions, ft		Simulation Time,** ms	Test Date
	HEST Array	BLEST Array*		
2A	64 x 96	158 x 222	18	19 Dec 74
2B	88 x 88	256 x 316	28	24 Aug 75
3	120 x 200	450 x 550	30	4 Dec 75

Notes: * The BLEST arrays were oval. The dimensions were the maximum spatial extent of the discrete charges in directions perpendicular and parallel to the long axis of the HEST area.

** Simulation time refers to the time to which the experimental pressure history is to match the design pressure history.

The simulations of the HARD PAN I Test Series did not produce crater- or direct-induced effects. This permitted the exclusive study of airblast-induced effects. However, even with this simplification, two types of airblast-induced ground motions are possible in layered media, viz., those resulting from local airblast effects and those resulting from upstream airblast effects or outrunning.

In conventional definitions of outrunning, such as that given in reference

3. Doran, J., HARD PAN I Test Series and Instrumentation Plans, AFWL-TR-75-249, Vol. 1, Air Force Weapons Laboratory, Kirtland AFB, New Mexico, December 1975.

4. HARD PAN I Test Series Design and Construction of Test Facilities, AFWL-TR-76-60, Air Force Weapons Laboratory, Kirtland AFB, New Mexico, June 1976.

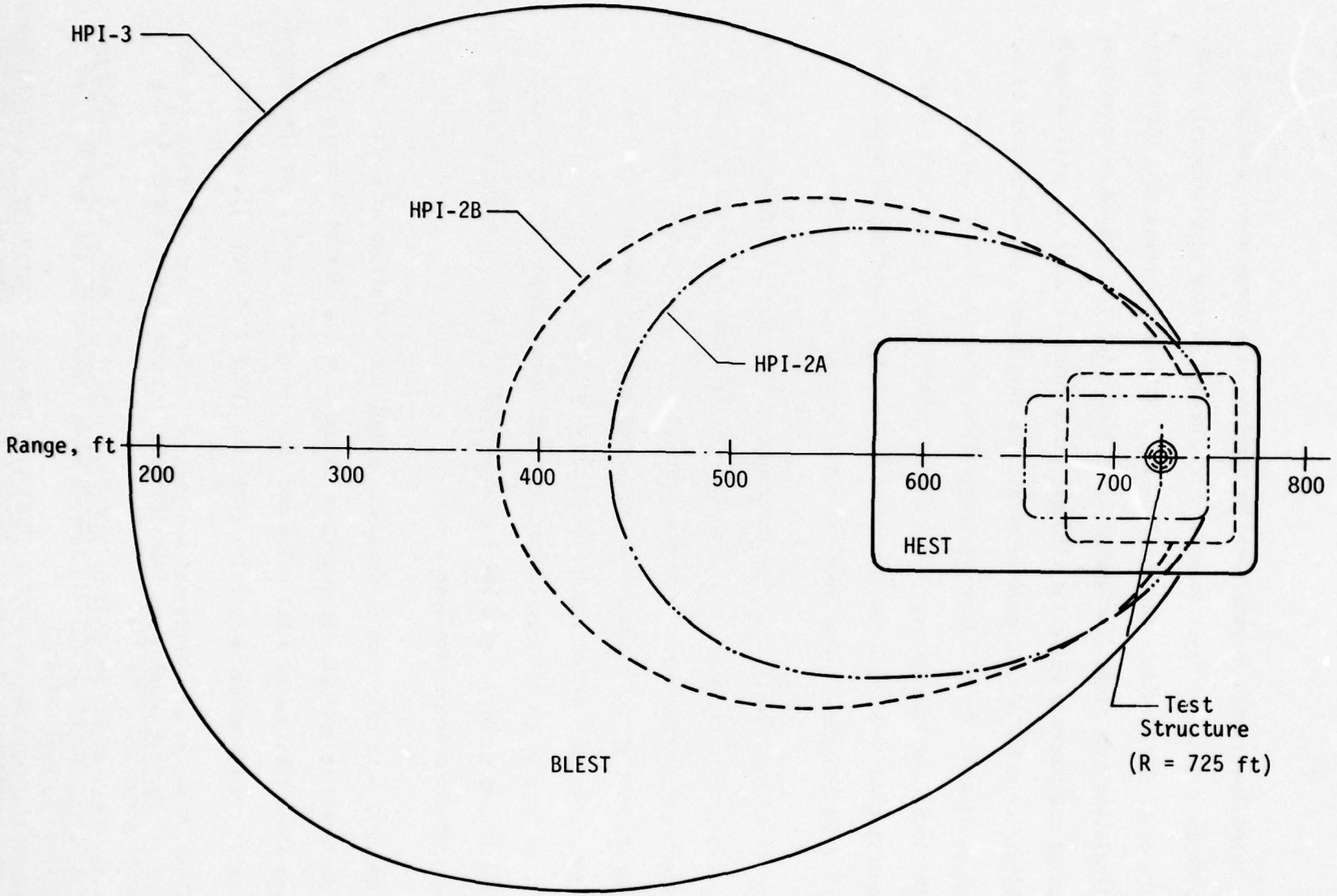

Figure 9. HARD PAN I Test Series Configurations

5, the outrunning region is considered to commence at a range where a headwave from a deeper refracting layer emerges at the ground surface simultaneously with the arrival of the airblast loading (fig. 10). Reference 2 presents a technique for calculating this range (designated R_2 in figure 10). It should be noted that outrunning may commence while the airblast shock front velocity, U, still exceeds the seismic velocity of the upper material. In this paper, the definition of outrunning is extended to include any ground motion resulting from a source other than the local airblast loading. This expanded definition of outrunning permits the contributions from upstream effects to be included regardless of their time-of-arrival with respect to the local airblast-induced ground motion.

Until fairly recently, outrunning ground motions were considered to be primarily associated with ranges corresponding to fairly low overpressures. This misconception may have resulted from the unique geology present at the Nevada Test Site, where most of the nuclear test ground motions data have been obtained. It is now known that outrunning ground motions can occur at high overpressure levels, so long as the geology consists of high seismic velocity layers located near the ground surface. HARD PAN I produced significant outrunning ground motions at the 1200 psi overpressure level.

Appendix A to reference 6, documents computer calculations of Event 3 which were performed to estimate the magnitude of the separate effects from the BLEST loading alone (designated BLEST only) and from the HEST loading alone (designated HEST only). The problems were calculated with TOODY II-A (ref. 7), a finite

5. Sauer, F.M., et al, "Empirical Analysis of Ground Motions and Cratering (Part Four)," Nuclear Geoplosics, DASA-1285(IV), Defense Atomic Support Agency, Washington, D.C., May 1964.
6. Auld, H.E., et al, ANALYSIS OF HARD PAN I FREE-FIELD DATA, Vol. 1: Summary of Test Data, AFWL-TR-78-66, Air Force Weapons Laboratory, Kirtland AFB, New Mexico, in publication.
7. Bertholf, L.D., Benzley, S.E., TOODY II-A Computer Program for Two-Dimensional Wave Propagation, SC-RR-68-41, Sandia Laboratories, Albuquerque, New Mexico, November 1968.

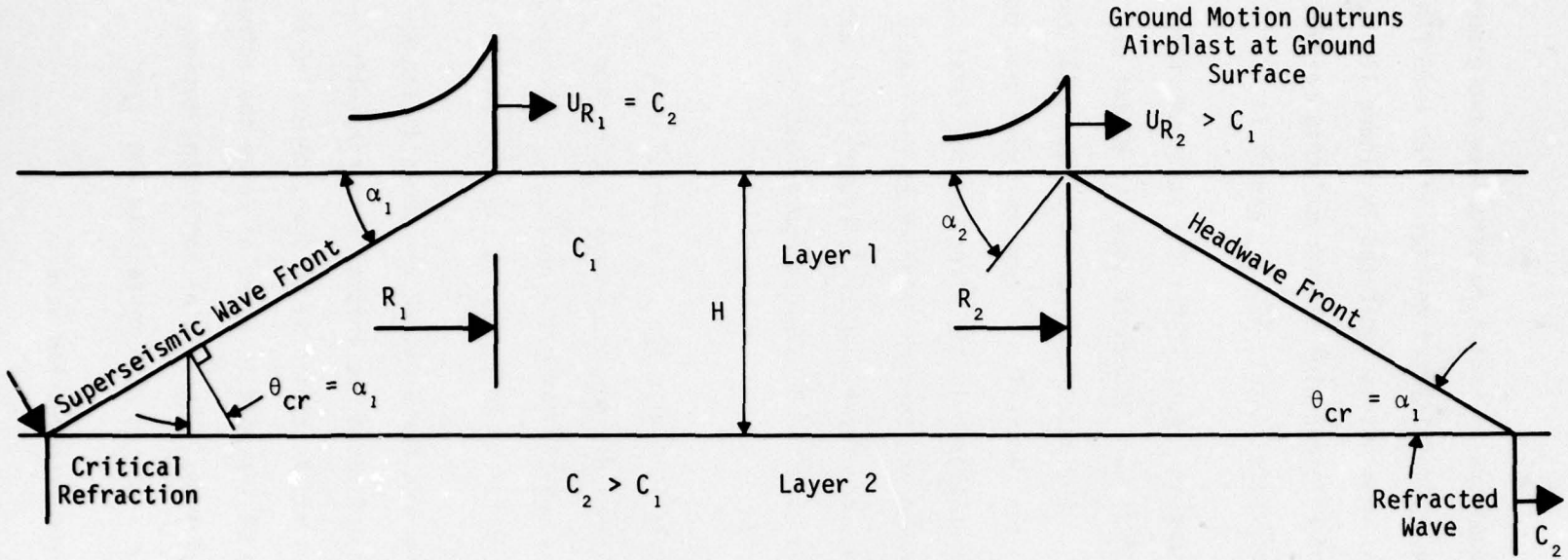

$U = f(R)$

$\sin\alpha_1 = C_1/U_{R_2}$

$\sin\alpha_2 = C_1/U_{R_2}$

$\sin\theta_{cr} = C_1/C_2$

$U_{R_1} = C_2$ when $\alpha_1 = \theta_{cr}$

Definitions:

R_2 = range at which headwave from layer 2 and airblast arrive simultaneously at ground surface

θ_{cr} = critical angle; refracted wave travels parallel to interface in underlying layer

Figure 10. Airblast Loading of Two-Layered Medium

difference code that uses Lagrangian equations of motion to calculate two-dimensional wave propagation in layered media. The typical layered geology of the HARD PAN I test site that was utilized in the calculations is indicated in figure 11. The water table is located at a depth of 8 ft and high seismic velocity refracting layers (C > U)* are located at depths of approximately 17, 32, and 52 ft.

Results of the calculations are shown in figure 12 for the structure range of 725 ft. The depths of 14, 30, and 56 ft were chosen to show the extent of the variation of the BLEST contribution. The outward component of the BLEST had a more significant relative effect than the vertical. In regions other than the outrunning limestone layer (56 ft), the BLEST had little effect on the first outward peak due to the HEST, but it increased the outward velocity significantly after this peak. In the outrunning limestone layer the BLEST-induced first arrival and the peak outward velocity associated with the BLEST were approximately four times the peak associated with the HEST.

Comparisons of these numerical simulations with the experimental data from the HARD PAN I Test Series reveals that they did not accurately predict the magnitude of the measured ground motions, particularly the horizontal component. However, the calculational trends were useful in interpreting the experimental data.

Typical outrunning ground motion records for Event 2B are shown in figure 13 for a depth of 48 ft. At this depth and range the initial motion results from outrunning. The initial vertical motion may be either up or down, depending on the local geology and whether the depth of interest is above or below the refracting layer generating the first-arriving headwaves. The initial horizontal motion will always be outward regardless of the location with respect to the layer.

* C = seismic velocity of refracting layer (compression wave).

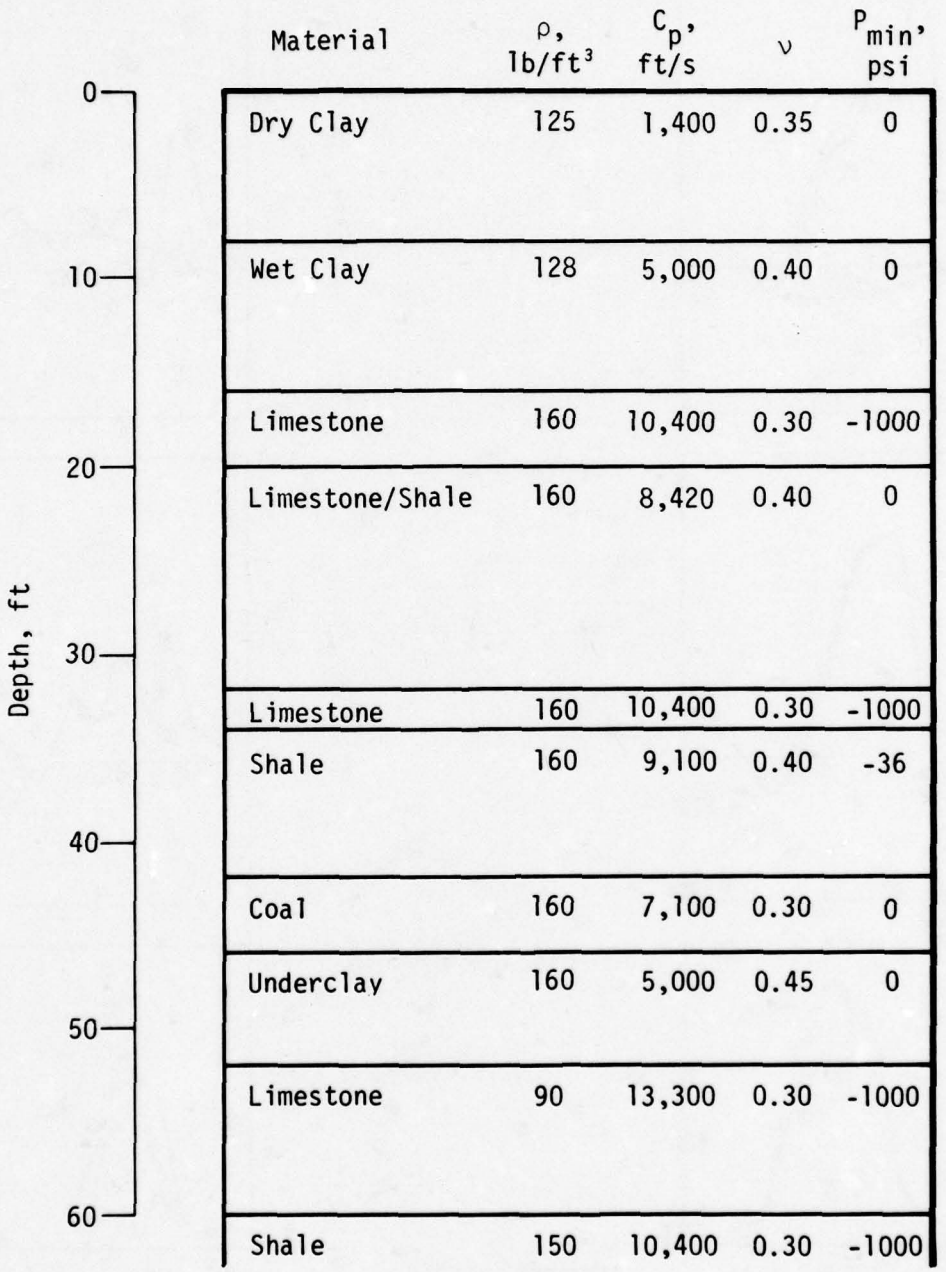

Material	ρ, lb/ft^3	C_p, ft/s	ν	P_{min}, psi
Dry Clay	125	1,400	0.35	0
Wet Clay	128	5,000	0.40	0
Limestone	160	10,400	0.30	-1000
Limestone/Shale	160	8,420	0.40	0
Limestone	160	10,400	0.30	-1000
Shale	160	9,100	0.40	-36
Coal	160	7,100	0.30	0
Underclay	160	5,000	0.45	0
Limestone	90	13,300	0.30	-1000
Shale	150	10,400	0.30	-1000

Figure 11. Typical Geologic Profile, HARD PAN I Test Site

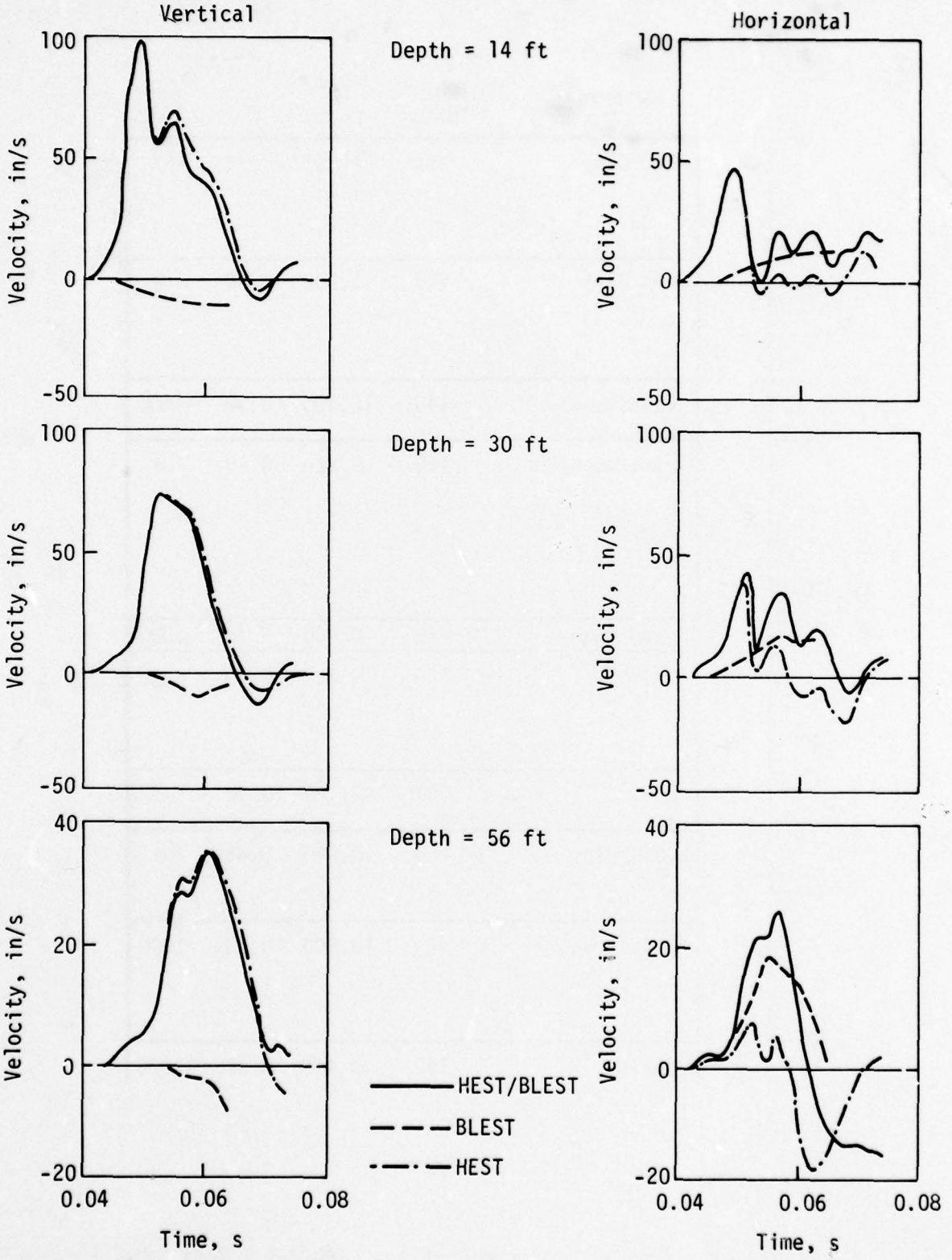

Figure 12. HEST and BLEST Contribution to Velocity Waveforms at 725-Foot Range

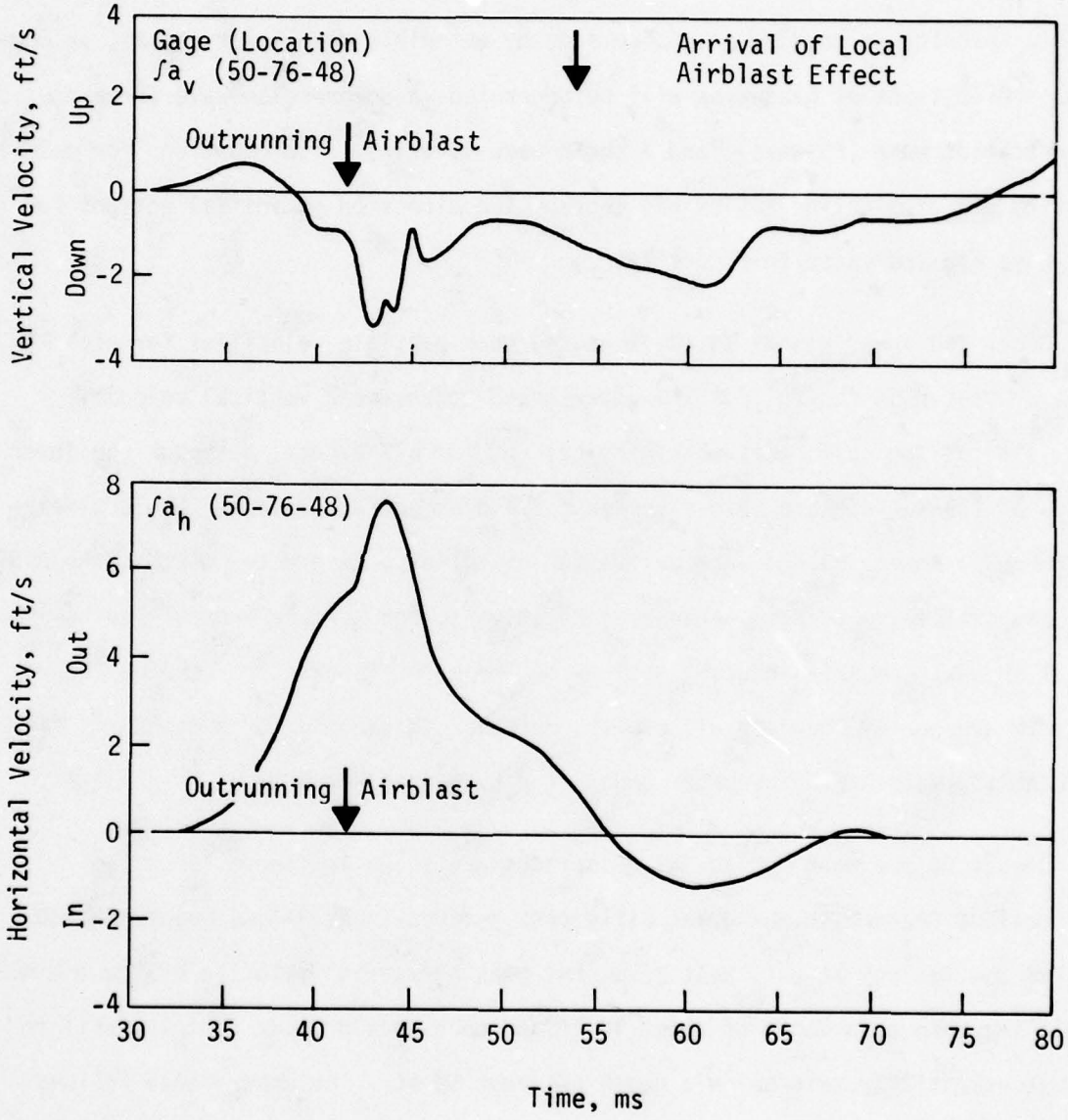

Figure 13. Typical Outrunning Ground Motions in Event 2B

Figure 14 illustrates the theoretical situation in which a layer with a high seismic velocity is bounded on either side by materials with lower seismic velocities. Three types of headwaves will be generated--a compression wave (P-wave), a von Schmidt wave (PS-wave), and a shear wave (S-wave). The equations for calculating the propagation angles and thereby the direction of initial motions for each wave are indicated in figure 14.

Upper and lower bounds to the measured peak particle velocities for each event are shown in figure 15. The upper bound to the peak vertical velocity (fig. 15a) at the surface is nearly coincident for all events, although the lower bounds at the surface are more divergent. In near surface layers, the local airblast (HEST) dominated the vertical motion histories. At greater depths, the HEST-induced particle velocities attenuated relative to the surface and outrunning (BLEST or upstream HEST-induced) motions became more important. The lower bounds at depth are nearly equal in all events, but the upper bound for Event 2A is significantly greater than the upper bounds for Events 2B and 3.

Bounds to the peak horizontal velocities are shown in figure 15b. The most obvious feature is the great difference between Event 2A and Events 2B and 3. For the geology at this test site, the peak horizontal velocity due to the HEST should increase to a depth of about 10 ft and then should decay rapidly until it becomes essentially zero below a depth of about 60 ft. The upper bound follows this pattern in the near-surface material, but it does not decay to zero. This indicates that outrunning had a large effect on the magnitude of the horizontal velocity below the near-surface material.

There is no generally accepted technique available for accurately predicting outrunning ground motions. However, empirical prediction techniques based on the available high-explosive ground motion data for the outrunning region are given

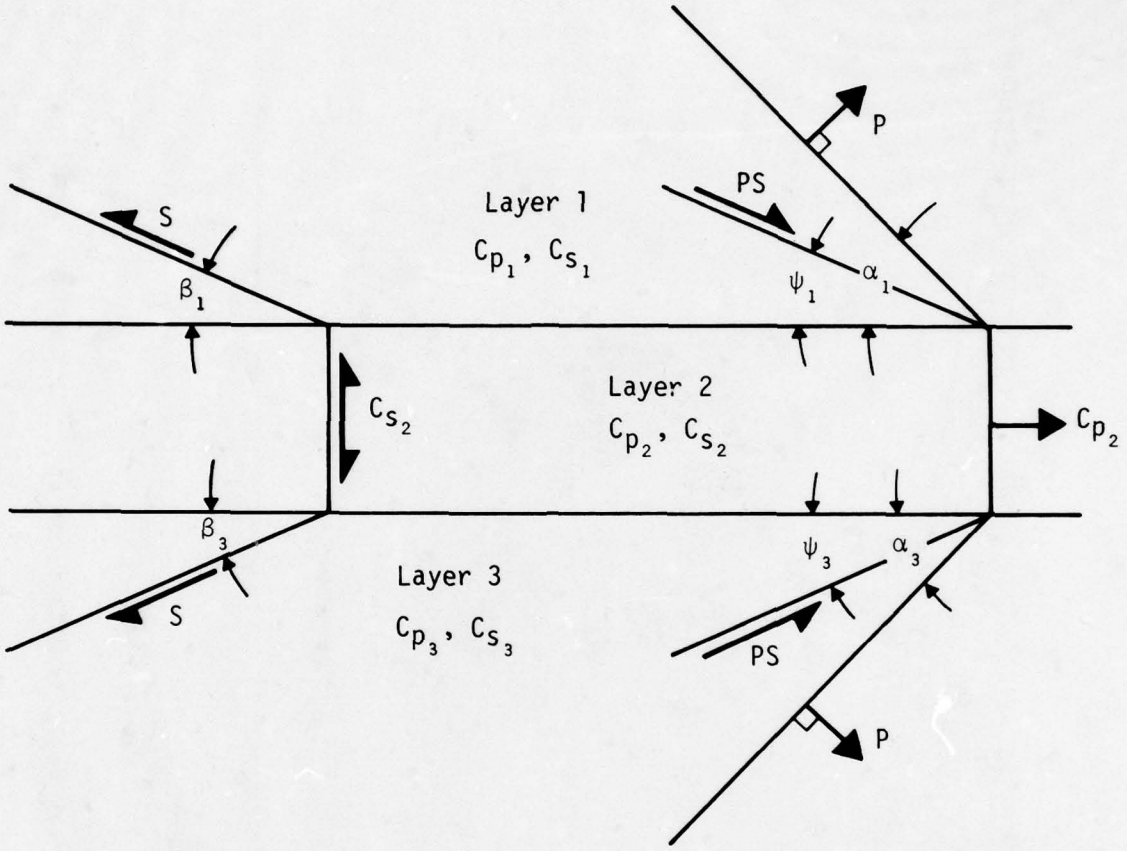

Definitions:

C = propagation velocity

P = compression wave

PS = von Schmidt wave

S = shear wave

→ indicates direction of first motion

$C_{p_2} > C_{p_1}, C_{p_3}$

$C_{s_2} > C_{s_1}, C_{s_3}$

$\sin\alpha_1 = C_{p_1}/C_{p_2}$

$\sin\alpha_3 = C_{p_3}/C_{p_2}$

$\sin\psi_1 = C_{s_1}/C_{p_2}$

$\sin\psi_3 = C_{s_3}/C_{p_2}$

$\sin\beta_1 = C_{s_1}/C_{s_2}$

$\sin\beta_3 = C_{s_3}/C_{s_2}$

Figure 14. Headwaves in Layered Medium

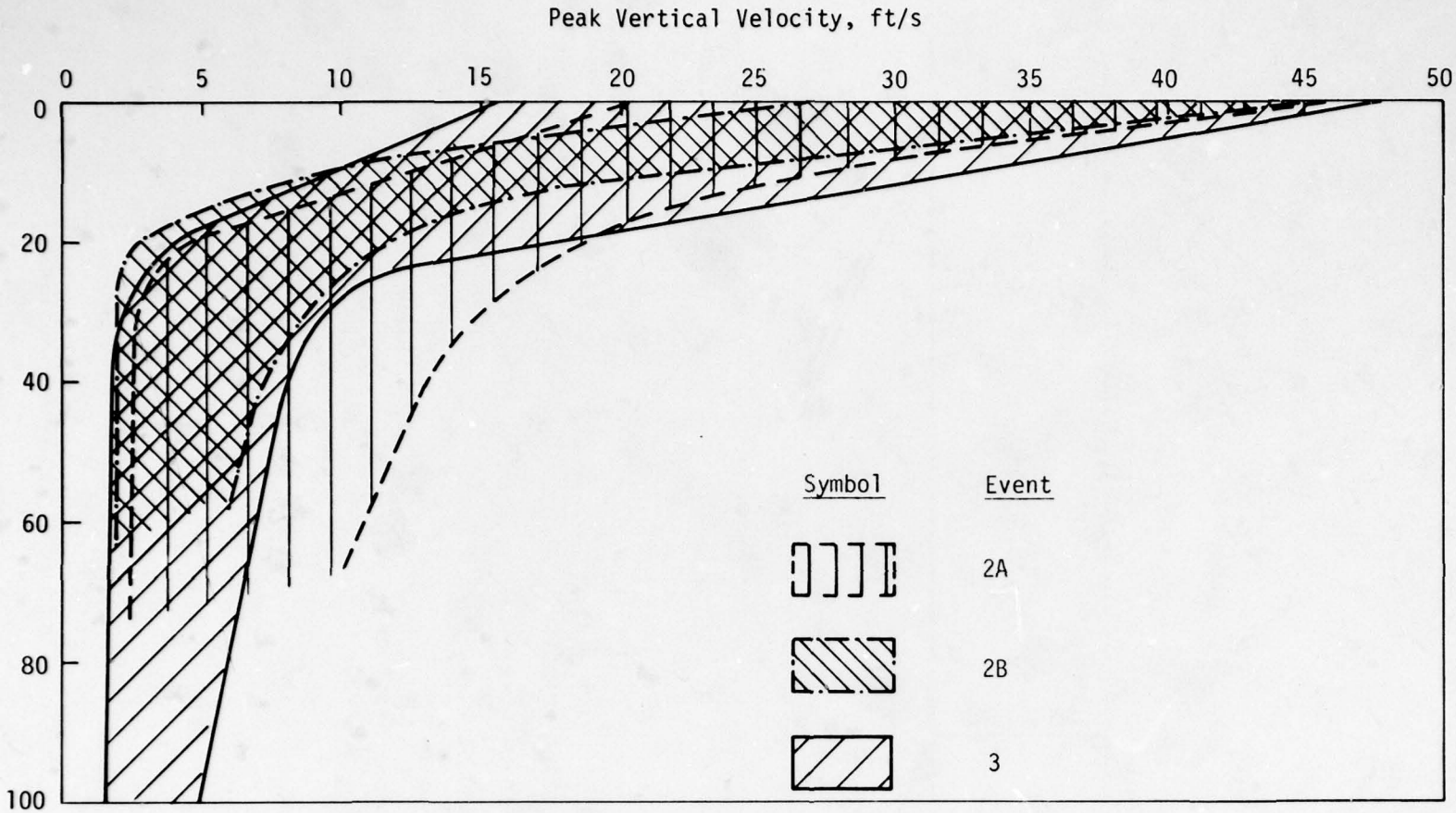

Figure 15. Upper and Lower Bounds to Peak Velocity Data (1 of 2) (a) Vertical Velocity

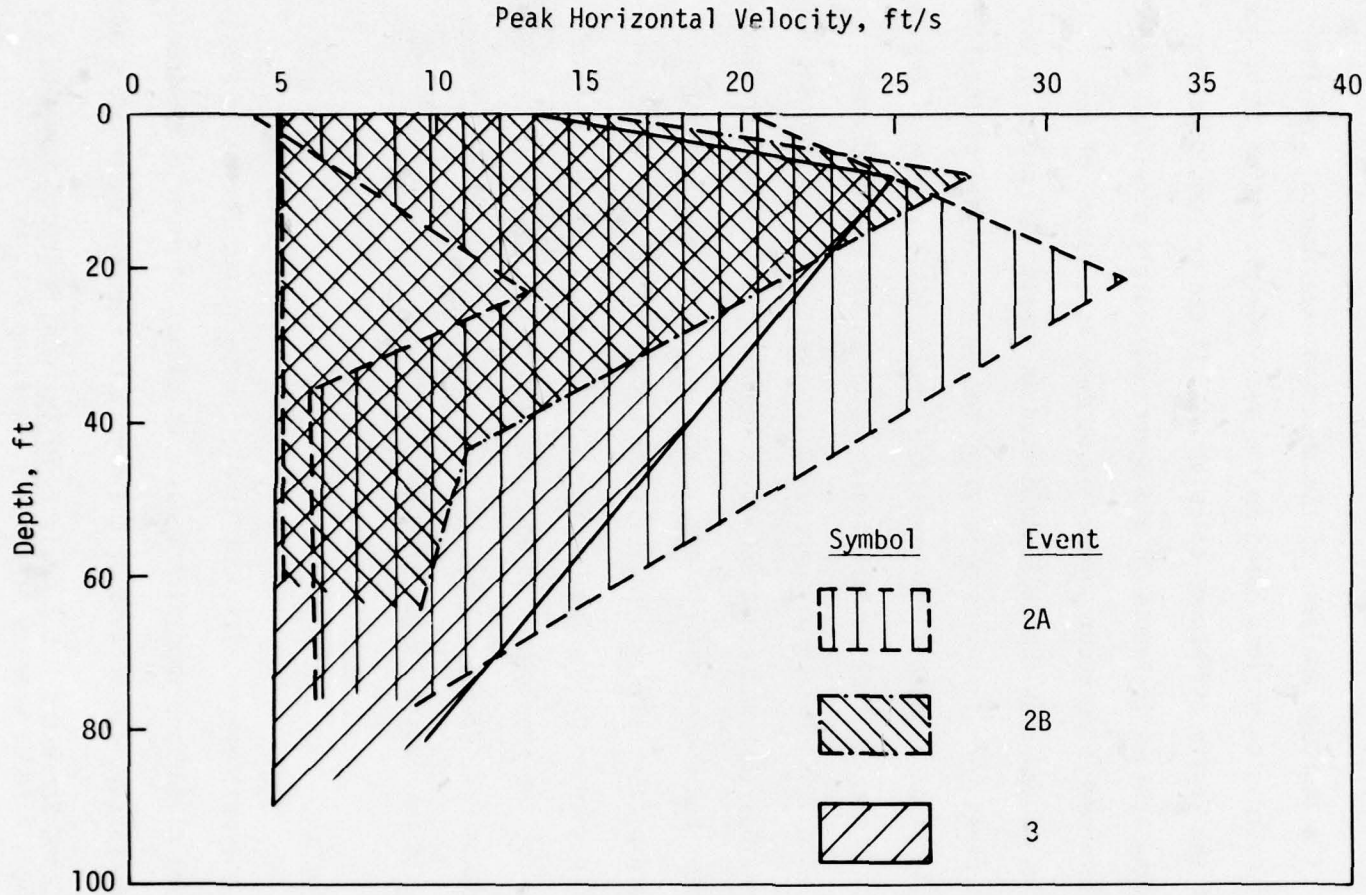

Figure 15. Upper and Lower Bounds to Peak Velocity Data (2 of 2) (b) Horizontal Velocity

in reference 8 and for the available nuclear data are given in reference 5.

On the basis of a thorough analysis of the observed experimental free-field data, estimates of outrunning motions based on the available prediction techniques, and the results of the finite difference calculations, it can be concluded that the outrunning ground motions in Events 2B and 3 were adequately simulated whereas in Event 2A they were over simulated; perhaps by as much as a factor of two. It can further be concluded that the BLEST generated an impulse in excess of the required amount in Event 2A. This thesis is supported by an analysis of the limited photopole and acceleration data that were available in the BLEST region of the experiment (ref. 9). After Event 2A, a BLEST calibration series was conducted at the HARD PAN Test Site using the same slurry used for Event 2A and subsequent events. The data from a previous test series at McCormick Ranch, which was used to design Event 2A, was suspect because of differences in the soil properties and minor differences in the explosive slurry. A consistent method for mapping overburden velocities was not developed during the McCormick Ranch series, which may have also been a portion of the problems. All HARD PAN BLEST data following the on-site calibration series was consistent. It has been concluded that BLEST arrays should be calibrated on site for future field tests or experiments.

POTENTIAL APPLICATIONS

The BLEST is the most energy efficient simulation technique currently available for application of surface impulsive loads. It cannot be used in the immediate vicinity of a test article because of the high stress levels which are produced.

8. Higgins, C.J., and Schreyer, H.L., Analysis of Outrunning Ground Motions, AFWL-TR-74-220, Air Force Weapons Laboratory, Kirtland AFB, New Mexico, May 1975.

9. Webster, J.B., III, Maj., and Suesy, F.E., "Simulation Performance for HARD PAN I, Event 2, Memorandum for the record, 22 January 1975.

However, valid simulation can be provided in cases where sufficient distances are available between the explosive plane and the test article.

Several applications of BLEST have been proposed and are currently under study. The current basing concept for the MX missile system envisions a large number of vertical shelters, a fraction of which are occuppied by missiles. The shelters surviving an attack may need to survive multi-burst effects, i.e., the effects from nearly simultaneous detonations on neighboring shelters. Because of the large spacing between shelters, it has been postulated that outrunning ground motions may be an important effect. Outrunning ground motions are not well understood from single bursts, and less well understood for multiple bursts. The BLEST offers potential for experiments at sufficiently large scale to increase understanding of both the single and multi-burst case. A major reason for large scale experiments is to permit experiments to be run on realistic geologies. The BLEST may not be technically or economically feasible at full scale, and other testing techniques may be required.

Deep underground missile basing concepts are also under study. The BLEST may also have potential for ground shock environment studies and small scale testing. Again, full scale may be technically and economically impractical because of the extremely large amounts of energy required.

POTENTIAL IMPROVEMENTS

Earlier in the paper it was stated that photopoles were the current tool for measurement of the impulse delivered by a BLEST array. While photopoles have performed better than accelerometers and stress gages, they are not without shortcomings. One of the basic difficulties with photopoles is that considerable care must be taken to avoid obscuring the field of view with overburden from other portions of the test bed. The photopole itself is simple

and inexpensive, but the data reduction process is fairly expensive and time consuming. Some effort will be expended in the next year in an attempt to identify potential alternative measurement techniques.

The calculations for loading area and loading time have been accomplished in the past with seismic velocities. This may be overly conservative, in that the important effects are probably better defined by peak propagation velocities. Peak propagation velocities have not been used in the past because of the obvious increase in design complexity. A useful study of load area and time would most likely include three-dimensional calculations and supporting field experiments. A substantial effort would be required if significant geologic variations were included.

The current recommendation that the BLEST be calibrated on site with the intended explosive may be excessively conservative. A theoretical model verified experimentally may allow adequate prediction from the soil density and the available explosive energy.

REFERENCES

1. Brode, H.L., Height of Burst Effects at High Overpressures, RM6301, The Rand Corps., Santa Monica, California, July 1970.

2. Crawford, R.E., Higgins, C.J., Bultmann, E.H., The Air Force Manual for Design and Analysis of Hardened Structures, AFWL-TR-74-102, Air Force Weapons Laboratory, Kirtland AFB, New Mexico, October 1974.

3. Doran, J., HARD PAN I Test Series and Instrumentation Plans, AFWL-TR-75-249, Vol. 1, Air Force Weapons Laboratory, Kirtland AFB, New Mexico, December 1975.

4. HARD PAN I Test Series Design and Construction of Test Facilities, AFWL-TR-76-60, Air Force Weapons Laboratory, Kirtland AFB, New Mexico, June 1976.

5. Sauer, F.M., et al, "Empirical Analysis of Ground Motions and Cratering (Part Four)," Nuclear Geoplosics, DASA-1285(IV), Defense Atomic Support Agency, Washington, D.C., May 1964.

6. Auld, H.E., et al, ANALYSIS OF HARD PAN I FREE-FIELD DA[illegible], Vol. 1: Summary of Test Data, AFWL-TR-78-66, Air Force Weapons Laboratory, Kirtland AFB, New Mexico, in publication.

7. Bertholf, L.D., Benzley, S.E., TOODY II-A Computer Program for Two-Dimensional Wave Propagation, SC-RR-68-41, Sandia Laboratories, Albuquerque, New Mexico, November 1968.

8. Higgins, C.J., and Schreyer, H.L., Analysis of Outrunning Ground Motions, AFWL-TR-74-220, Air Force Weapons Laboratory, Kirtland AFB, New Mexico, May 1975.

9. Webster, J.B., III, Maj., and Suesy, F.E., "Simulation Performance for HARD PAN I, Event 2,"Memorandum for the record, 22 January 1975.

GROUND SHOCK SIMULATION USING DIHEST

by

Kenneth B. Simmons

Cornelius J. Higgins

Civil Engineering Research Facility

PRECEDING PAGE BLANK-NOT FILMED

CONTENTS

Section	
I	INTRODUCTION
II	DIHEST CHARACTERISTICS
III	GROUND MOTION PREDICTION
IV	GENERALIZED EMPIRICAL PERFORMANCE CHARTS
V	DESIGN PROCEDURE
VI	CONCLUSIONS

LIST OF ILLUSTRATIONS

Figure	
1	DIHEST Ground Motion Simulator
2	Effect of Finite Array Dimensions on Peak Ground Shock Attenuation
3	Plan - SIMQUAKE I Test Bed Layout
4	Elevation - SIMQUAKE I
5	Comparison of SIMQUAKE I Acceleration Data and Predictions
6	Comparison of SIMQUAKE I Velocity Data and Predictions
7	Comparison of SIMQUAKE I Displacement Data and Predictions
8	DIP IIA and MSQ-F Accelerations Compared with Predictions
9	DIP IIA and MSQ-F Velocities Compared with Predictions
10	DIP IIA and MSQ-B Displacements Compared with Predictions
11	Soil DIHEST Accelerations
12	Soil DIHEST Velocities
13	Soil DIHEST Displacements
14	Relationships Between DIHEST Variables

I. INTRODUCTION

The Direct-Induced High Explosive Simulation Technique (DIHEST) is a method of simulating ground shocks which result from the direct coupling of energy from large explosions. The original weapons simulation work was accomplished by the Air Force Weapons Laboratory (AFWL) and the University of New Mexico Civil Engineering Research Facility (UNM/CERF) with funding from the Defense Nuclear Agency (DNA). Recent earthquake simulation work has been accomplished at UNM/CERF with funding from the Electric Power Research Institute (EPRI) and the National Science Foundation.

A typical DIHEST array consists of a row of vertical drill holes in the ground which are filled to some height with explosives and then stemmed with sand or grout (Fig. 1). Multiple detonators are placed in each hole and fired simultaneously to create a shock wave which is approximately planar. DIHEST arrays have been fired with total explosive charges as large as 40 tons. Array dimensions have been as large as about 300 ft deep and over 1100 ft long.

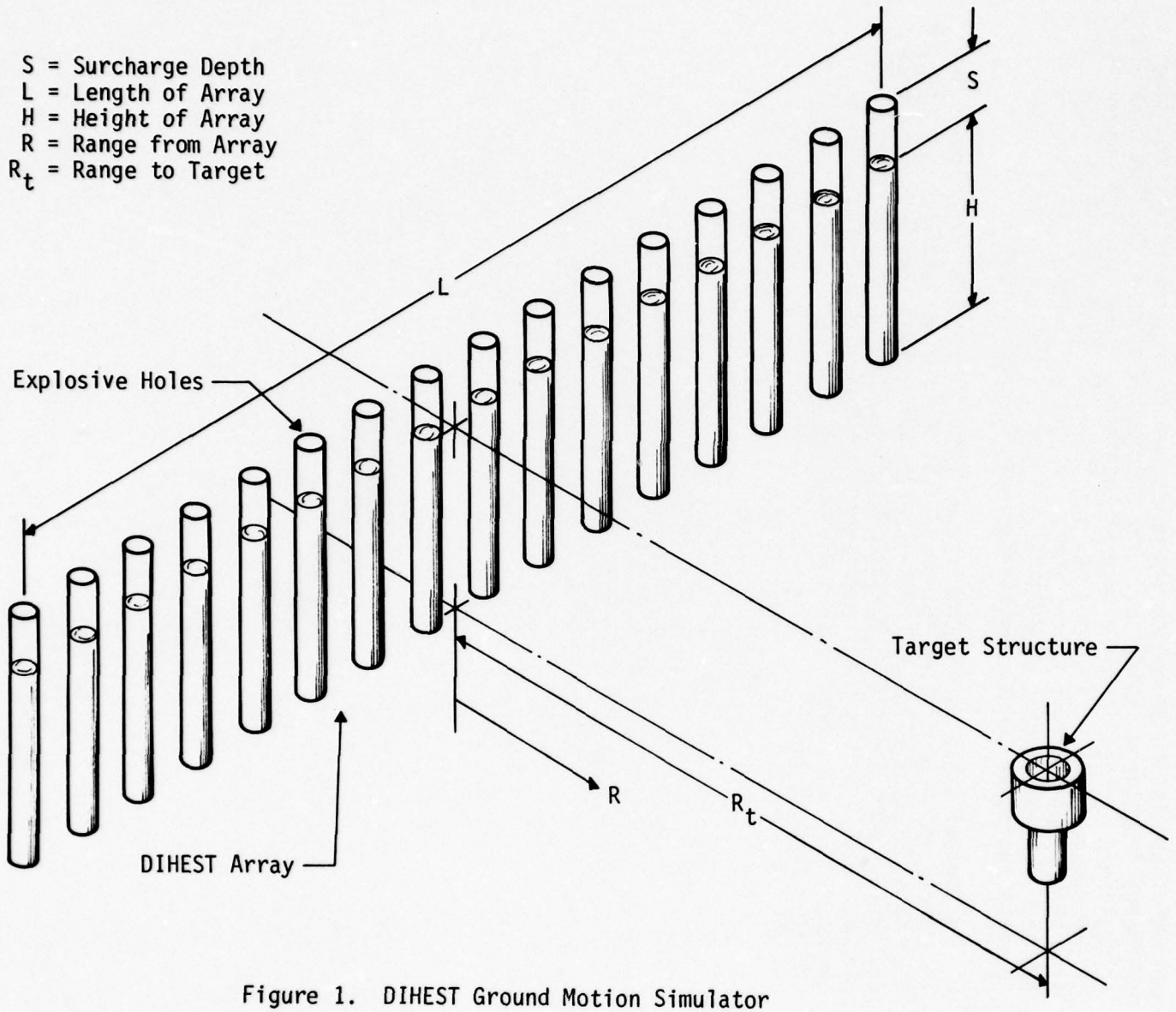

Figure 1. DIHEST Ground Motion Simulator

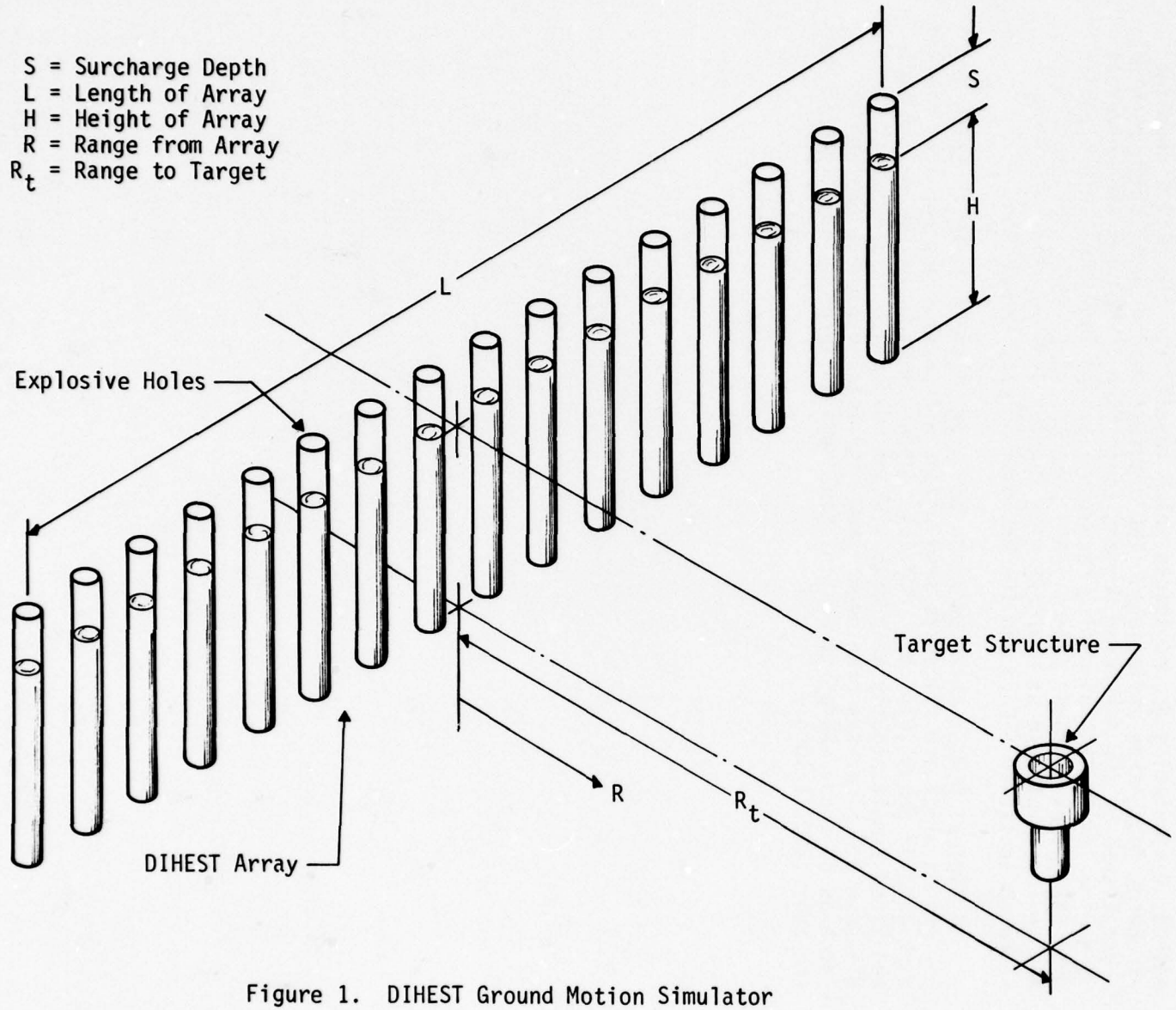

Figure 1. DIHEST Ground Motion Simulator

II. DIHEST CHARACTERISTICS

The peak ground motions resulting from a DIHEST array are expected to attenuate with range approximately as shown in Figure 2. At ranges near the array, the relief effects do not affect peak parameters of acceleration (a), velocity (v), and displacement (d); and the attenuation is planar and due only to inelastic effects. Beyond some range, relief waves from the top and bottom of the array begin to overtake the loading waves and cause the attenuation rates to approach cylindrical conditions. Finally, at some greater range, relief waves from the ends of the array overtake the loading waves; and a transition to spherical attenuation might be expected (although few DIHEST data have been recorded in this region). The transition regions for the parameters of acceleration, velocity, and displacement are expected to be different. The accelerations transition over a short range, the displacements over a longer range, and the velocities somewhere in between. The transition region between two zones has been taken as a point, called the transition-point range, R_o.

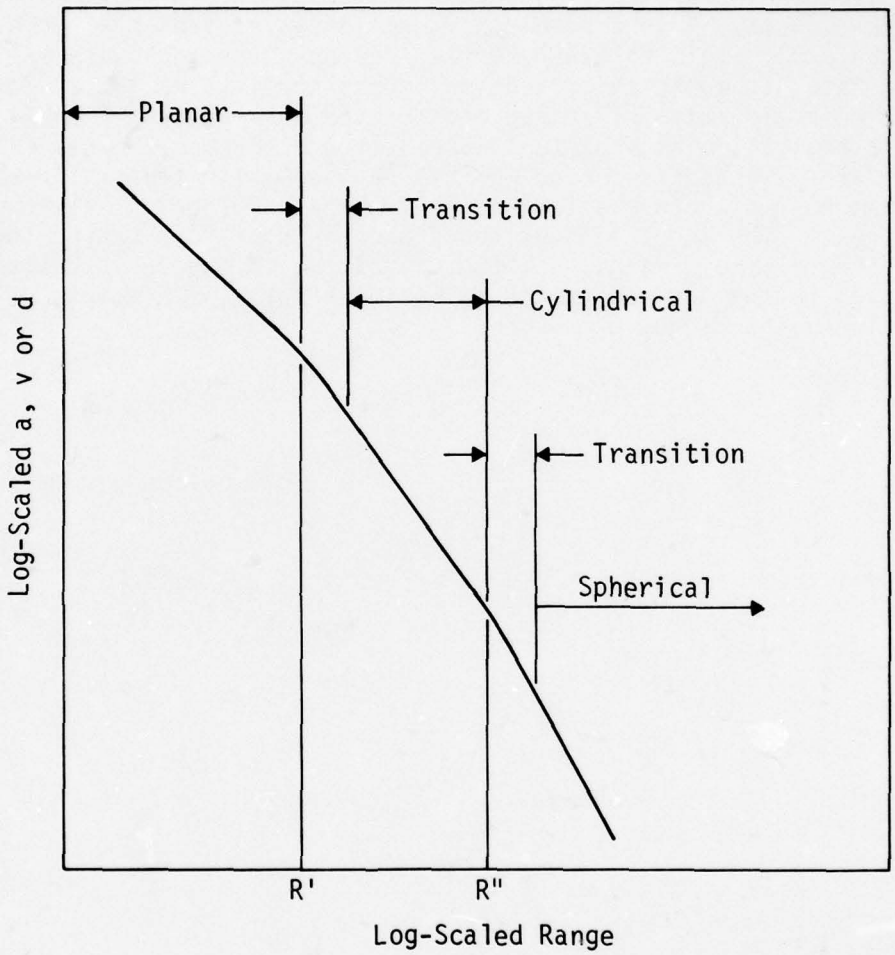

Figure 2. Effect of Finite Array Dimensions on Peak Ground Shock Attenuation

III. GROUND MOTION PREDICTION

The major ground motion quantities of interest are peak horizontal acceleration, particle velocity, and displacement. In the absence of material property variations, the parameters which control DIHEST ground motions are:

- Areal Charge Density, α
- Array Height, H
- Array Length, L
- Surcharge Above the Explosive, S
- Range to the Point of Interest, R

The surcharge term, in effect, is a measure of the location of the free surface. Gravity may also be influential, but there are insufficient data available at present to understand its effect.

Dimensionally consistent scaling relations between the ground motions and the array parameters are:

$$a \cdot \alpha = f_1 \, (R/\alpha, \, H/\alpha, \, L/H, \, R/S)$$

$$v = f_2 \, (R/\alpha, \, H/\alpha, \, L/H, \, R/S)$$

$$d/\alpha = f_3 \, (R/\alpha, \, H/\alpha, \, L/H, \, R/S)$$

It has been observed experimentally that if L is greater than about 2H and if R is less than 2L, the effect of L can be assumed to be small. Also, if observations are restricted to the mid-depth of the array, the effect of S can be assumed to be small. With these assumptions, the relations at the mid-depth of the array are:

$$a \cdot \alpha = f_1 \, (R/\alpha, \, H/\alpha)$$

$$v = f_2 \, (R/\alpha, \, H/\alpha)$$

$$d/\alpha = f_3 \, (R/\alpha, \, H/\alpha)$$

The scaled motion quantities are usually plotted versus scaled range, R/α. The effect of H/α is evident from the relative positions of the results from individual experiments with varying H/α.

The DIHEST data available prior to the recent SIMQUAKE I test series are found in References 1, 2, 3, 4, 5, and 6. These data are analyzed in Reference 7. The prediction relations for motion amplitudes at the mid-depth of DIHEST events, which were derived from these data and a large number of finite difference calculations (see Ref. 7), are as follows:

$$a \cdot \alpha = 2900\ (R/\alpha)^{-0.89} \qquad \text{for } R/\alpha \leq 2(H/\alpha)^{0.6}$$

$$a \cdot \alpha = 11{,}680\ (H/\alpha)^{1.21}(R/\alpha)^{-2.9} \qquad \text{for } R/\alpha > 2(H/\alpha)^{0.6}$$

$$v = 49\ (R/\alpha)^{-0.16} \qquad \text{for } R/\alpha \leq 2.6(H/\alpha)^{0.52}$$

$$v = 313\ (H/\alpha)(R/\alpha)^{-2.1} \qquad \text{for } R/\alpha > 2.6(H/\alpha)^{0.52}$$

$$d/\alpha = 10.5(R/\alpha)^{-0.12} \qquad \text{for } R/\alpha \leq 1.15(H/\alpha)^{0.75}$$

$$d/\alpha = 13.3(H/\alpha)^{1.28}(R/\alpha)^{-1.82} \qquad \text{for } R/\alpha > 1.15(H/\alpha)^{0.75}$$

where

a = acceleration in g's

v = particle velocity in ft/s

d = displacement in in

H = array height in ft

R = range in ft

α = areal charge density in lb/ft^2 of TNT

Three important points should be made with regard to these relations. First, the normalized transition range, R_o/H, is dependent upon H/α. The dependencies are:

Acceleration: $R_o/H = 2.0(H/\alpha)^{-0.4}$

Velocity: $R_o/H = 2.6(H/\alpha)^{-0.48}$

Displacement: $R_o/H = 1.15(H/\alpha)^{-0.25}$

These relations are not evident in the data alone because of scatter, but they are derived from finite difference calculations.

The second important point is that shallow events (array mid-depth within about 15 ft from the surface) produce greater scaled horizontal displacements than deep events. The reason for this behavior is not clear, but material property differences near the surface and/or gravity are possible causes. The displacement equations given above are for deep events. Displacement from shallow events will be about twice those estimated from the given equations.

Third and last, most confidence can be given to the equations beyond the transition range. The behavior in the planar region remains more uncertain because very few data are available in this region.

The SIMQUAKE I tests (Ref. 8) were the most recent DIHEST events in soil. They were conducted at the McCormick Ranch test site of the University of New Mexico in May and June 1977. The main objective of the tests was to excite models of nuclear power plants with horizontal ground motions having amplitudes and frequency contents on the order of those expected in very strong earthquakes (Richter Magnitude of 7 to 8). Figures 3 and 4 show plan and elevation views of the test site. The test was originally to consist of two arrays 75 ft deep by 200 ft wide with 25-ft surcharge. The back array, designed to fire first, was loaded with 6.28 lb/ft^2 of ammonium nitrate/fuel oil (ANFO) (approximately 5.65 lb/ft^2 TNT equivalent). The front array was loaded with 3.84 lb/ft^2 of ANFO (3.45 lb/ft^2 TNT equivalent). The arrays were separated by 100 ft to insure the integrity of the front array since the time delay was set at 1.5 s.

Due to a firing system malfunction, only the back array fired during the main test*. The front array remained intact and was fired a few weeks later. As a result, two complete sets of DIHEST data were obtained. The back array test has been designated SIMQUAKE IA (SQIA) and the front array test SIMQUAKE IB (SQIB).

In Figures 5, 6, and 7, the horizontal motion data for SQIA and SQIB at the mid-depth of the arrays are compared with the prediction relations given earlier. The level of agreement is quite reasonable with the exception of the acceleration prediction for SQIB which is low by about a factor of two. Since the prediction relations were developed independent of the data, the quality of agreement suggests that future DIHEST events in soil may be predictable within a reasonable level of confidence.

*Two sequentially timed arrays were recently fired in SIMQUAKE II at McCormick Ranch.

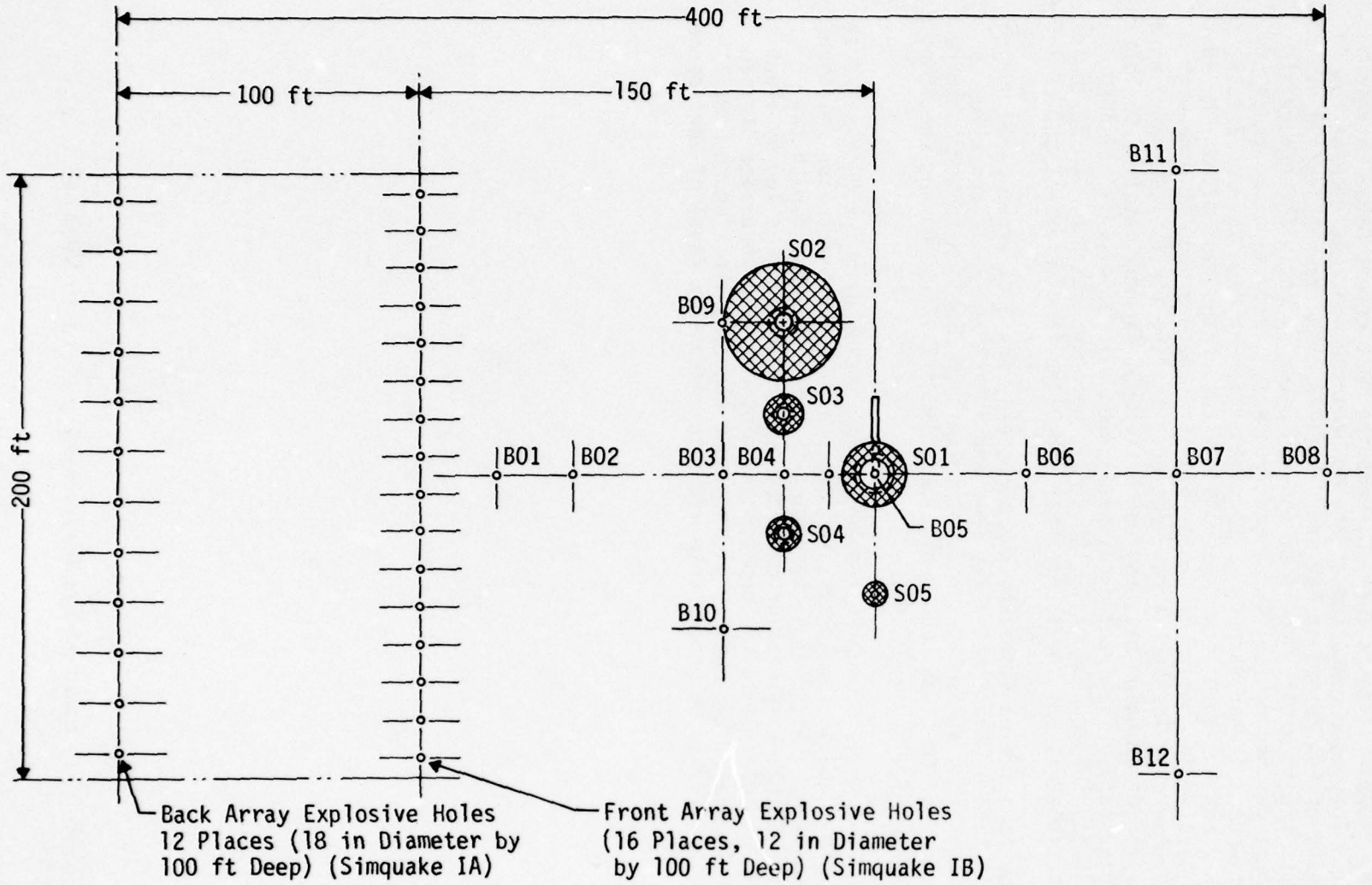

Figure 3. Plan - SIMQUAKE I Testbed Layout

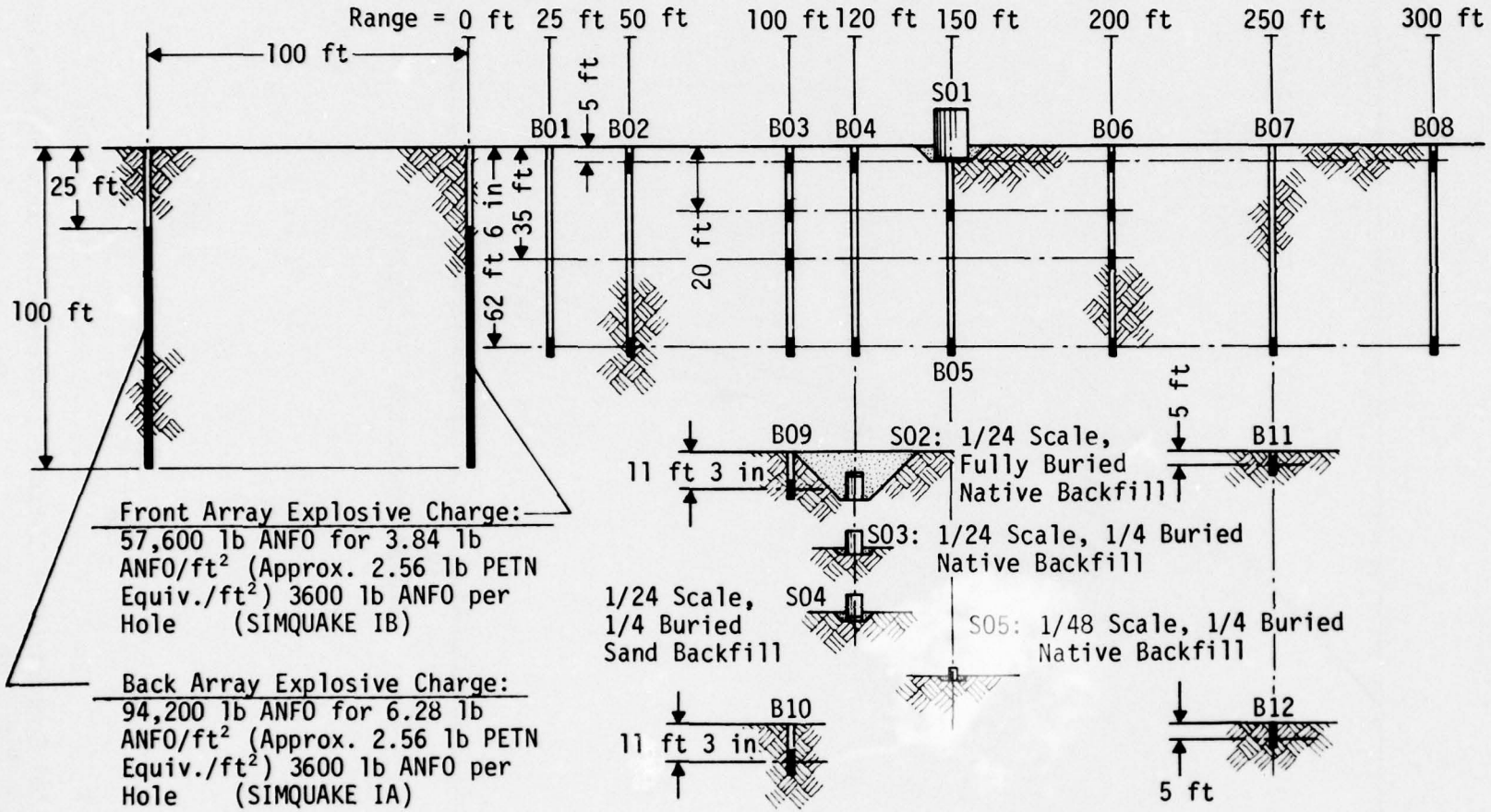

Figure 4. Elevation - SIMQUAKE I

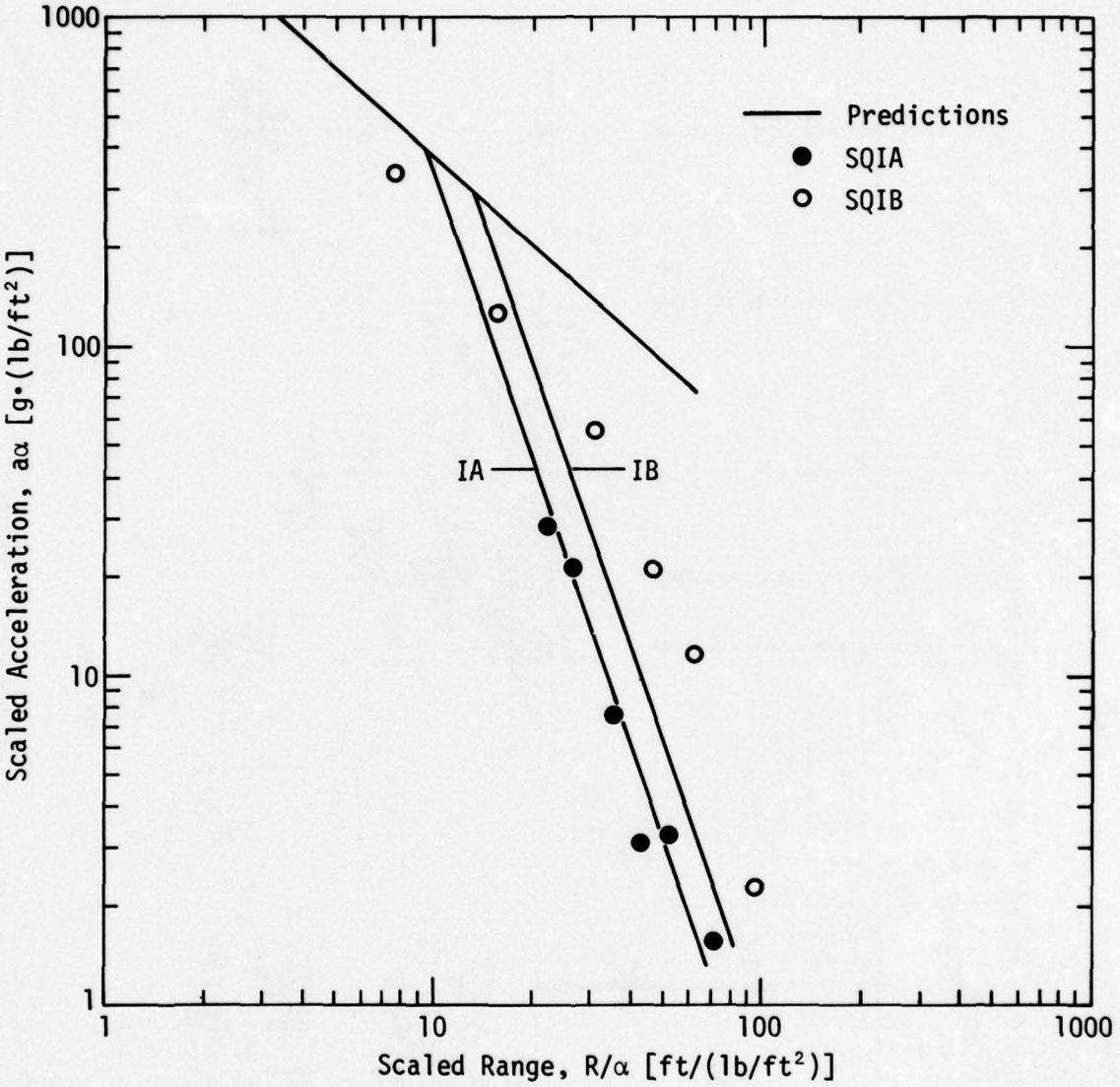

Figure 5. Comparison of SIMQUAKE I Acceleration Data and Predictions

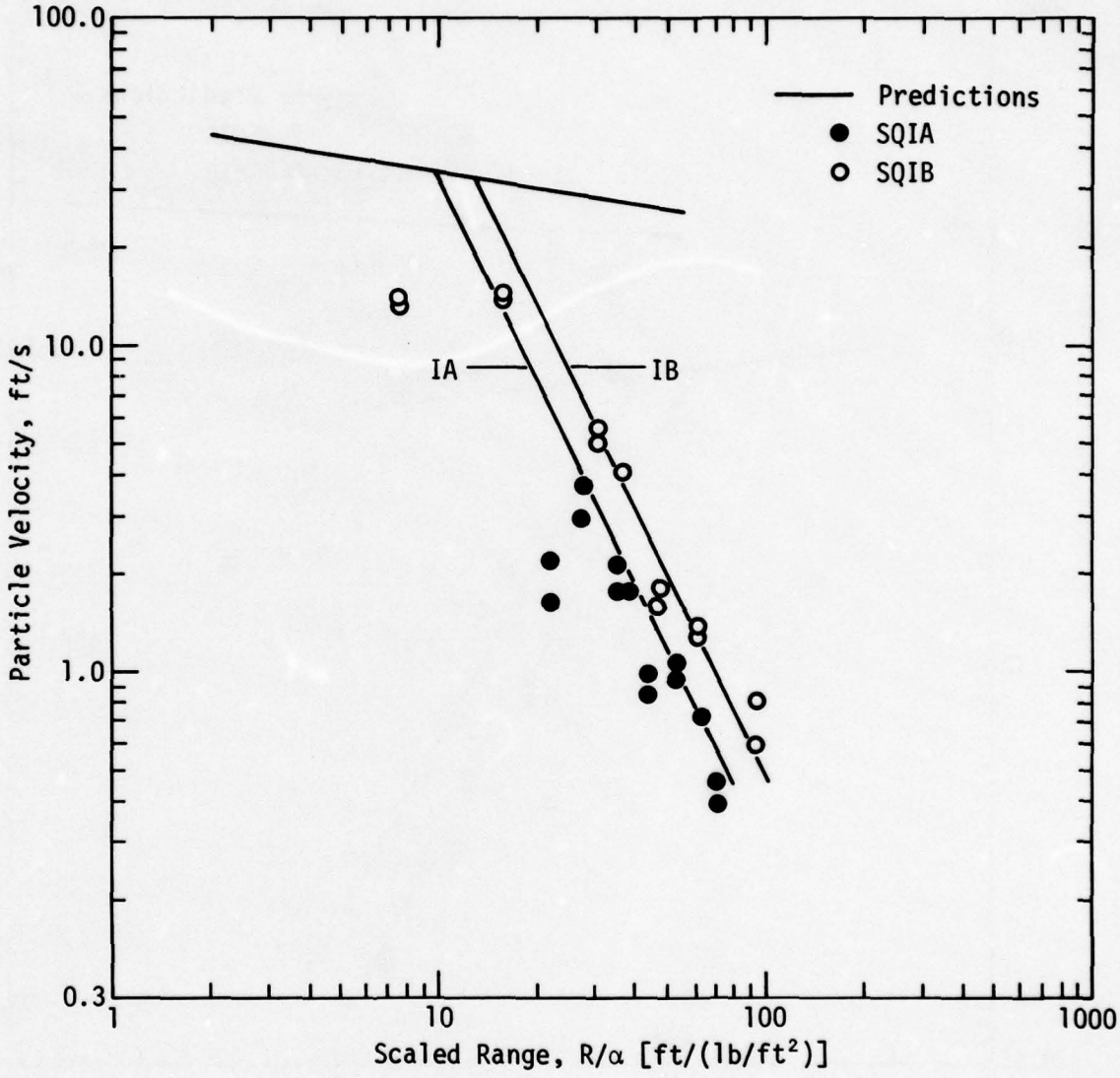

Figure 6. Comparison of SIMQUAKE I Velocity Data and Predictions

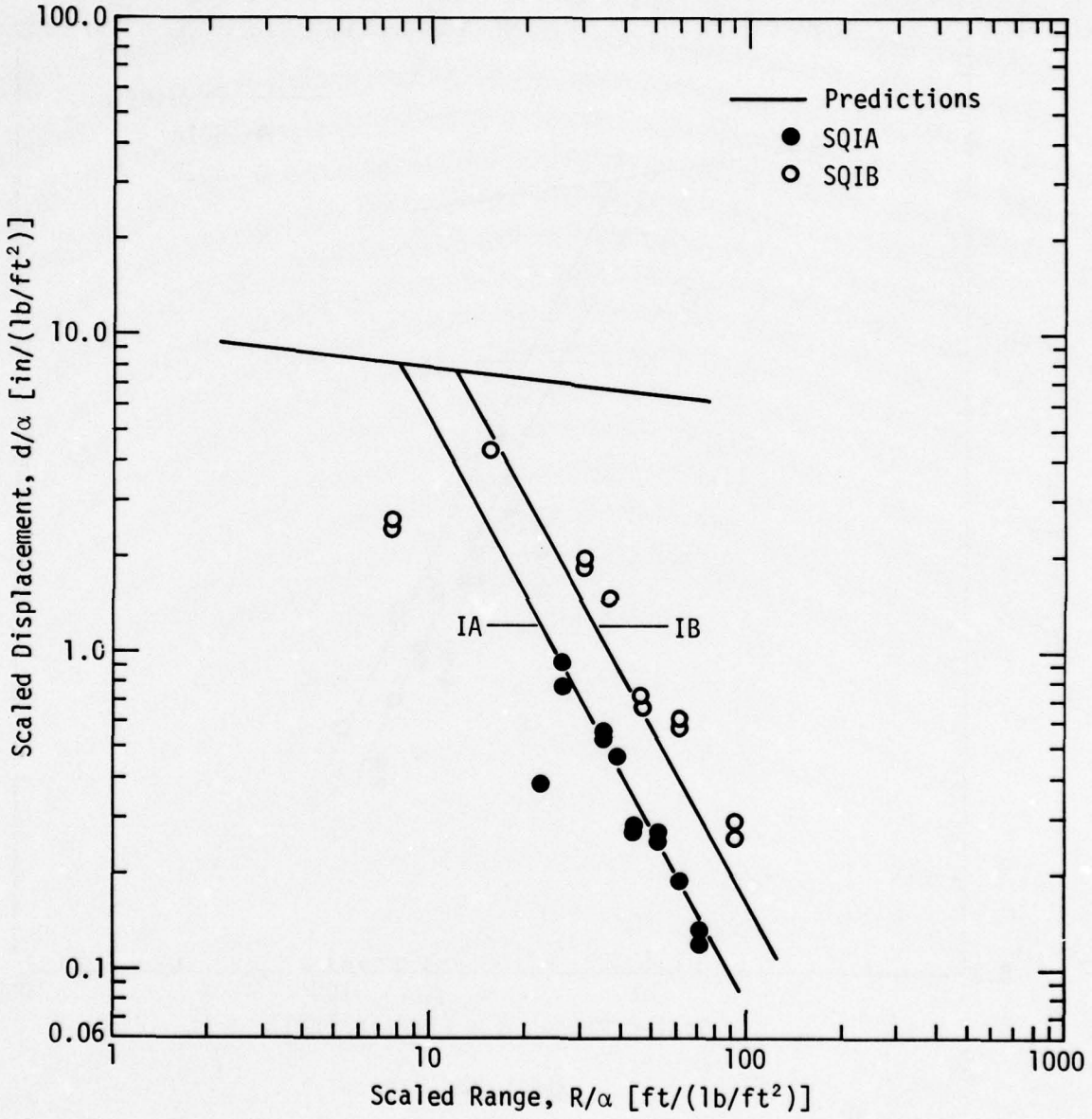

Figure 7. Comparison of SIMQUAKE I Displacement Data and Predictions

IV. GENERALIZED EMPIRICAL PERFORMANCE CHARTS

In order to prescribe a DIHEST design procedure, it is desirable to have generalized performance charts of a relatively simple nature. The major complication of the empirical equations presented in the previous section is the dependence of the normalized transition range, R_o/H, on H/α. For DIHEST events with H/α in the range of 1 to about 50, average R_o/H values for acceleration, velocity, and displacement are 0.75, 0.82 and 0.61. Figures 8 and 9 compare acceleration and velocity data from DIHEST Improvement Program Test IIA (DIP IIA) and Mini-SIMQUAKE-F (MSQ-F) (Ref. 7) with predictions using the equations with variable R_o/H, and with predictions using the constant values of R_o/H given above. DIP IIA and MSQ-F span over more than an order of magnitude in both areal charge density and scaled array height. It can be seen that constant values of R_o/H provide predictions which are low by about a factor of 2.5 for DIP IIA and high for MSQ-F.

A similar comparison for displacements in DIP IIA and MSQ-B is given in Figure 10. MSQ-B is used because MSQ was a double-array event and displacements from MSQ-F cannot be estimated accurately because of their interaction with MSQ-B. The predictions for MSQ-B used the modification for shallow events discussed earlier (Section III). In Figure 10, the predictions for DIP IIA using constant R_o/H is about 60 percent low. The predictions for MSQ-B are about 10 percent high.

If deep events are considered, the assumption of constant R_o/H results in errors ranging approximately from a factor of -2 at small H/α to a factor of +2 at large H/α. At intermediate values of H/α, the error will be less. For preliminary design purposes these results will usually be acceptable.

Figures 11, 12 and 13 are generalized performance charts for DIHEST arrays in soil, based on the constant R_o/H values given previously. Figure 11 shows scaled accelerations ($a \cdot \alpha$) versus scaled range (R/α), where the scaling factor, α, is the areal charge density of the DIHEST array in lb/ft^2. Figure 12 shows particle velocity (v) versus scaled range. Figure 13 shows scaled displacement d/α versus scaled range.

Figures 11, 12 and 13 can be used to predict the approximate centerline, midheight ground motions from a given soil as follows:

(a) For the particular parameter of interest, determine the transition-point range, R_o, by multiplying the array height, H, by the appropriate constant (0.75 for acceleration, 0.82 for velocity, and 0.61 for displacement).

(b) Plot the planar attenuation zone down to the scaled transition-point range (R_o/α). Then plot the cylindrical attenuation zone (interpolating where necessary).

(c) The resultant plots can be "unscaled" by using the appropriate value of α to yield direct plots of a versus R, v versus R, and d versus R.

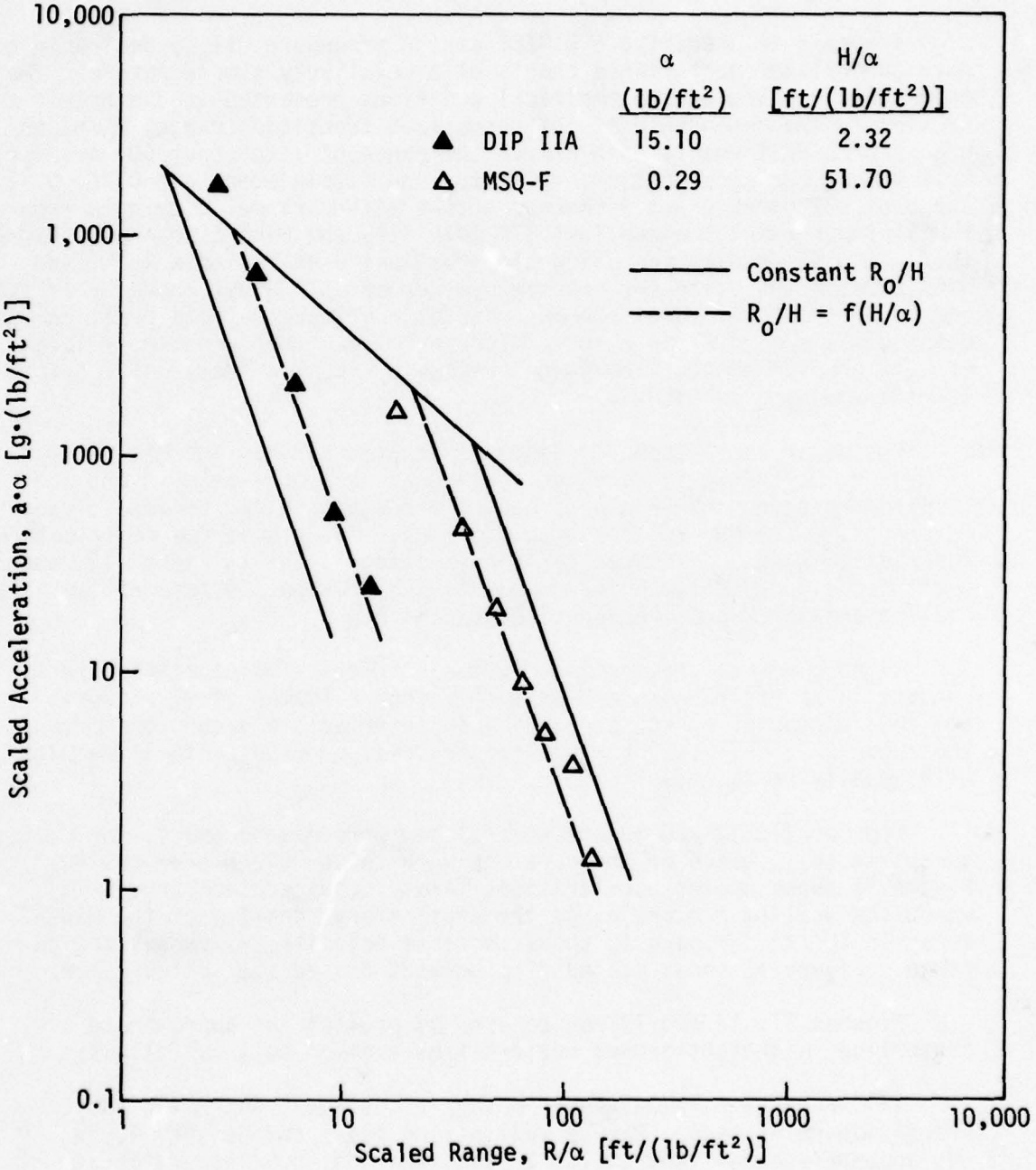

Figure 8. DIP IIA and MSQ-F Accelerations Compared with Predictions

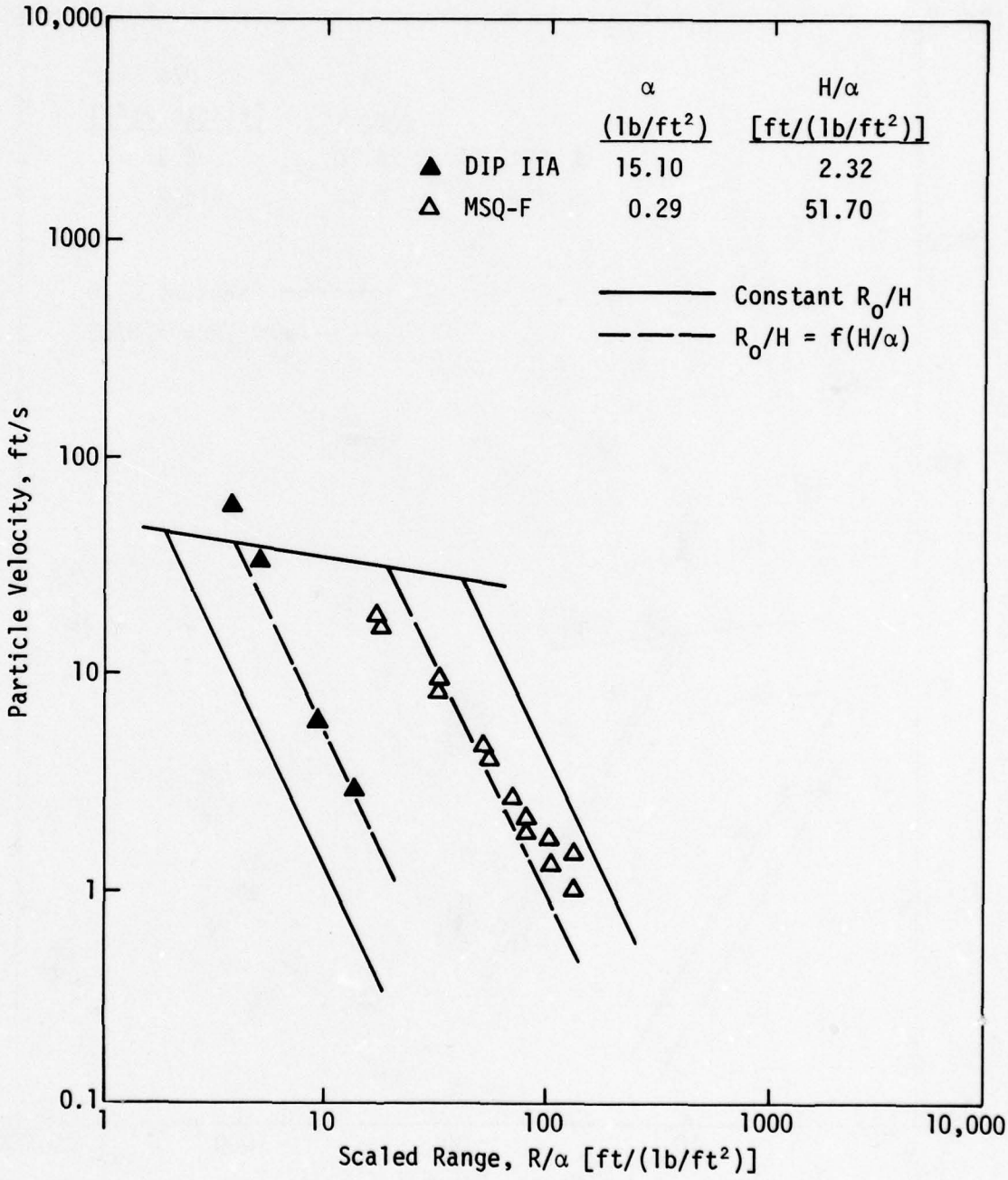

Figure 9. DIP IIA and MSQ-F Velocities Compared with Predictions

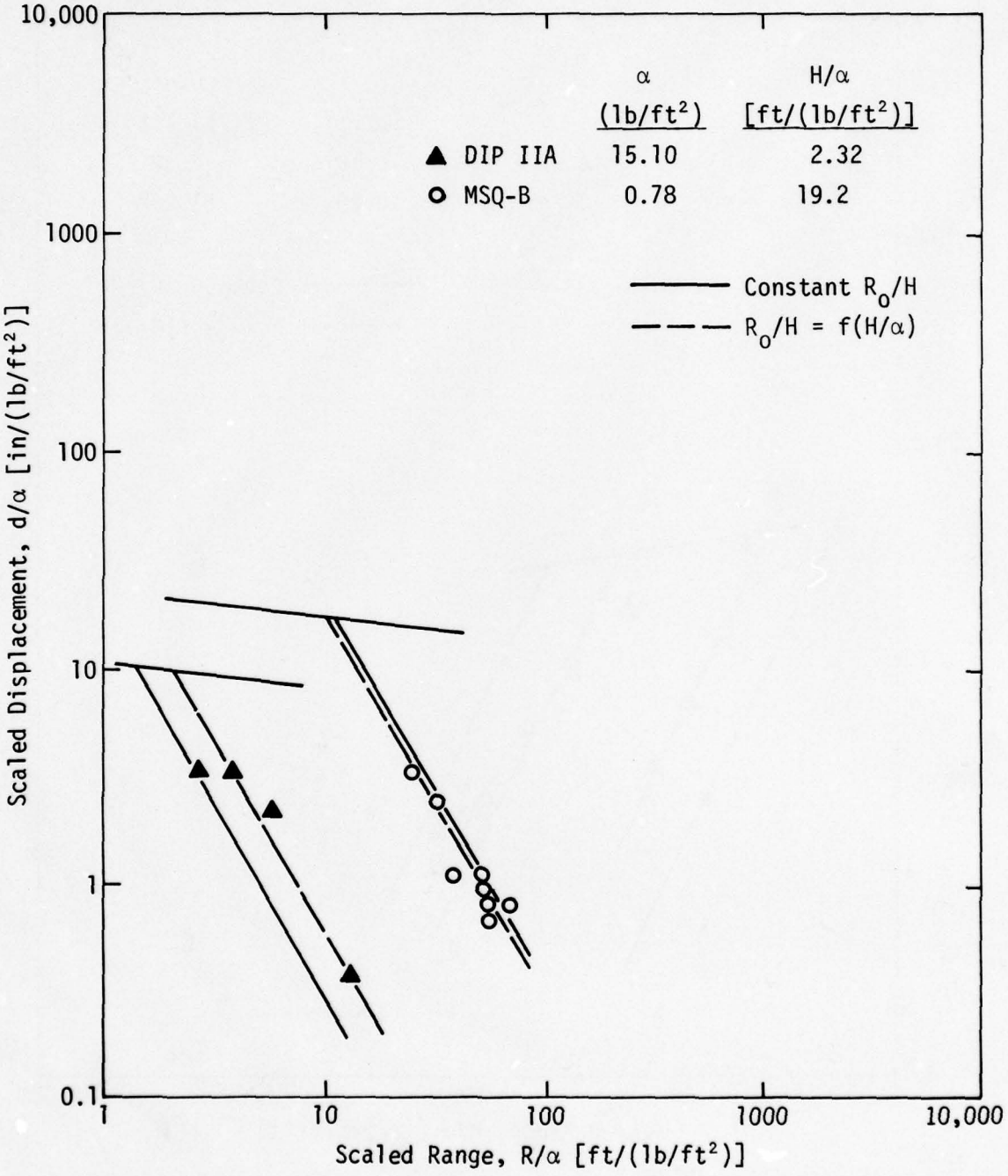

Figure 10. DIP IIA and MSQ-B Displacements Compared with Predictions

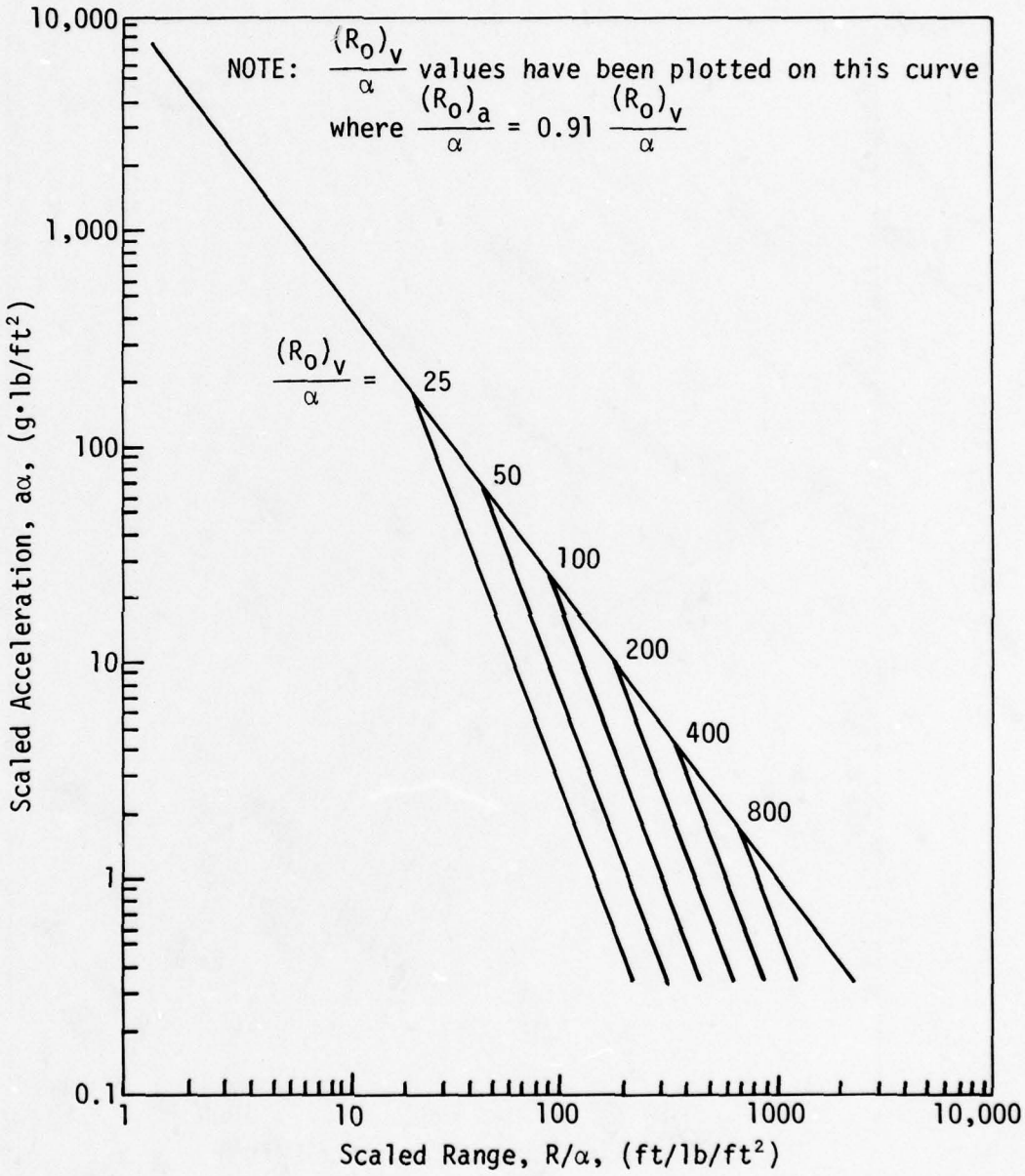

Figure 11. Soil DIHEST Accelerations

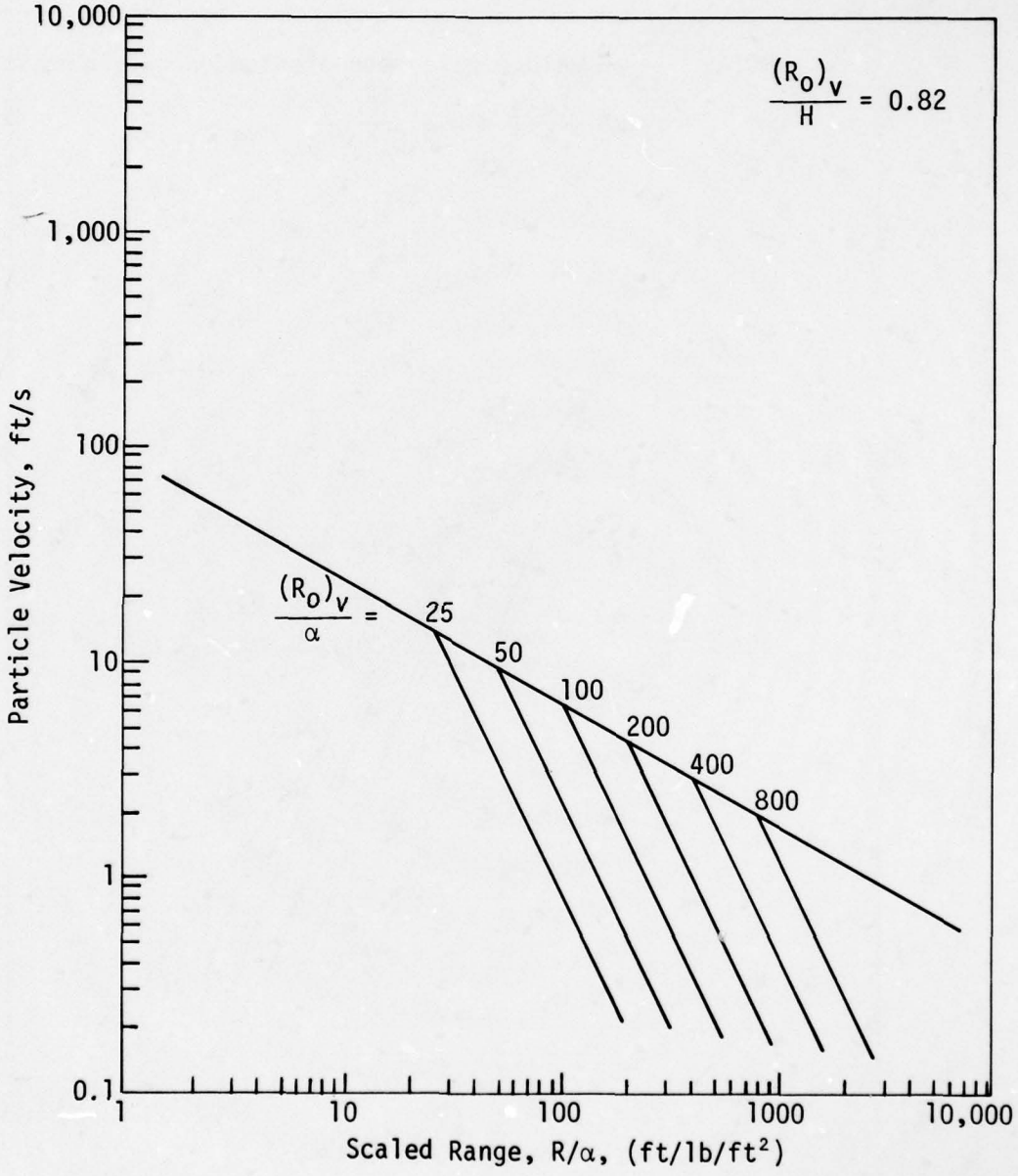

Figure 12. Soil DIHEST Velocities

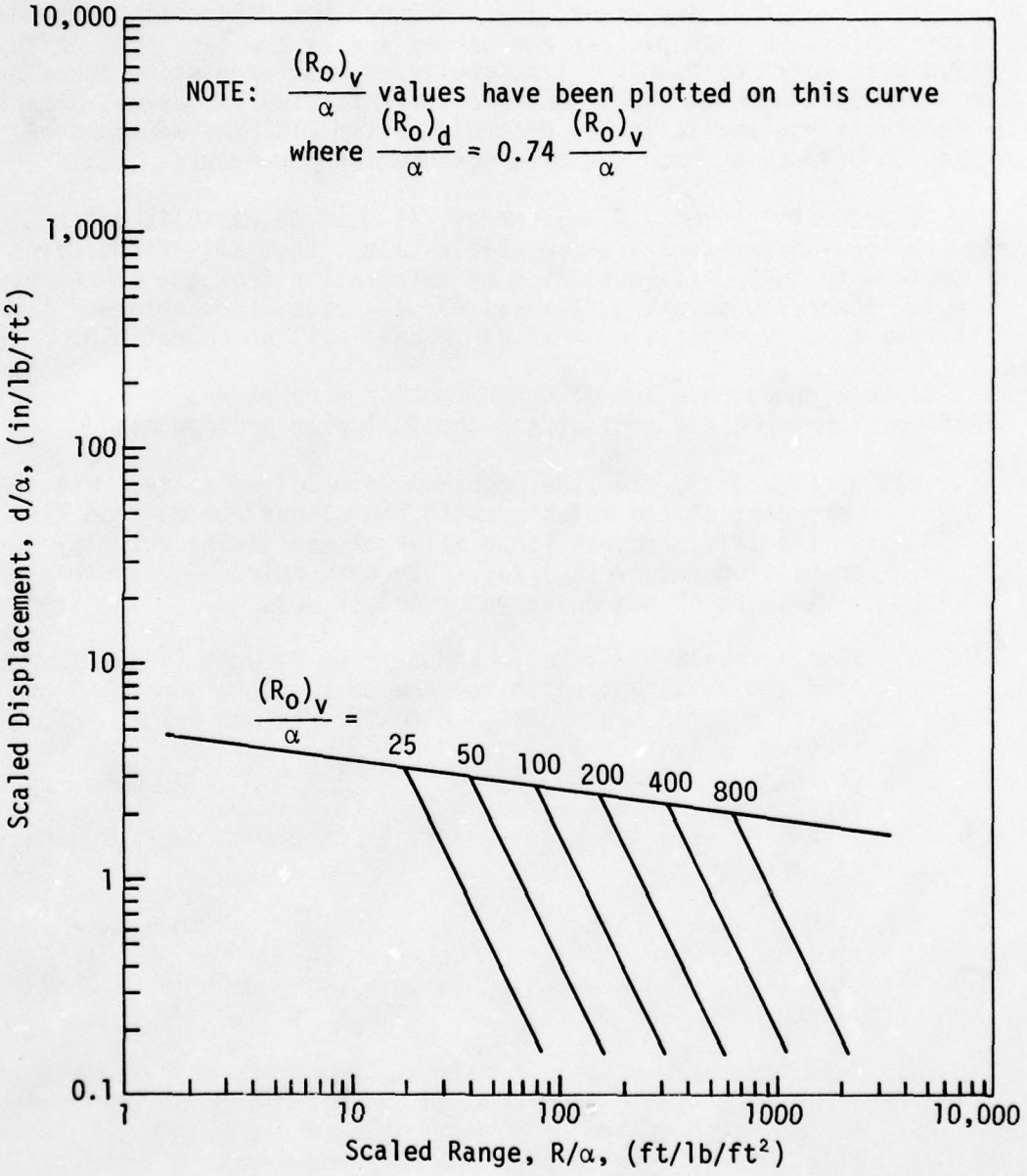

Figure 13. Soil DIHEST Displacements

V. DESIGN PROCEDURE

The design of a DIHEST array to simulate a given weapon yield has not previously been a well-defined procedure. It has been limited by the lack of a consistent prediction procedure for determining ground motions resulting from nuclear explosions and by the lack of a definite design procedure for DIHEST. It is believed that prediction procedures for large single-point explosions are still lacking. However, a design procedure is now available for determining the DIHEST dimensions required to produce a given set of ground motion parameters.

In order to design a DIHEST array, it must be established that the required peak parameters are compatible (i.e., that all of the peaks can be derived through differentiation or integration from the other waveforms). Generally speaking, any set of peak parameters obtained from data from a large explosion or an earthquake will be compatible.

Given a compatible set of ground motion parameters, the current DIHEST design technique consists of the following procedures:

(a) On Figure 12, plot the required value of velocity. Use the intercept of the velocity with the planar attenuation line as the initial guess for a value of the scaled velocity transition range $[(R_o)_v/\alpha]$. Use this value also as the initial value of scaled target range (R_t/α).

(b) Plot the value of $(R_o)_v/\alpha$ and R_t/α on Figures 11 and 13 and find the resultant value for scaled acceleration $(a\cdot\alpha)$ and scaled displacement (d/α). With the desired value of acceleration, solve for a required α. Also solve for α using the desired value of displacement. If the two values of α do not agree, select a new value of $(R_o)_v/\alpha$. If the α for acceleration is smaller than the α for displacement, decrease the value of $(R_o)_v/\alpha$.

(c) With the newly selected value of $(R_o)_v/\alpha$, go to Figure 12 and find the required value of R_t/α [which now will be different from $(R_o)_v/\alpha$]. Repeat step b until agreement is reached between the values of α.

(d) Using the values of $(R_o)_v/\alpha$ and α found above, calculate the array height, H. Check the ground motions which result from the selected values of α and H using the equations of Section III. Assume a value of L (usually about 2 to 3 times H) to calculate the charge weight of the total array.

It should be noted that the above design procedures are based on ground motions along the centerline of the array. This is adequate for deeply-buried target structures. However, for surface target structures a correction is necessary. The procedure for this correction is given in Reference 7 and can cause changes up to about a factor of two. In general, all parameters (acceleration, velocity, and displacement) increase as the surface is approached. Acceleration is approximately

the same; velocity is increased by about 50 percent; and displacement is increased approximately 100 percent.

The relationships between the DIHEST array variables of H, α, $(R_o)_v/\alpha$, and total charge are shown in Figure 14. The array length-to-height ratio was assumed to be three. This plot shows that large values of $(R_o)_v/\alpha$ rapidly lead to large array heights and very large total charge weights. It is therefore necessary to minimize the values of $(R_o)_v/\alpha$ used in the above design procedure. Sometimes this may require some degree of compromise in the required ground motion parameters (such as reducing displacements or allowing larger accelerations). While using Figure 14, it should be noted that H is usually limited by geology (bedrock or water table) or by drilling limitations, i.e., depth limitation of available drilling equipment. In-place explosive costs vary considerably, due primarily to the drilling characteristics of the geology. Recent experience with 70-ton DIHEST arrays in soil with drilling depths of 100 ft suggest in-place array costs of approximately $1000/ton of explosive. This approximation allows Figure 14 to be used directly as a DIHEST cost chart with the total explosive weight read as kilodollars.

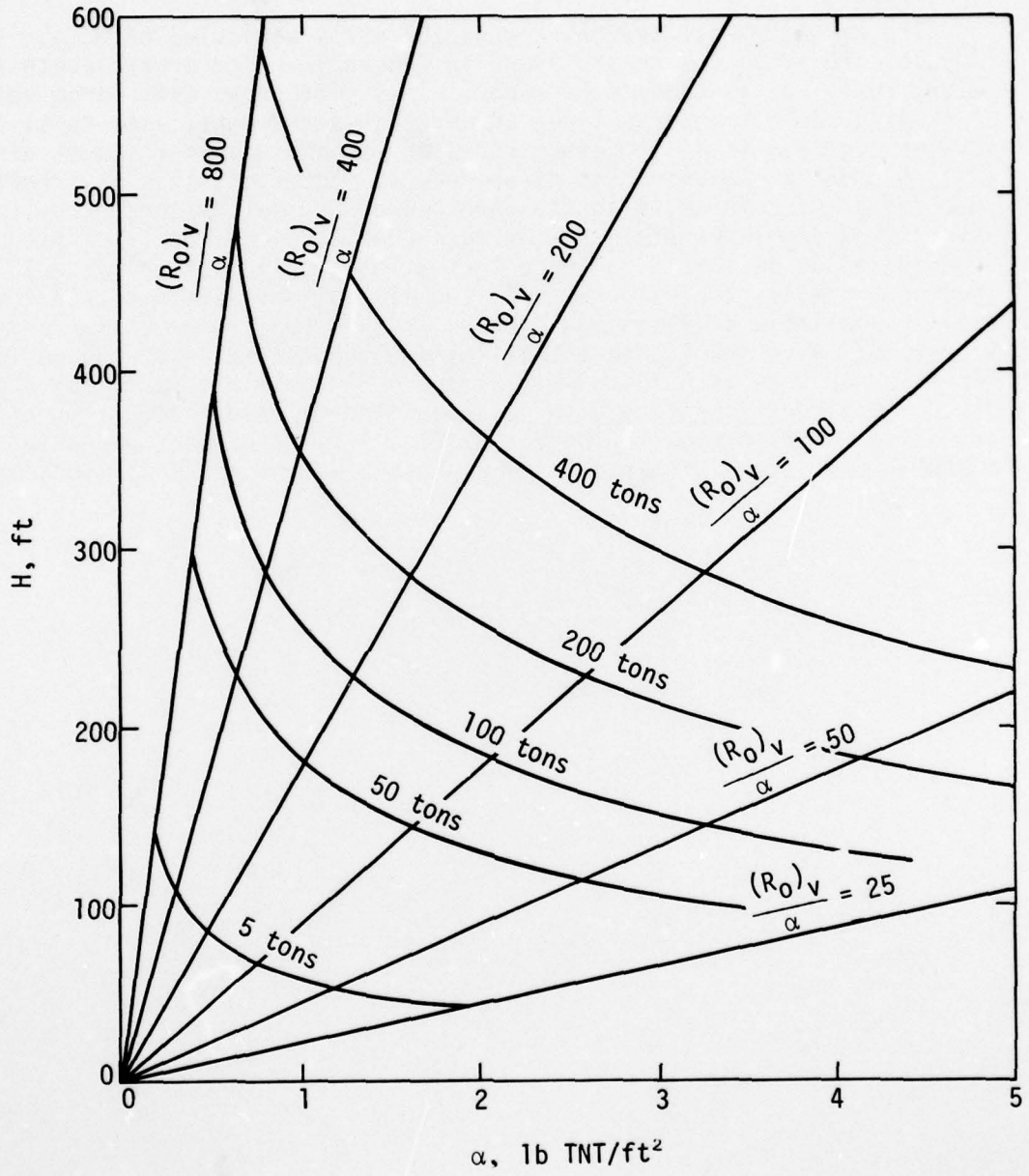

Figure 14. Relationship Between DIHEST Variables

VI. CONCLUSIONS

During the past few years, considerable gains have been made in understanding the performance of DIHEST arrays in dry soils and in the ability to design and predict their performance. In the analysis of previous data, the scaling relationships and generalized performance charts were developed. An empirical design procedure was also developed. It is therefore now possible to design and predict DIHEST array performance in dry alluvium soils with a reasonable level of confidence.

Methods of analysis and prediction are now at a level at which design relationships can be developed for a new site and for different geologies with only a limited number of calibration shots.

Ground motion experiments can be designed to have amplitudes and frequency contents comparable to the range of those expected in the ground-roll region of nuclear events and to those of very strong earthquakes.

REFERENCES

1. Schlater, D.R., *DIHEST Improvement Program Test--DIP IA Data Report*, AFWL-TR-71-120, Air Force Weapons Laboratory, Kirtland Air Force Base, New Mexico, April, 1972.

2. Schlater, D.R., *DIHEST Improvement Program Test--DIP IIA Data Report*, AFWL-TR-72-35, Air Force Weapons Laboratory, Kirtland Air Force Base. New Mexico, April, 1972.

3. Simmons, K.B., *Direct Induced High Explosive Simulation Motion Enhancement Techniques in Soil*, AFWL-TR-72-233, Air Force Weapons Laboratory, Kirtland Air Force Base, New Mexico, Novemeber, 1973.

4. Schlater, D.R., *DIHEST Improvement Program Test--DIP IIIA* AFWL-TR-74-16, Air Force Weapons Laboratory, Kirtland Air Force Base, New Mexico, April, 1974.

5. Simmons, K.B., *Direct-Induced, High Explosive Simulation Technique Improvement Program Tests (DIP IVA and DIP VA)*, AFWL-TR-74-238 Air Force Weapons Laboratory, Kirtland Air Force Base, New Mexico, March, 1976.

6. Higgins, C.J., Simmons, K.B., Pickett, S. and Crawford, R.E., *Quick-Look Report on Mini-SIMQUAKE, A Small Explosive Test Designed to Simulate Earthquake-Like Ground Motions.* University of New Mexico Civil Engineering Research Facility Report to the Electric Power Research Institute, Palo Alto, California, May 1977.

7. Higgins, C.J., Johnson, R.L., and Triandafilidis, G.E., *The Simulation of Earthquake-Like Ground Motions with High Explosives*, Final Report No. CE-45(78)NSF-507-1, The University of New Mexico, for National Science Foundation under Contract NSFENG 75-2150, July 1978.

8. Higgins, C.J., Simmons, K.B., and Pickett, S., *SIMQUAKE I - A High Explosive Test Series Designed to Simulate the Effects of Earthquake-Like Ground Motions on Nuclear Power Plant Models*, Summary Report, University of New Mexico Civil Engineering Research Facility, prepared for Electric Power Research Institute, Palo Alto, California (in progress).

SIMULATION VERSUS STIMULATION

by

R.J. Port

R&D Associates

ABSTRACT

SIMULATION VS STIMULATION

by

Robert J. Port
Henry F. Cooper, Jr.

Testing plays a central role in all engineering and scientific enterprises. Tests often supply fuel to the creative process of conceiving and evolving new concepts; they refine and focus ideas in the engineering development and validation of designs, and they provide a basis for monitoring the quality of the products. In particular, testing has played an essential role in evolving U.S. land-based strategic systems, and in providing confidence in their survivability to nuclear attack. Since the atmospheric test ban constrains, and in many cases prohibits, actual exposure of many system components to the expected nuclear environment, the U.S. has expended significant resources to develop and apply test procedures to subject system components, and entire systems, to simulation environments. The fidelity of the simulation achieved in these tests has varied depending on test objectives, our knowledge of the environments being simulated, and our testing ability.

This paper reviews the history of blast and shock testing for land-based systems, comments on the degree to which previous testing procedures has reflected our changing understanding of the nuclear environment and our ability to test, and discusses the requirements for high- vs low-fidelity testing, i.e., simulation vs stimulation. Both design and targeting applications will be considered.

BACKGROUND

In any engineering endeavor, tests/experiments play key roles in:

- understanding phenomena and conceiving systems . . . developing basic principles.
- evolving designs . . . identifying and correcting problems/improving concepts
- proving designs in their final stage . . . proof/acceptance testing
- assuring design is implemented in production . . . quality control
- assuring system is maintained as designed . . . quality assurance.

Nuclear weapon systems are no exception.

However, nuclear weapon systems are distinctive in at least one sense. The final proof of the utility/success of a system/product is usually measured by its operational performance following production . . . presumably under the conditions for which it was designed. In contrast, nuclear weapon systems have not been employed under anything approaching realistic wartime conditions, with the possible exception of the bombs dropped in Hiroshima and Nagasaki under a benign resisting environment. We are totally reliant on peacetime studies and testing for our understanding of the nuclear survivability and wartime reliability of our nuclear weapon systems.

Everyone hopes the acid test will never occur. Indeed, the stated national purpose for such systems is to <u>deter</u> nuclear conflict, and in a major sense they will have failed in their purpose if they are ever used. Nevertheless, confidence that the systems will perform as designed in the event of a nuclear conflict is very important . . . otherwise their deterrent value would be significantly eroded.

In particular, this confidence is crucial in assuring the existence of a second-strike posture, a keystone of U.S. strategic policy. This policy requires that we have the capability to absorb a nuclear first strike before retaliating with nuclear weapons. This second-strike policy places a premium on assuring the survivability of our strategic forces. If either we or our adversaries doubt that our forces are survivable, a potential instability could lead

to nuclear war. If we have doubts, our adversary might perceive that we might not resist the temptation to preempt and minimize our losses under times of stress; hence, they could be motivated to preempt. To counter such unstable tendencies (which exist as part of Soviet doctrine and expectation of history), it is important that they believe our forces are survivable and that preemptive attack is an unattractive option in any case--whether in times of stress or "out-of-the-blue".*

A key question is "what does it take to provide such confidence to ourselves and our adversaries?" Testing constitutes an important part of the answer to this question, and no single test could be more impressive than a missile launch from an operational site following the detonation of a megaton surface burst a quarter of a mile away. For political, environmental, and other practical reasons, we cannot conduct such a test. Rather, we provide confidence in peacetime reliability by routinely flying missiles from Vandenberg AFB (under benign environments), and we have built some confidence in the wartime reliability of our silo systems by subjecting model and operational missile systems and components to test environments that simulate to some degree the nuclear environment expected under nuclear attack conditions. The integration of results from these less than perfect tests provides the basis for our confidence in the hardness of our silo-based missile systems.

Thus, it is important to consider the attributes of simulation testing and associated analysis procedures . . . including the key question: "How much fidelity in simulating the actual nuclear environment is necessary?"

A purest desires a high-fidelity simulation as a matter of principle. On the other hand, a pragmatist recognizes that no simulation is perfect; and furthermore, under some circumstances either the conditions for a "perfect" simulation cannot be defined or the simulation test requirements are prohibitive. In addition, he notes that, if the system survives "overtest" conditions, confidence would be assured and the entire question of test fidelity would be moot.

Such an "overtest" is very desirable, and under some conditions is quite credibly possible. In other cases, the

---

*It should be noted that whoever preempts enjoys an advantage since peacetime reliability must be higher than wartime reliability . . . but it might not be good enough and this uncertainty adds to deterrence. U.S. survivability testing should have as a goal the maximizing of this uncertainty in the mind of our adversary.

uncertainties are so large that overtesting bounds provide very severe loading conditions, and the cost of assuring a sufficient hardness condition could be very high. Furthermore, if the environment of primary concern is not known, or cannot be bounded with confidence, then it is not logically possible to define an overtest.

For blast and shock testing, an input boundary condition is applied to the material within a control region, and measurements are made of both the loading and response parameters. A typical example is a structural response experiment where the loads are applied to the boundaries of the structure, and the prime output measurement is the stress and motion time history of the responding structure. Other examples involve experiments which load the air/ground interface over an earth half-space, loadings on soil and/or fluid islands around structures, loading on structures and portions of structures, and loadings on internal system and components.

All the above experiments stimulate the test article in that they apply a loading to the boundary of a control region and excite a response of the material within the region. When the stimulation boundary condition duplicates or reproduces some aspect of a nuclear weapon effects input boundary condition, the experiment is said to simulate that aspect of the nuclear event. The simulation portion of the experiment must be accurately qualified to define the precise aspect of the nuclear environment that is being simulated, and the temporal and spatial extent of the simulation.

Tests that provide high-fidelity simulation loadings are not necessarily a preferred means of understanding or qualifying the response of a test article. There are many problems which are better solved by developing the response function to a group of stimulation experiments. As an example, the analytic response functions from step loading and impulsive loading (Green's function) can be combined to solve for the response of a complicated linear system to a complicated nuclear loading function. A similar procedure has been proposed to estimate the structural response from nuclear environments using a combination of the structural response measurements from a constant-pressure step input and an impulsive loading experiment.

The fidelity of the test loading conditions refers to the exactness of the nuclear simulation and not the quality of the experiment. A low-fidelity stimulation test should possess all of the qualities of predictability, repeatability, and measurability required in any worthwhile experimental research.

ENVIRONMENT FIDELITY ISSUES

In attempting to conduct simulation experiments, we must know the environment well enough to define the simulation goals, and we must define and measure the test loading conditions well enough to meet these goals. This task is not easy. The first main problem is in specifying the nuclear environment to be simulated. As we will see in the next section, there are large uncertainties in defining nuclear environments, and many past programs have spent considerable resources generating a high-fidelity simulation of someone's best estimate of a very uncertain nuclear environment. While this approach may be appropriate for some applications, we feel that an alternative approach of providing clear bounding overtests with lower fidelity experiments might provide higher confidence in test programs where demonstrating survivability is the objective.

The large uncertainties in nuclear environments make it extremely difficult to address the actual fidelity issues within a given test program. When the environment is uncertain by factors of two or three, then any test that provides an environment even close to the nominal design goals can realistically be considered to represent the salient features of a possible nuclear occurrence.

One of the biggest problems in dealing with nuclear weapon effects uncertainties is differentiating between the random uncertainties and the systematic biases or ignorance uncertainties. The random uncertainties (such as variations in structural material strengths about their mean values, or the azimuthal variation of weapon effects) can be evaluated with test environments that simulate nominal nuclear weapon effects. Such nominal environments can be used to predict the average results of a large number of weapons against a large number of targets, because the random uncertainties tend to integrate out to the nominal values.

Systematic uncertainties, involving ignorance of either the nuclear weapon effects environment or the resulting system response analysis, cannot be addressed so easily in establishing the fidelity requirement for a test program. Our present prediction techniques generally cannot resolve systematic variations in the phenomenology of less than a factor of two, and sometimes the possible bias errors are much larger. As an example of the difficulties resulting from these systematic uncertainties, consider the problem of designing a ground motion simulator to exercise the shock isolation system within a structure at a given site. What environment goal should be used? Since only one nominal

environment is correct and we just do not know what it is, it seems obvious that the philosophy of developing a conservative overtest is mandatory. It also seems obvious that high fidelity for a conservative overtest should not be a mandatory requirement if achieving that fidelity is either difficult, time-consuming, or expensive.

The question about fidelity is also strongly influenced by the ability to design and measure the test environment. There are some weapon effects, such as fireball temperatures, that cannot easily be simulated without rather large and very expensive test programs. Although the test program objectives may demand such tests, the available manpower, funding, and/or state-of-the-art simulation technology may not be available. It may therefore be necessary to settle for a low-fidelity stimulation test program and/or analysis effort to provide a low-confidence estimate of the required system response.

The size of an experimental program and its required fidelity are strongly related. It may be very realistic to conduct high-fidelity experiments on statistically significant numbers of component level tests, but prohibitively expensive to conduct a large number of full-scale experiments. Almost all large-scale tests consist of only one or two samples. Those who have studied the extrapolation of the results of experimental programs that have only a few data points will realize that it is not possible to make high-confidence statements about system response issues from so little data. When the program plan is designed in such a way as to preclude high-confidence statements, one should seriously question any requirement for high-fidelity experiments.

Any experiment that does not achieve a perfect simulation must address the significance of the nonsimulation response. There are two issues involved: those characteristics that are within the nuclear environment but are not part of the simulation test, and those characteristics that are within the simulation test that are not part of the nuclear environment. Both issues are extremely important to the interpretation of the test results.

It is also possible to have a high-fidelity simulation of one portion of the nuclear environment, such as vertical motion, and not attempt to simulate another portion such as the horizontal motion. The test could then be both a high- and low-fidelity simulation, and the judgment of the system response implications would depend on the critical failure mode analysis. We have had vertical simulation tests on

large-scale systems which turned out to be extremely vulnerable to the horizontal environment that was omitted from the test. One should now classify such a test as a low-fidelity system experiment.

We also have performed tests that failed structures with some aspect of the test environment which did not simulate any nuclear weapons effects (such as debris impact from the HEST overburden). Such tests are difficult to interpret, and may be very misleading. It is therefore important to evaluate the fidelity requirements, and assess the impact of potential or planned low-fidelity aspects of the environment early in program formulation.

ENVIRONMENT UNCERTAINTIES

The first question one should ask when discussing simulation testing is what environment should we be trying to simulate. It will become very apparent if one studies nuclear weapon prediction techniques in any detail that our understanding of weapon effects environments is very uncertain. Table 1 displays the approximate peak value uncertainties of several critical blast and shock environment parameters. Note that the blast and shock uncertainties are measured as factors expressing the ratio of upper to the lower bound estimates. Note also that the minimum entry in the table is the factor of two uncertainty in peak overpressure. This means we cannot estimate the peak overpressure at a given range from a nuclear detonation to better than a factor of two, and all other nuclear environments are more uncertain than the overpressure.

The risetime to the peak overpressure is also very uncertain in some overpressure regions, and may be a strong function of the properties of the ground surface material. Figure 1 shows pressure-time data along three specially prepared radial lines from a single nuclear event: an asphalt line, a water line, and a desert line. Note that the asphalt and desert lines show a distinct precursor arrival before the main overpressure waveform. The water line is seen to approach the predictions for an ideal surface (also shown in Figure 1). It is assumed that the finite width and depth of the water line is the main reason for its less than ideal behavior, since a water surface should act like an ideal surface.

There have been a number of airblast experiments that have attempted to provide high-fidelity simulation of the ideal waveform shown in Figure 1. In particular, there are currently such efforts in support of a system to be deployed

AD-A073 766 GENERAL ELECTRIC CO SANTA BARBARA CA TEMPO F/G 19/4
PROCEEDINGS OF THE NUCLEAR BLAST AND SHOCK SIMULATION SYMPOSIUM--ETC(U)
DEC 78 DNA0001-79-C-0081

UNCLASSIFIED DNA-4797P-2 NL

3 OF 4
ADA 073766

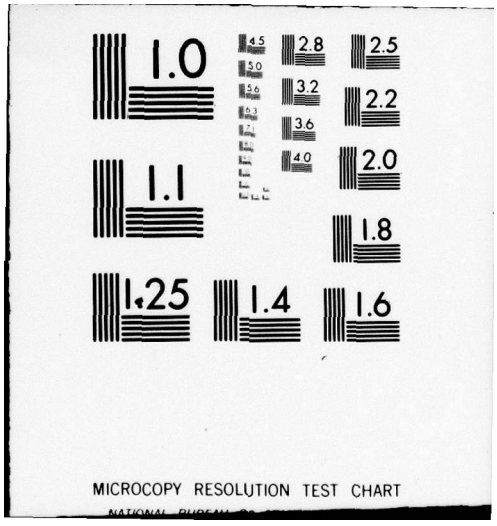
1.0
1.1
1.25
1.4
1.6
1.8
2.0
2.2
2.5
2.8
3.2
3.6
4.0
4.5
5.0
5.6
MICROCOPY RESOLUTION TEST CHART

Table 1. Approximate Uncertainties in Blast and Shock Environments

ENVIRONMENT	ENVIRONMENT UNCERTAINTY	RANGE UNCERTAINTY
AIRBLAST	FACTOR OF:*	FACTOR OF:
OVERPRESSURE	2	1.25
DYNAMIC PRESSURE	$\gtrsim$ 2.5	$\gtrsim$1.35
AIRBLAST-INDUCED GROUND MOTION	4	1.6
CRATER RADIUS		
SURFACE BURST	6	6
EARTH PENETRATOR	2	2
CRATER-RELATED GROUND MOTION	9	2
DEBRIS DEPTH	16	2.5

*UNCERTAINTIES EXPRESSED IN RATIO OF UPPER TO LOWER BOUND ESTIMATE

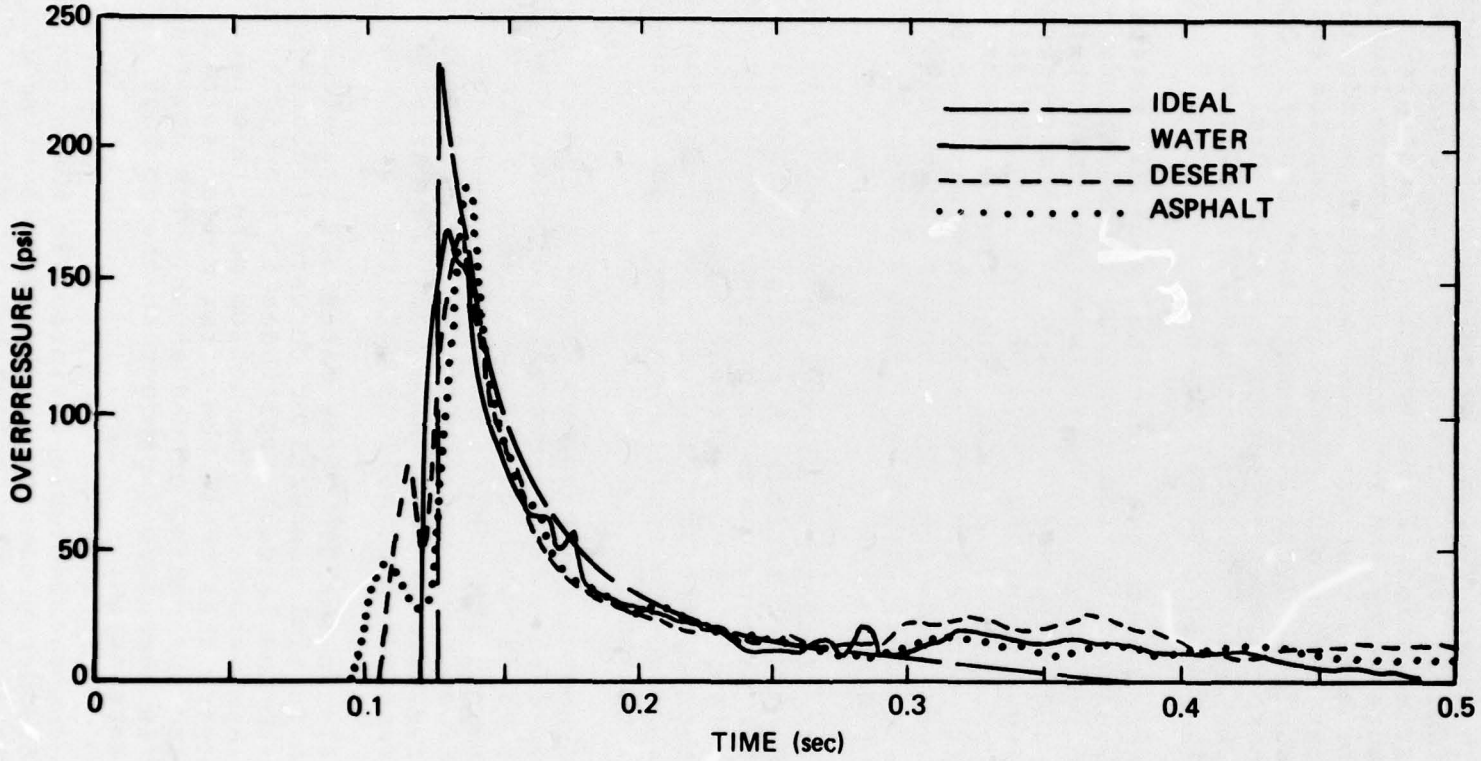

DATA FROM TEAPOT SHOT 12-22 kT AT 400 ft HOB[1]
IDEAL CURVE FROM BRODE DASA 2506[2]

Figure 1. Overpressure Waveform Variations with Different Ground Surface Materials

in a southwestern desert region. We maintain that to reproduce the high-fidelity ideal curve actually would provide a low-fidelity stimulation of the expected nuclear precursed overpressure waveforms for some overpressure levels. It should also be noted that the ideal waveform bounds the peak pressure, but need not bound the initial impulse and does not bound the peak dynamic pressure (not shown). One should be very careful when extrapolating such ideal waveform tests to make survivability estimates for systems deployed in regions with nonideal surfaces.

Ground motion experiments have shown that geologic materials are not homogeneous and isotropic and can introduce additional uncertainties in ground motion waveform characteristics induced by the overpressure loading at the air-ground interface. Figure 2 shows the range of waveform variations observed on six azimuths at a given range from a 20-ton explosive source. Such azimuthal variation might also be expected in the ground motions from nuclear explosions. Peak ground motion is seen to vary by at least a factor of two for this single experiment.

Note also in Figure 2 that the transverse motion is at least 25 percent of the radial motion. A word of caution is directed to system designers who think the ground only moves radially and vertically in the vertical plane passing through the axis of symmetry. The amplitude of such transverse motion has often been observed to approach the amplitude of the vertical and radial motions.

The vertical and horizontal waveforms shown on Figure 3 display potential variation from different geologies. The data were measured at ~5-ft depth at ~100 psi from surface tangent high-explosive events that delivered approximately 100 tons of equivalent TNT energy. Unfortunately, the hard-rock experiments did not have data at this range, and the variation shown in Figure 3 is restricted to soil or soft rock geologies.

The first arrivals in the top three materials (waveforms) of Figure 3 show an initial downward or outward airblast-induced ground shock, with the largest amplitudes in the highly compressible dry playa material. The bottom materials have near-surface water layers that cause the first motion to be an upward and outward outrunning ground shock. The direction of first motion is therefore dependent on the geology and range from the detonation.

Figure 3 also shows considerable variation in the number of cycles and the frequency content of the overall waveforms. It is interesting to note that motion has not stopped after

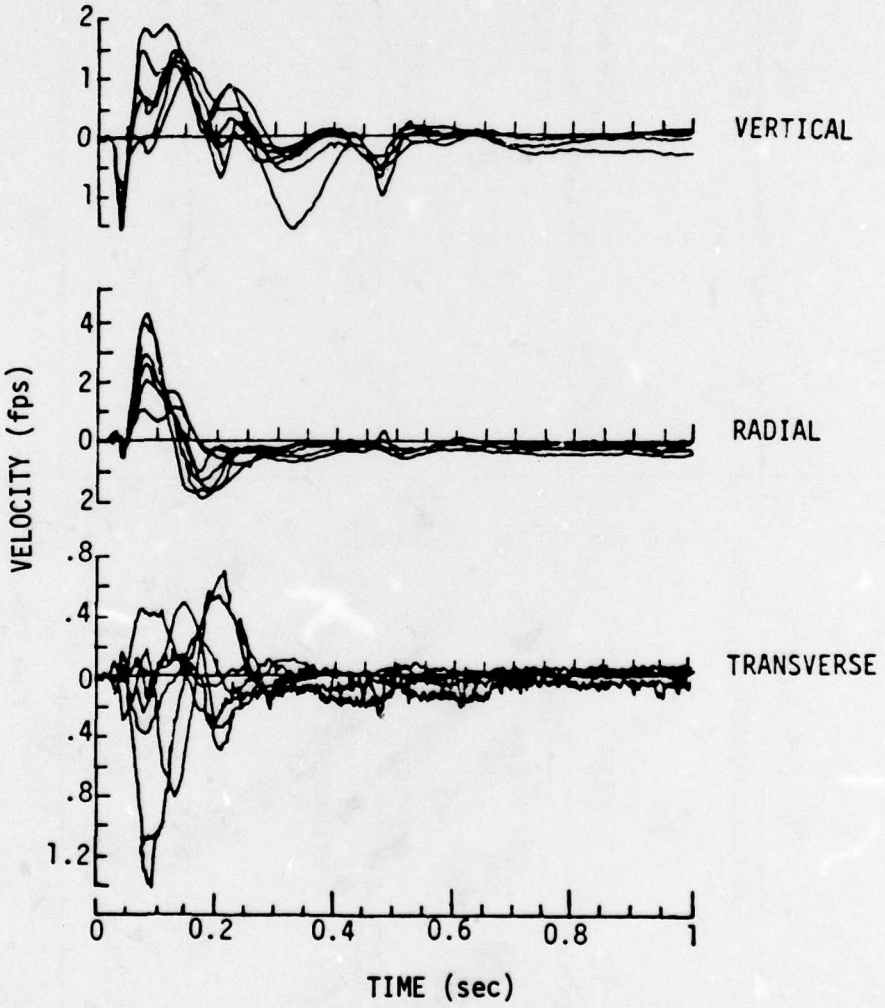

Figure 2. Symmetry Experiment on Flattop III (Range = 65 ft, Depth = 17 ft, from 20 tons High Explosive Half Buried Event)[3]

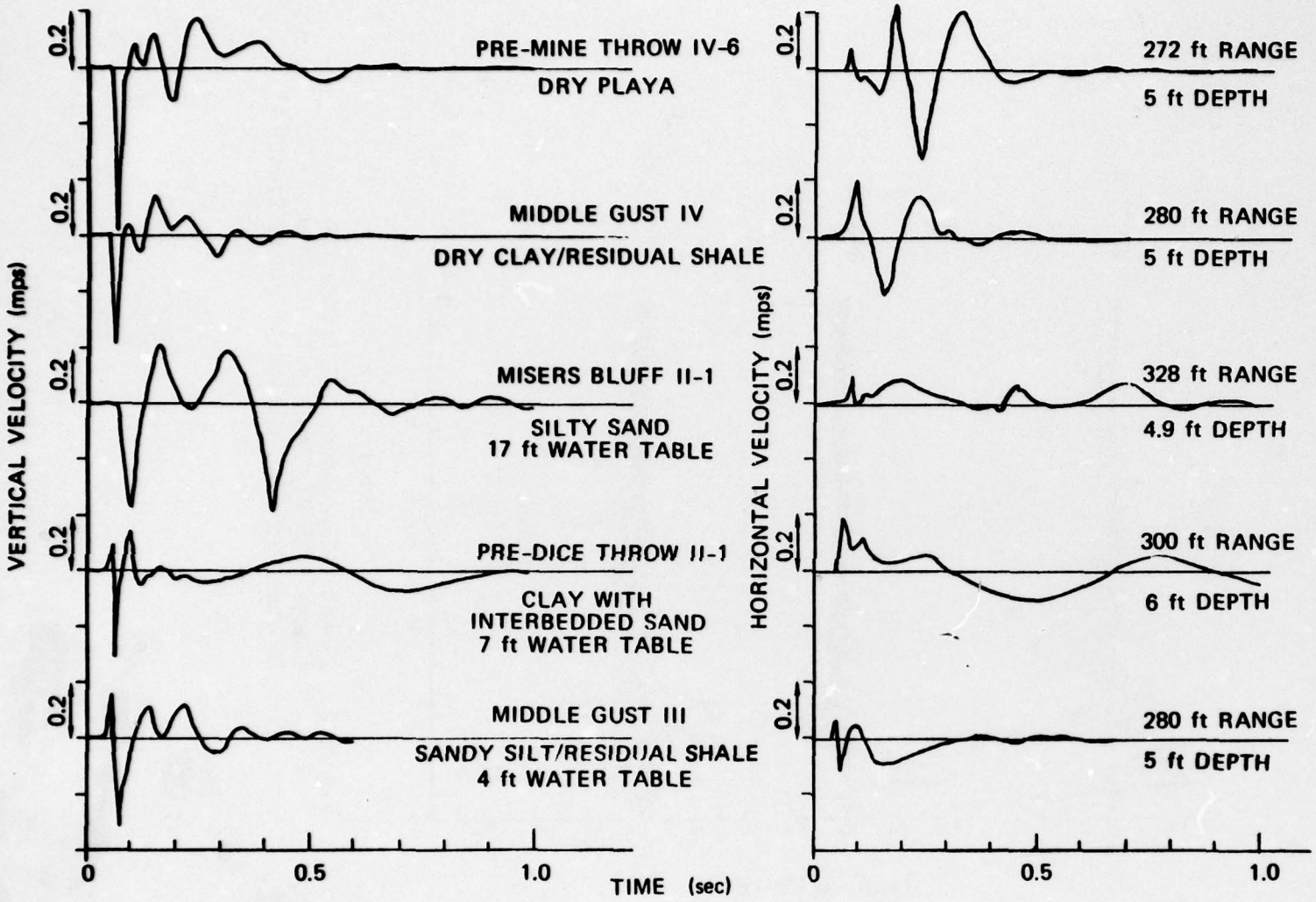

ALL THE DATA IS ∿5 ft DEPTH AT ∿100 psi FROM ∿100 ton SURFACE TANGENT
HE EVENTS IN SOIL OR SOFT ROCK EXPERIMENTS[4]

Figure 3. Ground Motion Waveform Variations with Different Test Site Geologies

one second from the 100-ton events, and less than 2-Hz frequencies are observed. If one is designing a system to be deployed in a range of geologies, it is necessary that the system performance be insensitive to the many and random details of the waveform characteristics.

An example question central to the subject of this paper is how should one design a ground motion simulator to represent the input to a shock isolation system that will be located at the 100-psi range from even a 100-ton high-explosive event, much less a 1-MT nuclear event. After studying Figure 3, one should quickly come to the conclusion that a single high-fidelity stimulation is not meaningful. The best approach would involve test procedures that vary the magnitude and direction of the initial motion, as well as the number of cycles and frequency content of the remaining wave trains.

SIMULATION HISTORY

The history of DNA simulation testing goes back to the Senate ratification of the Limited Test Ban Treaty in 1963. The chart on Figure 4 shows over 60 major experiments that have occurred over the past 14 years in support of several strategic weapon systems. We believe the chart includes all experiments that involved more than 20 tons of high-explosive and/or tested structures of larger than 1/6 scale. The overpressure ranged from a few to several thousand psi, and the simulated yields ranged from 20 tons to a few megatons. The overall cost has not been compiled, but it is of the order of a few 100 million dollars.

It is interesting to note there is almost no duplication. Only one or two experiments are repeats of previous experiments. In all other cases, sequential tests in the overall program have made significant changes in the yield, overpressure, scale size, geology, or structure being tested. In other words, there has not been a statistically significant sample size in the entire program. The forces that mold program plans tend to lead to only a few large-scale system tests for satisfying the stated program objectives. One should seriously think about the confidence level that can be achieved with only a few data points, before making decisions on developing high-fidelity simulators for proposed future test programs.

The structural systems involved in these test programs include Minuteman, shelter and trench MX, deep underground basing, generic targets, bridges, POL, vehicles, tanks, and military equipment. Although several experiments raised more questions than they answered, they usually satisfied

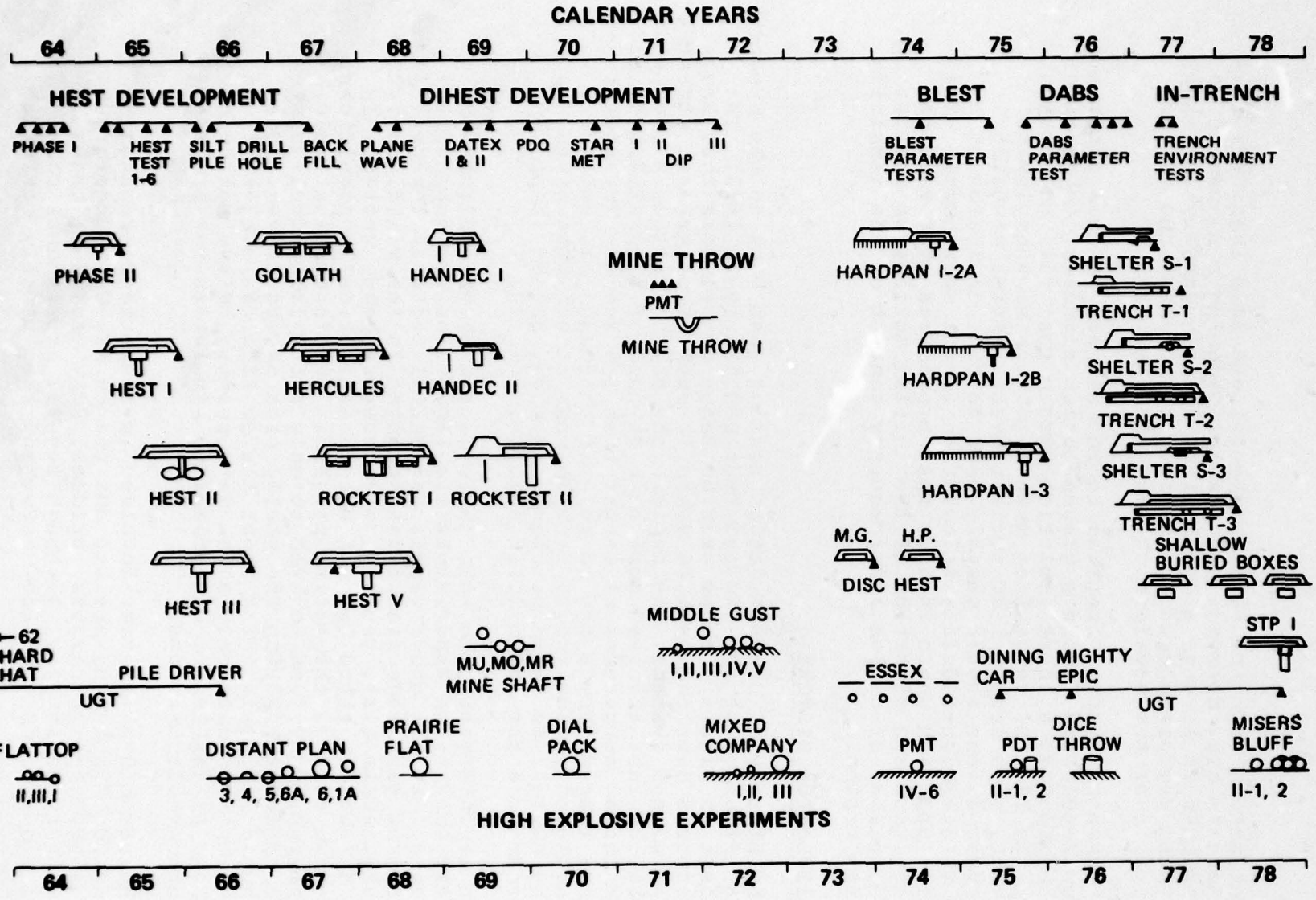

Figure 4. Airblast and Ground Shock Simulation Experiments

the objectives or the specific system questions being addressed by the test program.

The question of fidelity in past simulations has to be answered as a function of time. Many previously purported high-fidelity experiments are now considered low-fidelity. In several instances, our understanding of the environment has changed, which would change our original interpretation of the fidelity of the experiment. We have also learned things about the system being tested which would indicate other environments were more critical than the design high-fidelity environment. In these cases, the experiment may have been a high-fidelity simulation of some portion of the environment but a low-fidelity system response experiment.

These experiments are unique test events that will probably never be repeated. The data, in some cases, provide the only useful means to check and extrapolate our prediction techniques to make estimates about the response of proposed systems. This extrapolation is usually difficult and uncertain because the test events usually did not include the correct structure and/or environment for direct application to future problems. This extrapolation does however represent one of the significant uses of the results of an experimental program, and may in some cases be more useful than the original experimental objective. Several experiments have uncovered phenomenology gaps that have completely changed the direction of the major research programs.

It is interesting to review the initial fidelity objectives of the past test programs. In general, the various simulation programs started off as low-fidelity experiments that gradually changed to produce better and more accurate simulations as the program continued. As an example, HEST testing was originally developed and applied because of a concern that low-level vulnerabilities might exist in a multi-silo attack scenario. The research community first attempted to provide a reasonably good simulation of the airblast loading. The emphasis on the overall fidelity of the HEST simulation came later.

The DIHEST development was designed to simulate a best estimate for the direct-induced ground motion input in a hard rock geology. It was fully recognized that the state of the art for predicting ground motion was very poor, but it was not as bad as the state of the art for predicting the system response to typical values for the horizontal input. The

DIHEST is therefore a low-fidelity simulation, in the terminology of this paper, that can be used to evaluate/develop system models for predicting direct-induced ground shock response.

The MINE THROW series was designed to provide a high-fidelity simulation of the crater-related ground motions. The program was supposed to evaluate the simulation capability by comparing first with JOHNNY BOY, and then the CACTUS nuclear events. Unfortunately, the program was stopped for political reasons before we were able to perform the CACTUS simulation at Eniwetok. As will be shown on a later chart, MINE THROW I produced a very good fidelity simulation of the low-frequency surface motion.

The BLEST was designed to provide a low-fidelity stimulation of the portion of the upstream airblast that would maintain the stress loading on the underground portions of a structure for the required simulation time. The BLEST is not and never was a high-fidelity simulation of the upstream airblast-induced ground motion.

The DABS was an attempt to develop an inexpensive low-fidelity simulator of high-pressure dynamic airblast loading. Alternative techniques that produce higher fidelity simulation were much more expensive, but did eliminate the dust and high explosive product environment loading on the structure. The DABS experiments actually produced much better fidelity than was originally expected.

The in-trench testing was clearly a low-fidelity test program since it was not known, within rather large uncertainty bands, what to expect for the in-trench environment.

The deep underground nuclear test events were phenomenological experiments that were designed to measure structural response and structural fragility under direct-induced ground shock loading. These experiments are obviously high-fidelity simulations of underground nuclear events, but of questionable fidelity for interpreting structural response to near-surface nuclear detonations.

The high-explosive events involving stacks or spheres of high explosives do a good job of simulating the low-overpressure regions of a nuclear surface event. Comparison between the HE and NE will be shown in the next section.

In summary, there are some high-fidelity aspects of all the past simulation experiments, but each test also has low-fidelity portions of the environments. The best simulations

have been performed on small-scale structures or at very low overpressures. All the high-overpressure experiments on full-scale structures have been, in our opinion, low-fidelity simulations.

SIMULATION COMPARISONS

The scope of this paper does not permit an effective review of the capabilities of all our simulation experiments, but we can comment briefly on some of the more important and most used techniques.

Stacks or spheres of high explosives have been used extensively in the study of ground shock phenomenology, and the study of structural response in the low overpressure regions. Figure 5 compares free-air airblast data from high-explosive events with the peak pressure from an equivalent point source of energy. A nuclear event would produce results similar to the point source curve. It can be seen that high explosives grossly underestimate the peak pressure and impulse in the high overpressure region (greater than a few tens of bars). This low-fidelity simulation in the high-pressure region makes it very difficult, if not impossible, to extrapolate the upstream airblast, direct-induced ground shock, crater-related ground shock, and late-time ground roll from near-surface, high-explosive events. Although the HE/NE extrapolation is questionable, the high-explosive tests are the only source of information in some geologies, and therefore are the only data to guide our predictions for nuclear weapons effects in these geologies.

At low overpressures, less than ten bars, the high explosive is seen to do a very good job of simulating both the peak pressure and waveforms. The HE to NE extrapolation for low-pressure, air-induced ground shock can be performed with much higher confidence. The response of structures can also be evaluated, to the low-overpressure waveforms, and thus provide confident predictions in the low-overpressure region.

In most cases, large-scale high-overpressure simulations have been peformed with some version of the HEST technique. Figure 6 shows six gauges, all located at the same range in the Hardpan I-3 HEST cavity. The heavy solid lines on the figure represent the desired nuclear overpressure waveform at the 1200-psi range from a 125-kT detonation at a 210-ft HOB.

Figure 6 shows that a HEST test only simulates the nuclear overpressure in a gross sense, since there are several

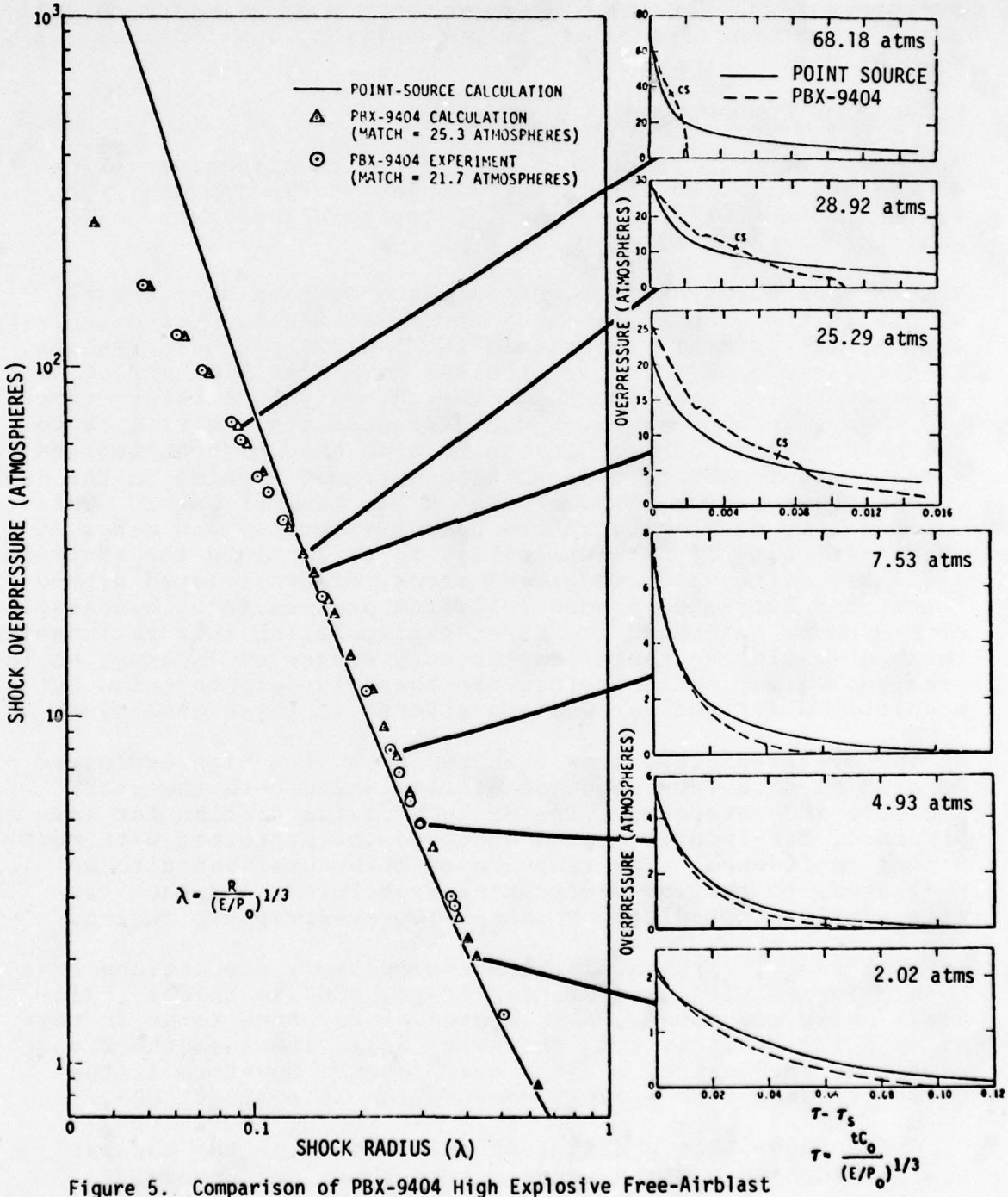

Figure 5. Comparison of PBX-9404 High Explosive Free-Airblast with that of a Point-Source Approximation

Reproduced from J. Carpenter and H. Brode Paper presented in Proceedings of 4th International Symposium on Military Applications of Blast Simulation, 9-12 September 1974 [5]

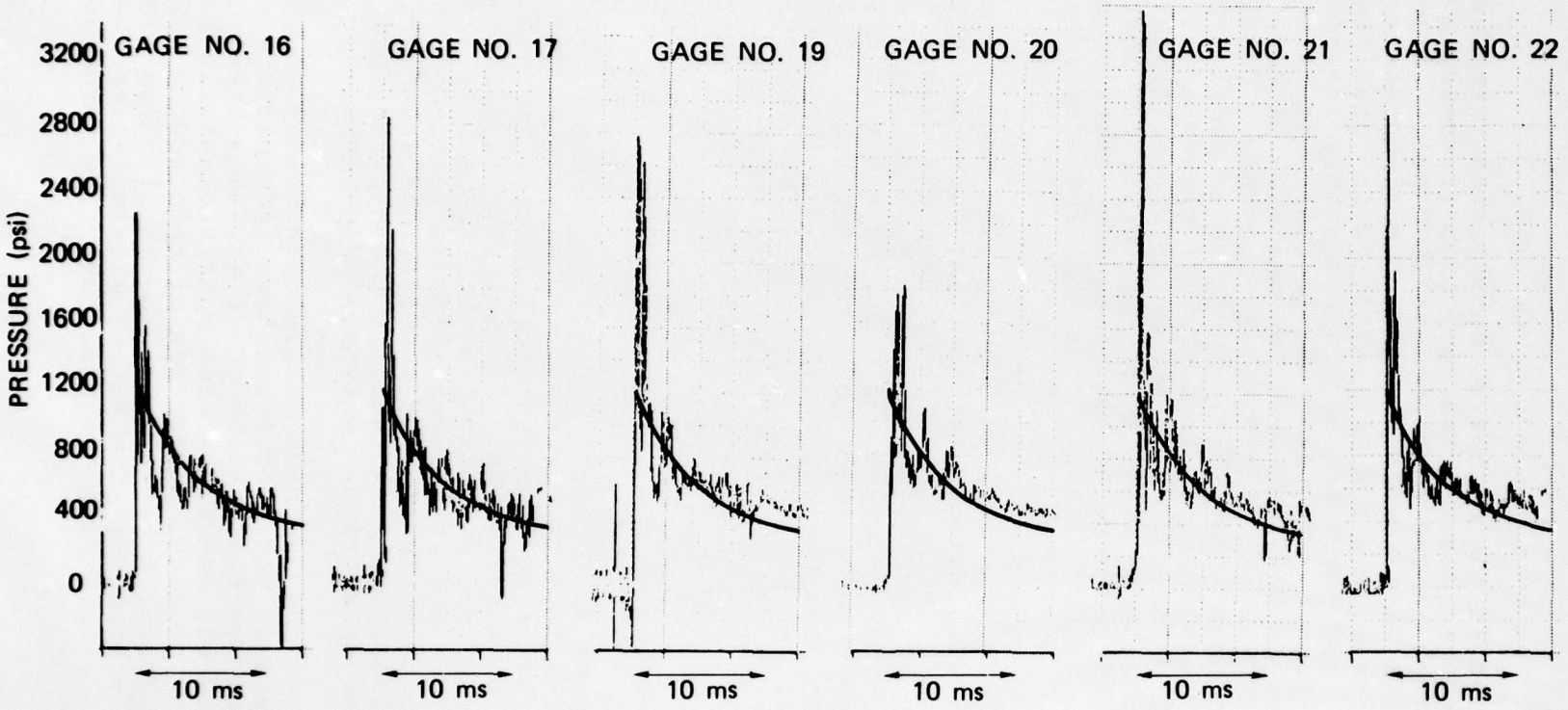

DATA REPRODUCED FROM AFWL DE-TN-76-013

Figure 6. Comparison of Hardpan I-3 HEST Overpressure with Desired Simulation of 1200 psi Ideal Surface Waveform from 125 kT at 210 ft HOB [6]

obvious disparities in the high-frequency region. The actual peak measured stresses occurred as very high frequency spikes with amplitudes that ranged from 1800 to 3600 psi. Large structural response experiments and ground motion phenomenology experiments generally are not sensitive to these high-frequency spikes, and therefore can be adequately tested with a HEST environment. The HEST waveform also contains several oscillatory signals between 500 and 5000 Hz that are not represented in the ideal nuclear waveform. Caution must be exercised when using HEST techniques on model structures where the characteristic frequency of higher order failure modes may approach these nonsimulation oscillatory levels. In ground motion experiments, the upper few feet of soil usually filters out the high-frequency oscillations, permitting a much better simulation of the predicted ideal nuclear waveform.

Figure 7 shows a comparison between the ground motion produced by the cratering effects of a nuclear event and the MINE THROW simulation technique. The JOHNNY BOY experiment was a 0.5-kT nuclear detonation at a 1.92-ft depth of burial. The MINE THROW I event was a buried stack of ANFO explosive that resembled a thick bowl configuration. The MINE THROW concept does not attempt to simulate the airblast, and therefore does not provide the initial airblast-induced motion in the JOHNNY BOY waveform. The direct-induced, crater-related, and late-time ground roll seem to be very similar to those of the nuclear event.

NEED FOR HIGH FIDELITY

Having reviewed some of the past history and compared the nuclear events with some of the simulated waveforms, the question remains as to what is the specific need for high-fidelity simulation experiments. Although the final answer to the question can only be evaluated with respect to the specific application and structural response problems under study, the following collection of observations are general to many applications. We will consider the applications in two very different categories: offense and defense.

In offense applications, we have complete knowledge of our weapon systems (yield, HOB, etc.) but have incomplete knowledge of the target systems. Although we may know the gross details of structures, we seldom know specific details such as the surrounding geology, percentage of reinforcing steel, strengths of structural materials, or amount of shock isolation on critical equipment. The target uncertainties therefore dominate the target response problems. The targeteer

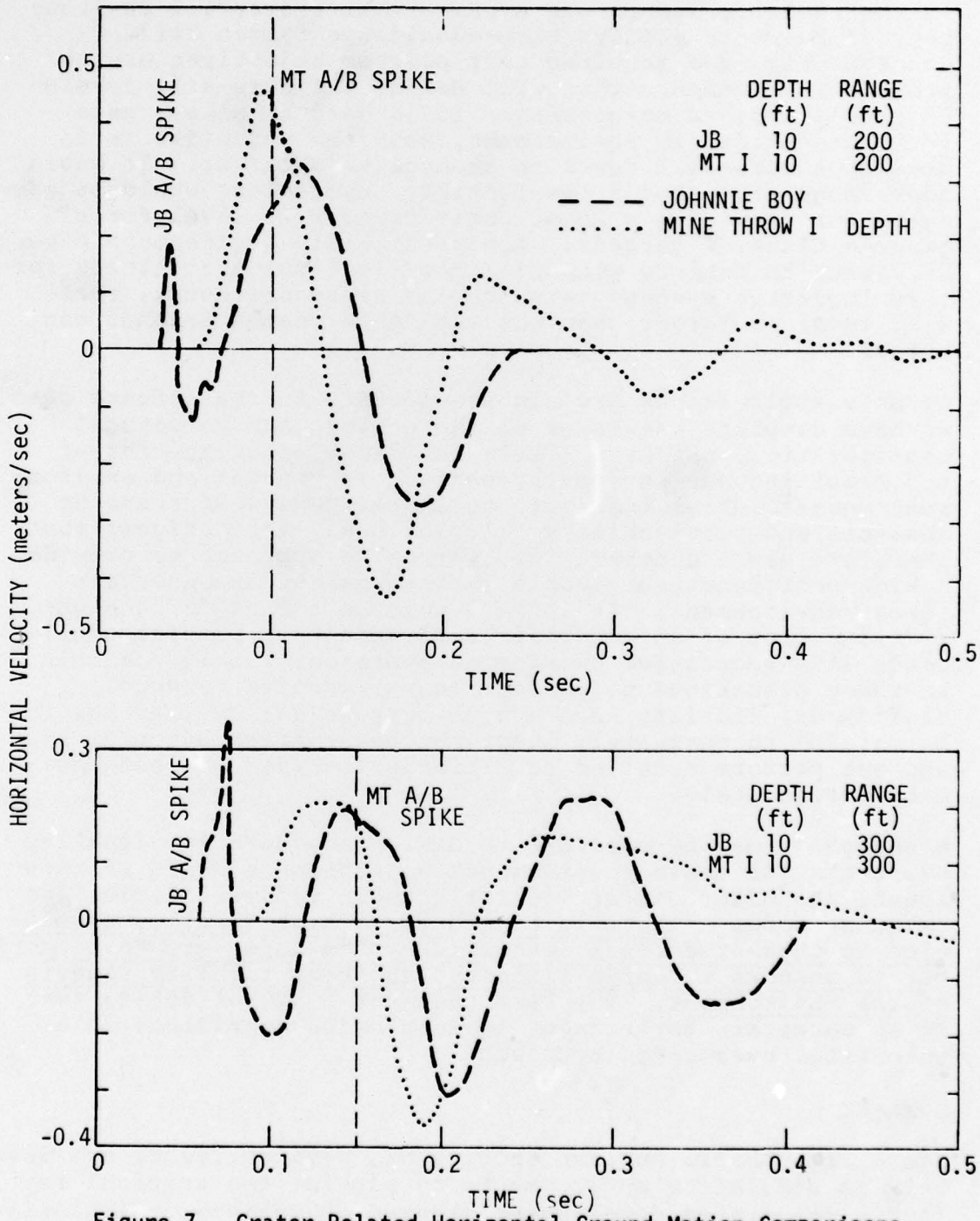

Figure 7. Crater-Related Horizontal Ground Motion Comparisons between JOHNNIE BOY and MINE THROW I DATA (Airblast Effects were not Simulated)

Reproduced from Physics International Report No. PIFR-365 Draft Final, April 1973 [7]

is therefore forced to use a conservative overkill environment if he is to achieve high-confidence target kill. Consequently, the required test program objectives are to provide environments that will define the sure-kill levels of poorly defined structures. It is hard to make a case for a high-fidelity environment, when the objective is to develop a sure-kill level on an uncertain target. It would seem in general that a low-fidelity environment would be adequate for providing a least upper bound kill level for a generic class of targets. A high-fidelity environment may be useful to explore potential low-level vulnerabilities for very important systems in which the high-confidence, sure-kill level is larger than the available weapon arsenal can afford.

Defense applications are almost opposite to the offense case. We have complete knowledge of the geology and structural configuration, but have little knowledge about the threat and resulting nuclear environments. The threat and environment uncertainties therefore dominate the system response analysis and survivability calculations. The designer must therefore use a conservative overdesign approach to provide a high-confidence survivable system against an uncertain threat environment. It is hard to make a case for a high-fidelity test of an uncertain environment to provide confidence in a successful overdesign approach. It is possible in these situations to perform cost tradeoffs between confidence, fidelity, and system overdesign; but one has to be careful to adequately treat the environment uncertainties, and not perform detailed cost tradeoffs based on best-estimate design goals.

Although it may be possible to design adequate low-fidelity overtests for those environments and response modes we know about, the major concern is for unknown vulnerabilities and response modes. There is a need for a high-fidelity simulation to check the final defensive system to insure that there are no unknown vulnerabilities to the high-fidelity aspects of the environment. The best case for a high-fidelity test of an uncertain environment is to provide confidence in a successful overdesign approach.

SUMMARY

Since atmospheric nuclear testing has been outlawed, one must rely on simulation environments to provide the critical test levels for system development program objectives. Simulation testing is therefore a fallback position, and the question is "how much fidelity in simulating the actual nuclear environment is necessary?"

The question of required simulation fidelity is not an easy one to answer. Just to say simulation implies that we know the environment well enough to define the simulation goals, and believe that we can measure and provide an environment which meets these goals. There are, however, large uncertainties in predicting the nuclear environments to be simulated. These large uncertainties may imply that almost any environment close to the design goals may be realistically considered as a possible nuclear occurrence. It seems clear that to attempt to provide a high-fidelity approximation to someone's best estimate of a very uncertain environment is not a sound program objective. It may be more desirable to bound the environment and provide a clear overtest to insure a system survivability (or system vulnerability for offense application). Such a test may be of lower fidelity but of higher confidence.

High-fidelity simulations are generally much more costly and require several calibration events to insure that the full system tests will meet the design test objectives. Low-fidelity overtests are generally less expensive and require less proof of capability prior to full-scale testing. One cannot neglect questions about scaling and nonsimulation response in selecting the more desirable fidelity for implementing a test program. Nor is it possible to ignore the ability to design and implement a test program before establishing the fidelity objectives. Whether for high- or low-fidelity objectives, a test environment must be predictable, reproducible, and measurable, consistent with good experimental practices.

The need for high-fidelity experiments depends strongly on how well we know the environment and the system response to the environment. When we know both the environment and response, then both high- and low-fidelity experiments can be designed and suitable cost tradeoff studies performed. When we know the environment but do not understand the system response, it is mandatory that we have a high-fidelity test environment. Otherwise, we would not be able to evaluate the deficiencies in a low-fidelity test program.

The most common case is when the environment is not known accurately, and we are trying to develop an understanding of the system response. The less we understand of the system, the more we desire a fidelity simulation; but the less we understand of the environment, the more difficult it is to assure a high-fidelity simulation. In many cases, it would be more desirable to channel resources into performing several low-fidelity experiments that emphasize different aspects of the environment, than it would to perform only one or two higher fidelity simulations of very uncertain environments.

In the past, DNA has funded several large-scale simulation tests for application on Minuteman, Hard Rock Silo, Minuteman Upgrade, several MX concepts, submarines, vehicles, tanks, and various military equipment. In many cases, the tests were advertised as high-fidelity simulations when in fact we learned more about the environment than we did about the system response. Many of the environment prediction techniques have changed over the years since the tests, which means the interpretation of the test results has changed from a high-fidelity to a low-fidelity application. Our understanding of the critical system response has also changed over the years, and some of the high-fidelity environments were not necessarily addressing the weakest links in the system design.

The data from large-scale system tests provide unique information that probably will never be repeated, and thus form the primary data base for estimating the response for upgraded as well as new and proposed system response. Since the test data are being extrapolated to regions beyond those considered in designing the original test program, the extrapolation is normally considered of low fidelity. Such low-fidelity extrapolations have, however, been one of the most useful results of many of our past large-scale test programs.

It seems clear that the pretest planning rationale has to seriously consider many issues before establishing the best fidelity for proposed test environments. Long-range considerations as well as immediate test objectives must be weighed before optimum decisions can be made. Stimulation versus simulation should therefore be a central issue of future DNA test program planning.

REFERENCES

1. D. C. Sachs, L. M. Swift, and F. M. Sauer, Operation TEAPOT Project 1.10--Airblast Overpressure and Dynamic Pressure Over Various Surfaces, Report No. WT1109, February 1955.

2. H. L. Brode, The Height-of-Burst Effects at High Overpressures, The Rand Corporation, DASA2506, July 1970.

3. F. M. Sauer and C. T. Vincent, FERRIS WHEEL Series FLATTOP Event Project 1.2A.3A--Earth Motion and Pressure History, Stanford Research Institute, POR3002 (WT-3002), 1967.

4. Private Communication with Mr. Steve Melzer of Air Force Weapons Laboratory, Albuquerque, New Mexico, November 1978.

5. J. Carpenter and H. Brode, "Height of Burst at High Overpressures," presented at Proceedings of Fourth International Symposium on Military Applications of Blast Simulation, 9-12 September 1974.

6. J. D. Shinn, HARDPAN I-3, Corrected Free Field Data, Appendix G, Air Force Weapons Laboratory, Technical Note No. DE-TN-76-013, September 1976.

7. D. Maxwell, J. Reaugh, and B. Gerber, JOHNNY BOY Crater Calculations, Physical International, Report No. PIFR-365, April 1973.

INSTRUMENTATION SESSION

PRECEDING PAGE BLANK-NOT FILMED

HE BLAST PRESSURE MEASUREMENTS

by

David J. Ray, Capt., USAF

Air Force Weapons Laboratory

HE Blast Pressure Measurements

by

Capt David J. Ray
Air Force Weapons Laboratory
Kirtland AFB NM

INTRODUCTION

The Air Force Weapons Laboratory, under sponsorship of DNA and SAMSO, through its in-house resources and its contract with the University of New Mexico Civil Engineering Research Facility, is developing methods of simulating nuclear blast and shock effects with high explosives. Two of the methods used are the High Explosive Simulation Test (HEST) and the Dynamic Airblast Simulator (DABS) test.

The measurement of transient pressure pulses in the range of 1 MPa to 138 MPa is typically required for these high explosive simulations carried on at AFWL and CERF.

THE NATURE OF THE PRESSURE TIME HISTORY

The transient pressure pulse in a nominal 5 MPa HEST resembles Figure 1, based on AFWL/CERF experience. This time history should be closely observed for several features. Figure 1 is an 80 ms plot. The initial peak appears to reach 15 MPa, but in actuality, was greater as the channel bandedge was 15 MPa. Therefore, the initial peak was three times or more the nominal 5 MPa effective cavity pressure. The rise time of the initial peak appears to be about 200 μsec, but the pressure rise was probably faster since the transducer was shielded from the direct blast effects. This rise time corresponds to a bandwidth of 1750 Hz.

Figure 2 is the 200 msec plot. The late time history of the pressure pulse must satisfy the boundary condition that the pressure returns to atmospheric pressure. If the correct final boundary conditions are met, the impulse should attain a final constant value. The pressure time history of Figure 2 appears to fail this test for validity, at least in this first 200 msec.

A known zero initial boundary conditions may also be used to evaluate transducer performance. Figure 3 gives a pressure time

history which fails to meet the initial condition due to light sensitivity of the transducer. This is a measurement from the HAVE HOST S-1 Event which was a large DABS facility.

THE PRESSURE-SENSING SCHEME

The transduction scheme typically used by AFWL/CERF for pressure measurements in HE events is the piezoresistive bridge diffused onto an edge-clamped disc of silicon. The pressure sensors are in steel mounts imbedded in concrete cylinders located in the floor of the HEST cavity, and the sensing surface is flush with the cavity floor.

For the DABS events the transducers are imbedded in concrete on surface-flush mounts or on concrete structures and sometimes on blast wings as in Figure 4. The gages on the wings may be mounted on the sides of the probes for incident overpressure or in the probe tips for stagnation pressure.

Suitable piezoresistive transducers are produced by Kulite Semiconductor Products, Inc., and ENDEVCO. Evaluations of the ENDEVCO 8511 series by AFWL/CERF are now scheduled with the objective of determining if it will perform as well as or better than the Kulite in a HEST environment. Figure 5 is a section view of a typical pressure transducer as is available from Kulite.

SOME PROBLEMS WITH PRESSURE TRANSDUCERS IN BLAST ENVIRONMENTS

One problem encountered in edge-clamped silicon discs is the resonance of the brittle disc which may crack if excited. Further, the resistance of the semiconductor bridge elements is quite temperature sensitive and, as mentioned earlier, light sensitive. Both the Kulite and the ENDEVCO transducers use a layer of GE TBS 758 silastic to protect the silicon diaphragm from temperature changes.

In Figure 3 the rounding of the trace just before shock arrival was determined to be the sensitivity of the piezoresistive transducer to the light radiation from the burning explosive-air interface. Interestingly, the transducer silicon sensing disc was covered with about 1 millimeter of silastic and still indicated sensitivity to the light from the burning interface. This led to the introduction of a line of pressure transducers by manufacturers which included a "photon barrier" on the sensing disc. This barrier is very thin and adds no significant mass to the disc but does shield the sensing elements from the offending light energy.

Experience at AFWL and CERF has shown that the further addition of materials such as RTV's silastics, and aluminum foil in front of the pressure-sensing surface may alter the response of such pressure transducers and may even cause failures at lower than rated pressure. Figure 6 is a shock tube test of a Kulite transducer with an additional layer of RTV (1 mm) and aluminum foil over that applied by Kulite. The overshoot is visible at about three times the pressure level seen after the gage oscillations have damped out. Figure 7 shows the overshoot with two layers of 1 mm RTV and a piece of aluminum foil. Again, the overshoot is about three times the late time pressure. Also, the resonant frequency has been lowered. AFWL concluded that additional silastics used to prevent drift due to temperature or light effects may cause gage failure when used in a HEST or DABS environment.

The construction materials used in HEST pressure cavities are varied and have, in the past, included metal rings, plywood, nails, screws and styrofoam. At detonation, these materials are propelled at high speed throughout the cavity. The potential damage to instrumentation from flying metal and wood is obvious, but burning pieces of styrofoam can also cause instrumentation problems. In order to protect the pressure gages, two shield schemes are used by AFWL and CERF. The blast diffusion plate (carport) and the debris shield are the two arrangements typically used. Figure 8 is the AFWL "carport." It is a 3/8-inch steel plate with a hole pattern drilled into it and mounted over the pressure transducer on 1-1/4 inch spacers. This plate also has the effect of slowing the rise time of the pressure spikes seen by the gage. The exact amount of rise time slow-down is not known, but test experience seems to indicate a slow-down of about 20 μsec. This would have the effect of lowering the initial peaks and enhancing gage survival.

Figure 9 is a side view of the AFWL debris shield. This shield was originally developed for head-on pressure measurements in the debris-laden DABS blast flow environment. It is a small cap with holes, as shown in Figure 10. It threads directly over the pressure gage with a 0.039-inch gap between the center of the shield and the surface of the pressure gage. Figure 11 is a photo of a shock tube test on a Kulite pressure transducer with the AFWL Mod VIII debris shield. The upper trace has the debris shield and shows a rise time slow-down of about 10 μsec.

An extensive shock tube investigation of debris shields was done by CERF at AFWL's request. This investigation used tested a cap with eight holes (Figure 12). During the test series, the eight holes were progressively enlarged and also tested with various spacing between the cap and the sensor face. Reference 1 gives the complete test results and CERF evaluation. The resultant eight-hole shields have been given numbers which correlate to their test number in the original investigation; therefore, eight-hole debris shield #10 is the configuration used in Test #10 of the attached original CERF report. Figures 13 and 14 give the test results for two of the more popular configurations; they are the #10 and #18 eight-hole debris shields. The #10 shield has a rise time of about 20 μsec, while the #18 rise time is about 150 μsec.

GAGE PLACEMENT IN THE TEST BED

The AFWL and CERF placement of pressure gages in HEST test beds has been guided in the past on the intuitive feeling that, by spreading the explosive cords at the positions of the pressure gages, maximum distance from the gage to the cords could be obtained, thereby increasing the survivability of the transducers. This is now felt to be in considerable error in that CERF calculations of pressure levels near multiple line explosive sources show an enhancement of the pressure midway between two such line sources of pressure. According to these CERF calculations, the position of minimum initial pressure is directly under the explosive cord, as shown in Figure 15.

Some test evidence of pressure enhancement has been seen on open detonating cord tests. Figure 16 shows the result of such a test and indicates a region of high pressure between the explosive cord as evidenced by the plate indentation.

CONCLUSION

A review of these experiences indicates that, for HE simulations, instrumentation survival cannot be left to chance or intuition. The fundamental problem in ensuring survivability is satisfying the sometimes mutually-exclusive conditions of choosing maximum gage range to ensure survivability during high initial spikes and minimum gage range to obtain the best signal-to-noise ratio in the data amplitudes for the resolution required for the particular test.

The following rules guide the AFWL in pressure measurements in HEST and DABS events and are current AFWL practice.

1. No silastics, RTV's, or other materials should be placed in contact with transducer face. The face should be left as it comes from the manufacturer with only the manufacturer's material covering the silicon sensing disc.

2. The initial detonation pressure peaks in the HEST depend on the location with respect to the explosive cord, but can be counted on to be greater than three times the effective cavity pressure. Therefore, gage ranges must be selected accordingly.

3. The Kulite HKS-375 series transducers have a history of suriving in HE events. The ENDEVCO 8511 transducers are new and after suitable evaluation may also be included in HE events in order to gather data as to their survivability and performance in such environments.

4. The AFWL carport should be used whenever possible to diffuse early-time spikes and to protect from flying debris in the HEST cavity. Carports should not be used in DABS events.

5. The AFWL Mod VIII or CERF eight-hole debris shield should be used to slow the rise time and further protect from flying debris.

6. The most successful combination for HEST pressure measurements in the AFWL's experience has been both the carport and the debris shield.

7. The pressure gages should be placed directly under the explosive cord and should not be placed symmetrically between two cords or at a constant radius from three or more equally spaced cords. As much distance as possible should separate the cord from the gage.

References

1. DE-TN-78-006, Evaluation of "Eight-Hole" Debris Shields for HEST Applications, D. Palmer.

2. DED-TN-78-010, Blast Pressure Measurements at the Air Force Weapons Labratory Civil Engineering Research Division 1968-1978, J. Quintana.

3. AFWL-TR-73-203, Air Pressure Transducer Evaluation, C. Nobel.

4. AFWL-TR-77-6, Dynamic Airblast Simulator (DABS) Instrumentation Development - Phase 1, N. Baum.

5. NBS Technical Note 961, Experimental Investigation of Means for Reducing the Response of Pressure Transducers to Thermal Transients, Hilten, Vezzetti, Mayo-Wells and Lederer.

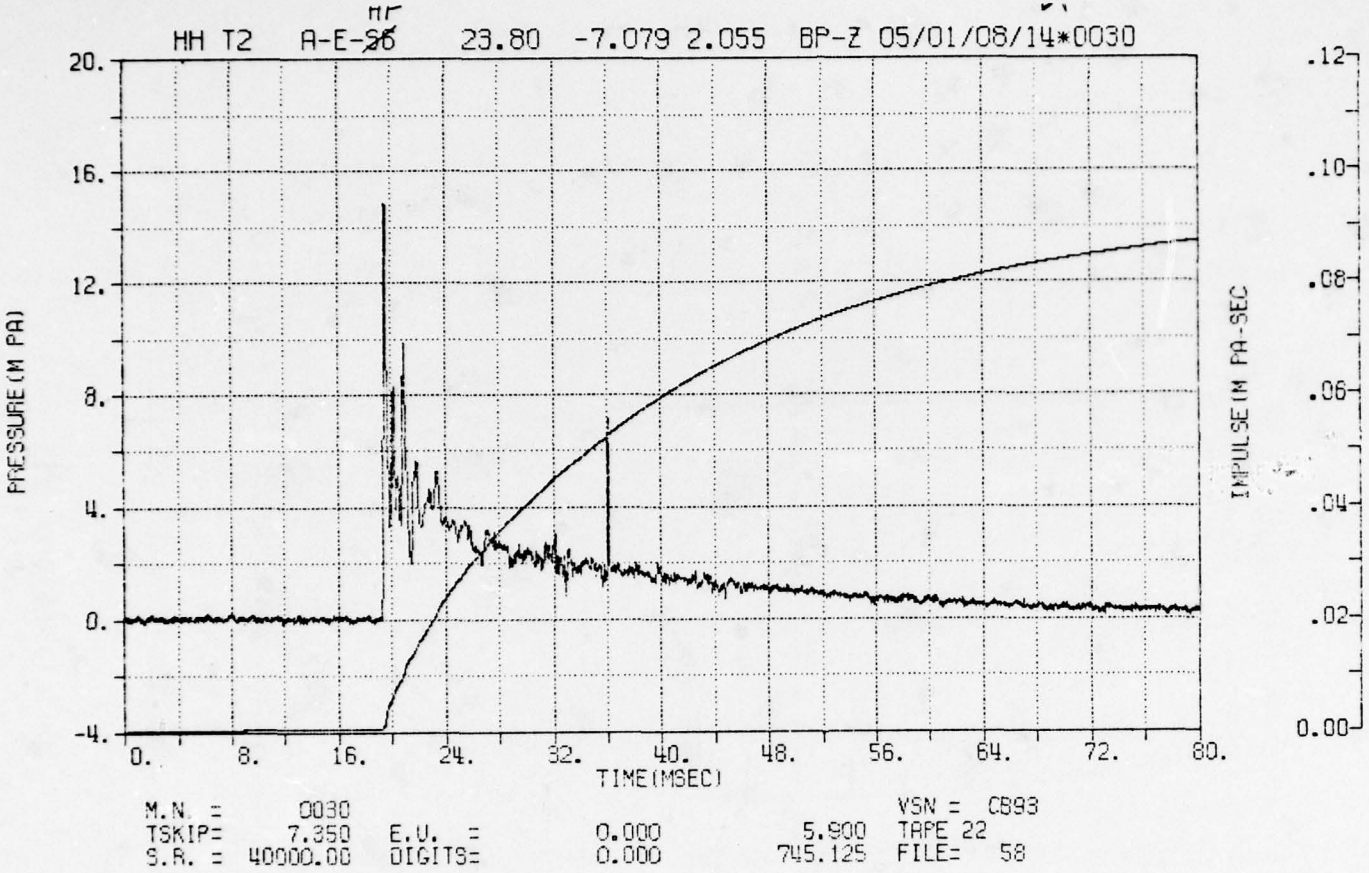
HH T2 A-E-26 23.80 -7.079 2.055 BP-Z 05/01/08/14*0030
PRESSURE(M PA)
IMPULSE(M PA-SEC)
TIME(MSEC)
20.
16.
12.
8.
4.
0.
-4.
.12
.10
.08
.06
.04
.02
0.00
0. 8. 16. 24. 32. 40. 48. 56. 64. 72. 80.
M.N. = 0030
TSKIP= 7.350
S.R. = 40000.00
E.U. =
DIGITS=
0.000
0.000
5.900
745.125
VSN = C893
TAPE 22
FILE= 58

FIGURE 1

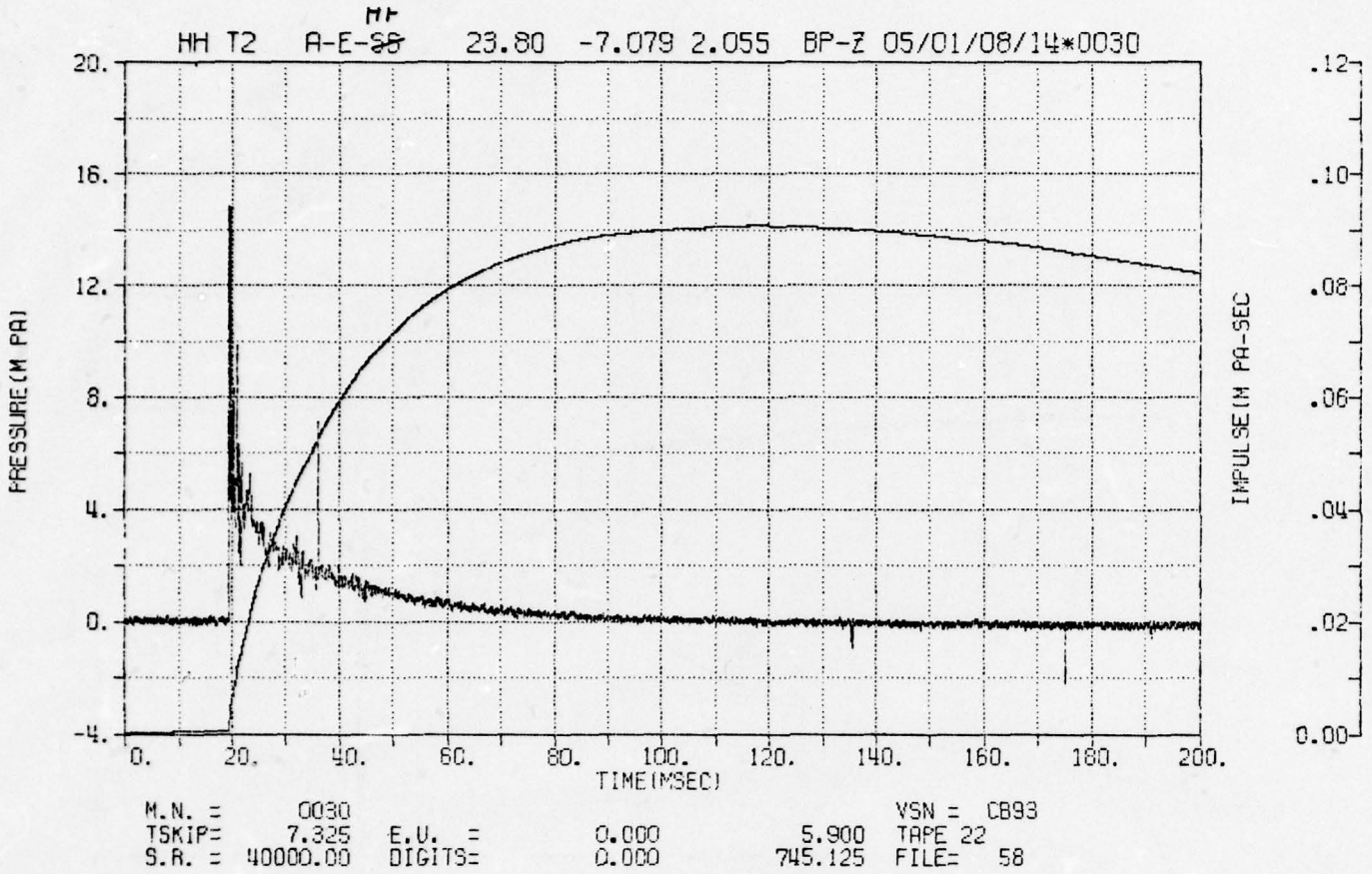
HH T2 A-E-MF 23.80 -7.079 2.055 BP-Z 05/01/08/14*0030
PRESSURE(M PA)
IMPULSE(M PA-SEC)
TIME(MSEC)
20.
16.
12.
8.
4.
0.
-4.
.12
.10
.08
.06
.04
.02
0.00
0.
20.
40.
60.
80.
100.
120.
140.
160.
180.
200.
M.N. = 0030
TSKIP= 7.325
S.R. = 40000.00
E.U. =
DIGITS=
0.000
0.000
5.900
745.125
VSN = CB93
TAPE 22
FILE= 58

FIGURE 2

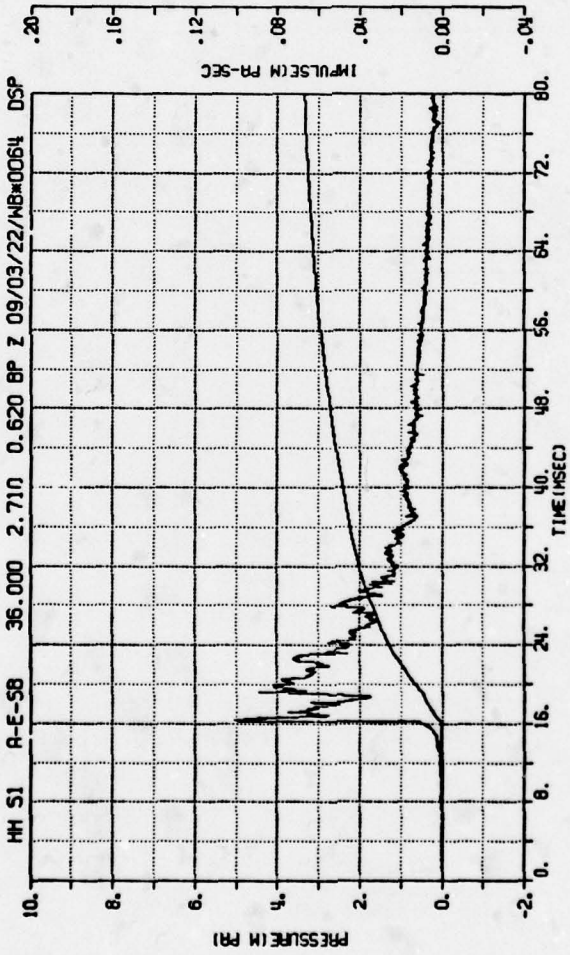
HH 51 A-E-SB 36.000 2.710 0.620 BP Z 09/03/22/NB=0064 DSP
PRESSURE(M PA)
IMPULSE(M PA-SEC
TIME(MSEC)
10.
8.
6.
4.
2.
0.
-2.
.20
.16
.12
.08
.04
0.00
-.04
0.
8.
16.
24.
32.
40.
48.
56.
64.
72.
80.

FIGURE 3

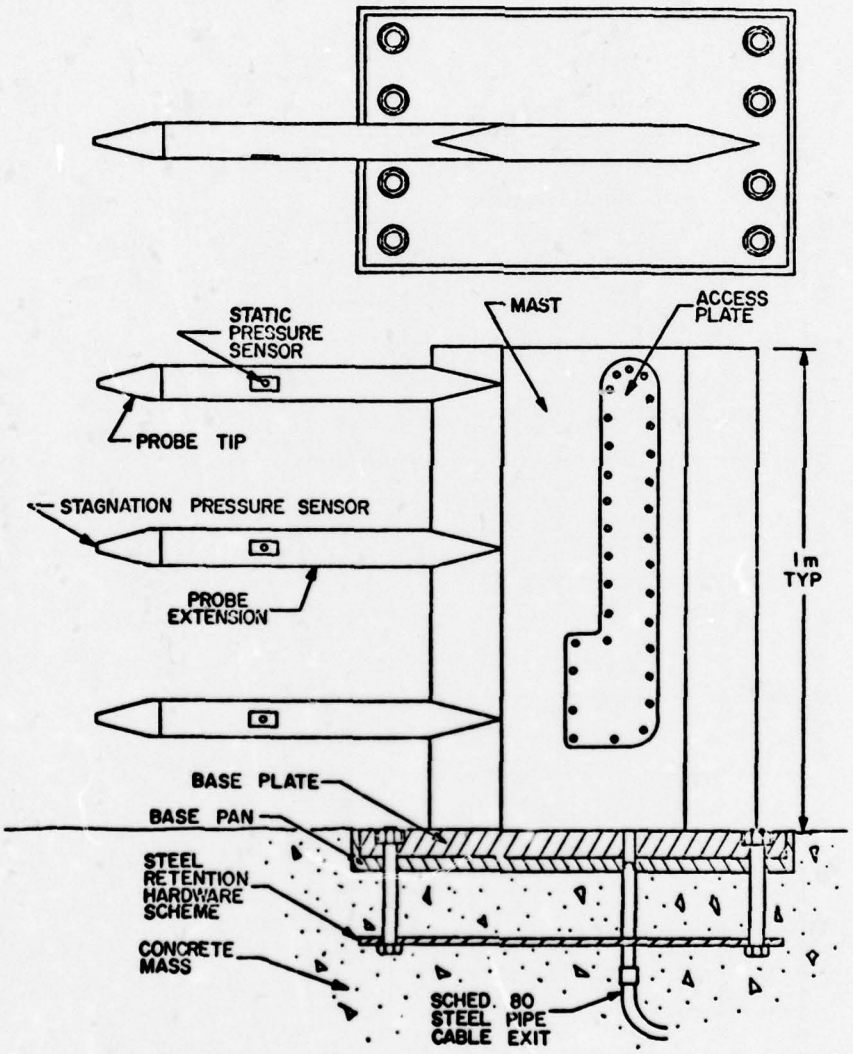
STATIC
PRESSURE
SENSOR
MAST
ACCESS
PLATE
PROBE TIP
STAGNATION PRESSURE SENSOR
PROBE
EXTENSION
1m
TYP
BASE PLATE
BASE PAN
STEEL
RETENTION
HARDWARE
SCHEME
CONCRETE
MASS
SCHED. 80
STEEL PIPE
CABLE EXIT

FIGURE 4

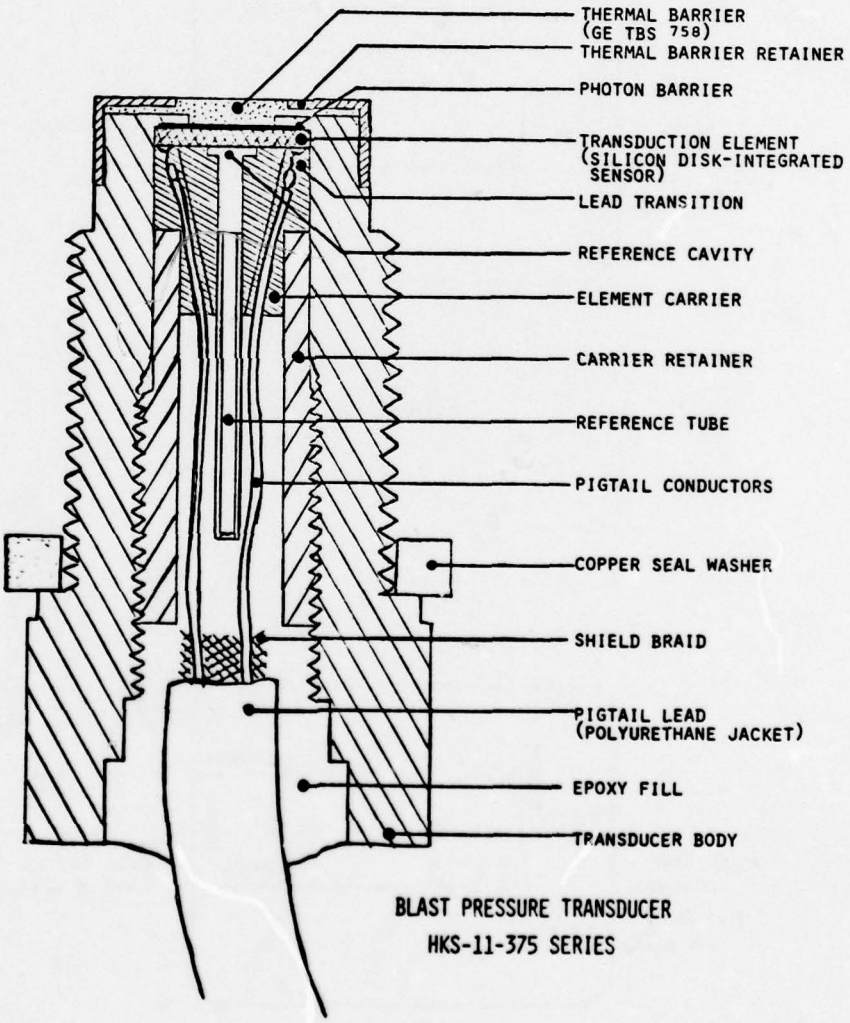
THERMAL BARRIER
(GE TBS 758)
THERMAL BARRIER RETAINER
PHOTON BARRIER
TRANSDUCTION ELEMENT
(SILICON DISK-INTEGRATED
SENSOR)
LEAD TRANSITION
REFERENCE CAVITY
ELEMENT CARRIER
CARRIER RETAINER
REFERENCE TUBE
PIGTAIL CONDUCTORS
COPPER SEAL WASHER
SHIELD BRAID
PIGTAIL LEAD
(POLYURETHANE JACKET)
EPOXY FILL
TRANSDUCER BODY
BLAST PRESSURE TRANSDUCER
HKS-11-375 SERIES

FIGURE 5

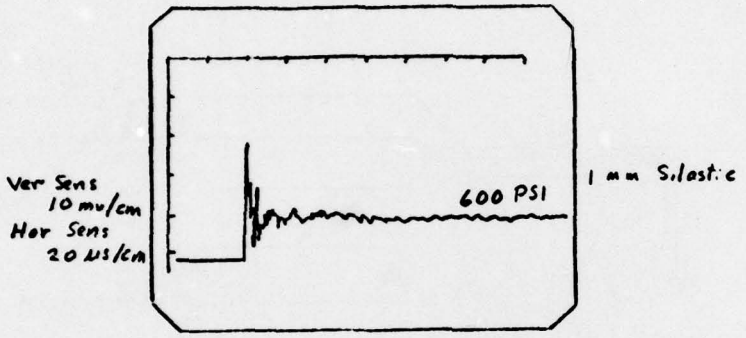

FIGURE 6

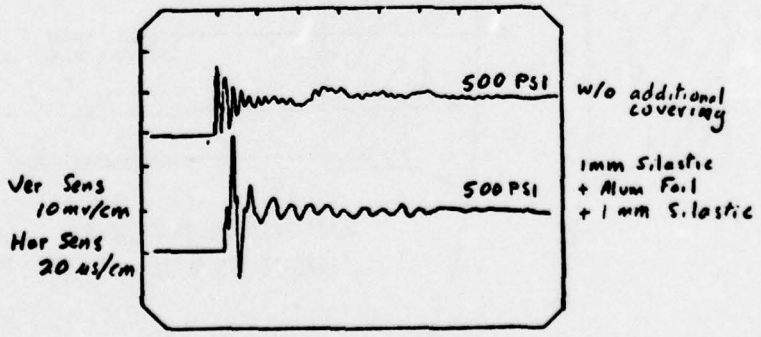

FIGURE 7

HEST CAVITY
BLAST PRESSURE MEASUREMENT
CARPORT SCHEME

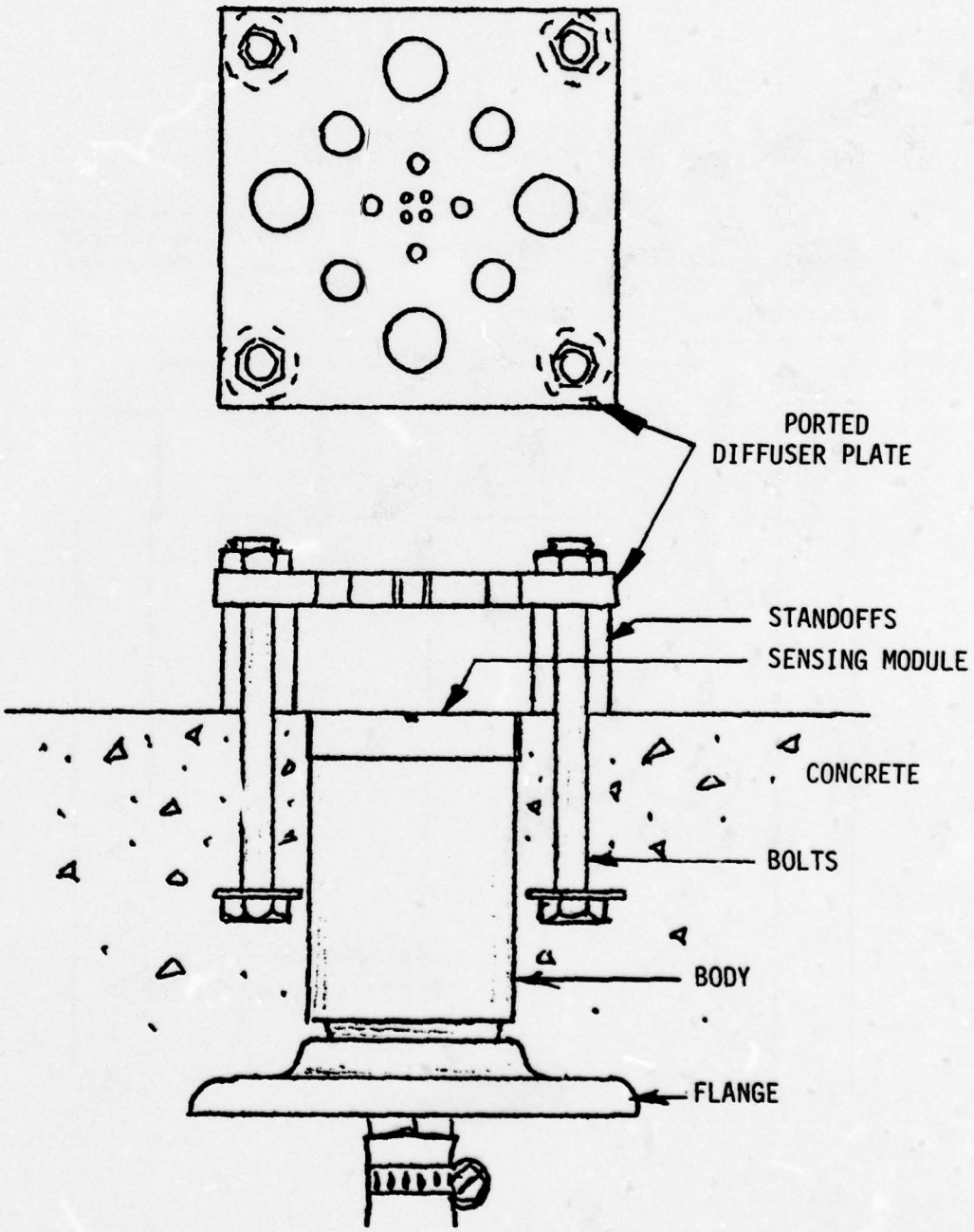

FIGURE 8

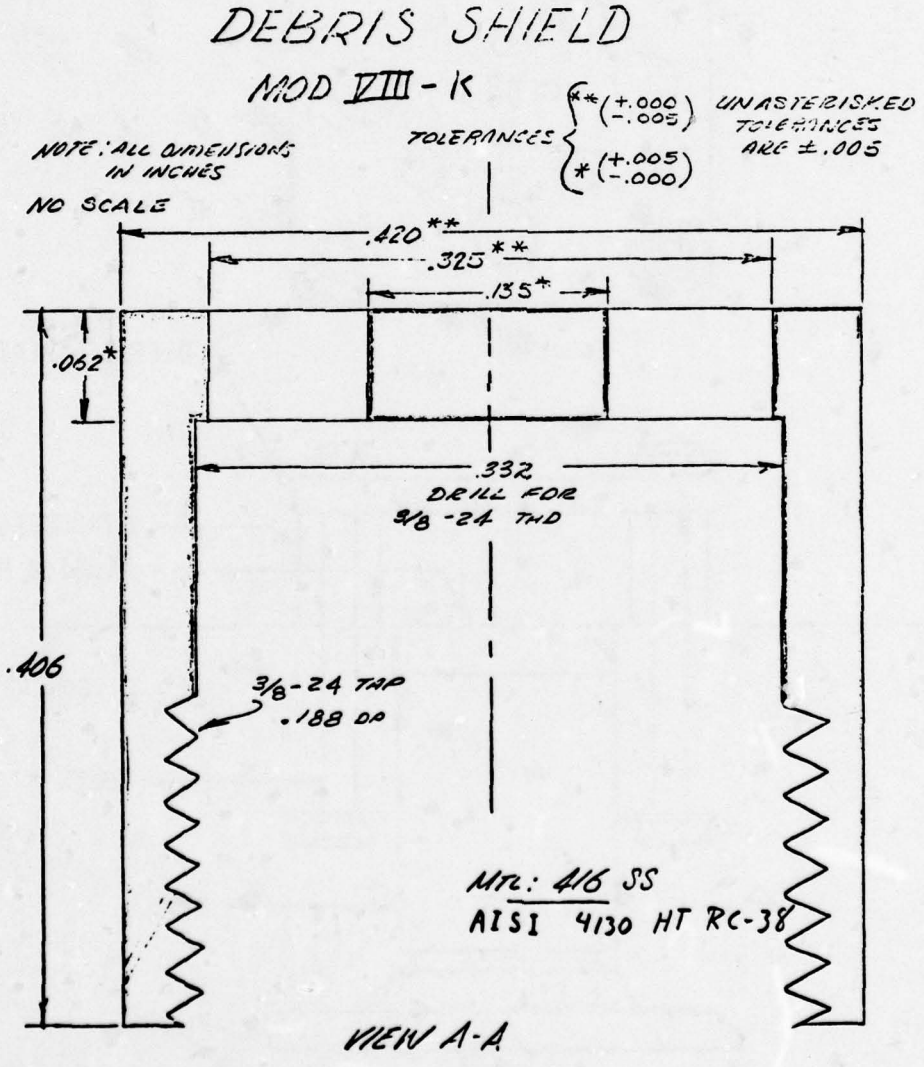
DEBRIS SHIELD
MOD VIII - K
NOTE: ALL DIMENSIONS IN INCHES
NO SCALE
TOLERANCES
** (+.000 -.005)
* (+.005 -.000)
UNASTERISKED TOLERANCES ARE ±.005
.420**
.325**
.135*
.062*
.332
DRILL FOR 9/8 -24 THD
.406
3/8-24 TAP .188 DP
MTL: 416 SS
AISI 4130 HT RC-38
VIEW A-A

FIGURE 9

DEBRIS SHIELD

MOD VIII - K

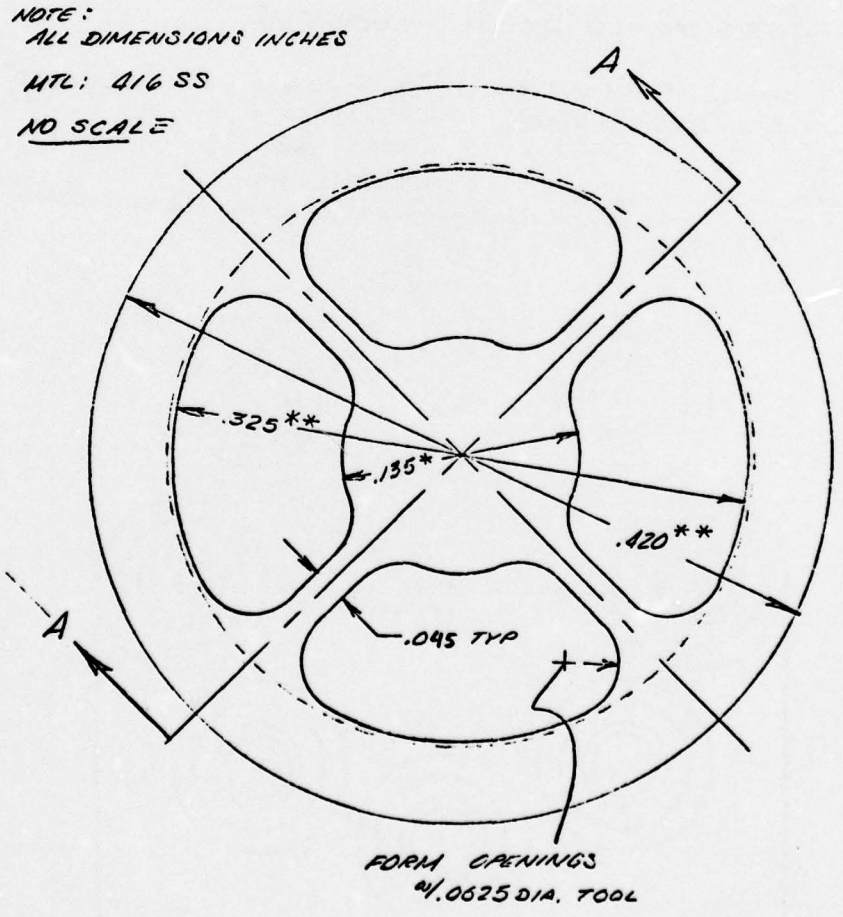

FIGURE 10

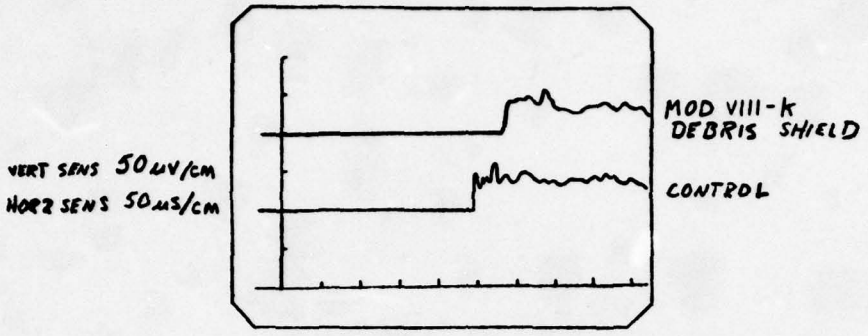

FIGURE 11

DEBRIS SHIELD DRILLING SEQUENCE

STEP
1 - DRILL 8 HOLES 0.0274" DIAM ON A HOLE CIRCLE 0.2225" DIAM.
2 - ENLARGE 8 HOLES TO 0.03875" DIAM.
3 - " " " " 0.0548" DIAM.
4 - " " " " 0.0775" DIAM.

NOTE: ALL DIMENSIONS NOMINAL, TOLERANCE ±0.001"

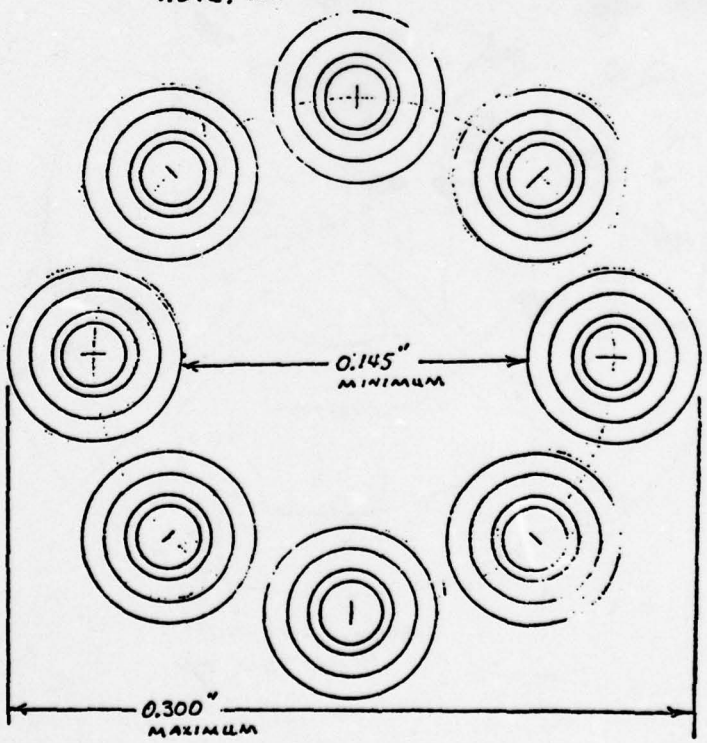

FIGURE 12

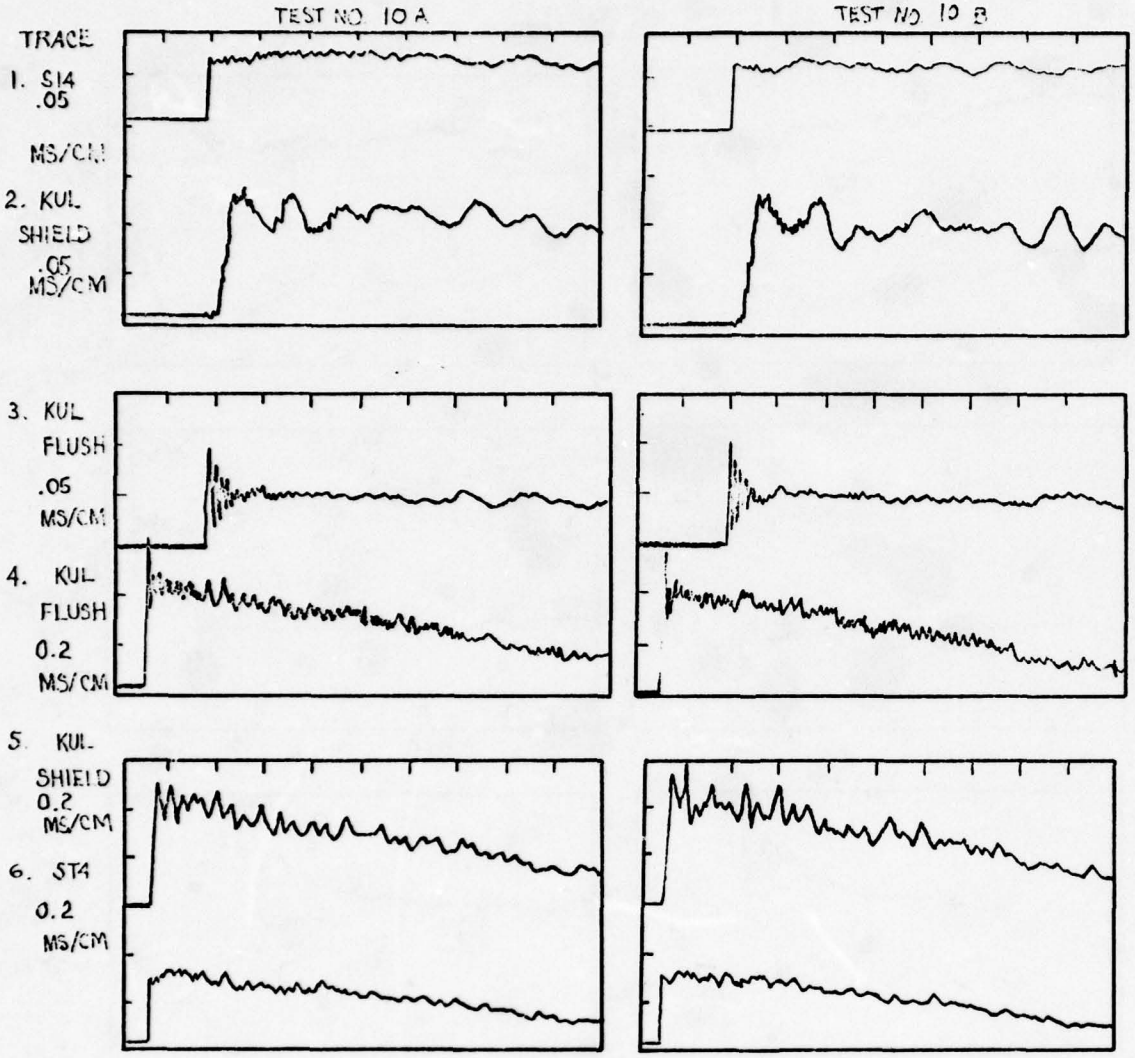
TEST NO 10 A
TEST NO 10 B
TRACE
1. S14
.05
MS/CM
2. KUL
SHIELD
.05
MS/CM
3. KUL
FLUSH
.05
MS/CM
4. KUL
FLUSH
0.2
MS/CM
5. KUL
SHIELD
0.2
MS/CM
6. ST4
0.2
MS/CM

FIGURE 13

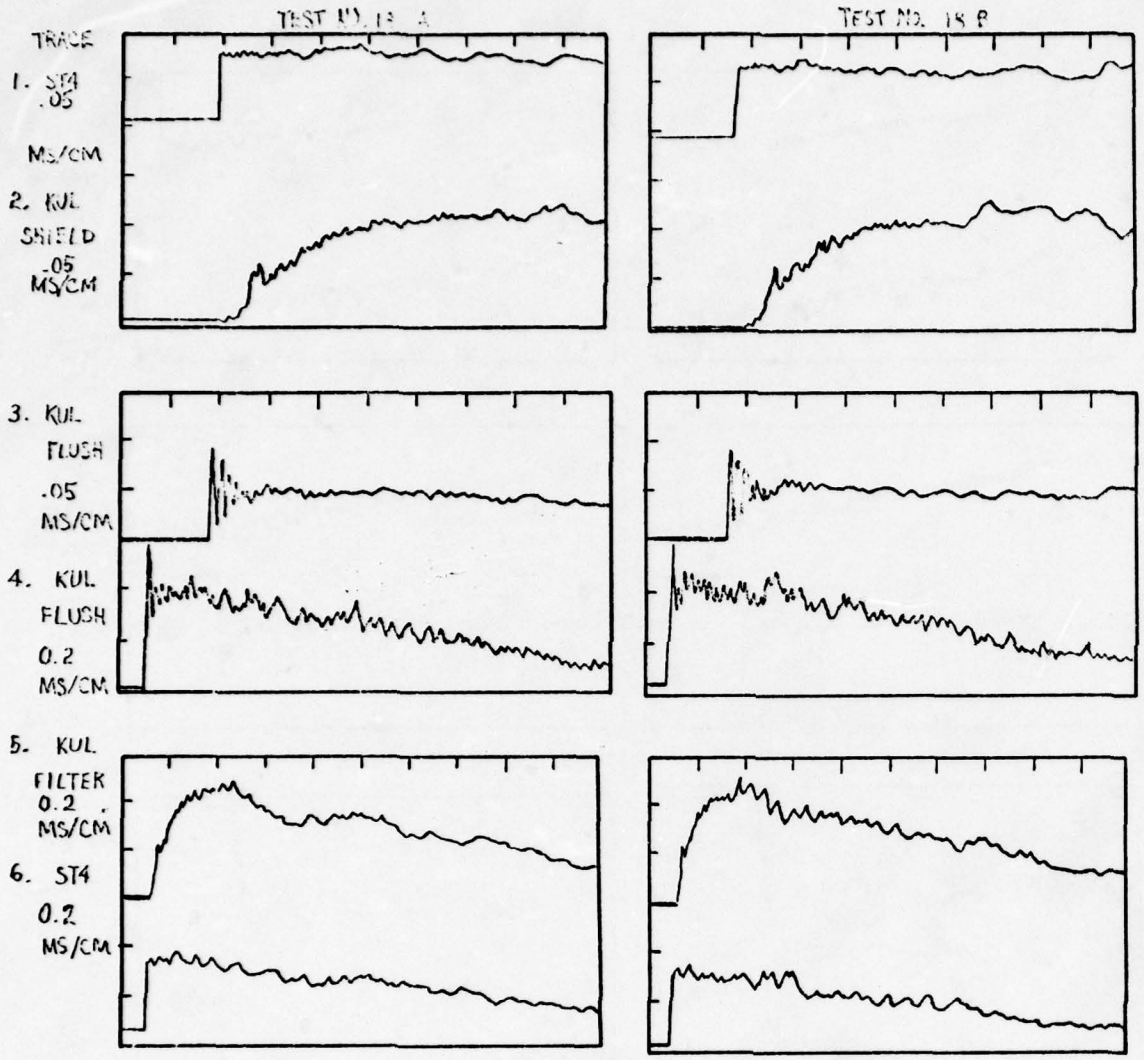
TEST NO. 15 A
TEST NO. 15 P
TRACE
1. ST4
.05
MS/CM
2. KUL
SHIELD
.05
MS/CM
3. KUL
FLUSH
.05
MS/CM
4. KUL
FLUSH
0.2
MS/CM
5. KUL
FILTER
0.2
MS/CM
6. ST4
0.2
MS/CM

FIGURE 14

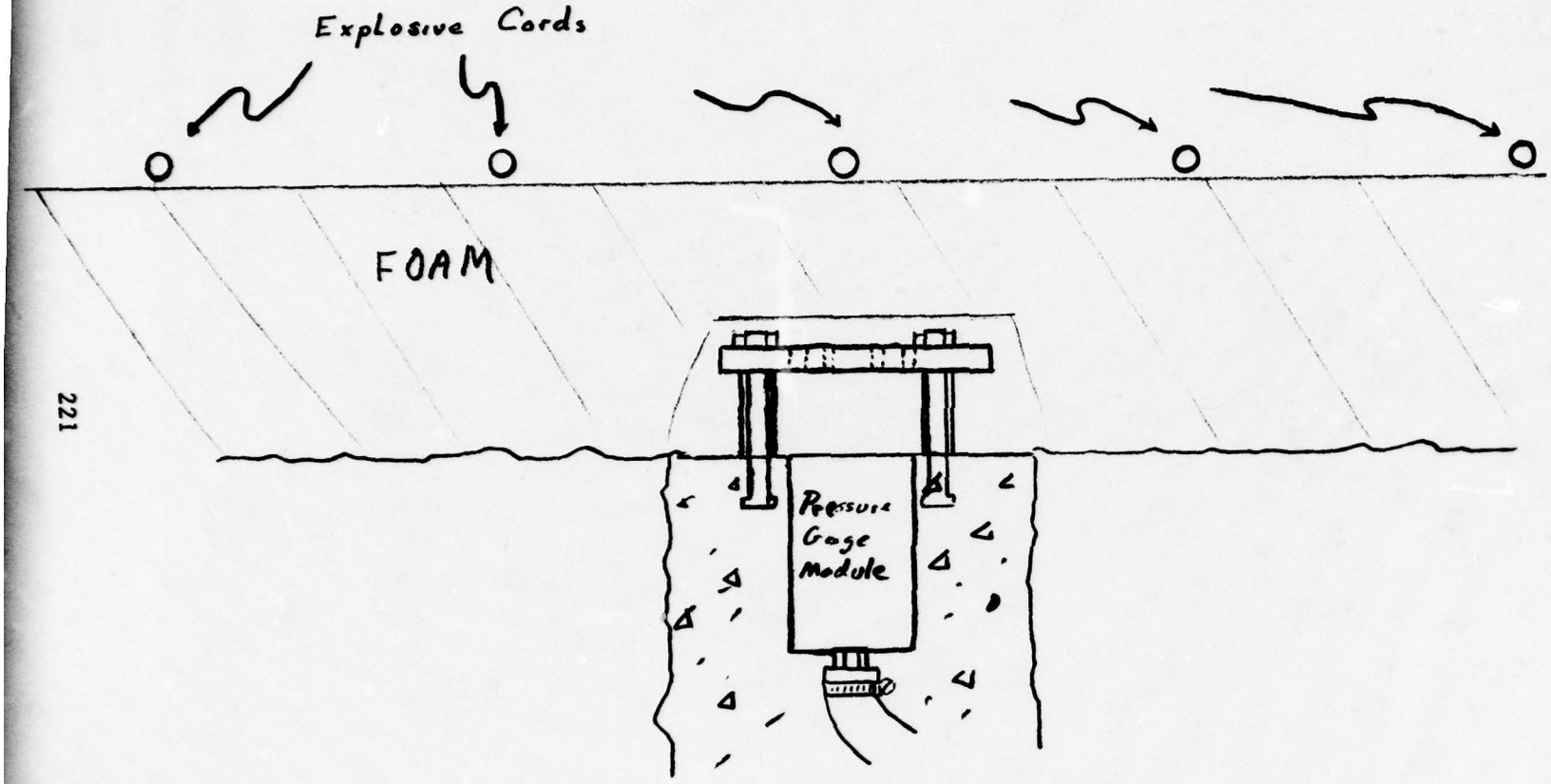

FIGURE 15

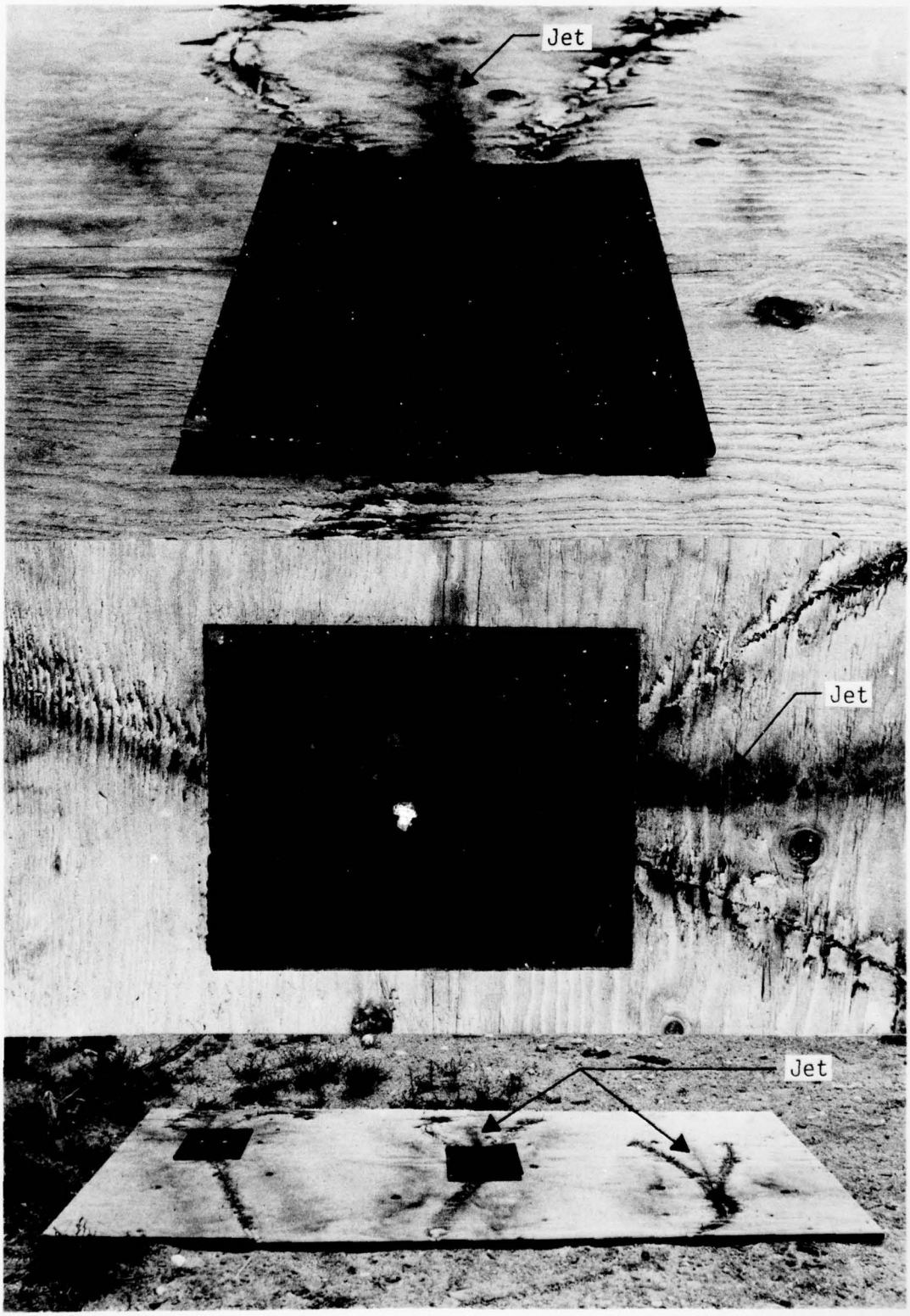

FIGURE 16

HIGH-ENERGY SIMULATION SESSION

MACH 130 AIR SHOCK ATTENUATION STUDIES

by

H.D. Glenn

H.R. Kratz

D.D. Keough

R.P. Swift

Lawrence Livermore Laboratory

MACH 130 AIR SHOCK ATTENUATION STUDIES*

H. David Glenn, Lawrence Livermore Laboratory
HOWARD R. KRATZ, Systems, Science & Software
DOUGLAS D. KEOUGH, SRI International
ROBERT P. SWIFT, Lawrence Livermore Laboratory

ABSTRACT

Voitenko compressors were used to generate ~ 4.5 cm/μsec air shocks in a steel and a grout outlet pipe. Diaphragm burst times and time-of-arrival data of shock-front luminosity along the 2-cm-i.d. exit pipes are provided by fiber-optic ports. Pressure profiles were obtained for this high enthalpy shock propagation for the first time and at many locations in both experiments. The Voitenko-grout experiment represents the first laboratory attempt to study shock propagation with this type of compressible wall material.

The primary purpose of these two experiments was to examine the effect of wall material on high-energy shock propagation. In the interval between 10- and 250-cm from the diaphragm the velocity and peak pressure of the shock front attenuated from ≈ 4.5 to 0.5 cm/μsec and ≈ 21 to ≈ 0.2 kb, respectively. Over this distance the shock propagation gave nearly identical results for both experiments within the range of experimental accuracy. This rapid attenuation of the shock front velocity and pressure is attributed to ablation and entrainment of wall material. An interesting feature that was observed, confirmed by multiple measurement techniques, was rapid oscillations of the pressure profiles. The results indicate that the shock propagation is independent of wall composition to the extent of materials considered over the 250-cm distance of the outlet pipes.

*Work performed under the auspices of the U.S. Department of Energy under contract No. W-7405-ENG-48; and DNA Subtask J24AAXIX955.

A primary threat to the MX vehicle in the buried trench basing mode is air shock propagation in the shallowly buried tunnel (Figure 1). Evaluation of this threat is based on numerical codes that simulate high-energy air shock propagation in open pipes.

For more than a decade experimental/theoretical studies have indicated that ablation and entrainment of wall material was the principal attenuation mechanism for high-velocity (> 1 cm/μsec) air shock propagation.[1-3] The above conclusion was primarily based on agreement between calculational predictions and experimental results for time-of-arrival (TOA) of the shock front at specific locations along open pipes containing air at ambient conditions. Improvements have been made[4,5] in the early[1] theoretical description of the ablation processes contained in these hydrodynamic codes. However, an expanded experimental data base is definitely needed to evaluate and/or improve the dynamic description of the ablation processes behind the shock front. For that purpose, a modified version[3,6] of the Voitenko compressor[7] was used to generate ~ 4.5 cm/μsec air shocks in a steel and a grout outlet pipe.

Figure 2 and Table 1 illustrate the experimental setup and diagnosti coverage used in the steel shock tube experiment. Details of the Voitenko compressor operation are given in reference 8 of this symposium proceedings.* Following diaphragm break the air shock propagates down an 0.02 m i.d. bore

*The diaphragm broke at a time of 58.1 μsec following detonation of the high-explosive.

for a distance of 6 m. Fiber optics located in the steel wall transmit luminosity associated with the air shock to two display boards that are scanned by streaking cameras. A framing camera focused on the first 0.20 m of outlet pipe indicated that no venting of gases occurred behind the shock front for > 40 μsec after the diaphragm broke. High explosive gases from the driver section obscured the field of view after this time. Pressure gages, at locations given in Table 1, provided pressure profiles and TOA information for the shock front. A summary of air-shock front TOA's for optical and electronic diagnostics, with respect to diaphragm burst time, is given in Table 2. These preliminary results indicate a close correlation for the various diagnostics data. Some of the pressure results will be presented below when comparisons with corresponding grout experimental results are shown.

Figure 3 and Table 3 show the experimental setup and diagnostic coverage used in the grout shock tube experiment. The Voitenko compressor and first 15-cm of the outlet pipe are identical with the steel experiment. Thus, experimental results for both experiments can be compared for similarity of flow conditions over the initial segments of the outlet pipes. The diaphragm broke at a time of 57.6 μsec following detonation of the high-explosive. This is a 0.5 μsec earlier than in the steel experiment and may be attributed to the slightly higher chamber pressure of 11 atmospheres compared to 10.66 atmospheres for the steel experiment. Following diaphragm break the air shock propagates down an 0.02 m i.d. bore for a distance of 3 m. The walls of the bore for the final ≈ 2.85 m are composed of DR-1 grout.[9] A summary of air-shock front TOA's for optical and electronic diagnostics, with respect to diaphragm burst time, is given in Table 4. Comparison indicates a very close correlation of the various diagnostics data.

A comparison of shock front TOA for both experiments are presented in Figure 4. These results indicate surprisingly similar propagation characteristics over the first 2.0 m with slightly greater attenuation seen between 2.0 and 2.5 m for the grout experiment.

A further confirmation of propagation similarities can be obtained by comparison of a few corresponding pressure profiles from bar gages. Figure 5 shows the pressure profiles at 0.10 m from the diaphragm.* Not only are the pressure peaks in relatively good agreement but the general shape appears reproducible for ≈ 20 μsec behind the shock front. Framing camera coverage of this area indicated a small amount of venting around the bar gage occurred at ≈ 25 μsec after diaphragm burst and continued until high explosive gases obscured the field of view approximately 20 μsec later. This may explain the reduction in the pressure profile at later times for the grout experiment. However, at the time venting is first detected the shock front has reached ≈ 0.80 m and consequently venting can expect to have little effect on conditions in and for some distance behind the front. The main purpose of this comparison is to illustrate the very similar initial conditions of the flow for both experiments.

Figures 6 and 7 show the pressure profiles obtained at 1.0 and 2.0 m from the diaphragm, respectively. Again we note the close agreement in peak values and general wave shape. A common characteristic of all the profiles shown is the large oscillations in pressure that appears to occur. The flat pack (SRI) gages in the grout experiments showed similar results for the first two or three oscillations both in peak magnitudes and spacing between the peaks. A piezoelectric (LLL) gage at 2 m in the steel experiment agreed generally with the bar gages in peak values and relative spacing between the peaks. However, both the flat packs and piezoelectric gage indicate a much smoother profile behind the first two or three oscillations than observed with the bar gages. Thus, although the first few oscillations are felt to be realistic, the subsequent oscillations are felt to be a problem related to the design or installation of the bar gages. At this time only peak values for the flat pack gages have been analyzed and thus no corresponding pressure profiles are available for comparison.

*The time axis for the following pressure profile comparisons refer to detonation of the high explosive and thus have not been corrected for diaphragm times.

Figure 8 illustrates the decay of the peak pressure in the shock front as a function of axial distance from the diaphragm. Although the peak pressures in the steel experiment are consistently lower than the grout experiment, except for the results at 0.10 m, it is not known whether these differences are really significant at this time.

Examination of the TOA and pressure profiles indicates a slightly larger attenuation for the air shock at 2.0 m and beyond for propagation in grout pipe compared to the steel pipe. To the extent of the experimental comparison, the rather surprising conclusion is that air shock propagation is rather insensitive to whether the wall material is composed of incompressible (steel) or relatively compressible (grout) material.

Reference to a company or product name does not imply approval or recommendation of the product by the University of California or the U.S. Department of Energy to the exclusion of others that may be suitable.

NOTICE

"This report was prepared as an account of work sponsored by the United States Government. Neither the United States nor the United States Department of Energy, nor any of their employees, nor any of their contractors, subcontractors, or their employees, makes any warranty, express or implied, or assumes any legal liability or responsibility for the accuracy, completeness or usefulness of any information, apparatus, product or process disclosed, or represents that its use would not infringe privately-owned rights."

References

1. B. K. Crowley and H. D. Glenn, "Numerical Simulation of a High-Energy (Mach 120-40) Air-Shock Experiment," Proceedings Seventh International Shock Tube Symposium, Toronto, Canada, 23-25 June 1969, pp 314-342.

2. B. K. Crowley, H. D. Glenn, and R. E. Marks, "An Analysis of Marvel - A Nuclear Shock Tube Experiment," J. Geophys. Res., May 10, 1971, pp 3356-3374.

3. H. D. Glenn and B. K. Crowley, "Comparison of High-Energy Gas Flow Experiments," J. Appl. Phys., December 1971, pp 5517-5521.

4. J. R. Barthel, "A Computational Model for Flow in Line-of-Sight Pipes," DASA-2554, Systems, Science and Software, May 1970.

5. J. R. Barthel and D. F. Patch, "Condensation Modeling in the FLIP Code," Systems, Science and Software Rept. SSS-R-75-2535, January 1975.

6. D. Sawle, "Characteristics of the Voitenko High Explosive Driven Gas Compressor," First International Colloquim of Gas Dynamics of Explosions, Sept. 18-21, 1967, Brussels.

7. A. E. Voitenko, "Generation of High Speed Jets," Soviet-Physics Doklady, 9, 860, April 1966.

8. P. S. Brown and M. L. Lohmann, "Computational Studies of a Voitenko Compressor," Lawrence Livermore Laboratory report UCRL-82010, November 1978.

9. T. L. Ellis, U.S. Army Engineer Waterways Experiment Station, private communication, April 1978.

TABLE 1

STEEL VOITENKO EXPERIMENTAL DIAGNOSTICS

Distance (cm)	Diagnostics
0	F (Fiber optics)
2	F
5	F
10	F, B (Bar gage), PM
20	F, B, PM
30	F, B
40	F
50	F, B, PY
75	F
100	F, B, PY
125	F
150	F, B
175	F
200	F, B, P*
250	F, B
300	F, B
350	F, B
400	F, B
450	F, B
500	F, B, P*
550	F, B
600	B

*P = 80,000 psi PCB GAGE 109A(D)
PM = Pressure manganin (SRI)
PY = Pressure ytterbium (SRI)

TABLE 2

VOITENKO STEEL EXPERIMENTS

AIR SHOCK TIME-OF-ARRIVAL

Axial Distance (cm)	Fiber Optics TOA (μs)	S^3 Bar Gage TOA (μs)	SRI & L^3 TOA (μs)
0	(58.1) 0.0	0.0	0.0
2	1.2		
5	2.1		
10	3.3	3.5	
20	5.9	6.7	6.35
30	8.5	11.7	
40	11.6		
50	14.4	17.6	14.55
75	22.6		
100	31.7	34.9	30.8
125	43.3		
150	57.8	59.9	
175	77.5		
200	103.8	102.6	106.
250	183. (223)	187.9	
300	295. (495)		
350	448. (595.-700.)		
400	611. (737.)		
500			1050.-1200

TABLE 3

GROUT VOITENKO EXPERIMENTAL DIAGNOSTICS

DISTANCE (CM)	DIAGNOSTICS
0	F (FIBER OPTICS)
2	F
5	F
10	F, B, (BAR GAGE)
20	F, B, P*, W**
30	F, B, P, W
40	F
50	F, B, P, W
75	F
100	F, B, P, W
125	F
150	F, B, P, W
175	F
200	F, B, P, W
250	F, B, P, W
300	B

*P = PRESSURE SENSOR (PIEZORESISTANT)

**W = WALL MOTION SENSOR (PARTICLE VELOCITY LOOP)

TABLE 4

VOITENKO GROUT EXPERIMENT

AIR SHOCK TIME-OF-ARRIVAL

Axial Distance (cm)	Fiber Optics TOA (μs)	S^3 Bar Gage TOA (μs)	SRI Flat Pack TOA (μs)	SRI Velocity TOA (μs)
0	(57.6) 0.0			
2	1.3			
5	2.7			
10	3.8	3.9		
20	5.7	6.6	6.8	5.6
30	8.6	9.6	9.4	9.4
40	11.4			
50	14.6	15.9	15.0	13.4
75	22.9			
100	31.8	35.1	32.4	32.6
125	43.0			
150	57.4	58.5	58.6	56.8
175	76.9			
200	107.7	111.2	108.4	107.4
250	208. (218)	211.9	193.4	

TRENCH PHENOMENA - Figure 1

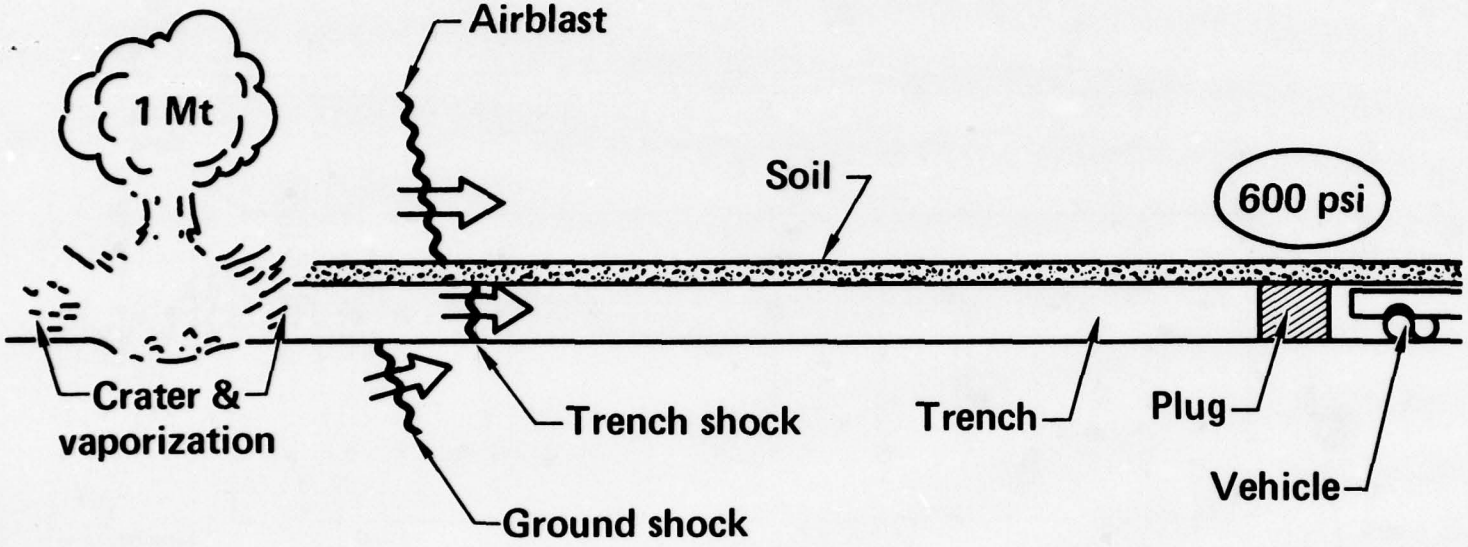

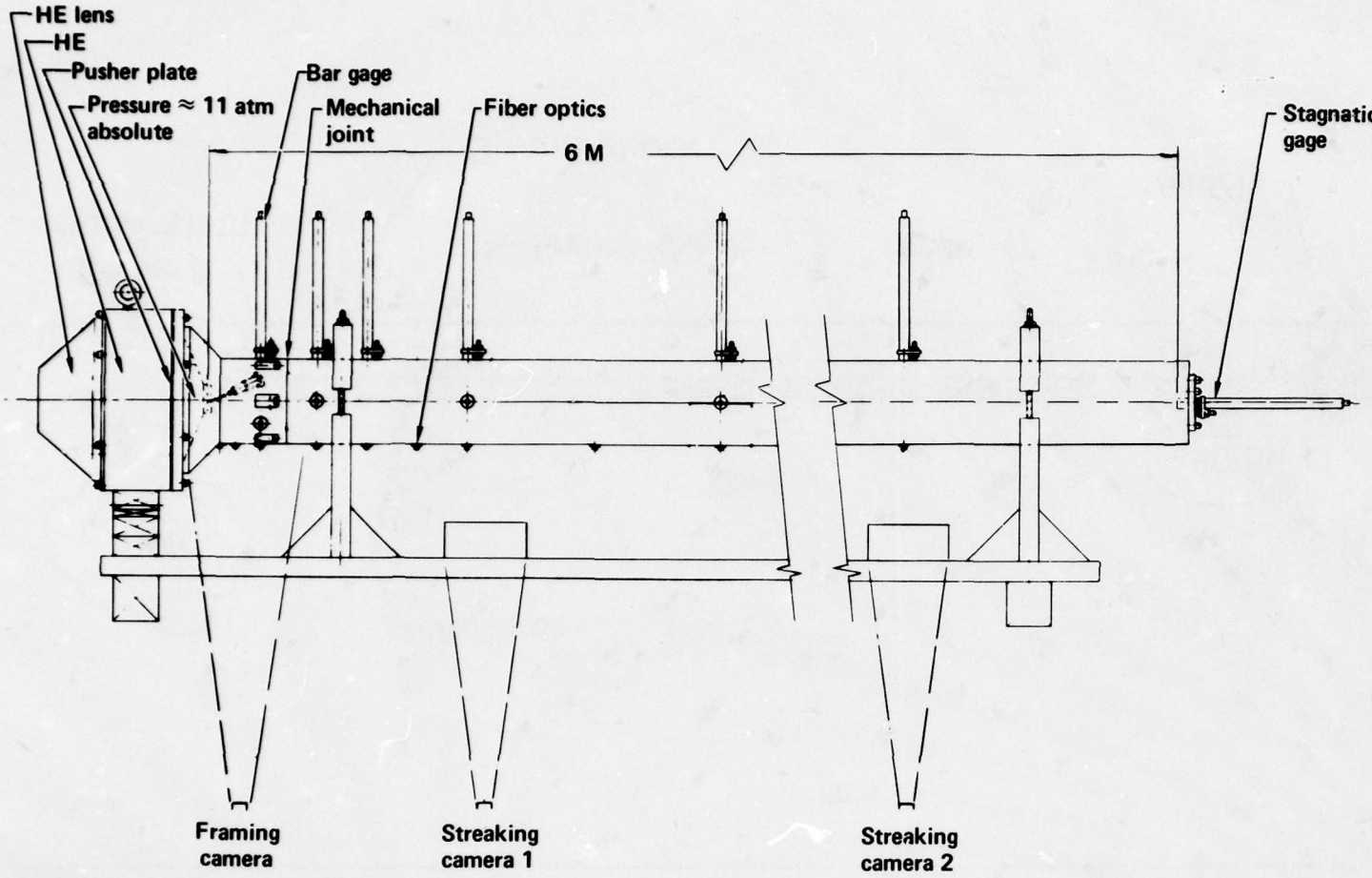

Figure 2. Compressor assembly, steel outlet pipe and diagnostics systems.

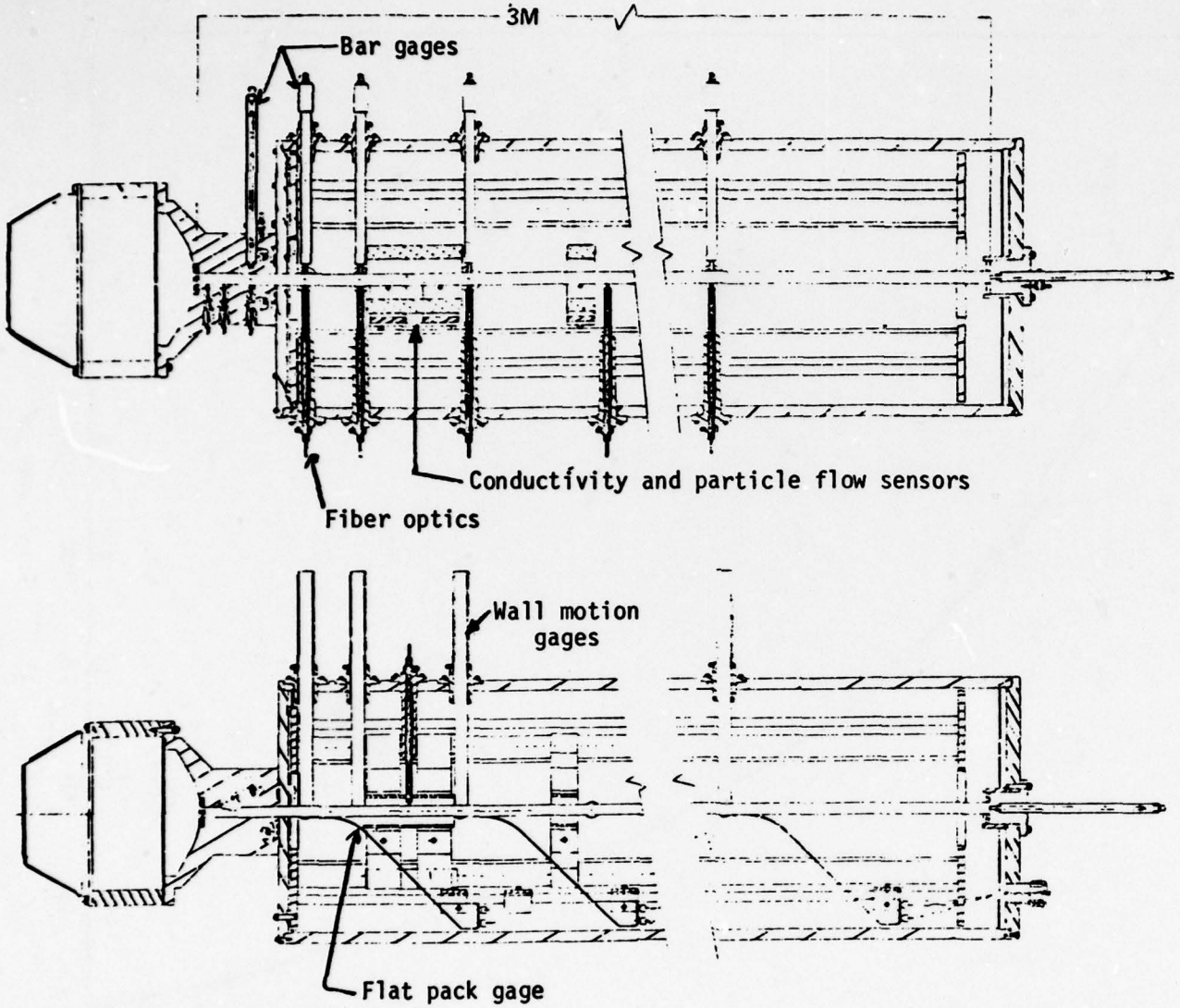

Figure 3. Compressor assembly, steel-grout outlet pipe and diagnostics systems.

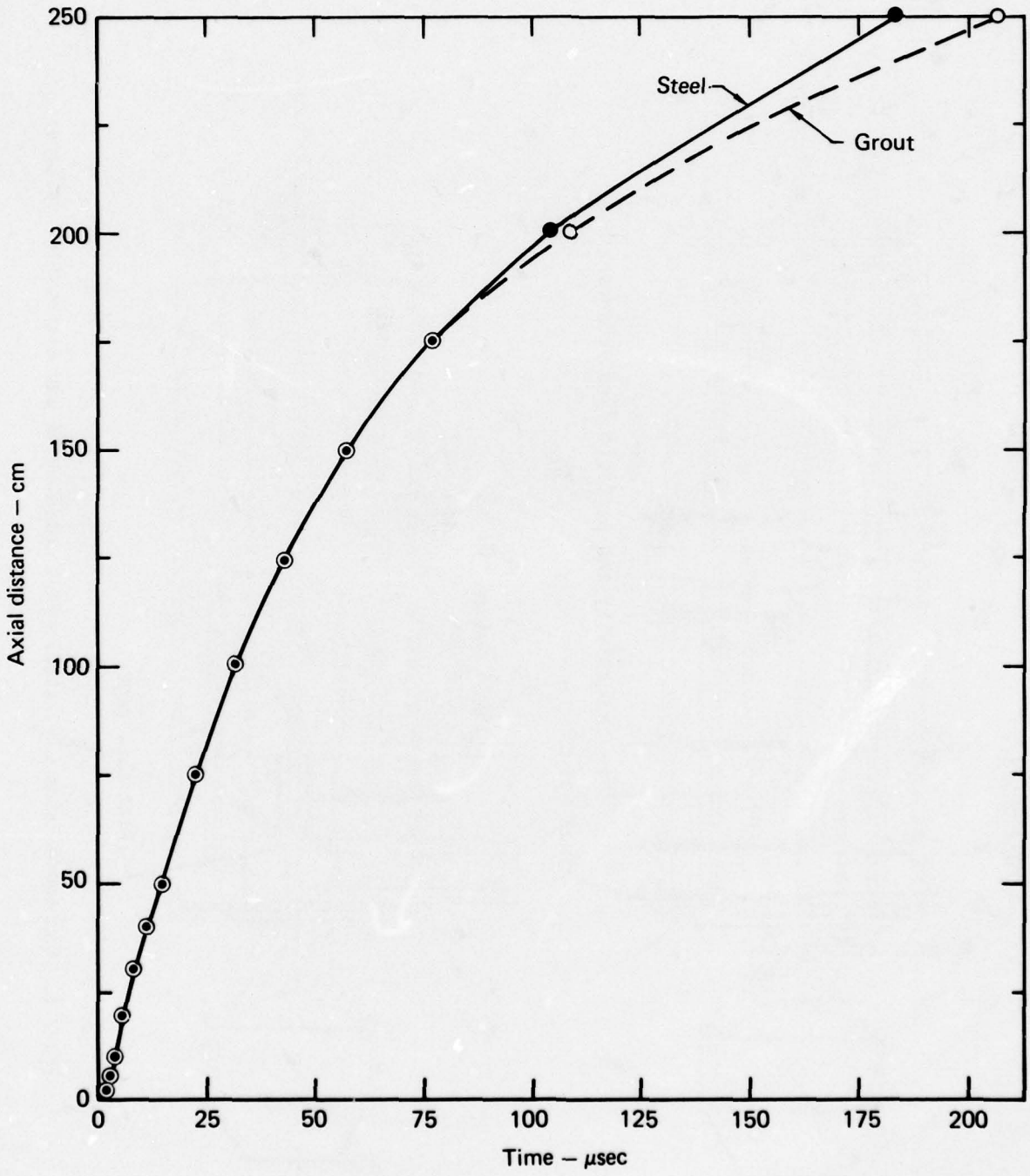

Figure 4 Air shock propagation in a steel and a grout pipe.

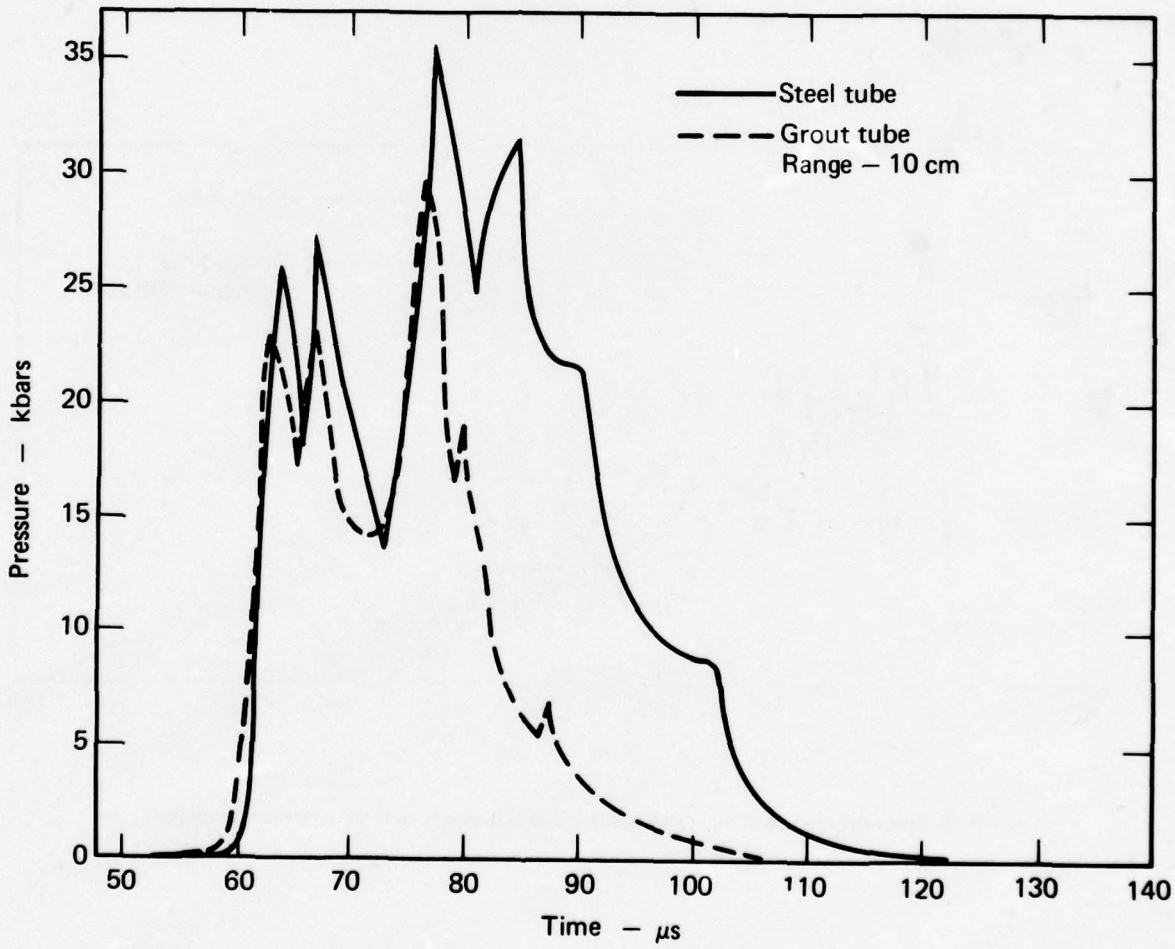

Figure 5 Pressure profiles obtained with bar gages at a distance of 0.10 m from the diaphragms.

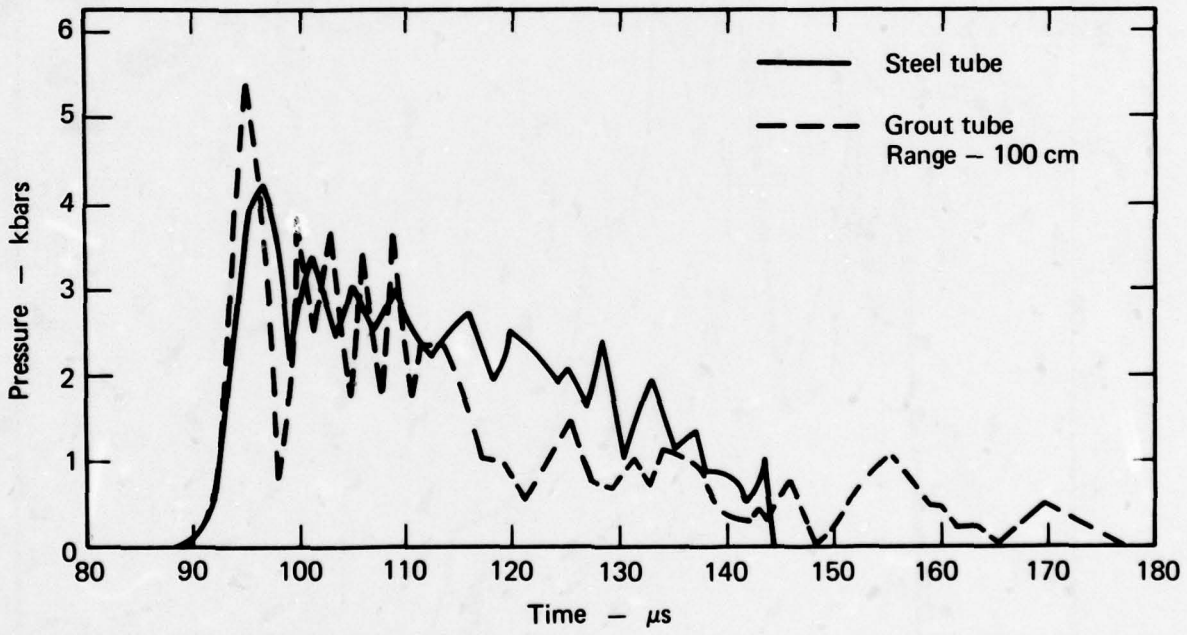

Figure 6 Pressure profiles obtained with bar gages at a distance of 1.00 m from the diaphragms.

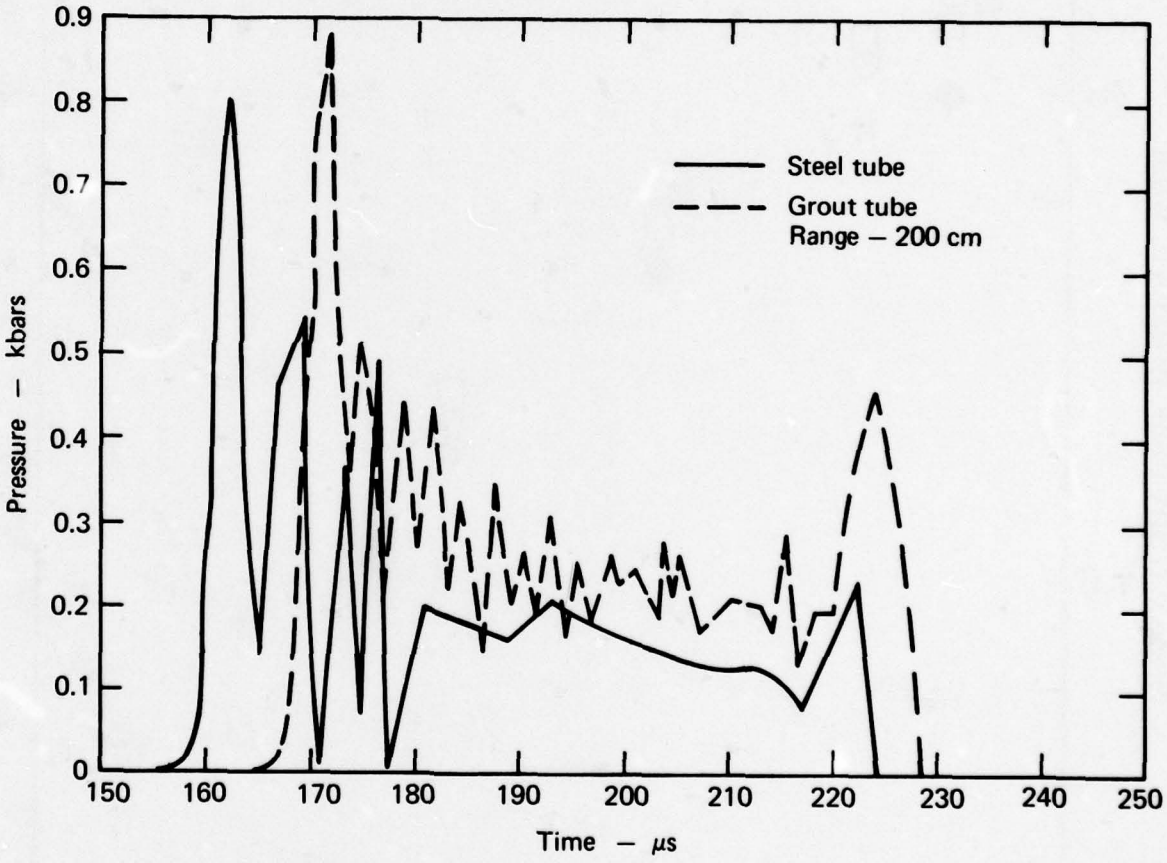

Figure 7 Pressure profiles obtained with bar gages at a distance of 2.00 m from the diaphragms.

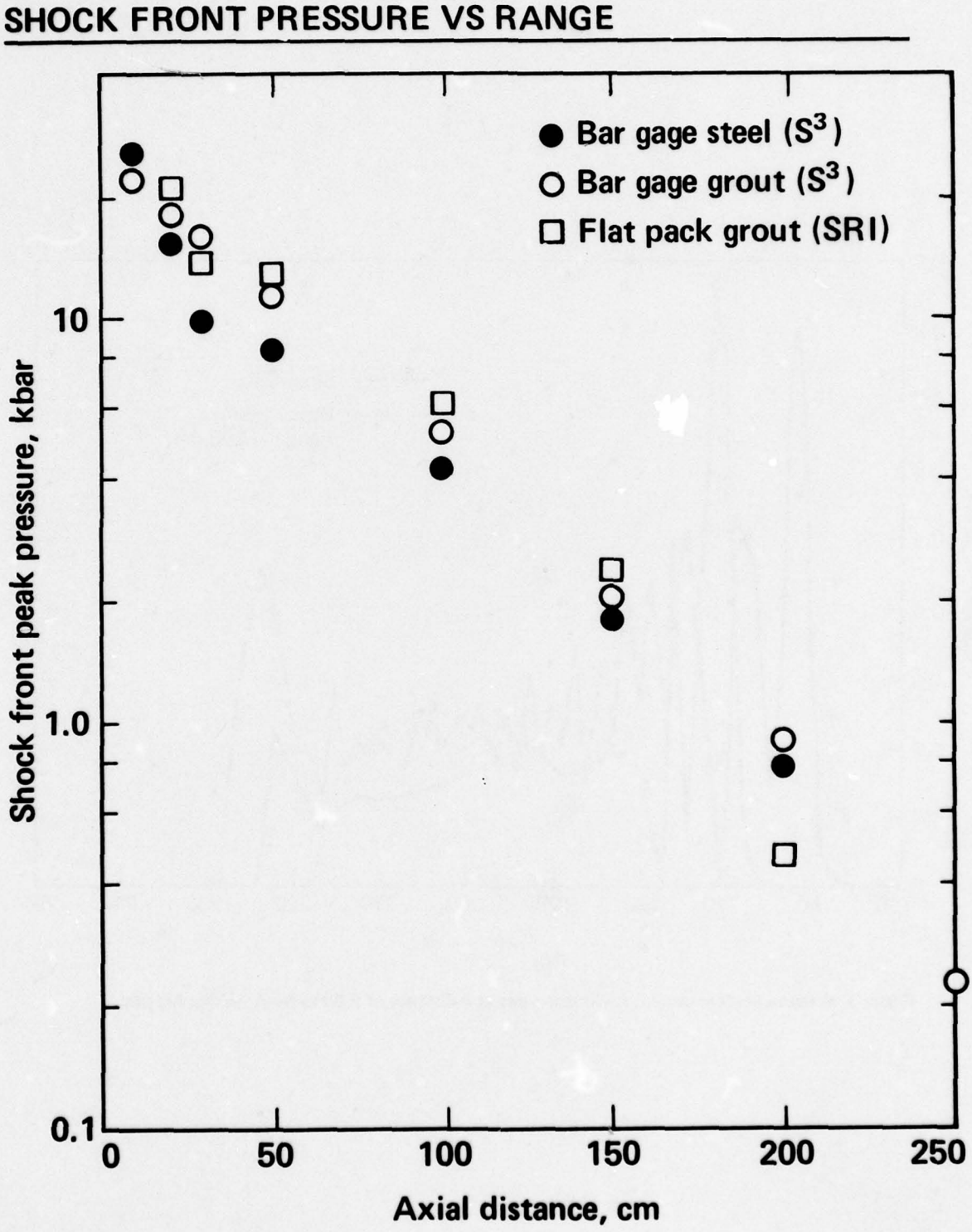

Figure 8. Peak shock front pressure versus axial distance from the diaphragm.

HE SIMULATION OF GROUND SHOCK-INDUCED MX TRENCH COLLAPSE

by

J.C. Baker

H.R. Kratz

F.I. Peterson

K.D. Pyatt, Jr.

L.E. Bailey

J.L. Waddell

Systems, Science and Software

HE SIMULATION OF GROUND SHOCK-INDUCED MX TRENCH COLLAPSE

J. C. Baker, H. R. Kratz, F. I. Peterson,
K. D. Pyatt, Jr., L. E. Bailey,
and J. L. Waddell

The work sponsored by the Defense Nuclear Agency

ABSTRACT

In order to establish the feasibility of HE simulation of ground shock-induced MX trench collapse, a calculation of the close-in ground shock from a 1 MT surface burst over desert alluvium was performed. In this way the pressure waveform arriving at a full-size trench buried 1.9 meters and situated 12.5 meters from the burst point was determined. The calculated direct-induced ground shock arrives at the trench 400 μsec after detonation, with a peak pressure of 90 kilobars that decays to half value in 200 μsec. This highly impulsive load initiates the collapse of the trench wall at the spall velocity (approximately 0.2 cm/μsec). Due to the extremely transient nature of the direct-induced loading, little wall displacement actually takes place during the passage of the waveform. Since the direct-induced ground shock also decays very rapidly with slant range, only about 12 meters of the trench are subjected to the very high initial closure velocities. However, airblast-dominated closure continues to pinch off the trench at much lower velocities out to several hundred meters. In defining the HE simulation experiment, only the simulation of the direct-induced ground shock was considered.

The simulation experiment consists of a rectangular slab of HE positioned over a buried trench. Calculations indicate that this source is capable of inducing a 90 kilobar shock at the trench wall. Moreover, the correct pressure-time history can be achieved by adjusting the thickness of the HE slab. The simulation experiments are conducted with 1/16th-scale trenches. The HE slab is 120-cm square by 6.93-cm thick and the scaled trench is a concrete pipe 26.5-cm ID with a 2-cm wall. The primary instrumentation is high-speed photography to record details of the collapse process. Pressure in the soil and inside the rapid closure region is measured. Pressure measurements are also made to assess the magnitude of induced flow in the pipe outside the rapid closure region. However, the emphasis of the simulation experiment is on energy coupling and not on pipe flow. Results from a pre-shot simulation experiment are presented.

The 30-day study group of MX trench testing requirements[1] concluded that strong, direct-induced ground shock resulting from a near-miss nuclear burst is an energy source for trench collapse that is highly uncertain and has a significant impact on the environment definition. Present uncertainties in the modeling of direct-induced ground shock collapse are manifest as order of magnitude uncertainties in the plug pressure environment. The study group further concluded that the data requirement for strong ground shock induced collapse was not being addressed in the then current MX experimental program, but that this requirement could be met by static HE tests. This paper will present the definition of the nuclear environment resulting from a 1 MT surface burst and the experiment designed tc simulate the effect of that environment on an MX trench.

Systems, Science and Software under separate contract had performed a detailed calculation of a 1 MT surface burst dubbed source 3/5. This calculation used STREAK which is a multi-material Eulerian radiation-hydrodynamic finite difference code. The calculation included a detailed description of the source, the nuclear fireball, airblast coupling, and detailed zoning in the shock region - both direct-induced and airblast-induced. This code was used quite successfully in the previous experiments on the underground tests Ming Blade and Husky Pup, which were designed to validate the predictive codes used in energy coupling calculations. Source 3/5 was carried to a final time of approximately 800 microseconds at which point the airblast

---

[1] A Review of MX Trench Testing Requirements, A Report of the Findings of the Joint DNA, SAMSO, and AFWL 30-Day Study Group, November, 1977.

is at a radius of approximately 85 meters and has a shock pressure of about 1.3 Giga Pascals (13 kbars). Figure 1 illustrates airblast values for a 1 MT surface burst. The curve marked "Max Surface Airblast" is the peak shock value of the blast wave at that time. The curve labeled "Min Surface Airblast" is the relatively constant (in space) value the pressure drops to behind the shock. Note that at times earlier than .1 msec these two curves come together. The well-formed blast wave does not appear until about this time following a 1 MT surface burst. The only data available lie at pressures below 100 MPa (1 kbar).

The calculation was monitored at points corresponding to the top of the MX trench (approximately 1.5 meters below the original ground surface) at various radii. Two of these curves are shown as dashed lines in Figure 1. The close-in values ($\leq$ 5 m) are not of interest to this problem since the question of direct coupling of the nuclear device to a trench was addressed in the underground test Hybla Gold. The 25 m curve on the downside is mostly an extrapolation from the end of the calculation. This range reaches pressures of approximately 1 GPa (10 kbars) which is lower than values of interest. The 12.5 m range shows a peak pressure of approximately 9 GPa (90 kbars) which is above levels usually available through airblast coupling using HE. Yet this value is in the interesting range for trying to understand how pipe crush will couple energy down the length of the trench.

Turning to Figure 2, in (a) is plotted the 100 GPa (1 mbar) and 10 GPa (100 kbar) isobars. This stress level does not occur at the same time at all locations so this plot is an amalgamation of several times. These curves are displaced downward at radii less than 5-10 m because the calculation included a cylindrical room roughly approximating another trench configuration directly under the explosion point. In Figure 2 (b) plotted as a solid line is the pressure at point A in 2 (a) as a function of time. The calculated ground shock arrives at the trench 400 microseconds after detonation, with a peak pressure of 9 GPa. This wave decays to half-value in 200 microseconds.

The highly impulsive load represented by this pressure-time history initiates the collapse of the trench wall at a spall velocity of approximately 0.2 cm/μsec. Due to the transient nature of the loading, most of the wall displacement actually takes place after the passage of the waveform. Since the direct-induced ground shock also decays very rapidly with slant range [cf: Figure 2 (a)], only about 12 meters of the trench are subjected to the very high initial closure velocities. However, airblast dominated closure continues to pinch off the trench at much lower velocities out to several hundred meters. Admittedly, there are uncertainties in this calculation of the predicted stress field following a 1 MT surface burst, but the calculation does suggest the environment to be simulated if one wants to study the energy untimately coupled to the pipe by the ground shock-induced collapse.

Figure 2 (b) also illustrates the type of scaled pressure-time history (dashed curve) obtainable from HE coupled directly into soil. The simulation experiment consists of a rectangular slab of HE positioned over a buried trench. Calculations indicate that this source is capable of inducing a 9 GPa shock at the trench wall. Moreover, the correct pressure-time history at this point can be achieved by adjusting the thickness of the HE slab. (The decay of pressure with depth will probably not be the same in the HE case as in the nuclear, but the nuclear calculation has not been carried to the point where the shock has totally traversed the trench location. From earlier data, it appears that the nuclear value might reach about 2.5 - 3.0 GPa at the trench bottom and the HE case about 1.5 GPa.) The simulation experiments are conducted with 1/16th - scale trenches. Table 1 lists some parameters of the HE. The slab is approximately 1.2 meter square by 6.93 cm thick (Comp C4 with a total mass of 166 kg. (This is about the maximum surface charge which can be fired at the S^3 Green Farm test site.) The areal size of the slab is dictated by efforts to avoid any edge effects affecting the ground shock until the wave has passed below the bottom of the trench.

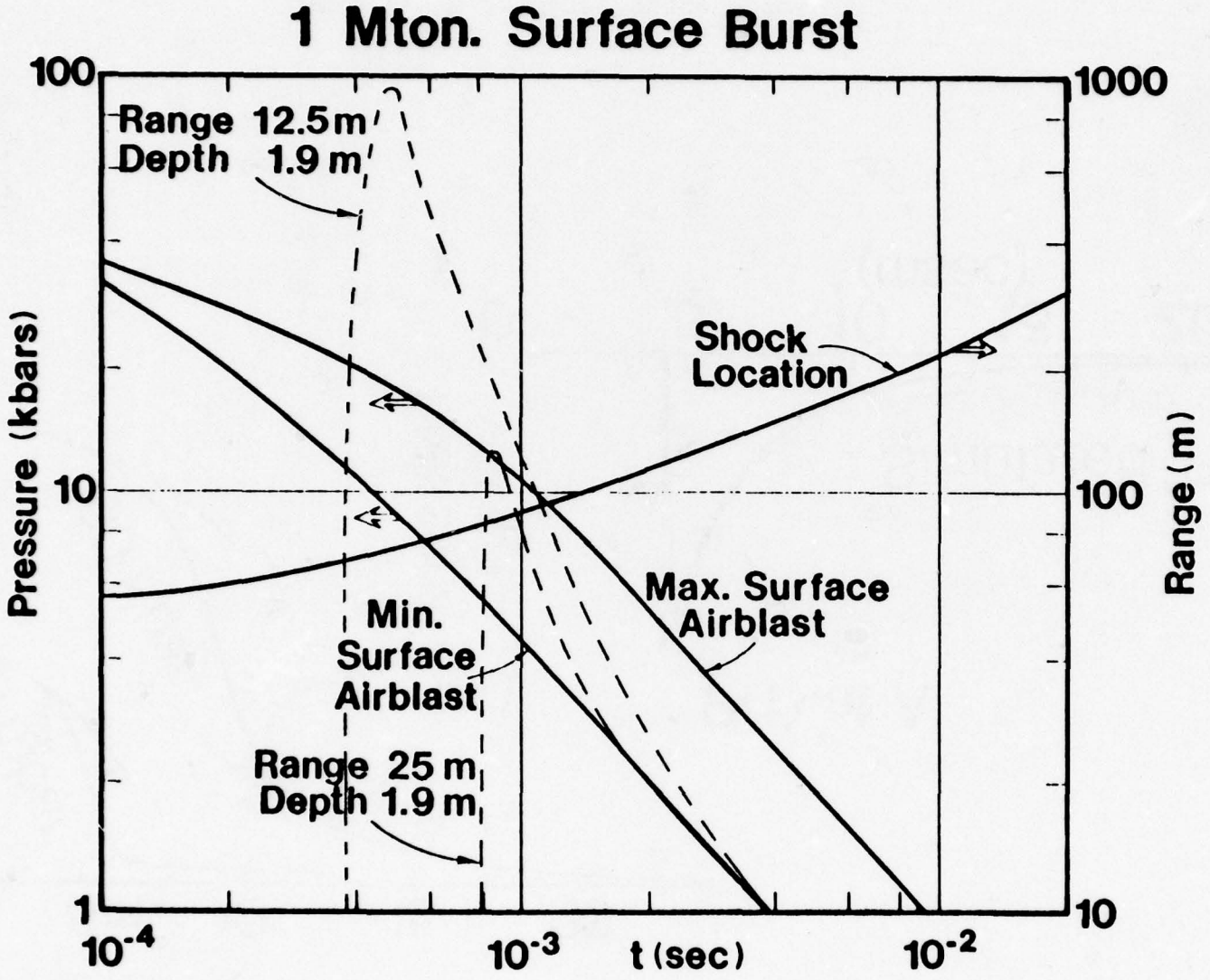

Figure 1. 1 Mton Surface Burst

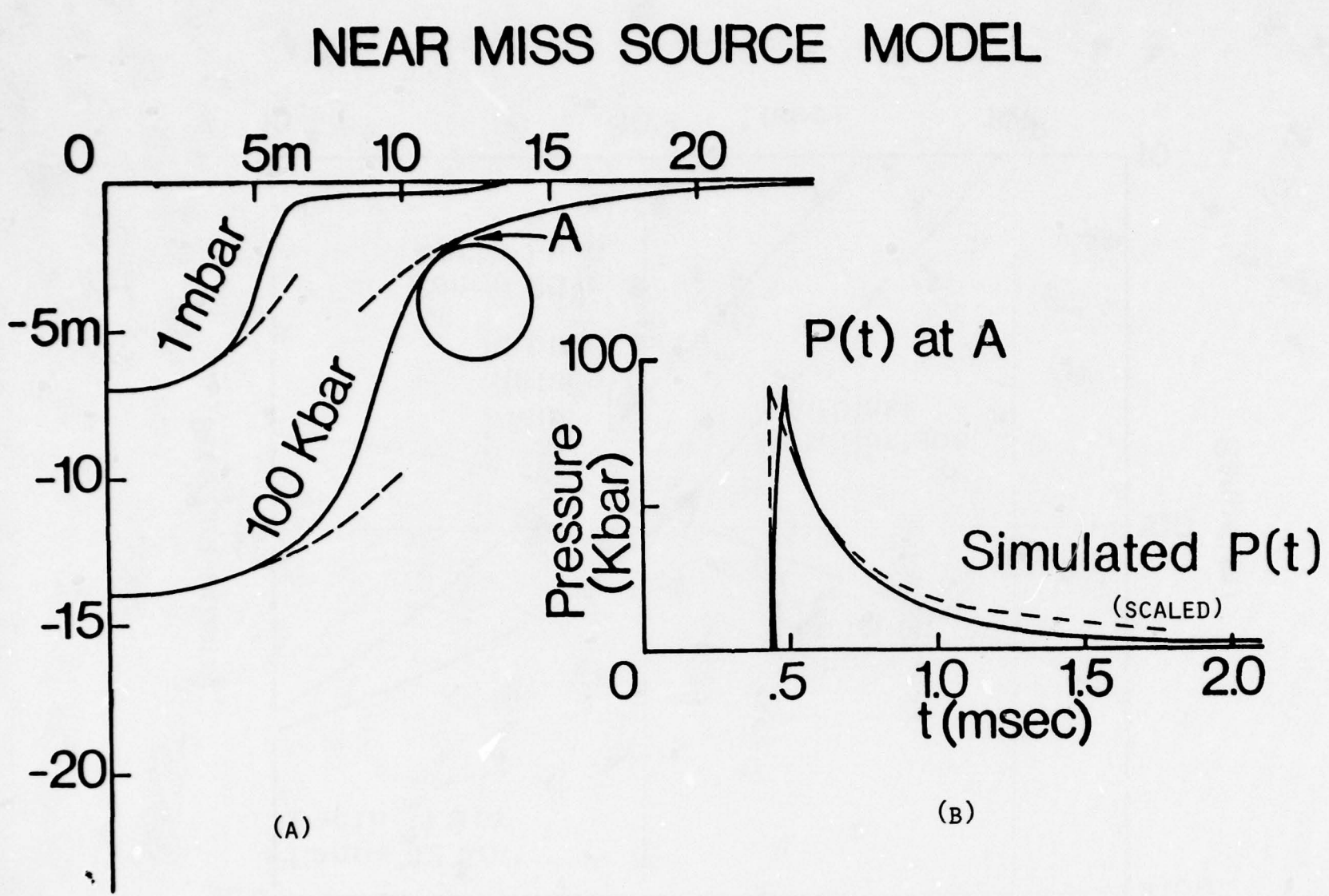

Figure 2. Near Miss Source Model

Table 1.

1/16 scale experiment

HE slab thickness	6.93 cm
Depth of pipe burial + liner thickness	7.62 cm + 2 cm
HE mass (1.2 m x 1.2 m)	166 kg

The scaled trench is a concrete pipe 26.5 cm ID with a 2 cm wall, 10 meters long. (The scaled depth of burial is 4 feet, rather than the 5 proposed for an MX trench, but since we are interested in energy coupling to the remainder of the pipe by the collapse, this is not a serious difference and it does allow one to reduce the amount of HE required.) Since concrete pipes with walls this thin are not available commercially, the pipe was cast by S^3 in sections about 72 cm long in specially built forms. The pipe is mounted in a trench which is back-filled with Overton sand, the top of the pipe being 7.62 cm below the top surface of the sand. (See Figure 3 for the experimental set-up.) Overton sand was chosen as the soil material rather than alluvium because of the necessity to pack the material around the pipe with a relatively uniform density. In back-filling the trench, the sand is "rained" into the trench to a density of approximately 1.8 gm/cm^3, with samples being measured to confirm the consistency. The HE charge is positioned on the surface of the sand directly above the center of the pipe as shown in Figure 3. (Note that the horizontal and vertical scales are different in this figure.) The HE charge is detonated simultaneously (to within ± 2 μsec) over its entire surface with two flying-plate-type detonators.

The main diagnostic to measure the rate and shape of the pipe collapse is high-speed photography, using a framing camera running at about microseconds per frame. The camera looks directly down the axis of the pipe via the turning mirrors indicated in Figure 3. The pipe is back-lighted from the opposite end with a high-explosively-driven argon "candle", the length of which is great enough that the shock wave does not arrive at the end of the candle until after the collapse of the pipe is complete. What is actually photographed is a shadowgraph of the collapsing pipe directly under the HE charge. In this way, both the rate of collapse and the cross-sectional shape of the collapsing pipe are determined. Using an opal glass window at the end of the argon candle was found to produce much more uniform backlighting than when a transparent window was used.

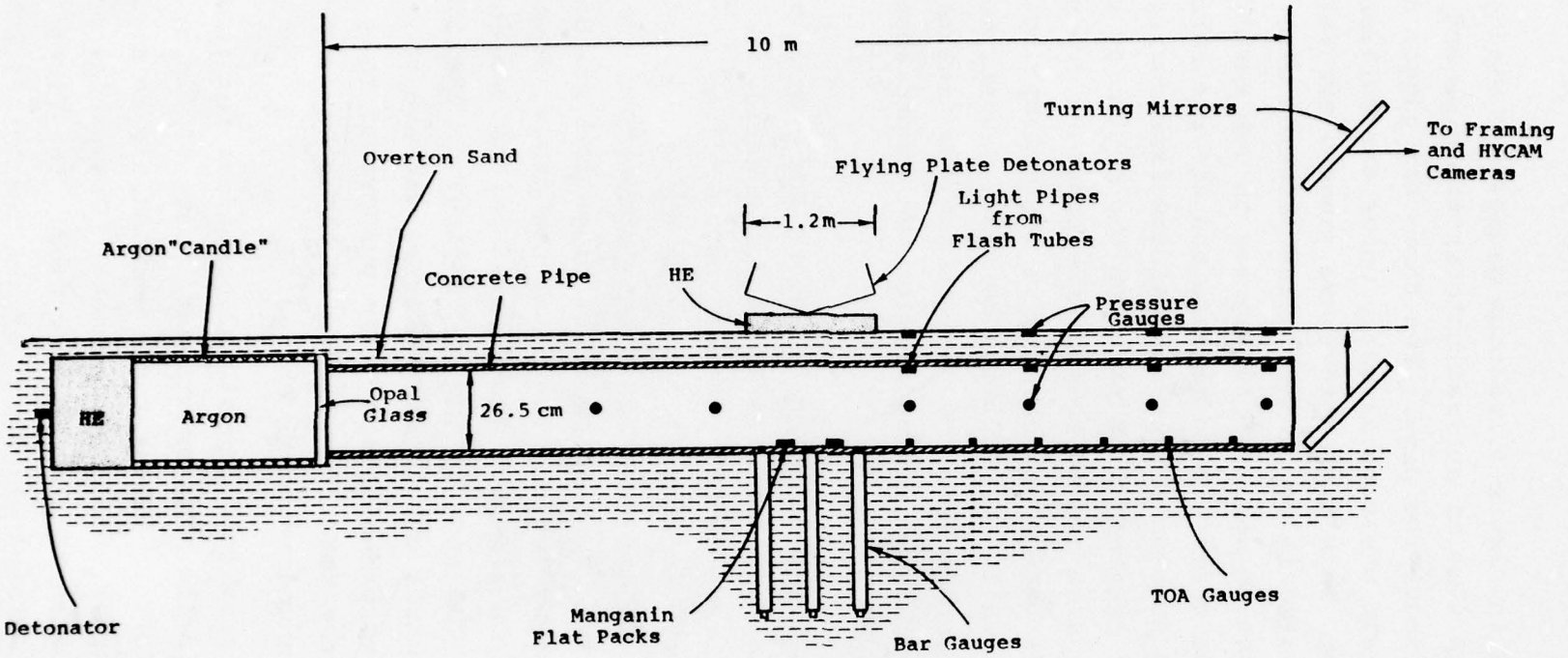

Figure 3. Experimental Setup

As indicated in Figure 3, various gauges are used to measure pressure and time of arrival both in the pipe and on the ground surface above the pipe. The three bar gauges shown are to measure the air pressure directly under the collapsing portion of the pipe. In addition to these gauges, two bar gauges are also located in the center plane perpendicular to the pipe axis, but at an angle of 20 degrees to the vertical. The purpose of these gauges is to measure the air pressure in the lobes which may form on either side of the axis during pipe collapse. The manganin flat packs on the bottom of the pipe under the HE charge are to measure the pressure produced by the impact on the bottom of the pipe of the collapsing upper portion of the pipe wall. In addition to these gauges, manganin gauges are also distributed in the sand at various distances below the HE charge. These gauges measure the ground shock incident on the pipe.

TOA and pressure gauges located along the inside of the pipe but outside the region of the HE charge measure the time-of-arrival and magnitude of the pressure pulse driven down the pipe by the collapse. Additional gauges on the ground surface above the pipe will measure the air blast incident on the ground outside the HE charge. Bundles of light pipes are mounted at various positions along the top inside of the pipe. These light pipes lead to flash tubes which are located beyond the end of the concrete pipe. The ends of the light pipes in the concrete pipe are pointed towards the turning mirrors and are photographed by a remotely-located HYCAM camera. The purpose of this arrangement is to measure the rate of collapse of the pipe outside the rapid closure region under the HE charge.

In order to prove the concept and get ideas for timing settings on scopes in the main experiment, a set of two pre-shot tests were performed. These tests were mainly to check out the optics and argon candle performance. Commercial 6 inch concrete pipe and scaled HE charges were used. The first test indicated that careful alignment of all the optics was absolutely essential for obtaining pictures of high enough

quality to analyze. The second pre-shot test used the same scaling as the first, but the inside of the pipe was coated with a black, non-reflective material. Both opal glass and a negative density filter were used to get uniform illumination of the pipe cross-section and more than a day was spent in getting good alignment of the mirrors and the pipe.

Figure 4 has four photographs relating to this 6 inch pre-shot test. Figure 4 (a) shows the pipe and turning mirror frame. The argon candle was later installed at the near end of the pipe. The bunker is beyond the truck visible in the background. Figure 4 (b) shows the sand bed over and around the pipe. A plastic tarp has been erected to keep direct sunlight off the HE after it is emplaced. The HE charge (approximately 3.5 cm thick in this case) and the flying plate detonator are visible in Figure 4 (c). A post-shot view of the test bed is shown in Figure 4 (d), with a technician standing in the main charge crater for scale. The large piece of plywood in the right foreground is part of the turning mirror framework seen in Figures 4 (a) and 4 (b).

A STREAK prediction calculation for the full scale experiment was performed to determine if there were any potential problems with the design. This was done in X-Y plane geometry, taking a cross-section of the pipe, soil, and charge. We were interested in pressures in the air as the pipe squeezed off and stagnation pressures at the bottom of the pipe. This calculation did not include either radiation or strength, since neither was significant for this regime. The code uses tracer particles to delineate material boundaries, and this is what will be shown in figures to come. Both the inside and outside boundaries of the pipe will be presented in the tracer plots. They will be compared with the photographs taken during the second pre-shot test described above. The calculated times will be scaled to the times for this particular event. Comp B JWL equation of state coefficients were used in the calculation.

6″ Pre-Shot Set Up

(A)

(C)

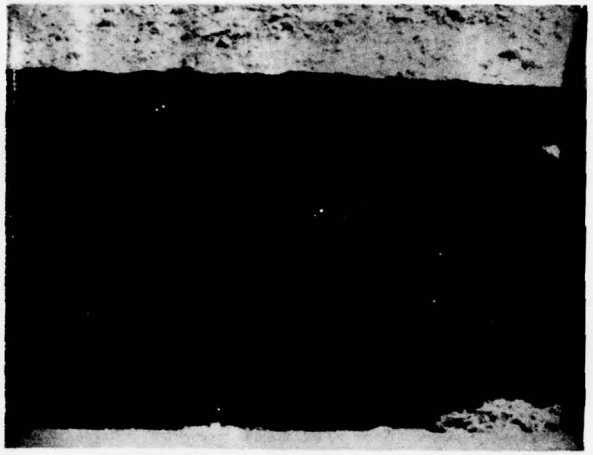

(B)

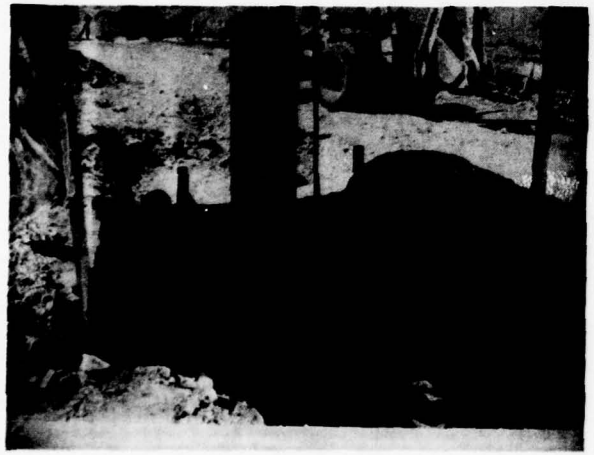

(D)

Figure 4. Six-Inch Pre-Shot Set Up

Figure 5 is the first of a series of plots comparing the event and the code. On the left [Figure 5 (a)] is a series of photos taken down the pipe while the collapse is in progress. There are 7.63 μsec between frames and the collapse started at about Frame 9, which is not shown. To the right [Figure 5 (b)] is an artist's rendition (dashed line) of the pipe shape at the central frame of the three presented. The heading indicates it is for the 6 inch experiment, it is Frame 11, and the time is 84 μsec from detonation of the main HE charge. The quality of reproduction of the photos is not good enough to show the sharp boundary which is apparent between the air and the pipe wall. Figure 5 (b) also has the calculated configuration over-laid on the photo rendition. The shape is remarkably similar and the location is in reasonable agreement. (The calculation used an equation of state of alluvium at density approximately 2.1 rather than sand at a density of approximately 1.6-1.7 as in this experiment.)

Figures 6 (a) and 6 (b) make the same comparison at 107 μsec, Figure 7 (a) and 7 (b) at 130 μsec, Figures 8 (a) and 8 (b) at 153 μsec, Figures 9 (a) and 9 (b) at 176 μsec, and Figures 10 (a) and 10 (b) at 199 μsec. In all of the photos there is no indication of a break-up of the pipe-wall/air interface. The calculation is in qualitative agreement with the observed behavior, although it is protruding more on axis. This is thought to be due simply to coarse zoning problems in the regions of the developing lobes. The lobe effect was not expected when the calculation was performed and thus was not adequately accounted for in the problem set-up. The air in these lobes reaches a calculated pressure of only about 100 MPa (1 kbar), which may not be effective in driving a strong shock down the length of the tunnel. The gauges on the main experiment will give data relating to the efficiency of the air compression and the validity of the numerical calculation. The experiment is currently set for detonation sometime during the week of December 4, 1978.

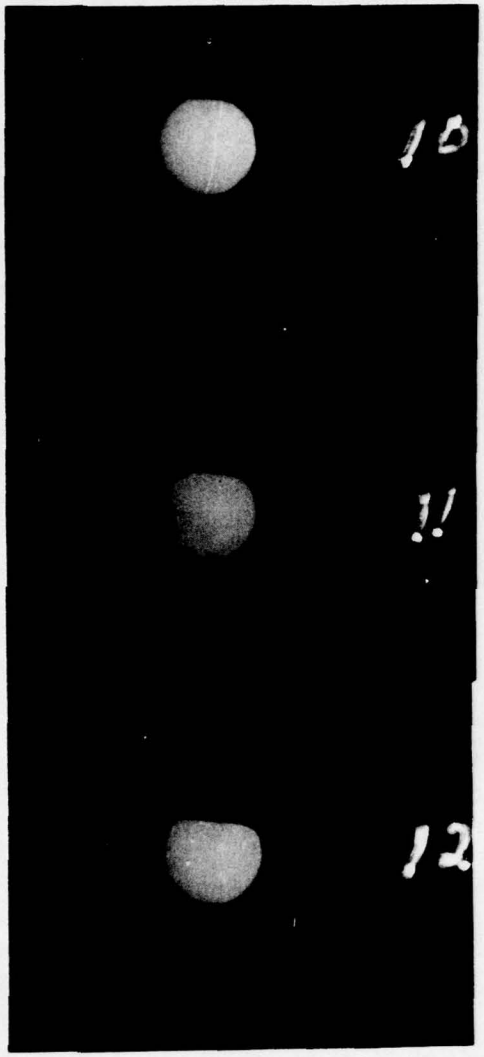

(A)

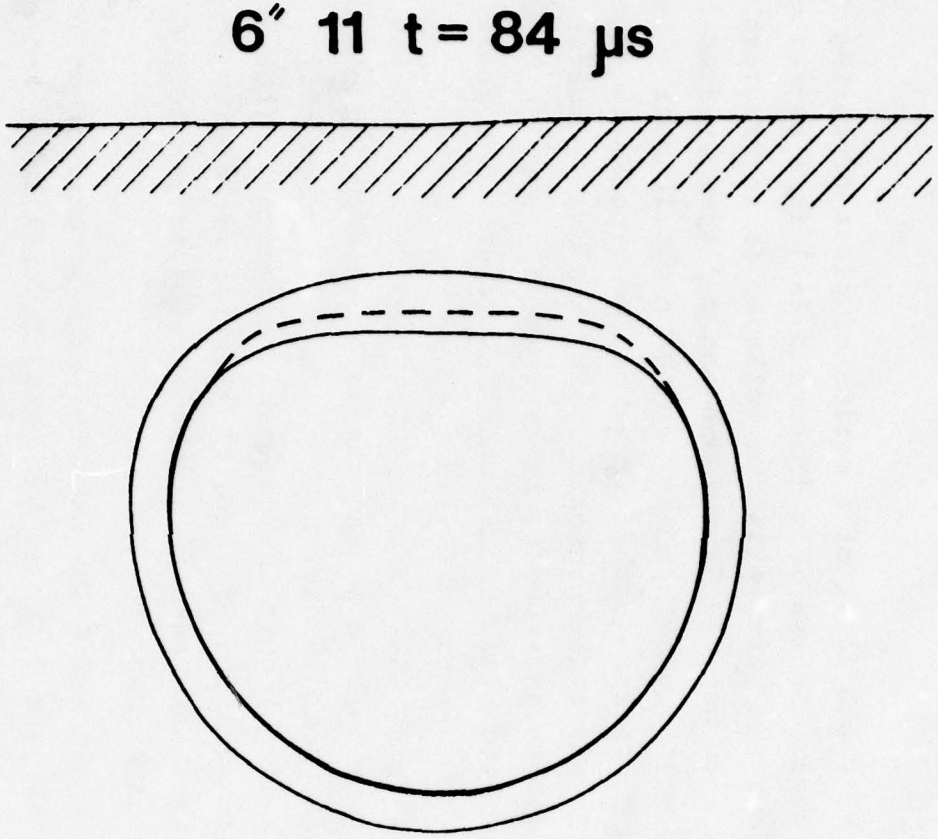

(B)

Figure 5. Experimental/Calculational Comparison

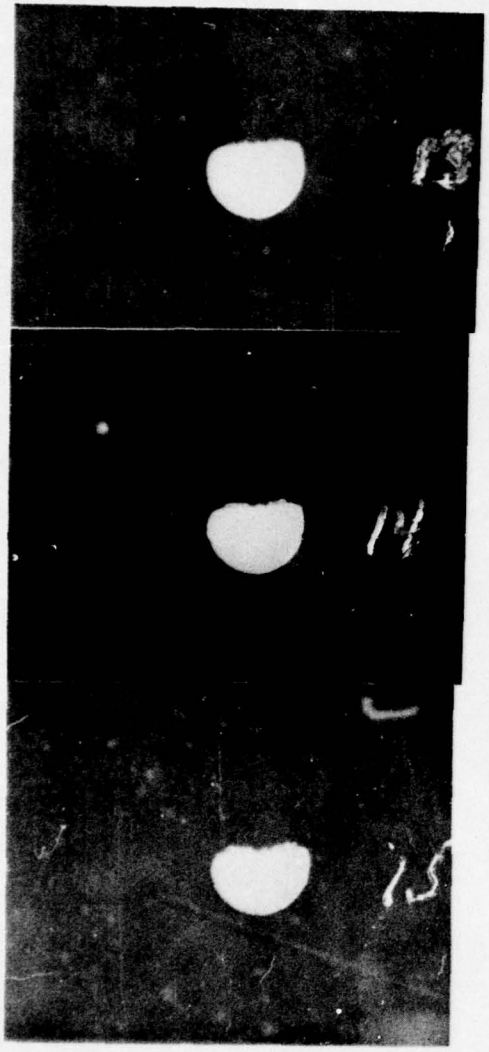

(A)

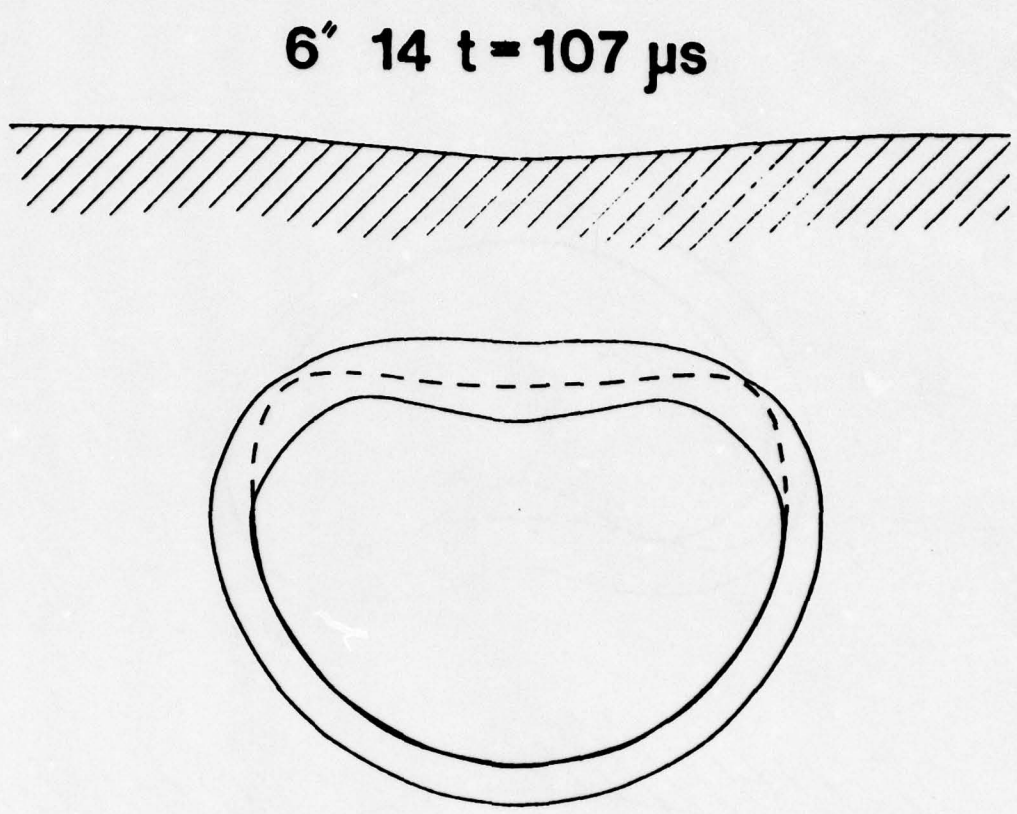

(B)

Figure 6. Experimental/Calculational Comparison

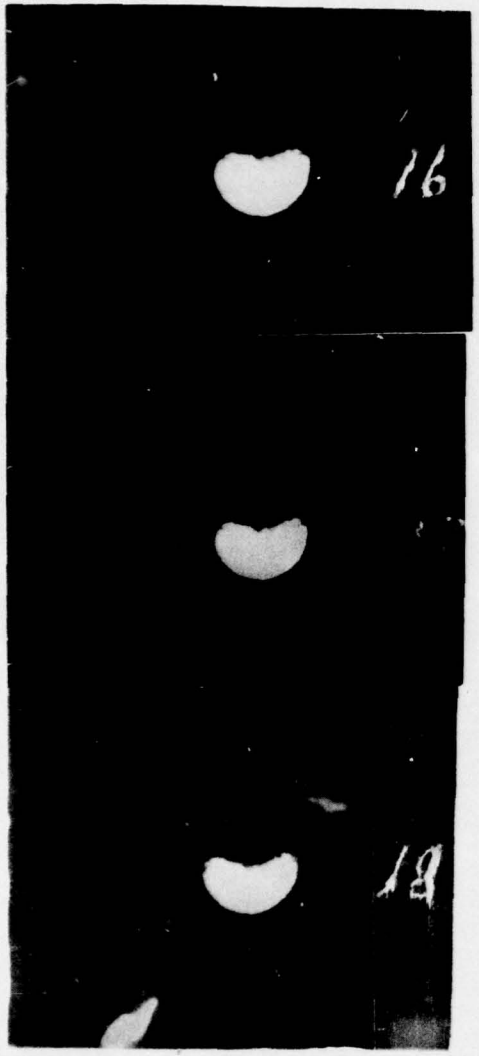

(A)

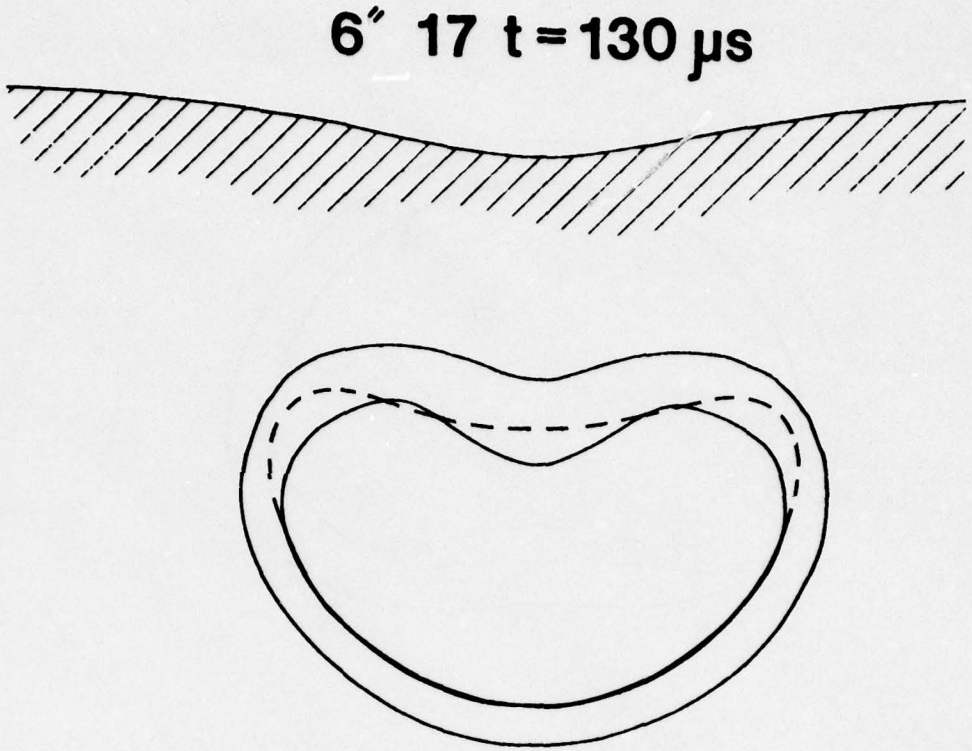

(B)

Figure 7. Experimental/Calculational Comparison

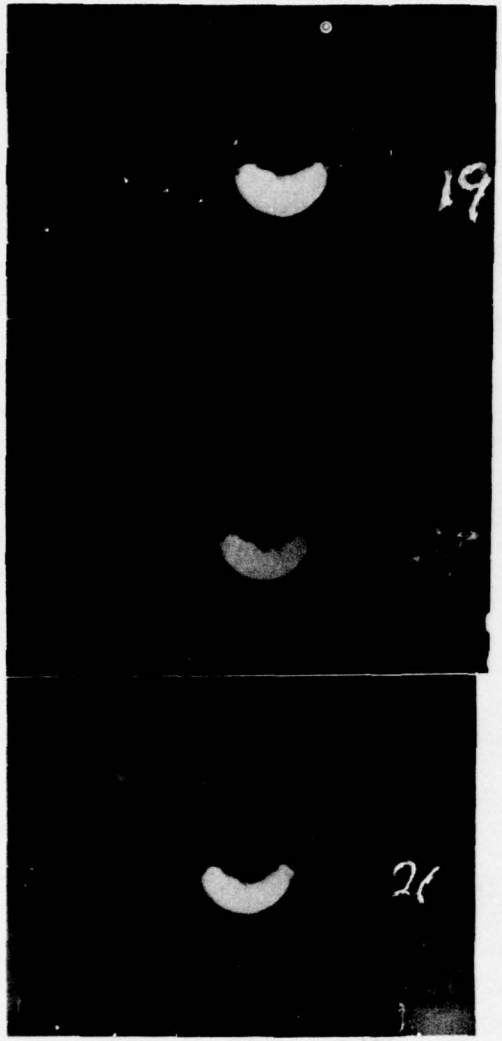

(A)

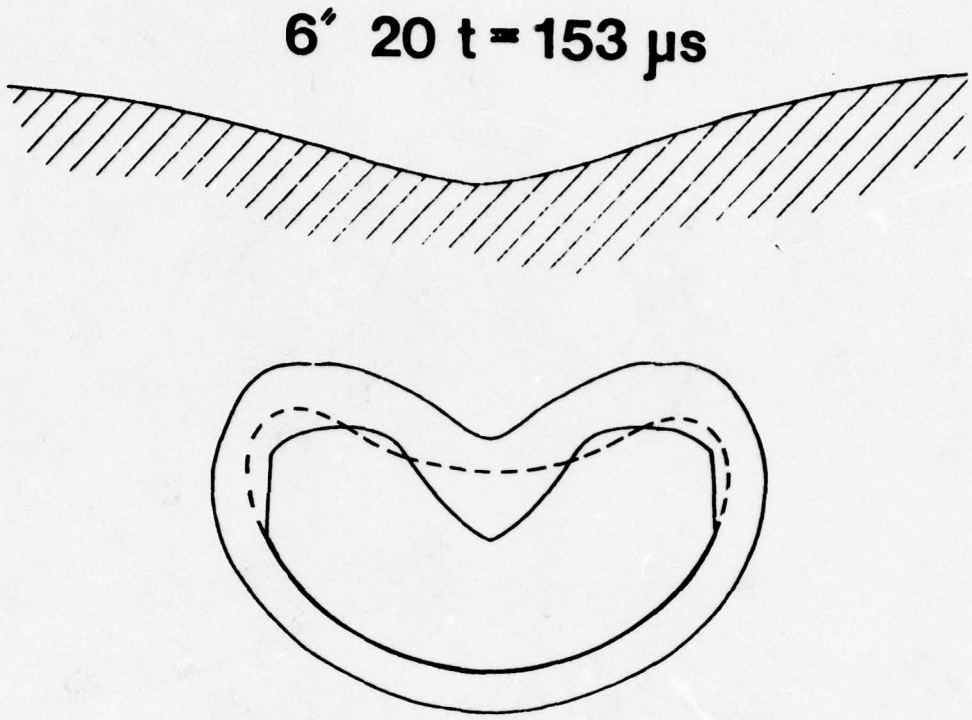

(B)

Figure 8. Experimental/Calculational Comparison

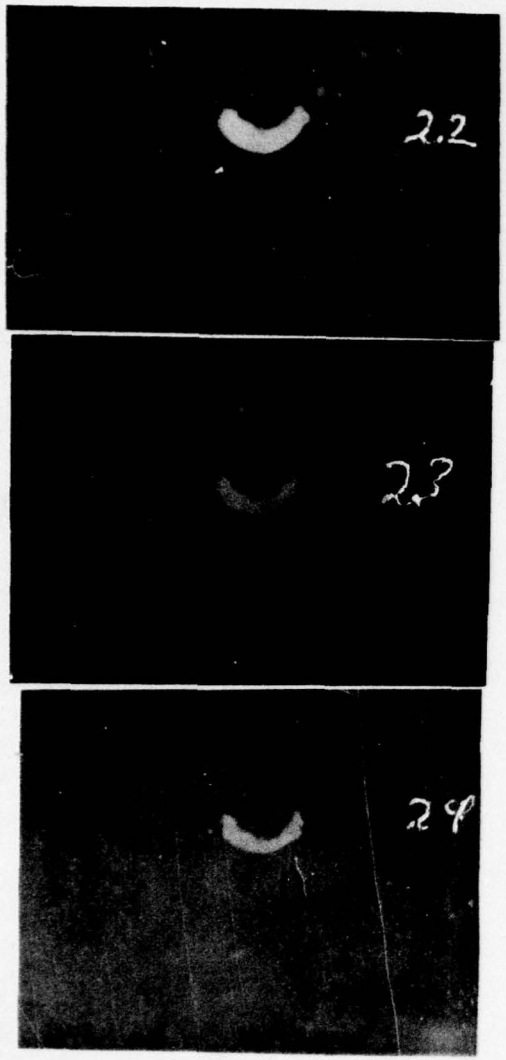

(A)

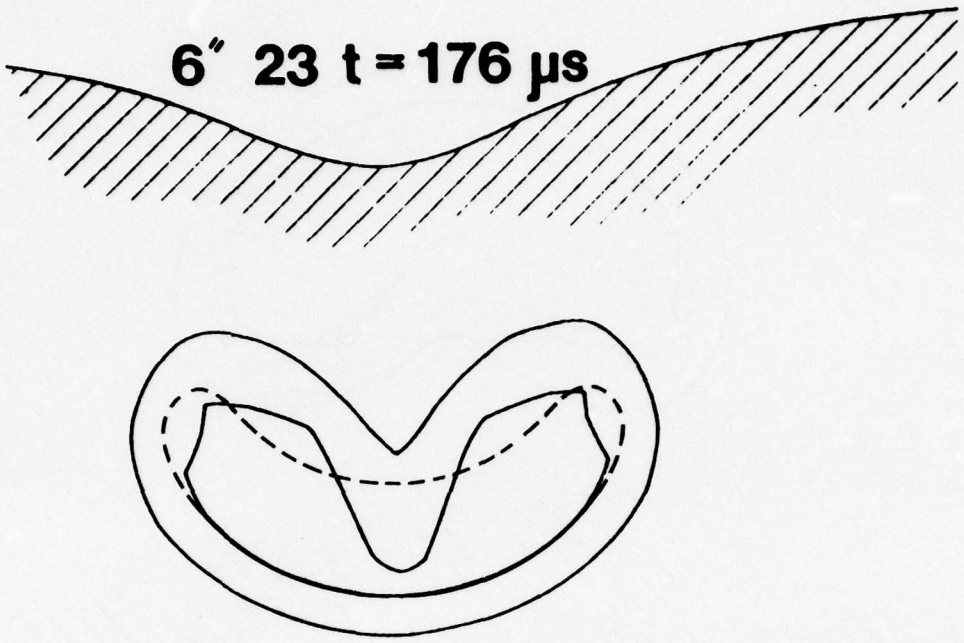

(B)

Figure 9. Experimental/Calculational Comparison

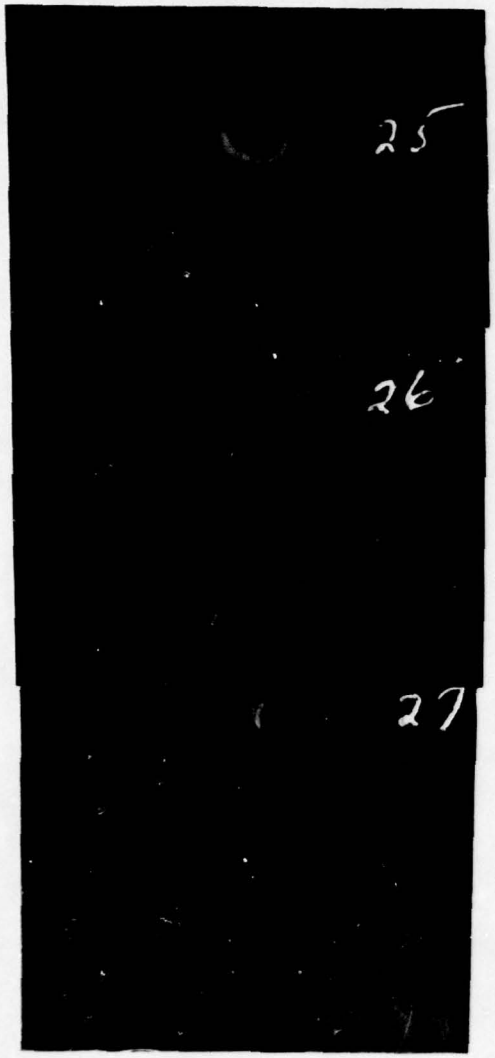

(A)

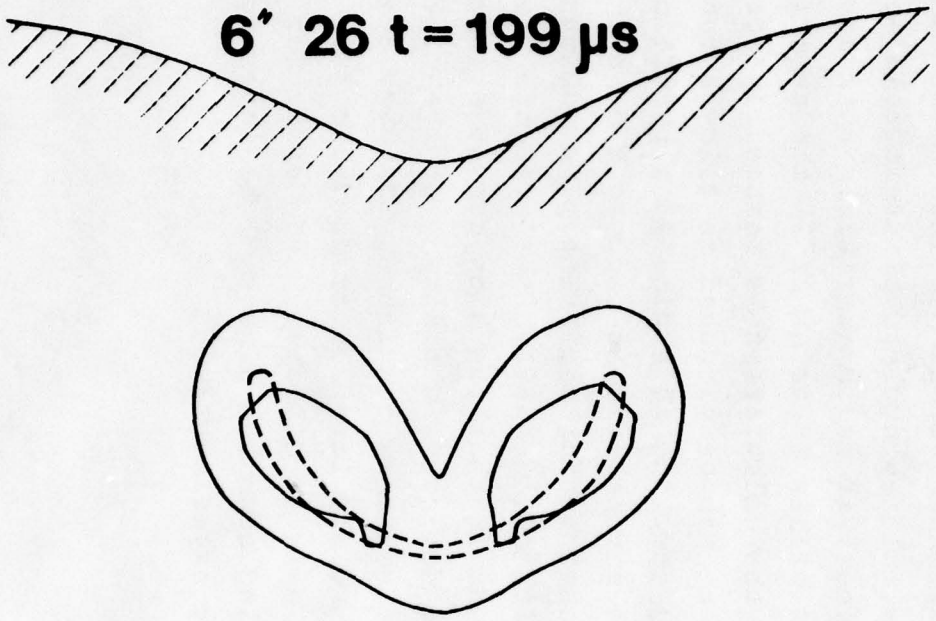

B)

Figure 10. Experimental/Calculational Comparison

In summary, then, it is possible to simulate with HE the very close-in calculated nuclear blast-induced environments. To a certain extent, it is immaterial in this case how accurate (at least to within a factor of 2) the numerical prediction is. Given that the calculation is reasonably correct, the simulated environment can be produced to allow a test of the effective energy coupling to a pipe as a result of collapse initiated by the strong, direct-induced ground shock. The photographic technique for measuring pipe collapse has been refined and confirmed. Finally, the evidence from the 6 inch pre-shot test is that the high pressure, impulsive loading of the pipe does not cause a break-up at the pipe-wall/air interface as the collapse continues. Rather, a distinct separation is maintained and lobes of trapped air form to either side of the vertical axis of collapse. The effect of this geometry on energy coupling down the pipe will be investigated in detail in the impending experiment.

COMPUTATIONAL STUDIES OF A VOITENKO COMPRESSOR

by

P.S. Brown

M.L. Lohman

Lawrence Livermore Laboratory

COMPUTATIONAL STUDIES OF A VOITENKO COMPRESSOR*

P. S. Brown and M. L. Lohmann
Lawrence Livermore Laboratory
Livermore, California 94550

ABSTRACT

Two successful shock tube experiments[1] were recently performed at the Lawrence Livermore Laboratory. The experiments simulated the high enthalpy flow conditions that might arise in the nuclear blast encounter of a tunnel-based missile. The experiments, using a modified Voitenko high explosive generator, produced megabar pressure conditions at the inlet of the 2 cm-diameter air-filled shock tubes.

Computer calculations have been done to model the 10^5-fold increase in air pressure in the Voitenko generator. These calculations are necessary to describe the source for the experiments and to permit better interpretation of the experimental data. A detailed understanding of the phenomenology of the compressor is also essential for optimization of future experiments, especially those involving scaling up to larger size shock tubes.

An arbitrary Lagrange-Eulerian computer code was selected to calculate the late-time high explosive driven motion of a steel plate into the bell shaped compressor section. We found that ordinary Lagrangian and Eulerian codes had difficulty in properly treating the steel-air interfaces, whereas an arbitrary Lagrange-Eulerian code was capable of modeling the complex flow of air past the steel interfaces in the compressor region. Using an improved equation of state for air, excellent agreement has been obtained in the source timing for the shock tube experiments, and we now have a much more detailed understanding of the Voitenko generator operation.

*Work performed under the auspices of the U.S. Department of Energy under contract No. W-7405-ENG-48; and DNA Subtask J24AAXIX955.

INTRODUCTION

In May and June of 1978 two shock tube experiments[1] were performed at Lawrence Livermore Laboratory in support of the MX trench program. The purpose of the experiments was to simulate the high enthalpy flow conditions that might be encountered in the nuclear attack of a tunnel-based MX missile. The air-filled shock tubes, one made of steel and the other of grout, each had a 2-cm inside diameter and were driven by a high explosive Voitenko[2,3] compressor. The compressor design was identical to that employed in a similar experiment[4] performed ten years earlier.

It is desirable to understand how the Voitenko compressor works for purposes of designing a more efficient device, especially if the compressor is to be scaled to larger sizes. Accordingly, calculations were done to model its operation. An additional motivation for doing the calculations was to provide a better understanding of experimentally observed pressure pulse shapes and pressure oscillations. Calculations of the Voitenko generator are difficult because of the complex air flow in the late stages of the air compression, which necessitates an Eulerian hydrodynamic treatment. The difficulties are increased when dissimilar materials like air and steel are mixed in an Eulerian cell. The steel mass in the cell overwhelms the air, preventing the air from moving past the steel surface, and in effect, the air sticks to the steel. We used an arbitrary Lagrange-Eulerian code to overcome these difficulties.

Calculational Methods

The Voitenko compressor is depicted in Figure 1. The air chamber pressure is 11 atmospheres, and the air in the exit shock tube is at 1.0 atmospheres. The high explosive burn and the first 20 μseconds of the compressor operation were done with the Vector HEMP[5-7] 2D Lagrangian code. The HEMP configuration at zero time is shown in Figure 2. The high explosive was initiated as a planar source along the left boundary of the problem, and the abscissa is an axis of symmetry. The HEMP configuration at 20 μseconds is shown in Figure 3. The initial motion of the steel plate into the chamber is planar except where the driver plate meets

the steel housing. This lack of planarity is not considered serious since this part of the plate soon impacts the hemispherical portion of the chamber. Only that portion of the HEMP problem between an axial position of 12 cm and 24 cm, and a radial position of 0 cm to 12.06 cm was linked to the Eulerian code.

The calculation was continued using the arbitrary Lagrange-Eulerian code in which problems are described by a quadrilateral Lagrangian grid. The code basically does a Lagrangian treatment using the TENSOR[8,9] difference equations. Individual nodes become Eulerian as needed, when the grid begins to distort or when relative zone thicknesses become too thin. At that time, the code does a second order accurate multifluid Eulerian treatment. The present calculations employed polynomial equations of state for the various materials. An improved equation of state[10] was used for the air and was modeled in the code by a 28 term ratio of polynomials. The code has recently acquired a strength of materials treatment, an option that was not available at the start of these calculations.

Results

The configuration and zoning at 20 μsecs are shown in Figure 4. The abscissa is an axis of symmetry and the upper boundary is a rigid wall. Figure 5 shows the configuration and velocity field at 23.2 μsecs. The beginning of a radial air jet is visible at a radius of 9 cm; and Figure 6 shows an expanded view of this jet. We had originally tried an ordinary Eulerian code to do this calculation and were unable to observe a radial jet, even when extremely fine zoning was used.

Figure 7 shows the configuration and velocity field at 27.25 μsecs. For economy of calculation, part of the problem from a radial position of about 7.2 cm up to 12.06 cm has been discarded. Figures 8-13 show the further motion of the plate into the chamber and the resulting air flow field. Note the formation of a thin bladder of air between the steel plate and the compressor wall. The plate slows down at 29 μsecs, and by 29.69 μsecs the bladder of air is expanding.

Figure 14 gives a closeup view of the air pouring into the central chamber region just prior to rupture of the diaphragm that separates the 11 atm air in the chamber from the 1 atm air in the shock tube. We estimate that the diaphragm breaks at about 29.75 μsecs which is in excellent agreement with the breakout times of the current experiments of 28.6 μsecs and 29.1 μsecs, and a breakout time of 30.1 μsecs as previously reported[4] for one of the earlier experiments. The breakout time for the earlier experiment has been reduced by 0.6 μsec to account for the shock transit time across a steel pad located between the plane wave lens and the high explosive. The breakout time is probably sensitive to the air chamber pressure which was somewhat different for the three experiments.

Figures 15, 16 and 17 depict the initial flow of the air down the shock tube. There is a significant amount of distortion in the steel plate and the steel housing near the throat of the shock tube at late times and this appears to be restricting the flow from the bladder into the shock tube. We believe that incorporation of strength of materials in the calculation might lessen this distortion and lead to enhanced flow of air into the shock tube. At times from about 30.0 to 30.7 μseconds, the downward radial air velocity in the bladder is about 0.7 cm/μsec at a radial position of 2 cm, the velocity through the constricted region between the plate and housing is about 1 cm/μsec, and the velocity down the shock tube is about 2 to 4 cm/μsec. At 30.7 μsecs we estimate that about 3 gms out of a total initial amount of 29 gms of air has entered the shock tube, and that about 2/3 of the total initial air is still available for flow into the tube (i.e., has not yet been trapped by the steel).

Figures 18, 19 and 20 show the pressure profiles of the air shock developing at late times in the shock tube region. These calculations are now being continued in order to follow the air flow down to the first pressure gage at a position of 30.7 cm (10 cm from the diaphragm). We hope eventually to get a comparison of the calculated pressure pulse with that measured at the 30.7 cm location.

Figure 21 gives the calculated energy delivered to the air as a function of time. The discontinuities in the curves at 27 μseconds result from discarding part of the problem above a radius of 7.2 cm. Only a fraction of the energy is lost in that process. Figure 22 compares the calculated plate and shock trajectories with those measured in the earlier experiments. The experimental points were taken from reference 4.

Conclusions

These calculations have given us a much better understanding of how the Voitenko compressor works. Its operation is considerably more complicated than we had originally conceived (we had not expected formation of an air bladder), and must be analyzed with relatively sophisticated computational methods. It appears that treatment of strength of materials in the steel sections may improve the computational results and allow the air to flow more readily into the shock tube; and it is planned to repeat the calculations including strength of materials.

The computations will be continued until the shock wave passes the location of the first pressure gage. We plan to examine the details of the convergent wave interaction in the inlet region to the pipe in order to explain some of the experimentally observed pressure pulse shapes and oscillations.

Acknowledgments

The authors would like to acknowledge Bob Barton, Gary Henderson, and Tok Suyehiro, without whose ready and able assistance, these calculations would not have been possible.

Reference to a company or product name does not imply approval or recommendation of the product by the University of California or the U.S. Department of Energy to the exclusion of others that may be suitable.

NOTICE

"This report was prepared as an account of work sponsored by the United States Government. Neither the United States nor the United States Department of Energy, nor any of their employees, nor any of their contractors, subcontractors, or their employees, makes any warranty, express or implied, or assumes any legal liability or responsibility for the accuracy, completeness or usefulness of any information, apparatus, product or process disclosed, or represents that its use would not infringe privately-owned rights."

REFERENCES

1. H. D. Glenn, H. R. Kratz, D. D. Keough, and R. P. Swift, High-Energy (Mach 130) Air Shock Propagation in Steel and Grout Pipes, these proceedings.

2. Voitenko, A. E., Generation of High Speed Jets, Soviet Physics-Doklady, 9, 860, April 1965.

3. Voitenko, A. E., Strong Shock Waves in Air, Soviet Physics-Technical Physics, 11, 128, July 1966.

4. B. K. Crowley and H. D. Glenn, Numerical Simulation of a High-Energy (Mach 120 to 140) Air-Shock Experiment, UCRL-71470, 1969.

5. E. D. Giroux, P. S. Brown, M. S. Heppler, and S. A. Leibee, Vector Hemp User's Manual, internal Lawrence Livermore Laboratory report, July 1978.

6. Vector HEMP; a 2D Hydrodynamics Code for the STAR and 7600 computers, in UCRL-50000-77-2, February 1977.

7. M. L. Wilkins, Calculation of Elastic-Plastic Flow, UCRL-7322, Rev. 1, Lawrence Livermore Laboratory, 1969.

8. G. Maenchen and S. Sack, The TENSOR Code, in "Methods in Computational Physics," (Academic Press, N.Y., 1964), Vol. 3, pp 181-210.

9. D. E. Burton and J. F. Schatz, Rock Modeling in TENSOR74, A 2-D Lagrangian Shock Propagation Code, UCID-16719, March 1975.

10. H. C. Graboske, A New EOS for Air, UCID-16901, Lawrence Livermore Laboratory, 1975.

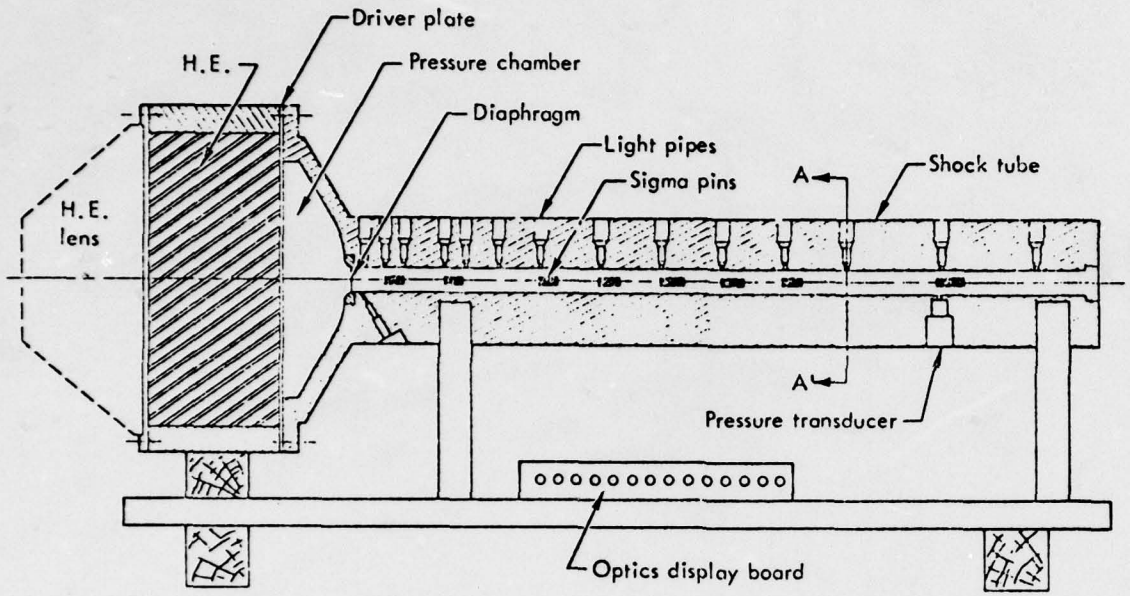

Figure 1. Voitenko compressor, outlet pipe and diagnostic systems.

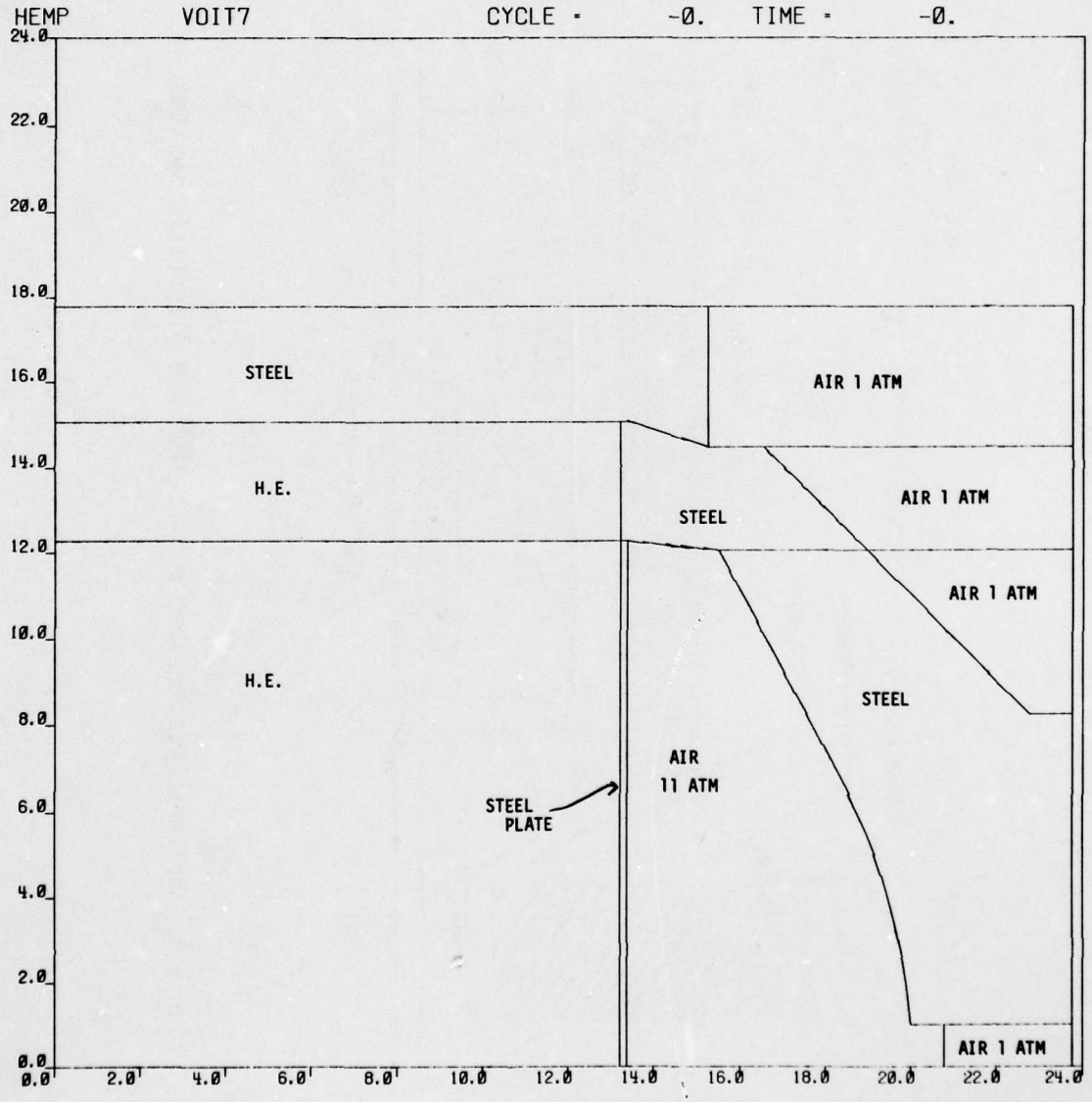

RAME 3

FIGURE 2. HEMP t = 0

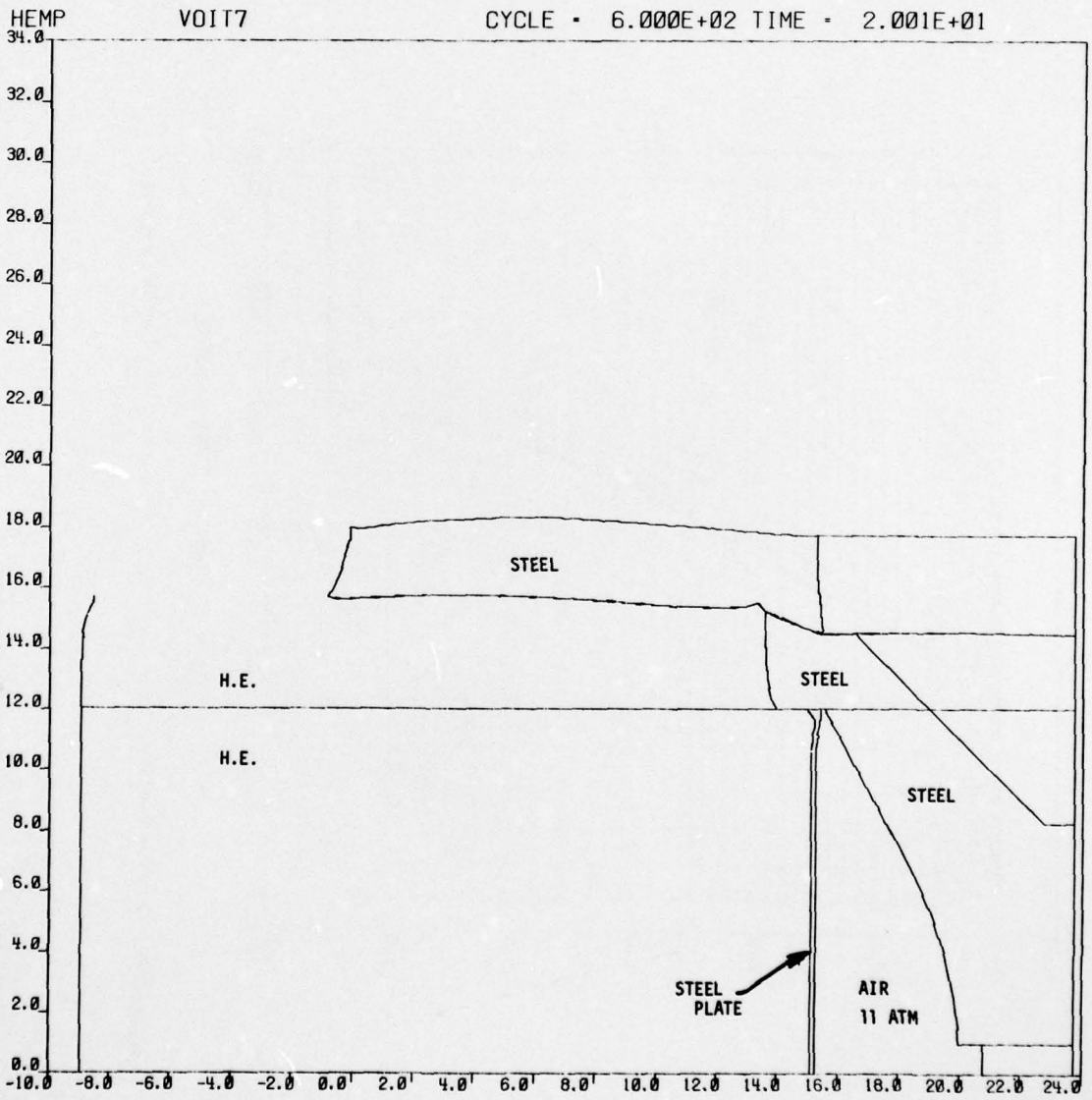

FIGURE 3. HEMP AT LINK TIME TO EULERIAN CODE t = 20.0 μsec.

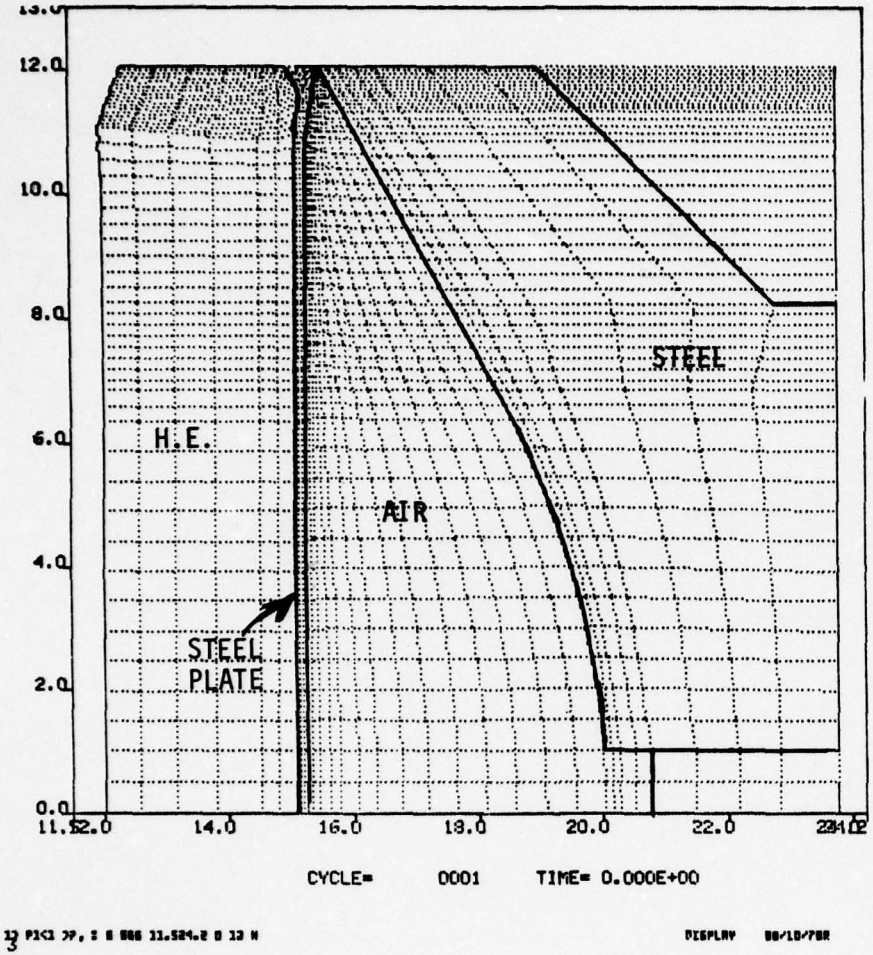

FIGURE 4. t = 20.0 μsec.

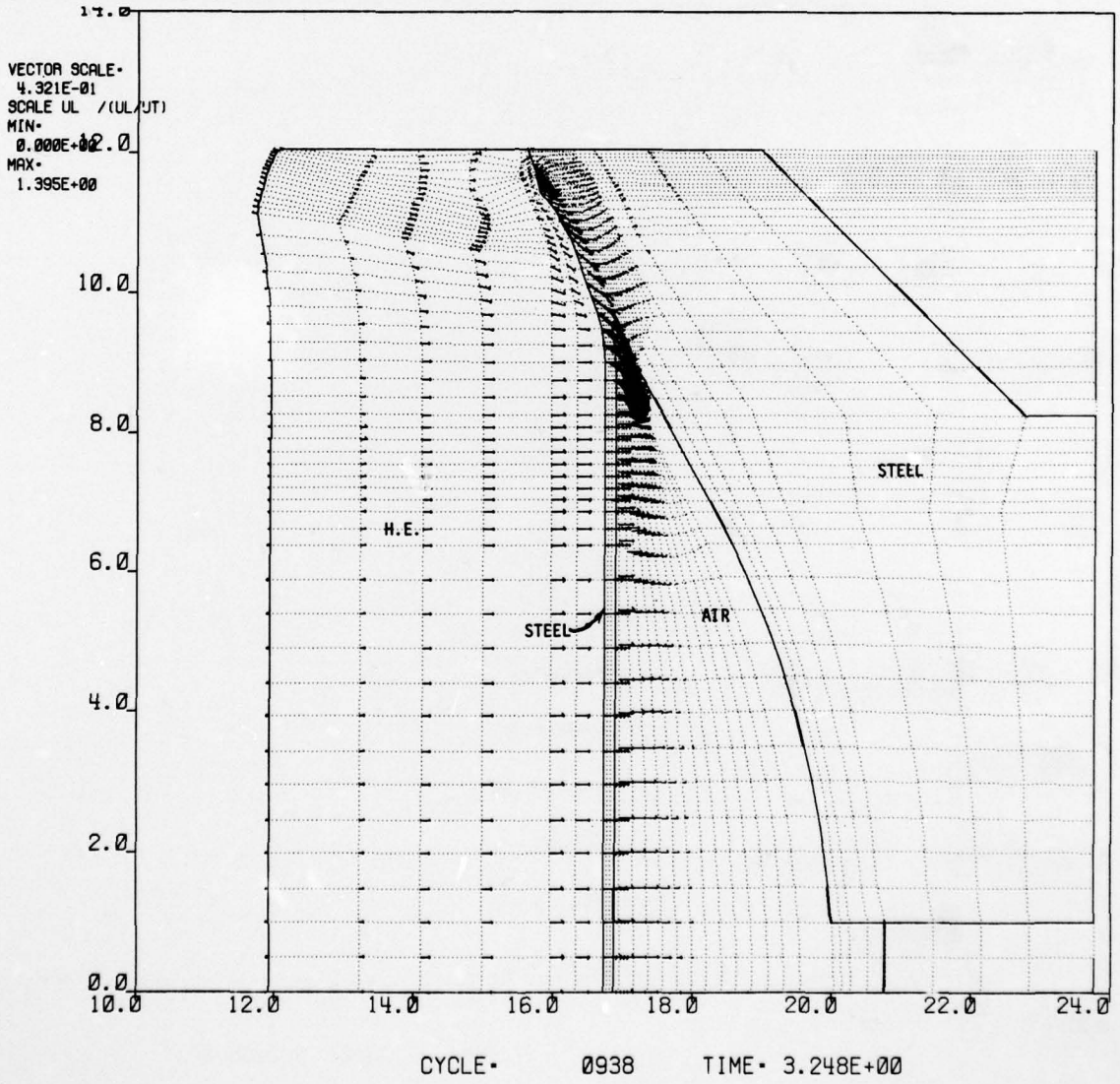

FIGURE 5. t = 23.2 μsec.

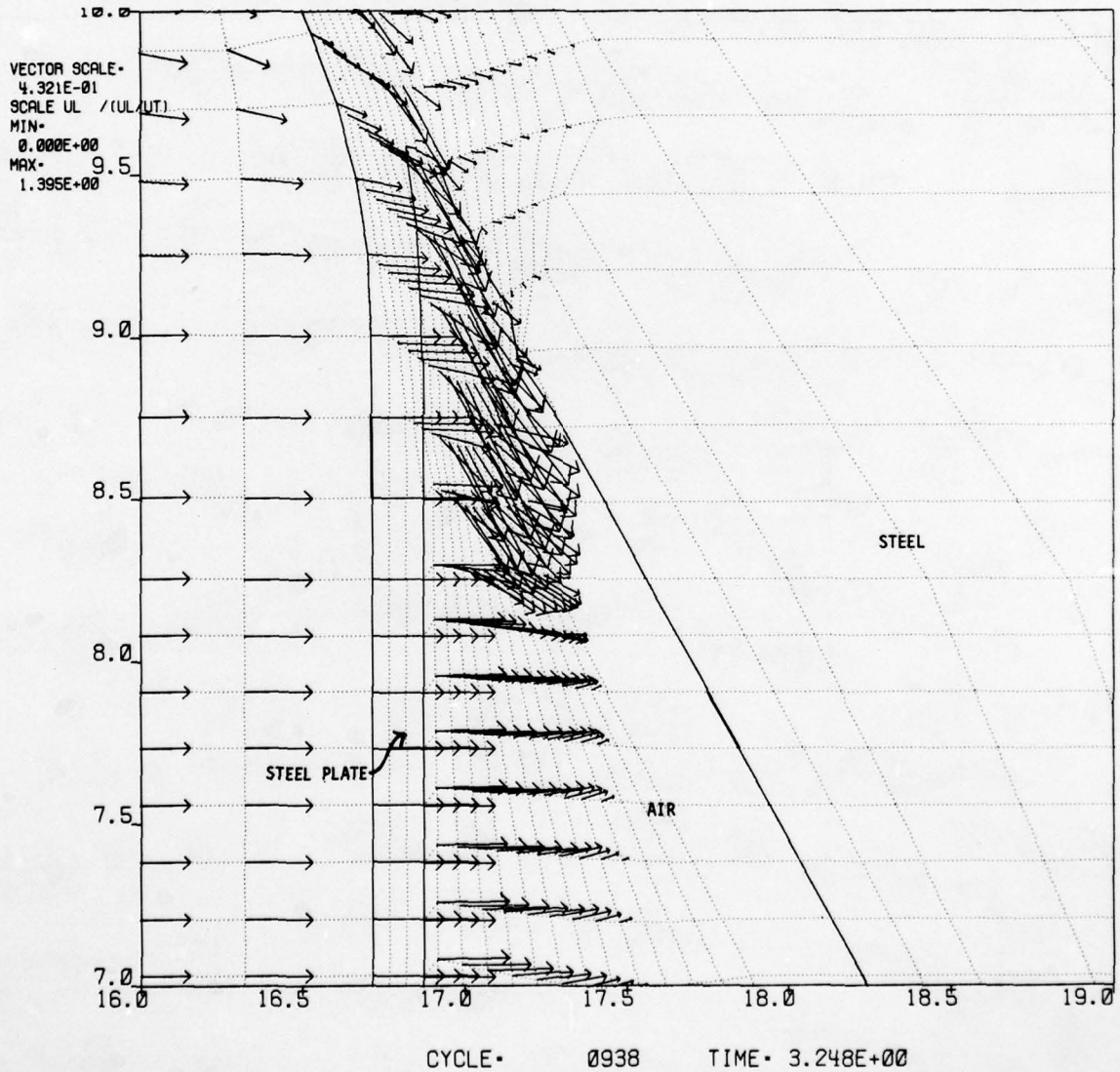

FIGURE 6. t = 23.2 μsec.

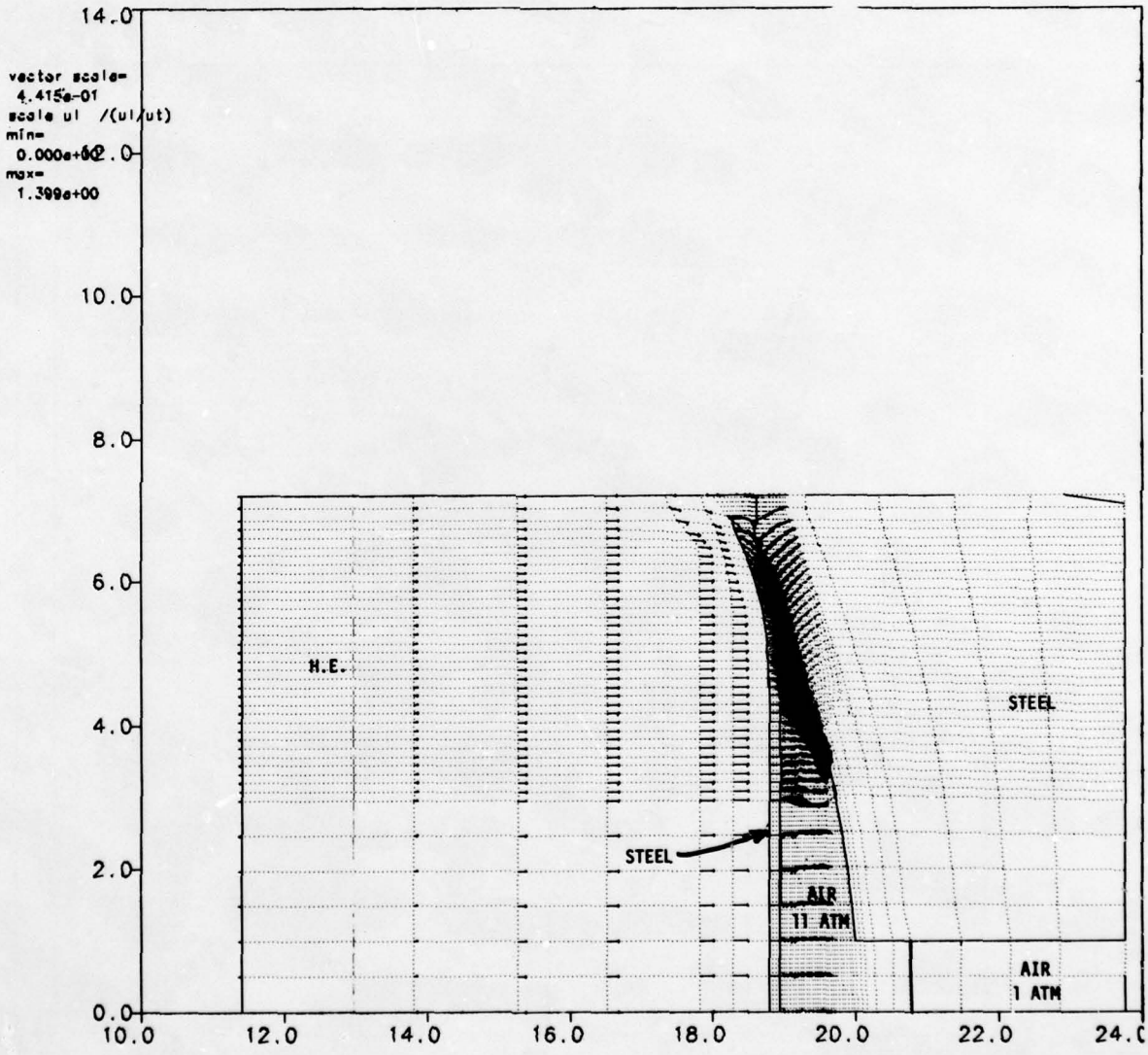

FIGURE 7 t = 27.25 μsec.

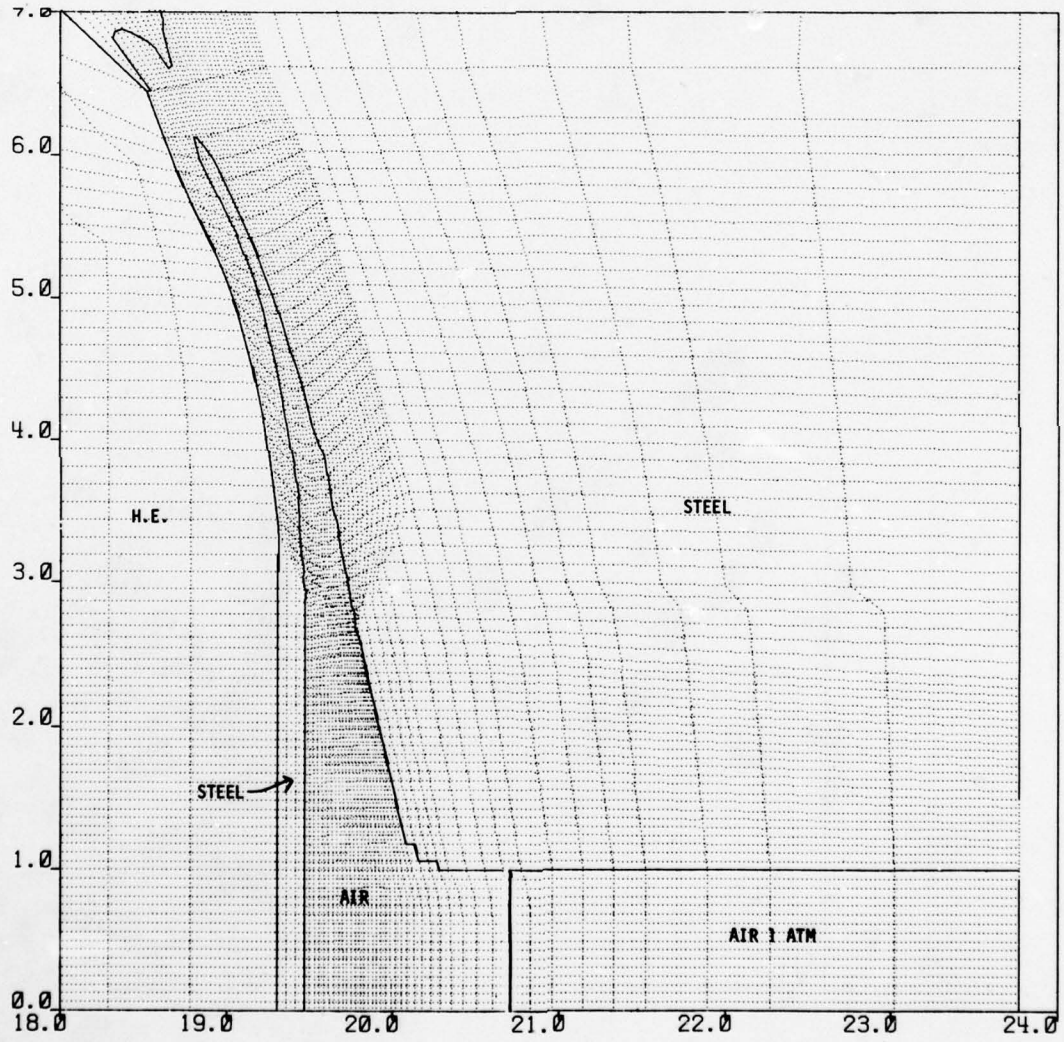

FRAME 3 PIC( )7, : FR80 105 H DISPLAY 10/25/78R

FIGURE 8. ZONING t = 28.25 μsec.

AD-A073 766 GENERAL ELECTRIC CO SANTA BARBARA CA TEMPO F/G 19/4
PROCEEDINGS OF THE NUCLEAR BLAST AND SHOCK SIMULATION SYMPOSIUM--ETC(U)
DEC 78 DNA0001-79-C-0081

UNCLASSIFIED DNA-4797P-2 NL

4 OF 4
ADA 073766

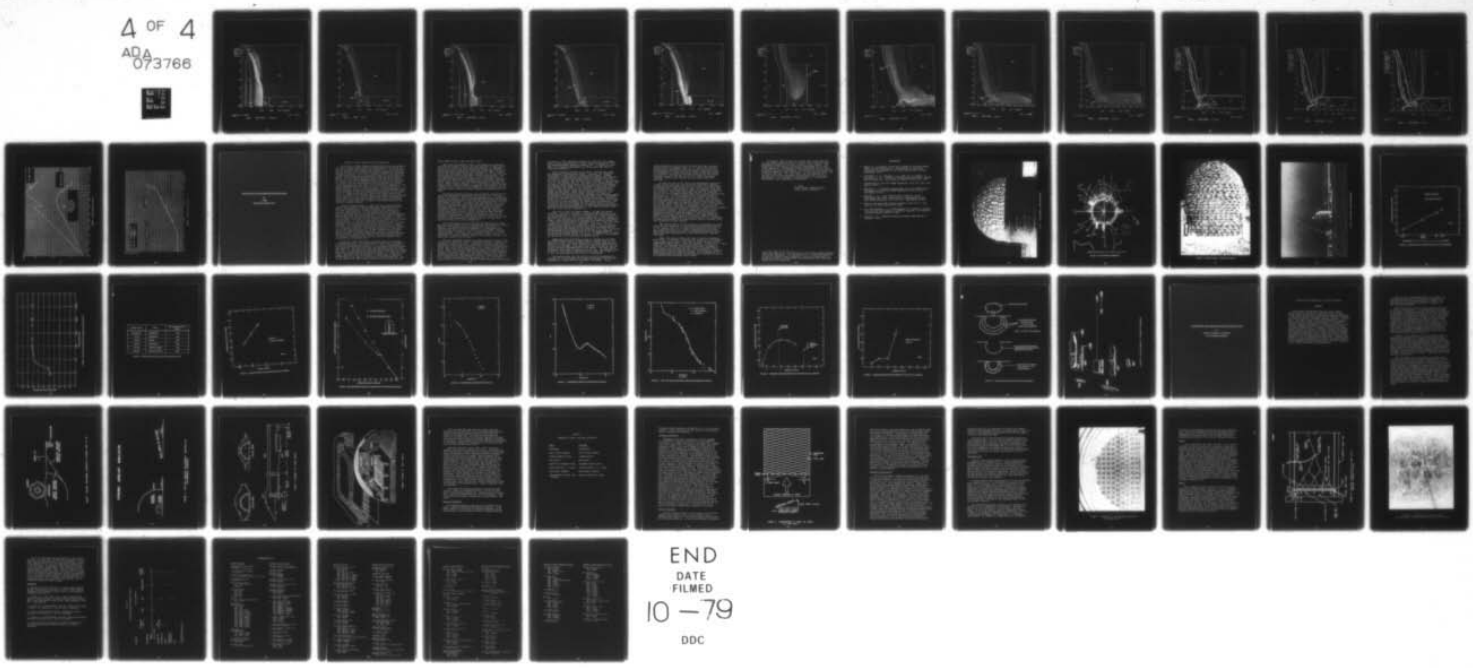

END
DATE FILMED
10 -79
DDC

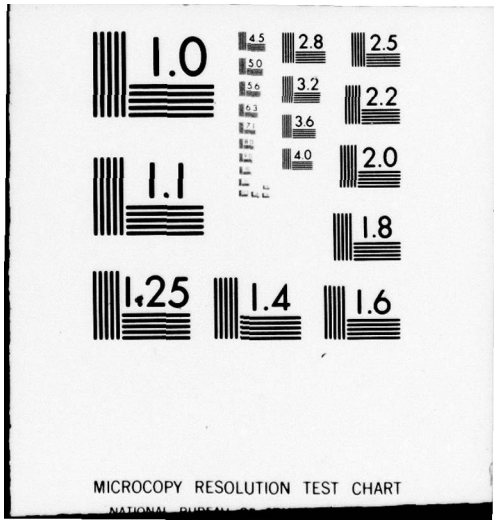
1.0
1.1
1.25
1.4
1.6
1.8
2.0
2.2
2.5
2.8
3.2
3.6
4.0
4.5
5.0
5.6
6.3
7.1
MICROCOPY RESOLUTION TEST CHART

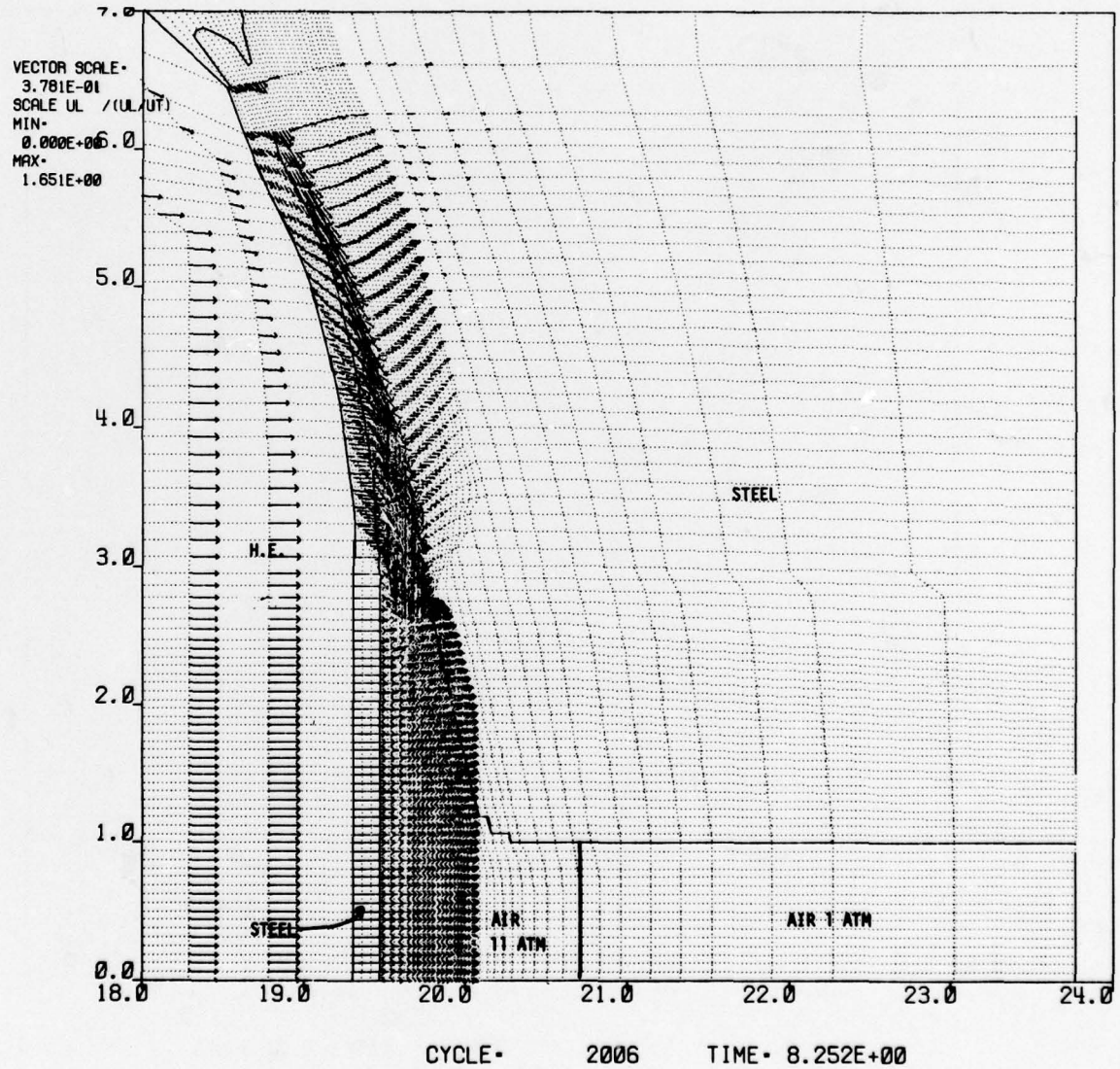

FIGURE 9. VELOCITY VECTORS t = 28.25 μsec.

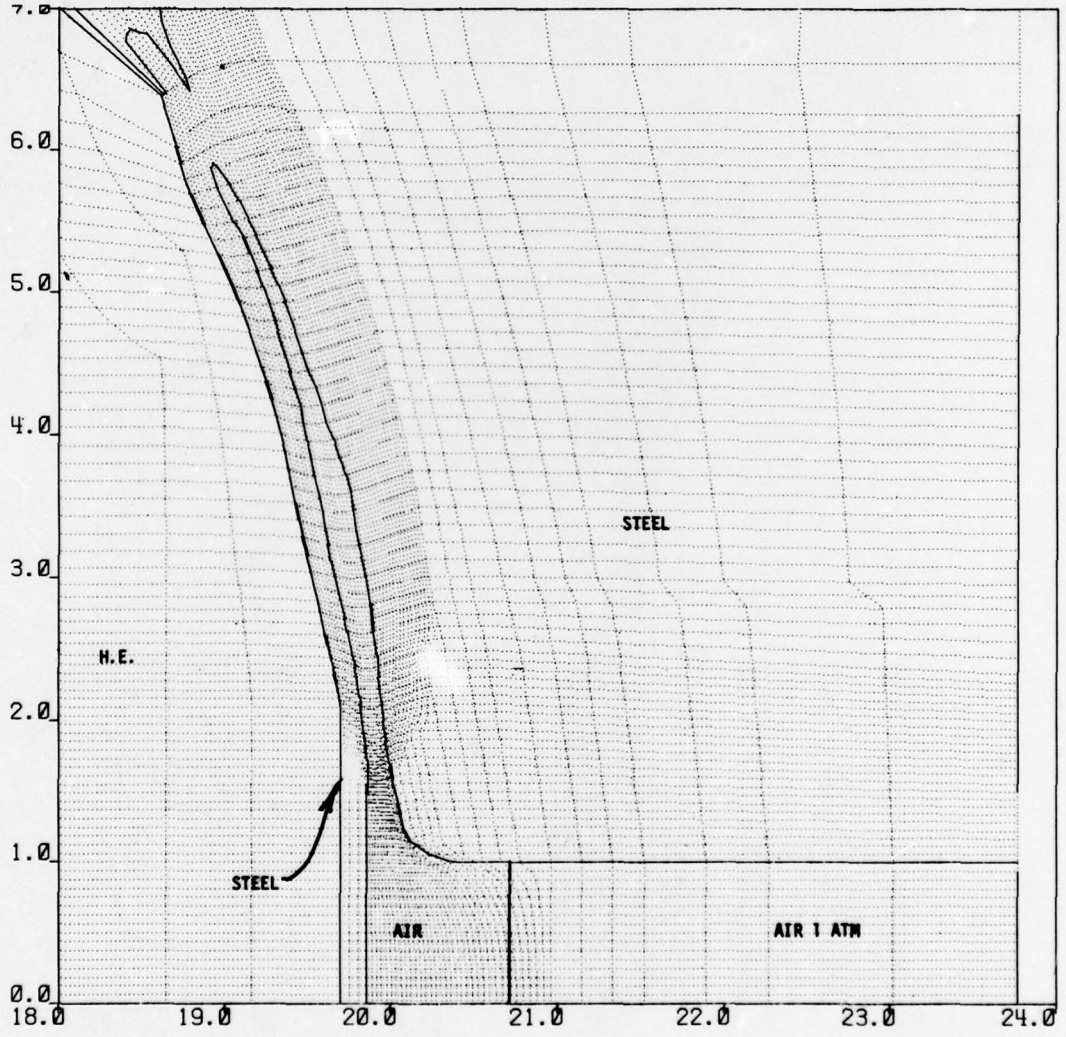

FIGURE 10. ZONING t = 29 μsec.

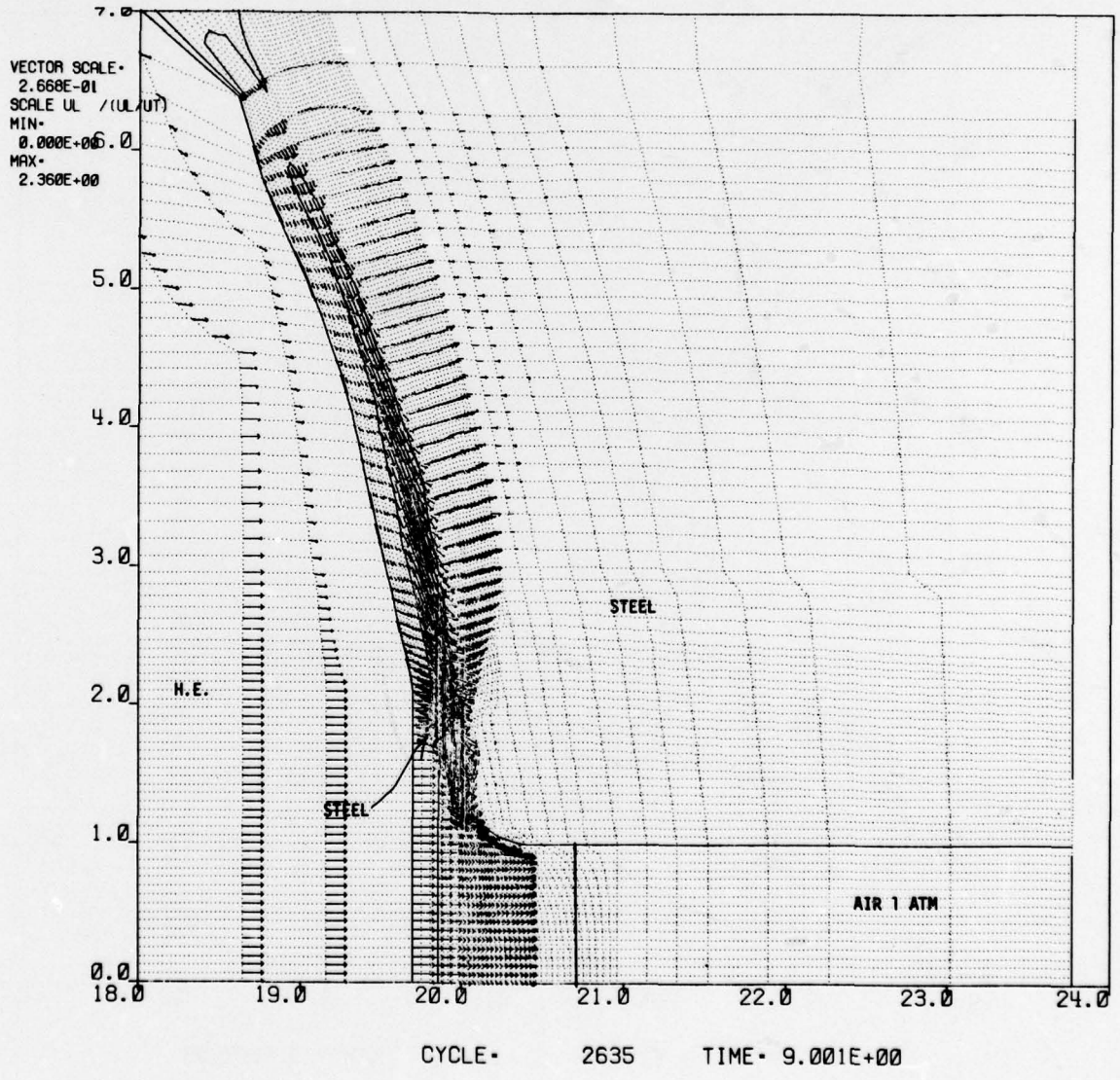

FIGURE 11. VELOCITY VECTORS t = 29 μsec.

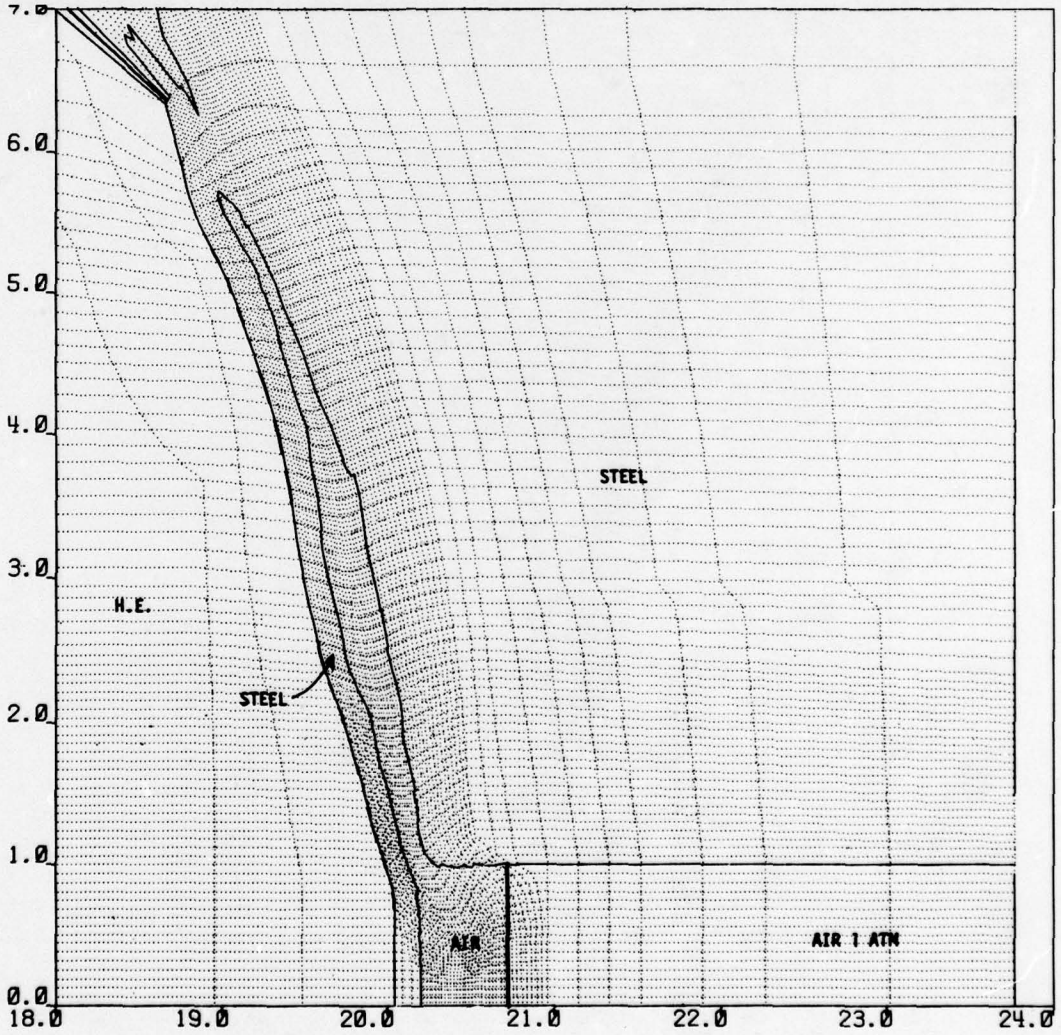

FIGURE 12. ZONING t = 29.65 μsec.

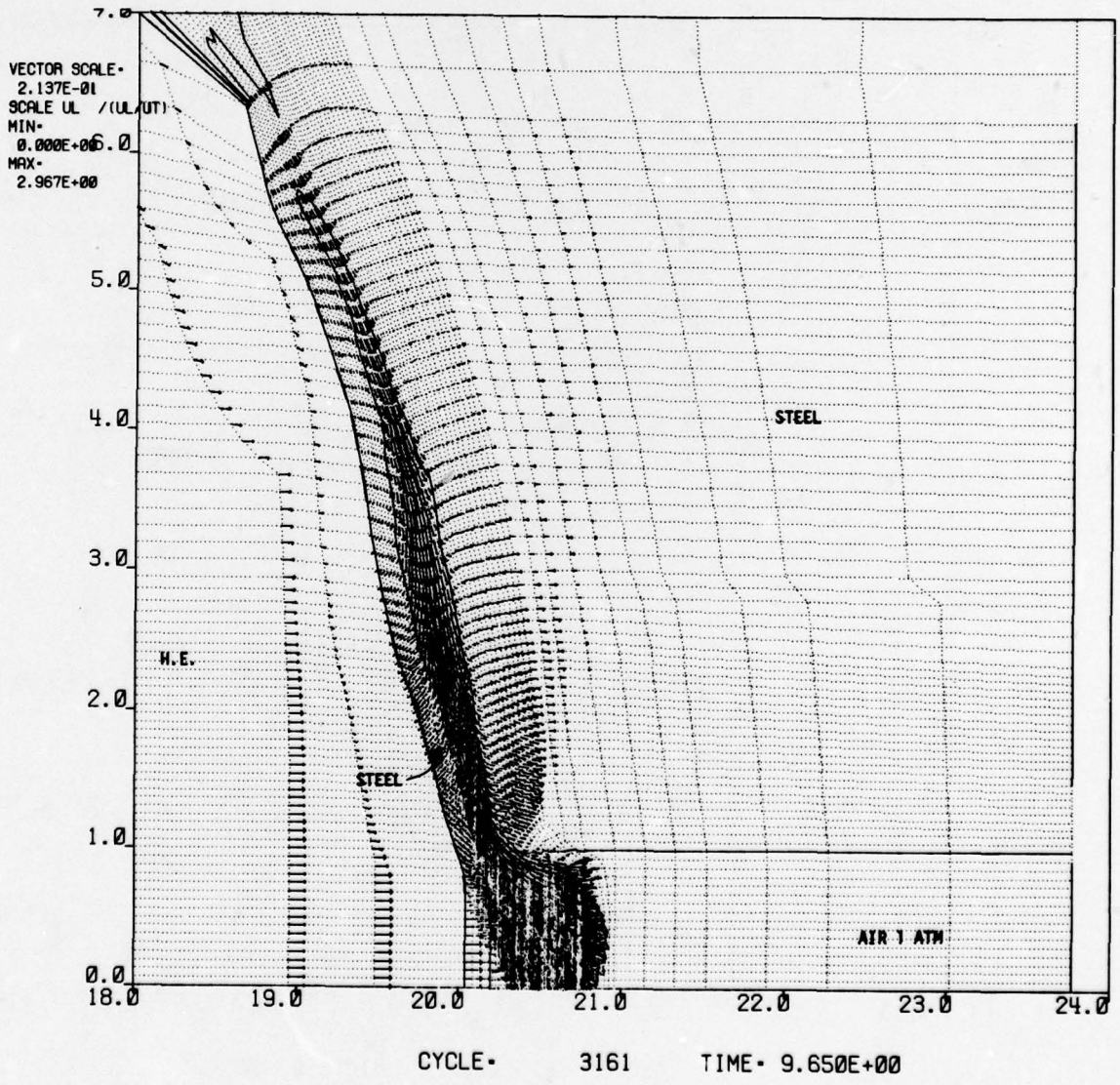

FIGURE 13. VELOCITY VECTORS t = 29.65 μsec.

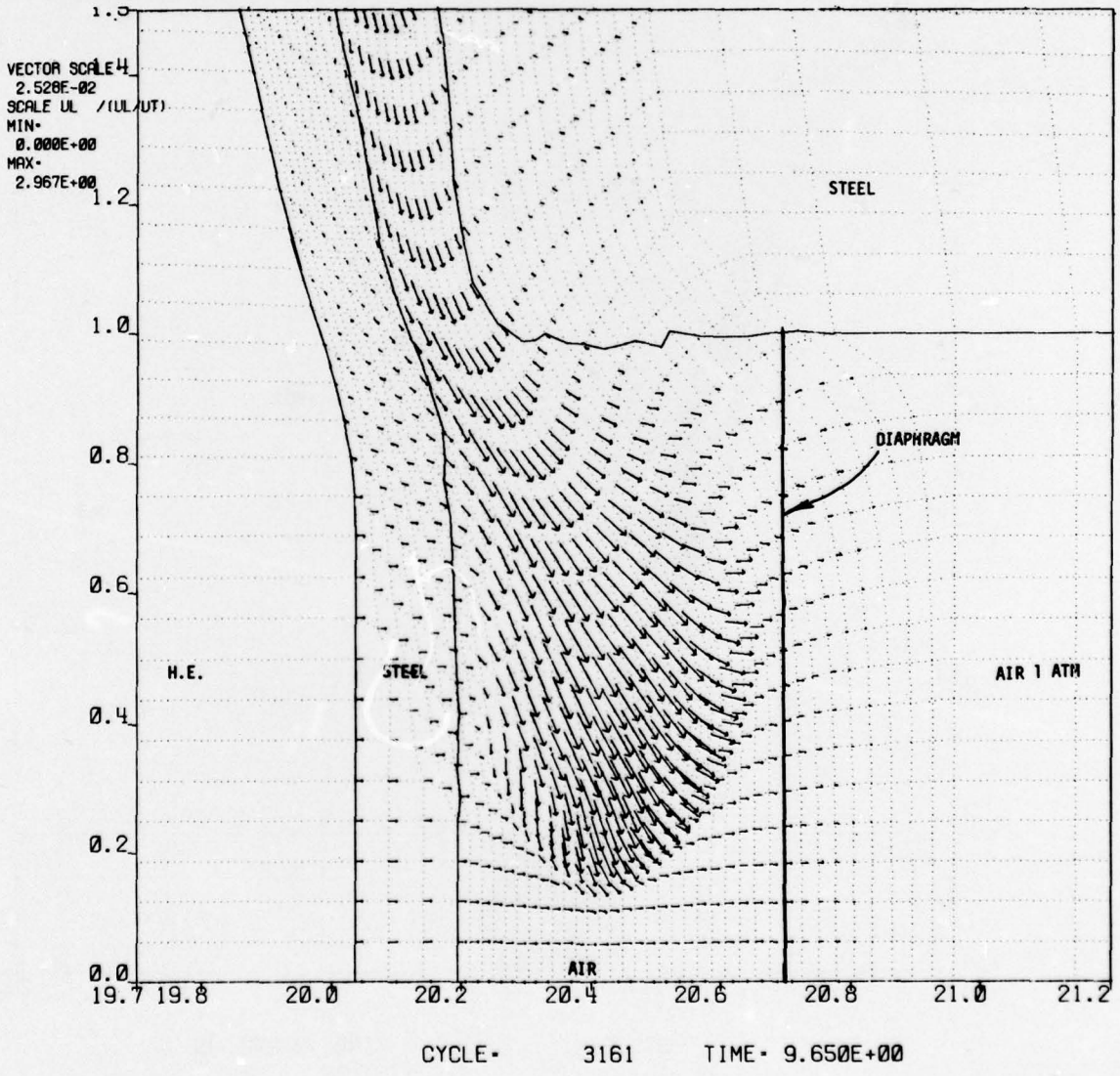

FIGURE 14. VELOCITY VECTORS t = 29.65 μsec.

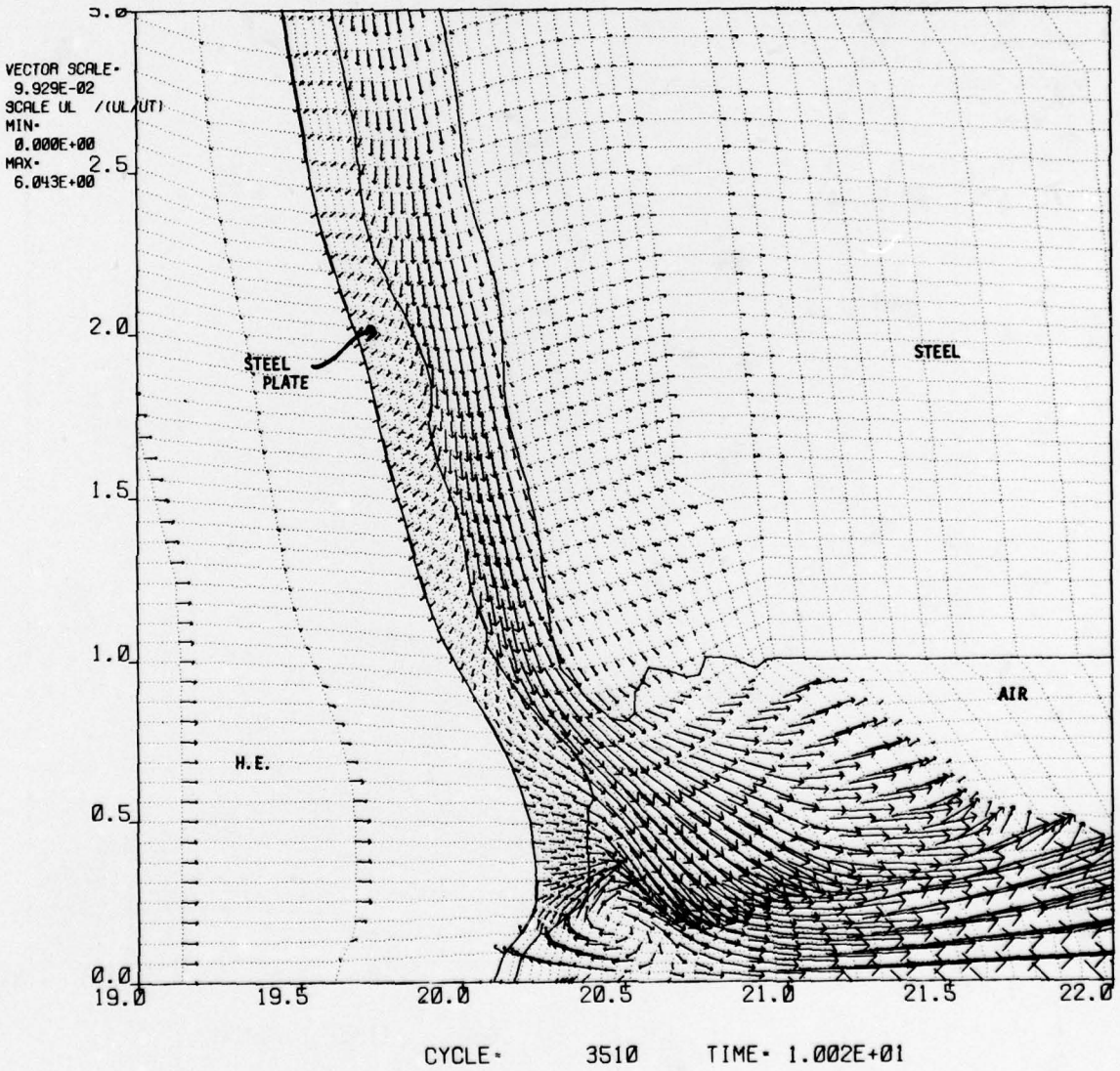

FIGURE 15. VELOCITY VECTORS t = 30 μsec.

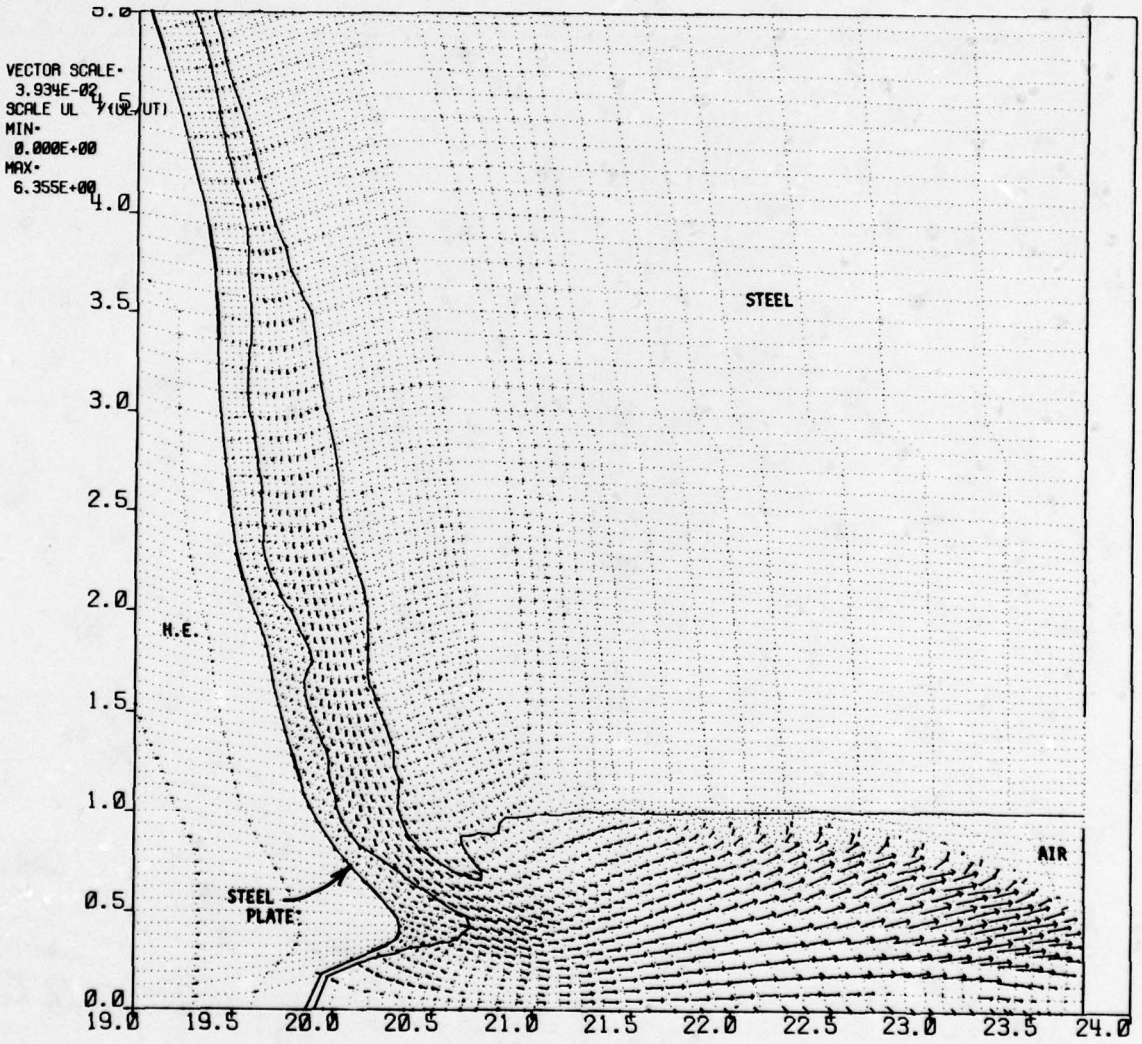

FIGURE 16. VELOCITY VECTORS t = 30.4 μsec.

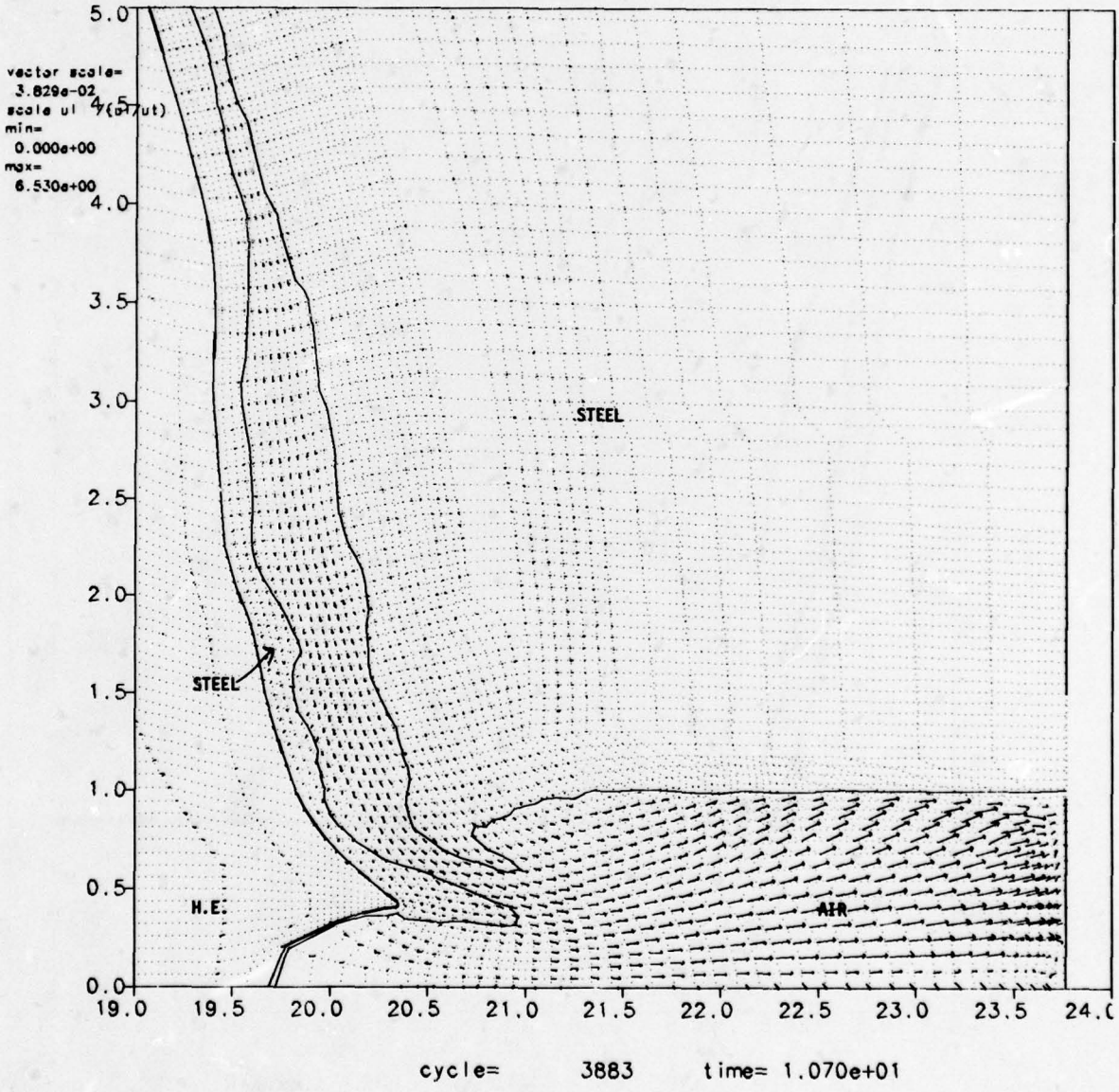

FIGURE 17. VELOCITY VECTORS t = 30.7 μsec.

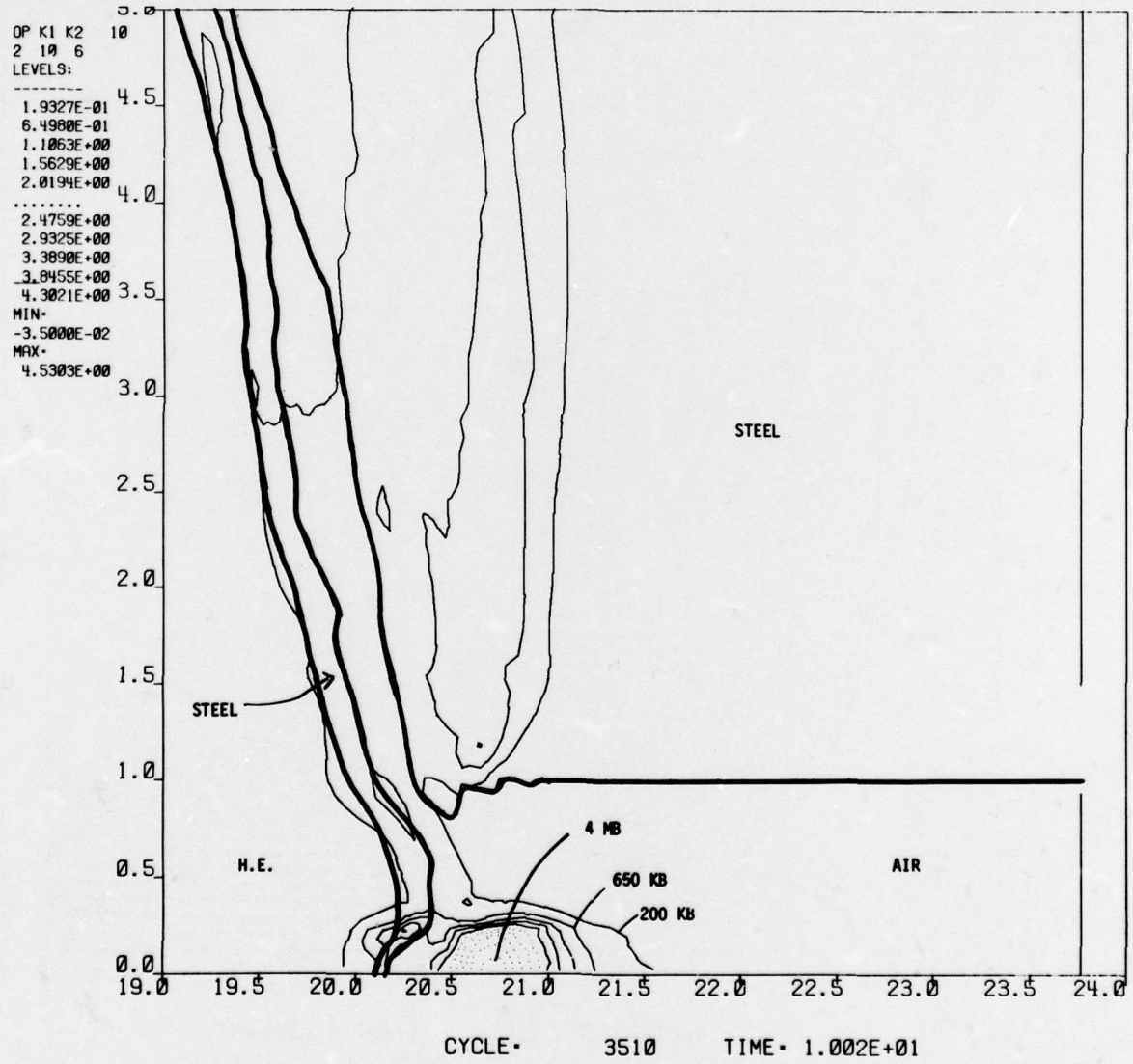

FIGURE 18. PRESSURE CONTOURS t = 30.0 μsec.

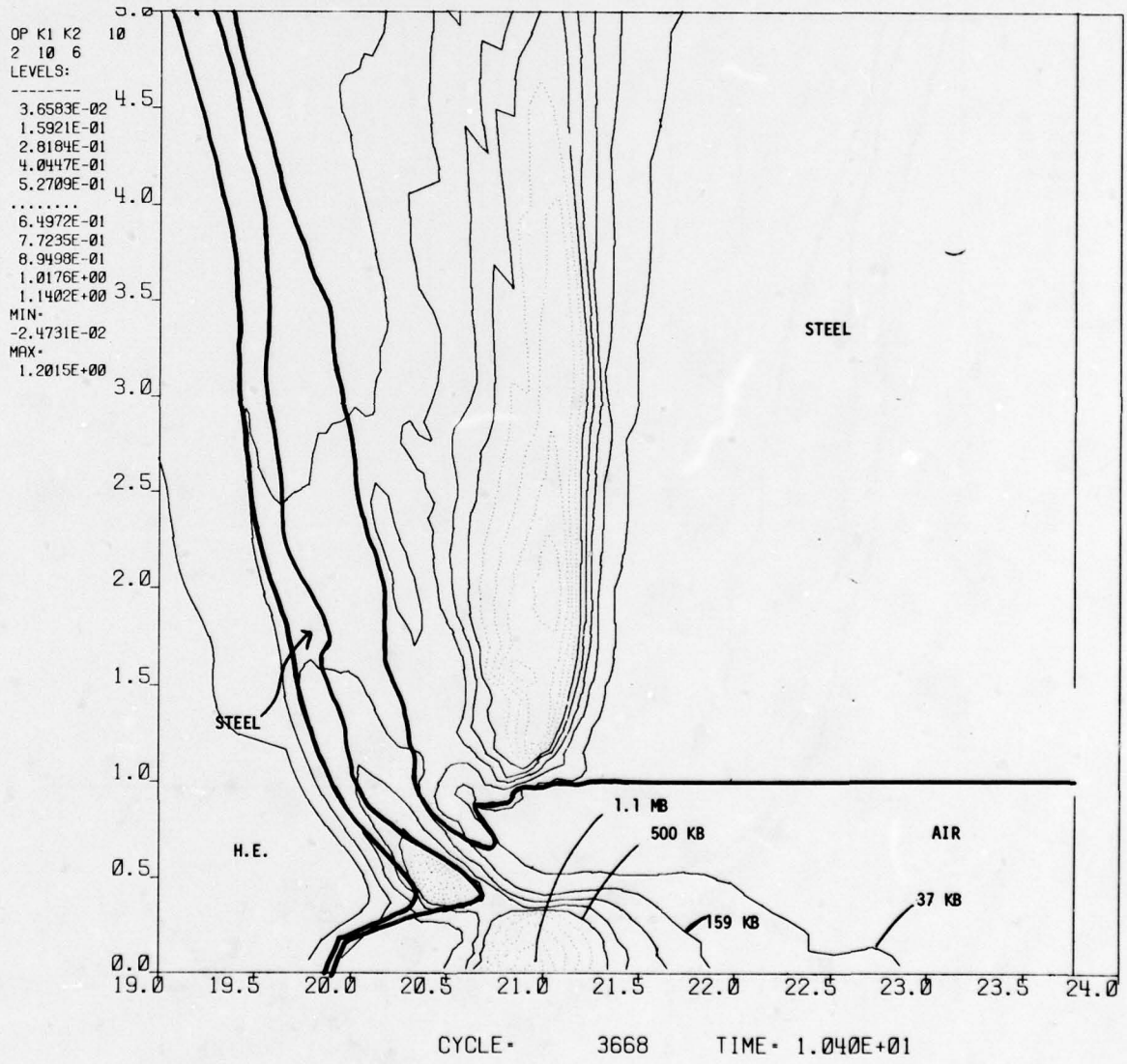

FIGURE 19. PRESSURE CONTOURS t = 30.4 μsec.

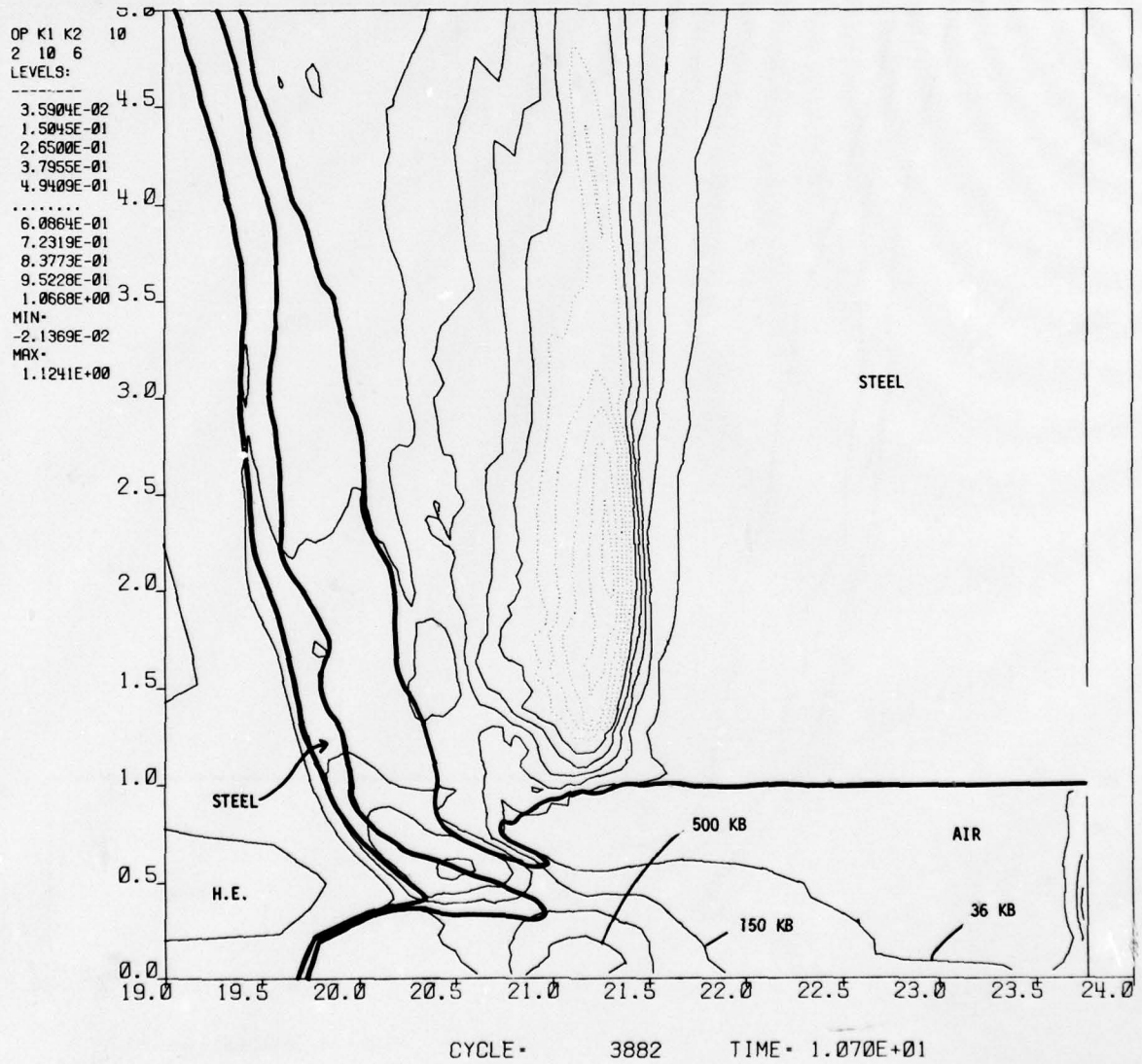

FIGURE 20. PRESSURE CONTOURS t = 30.7 μsec.

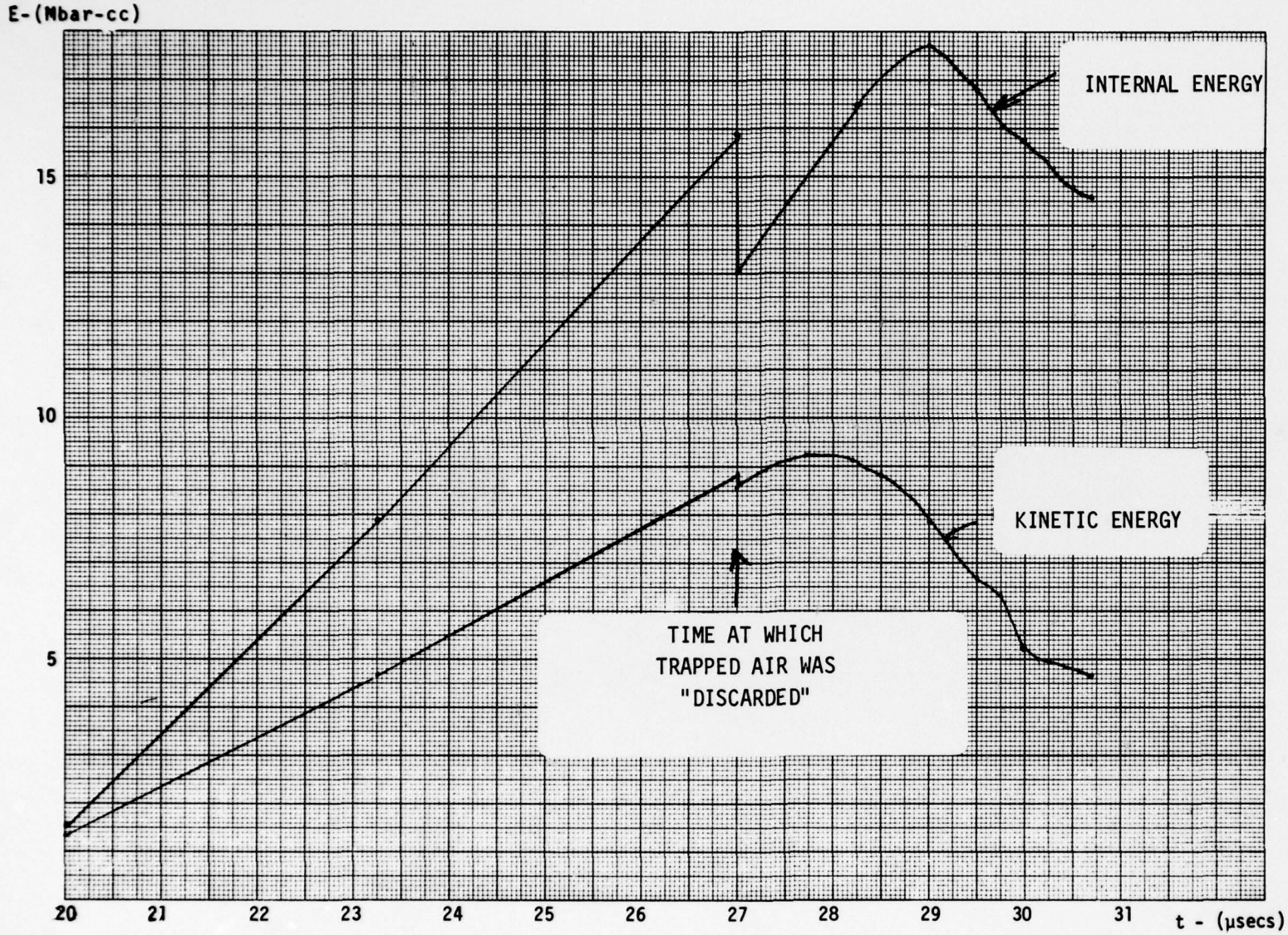

FIGURE 21. Energy delivered to the air.

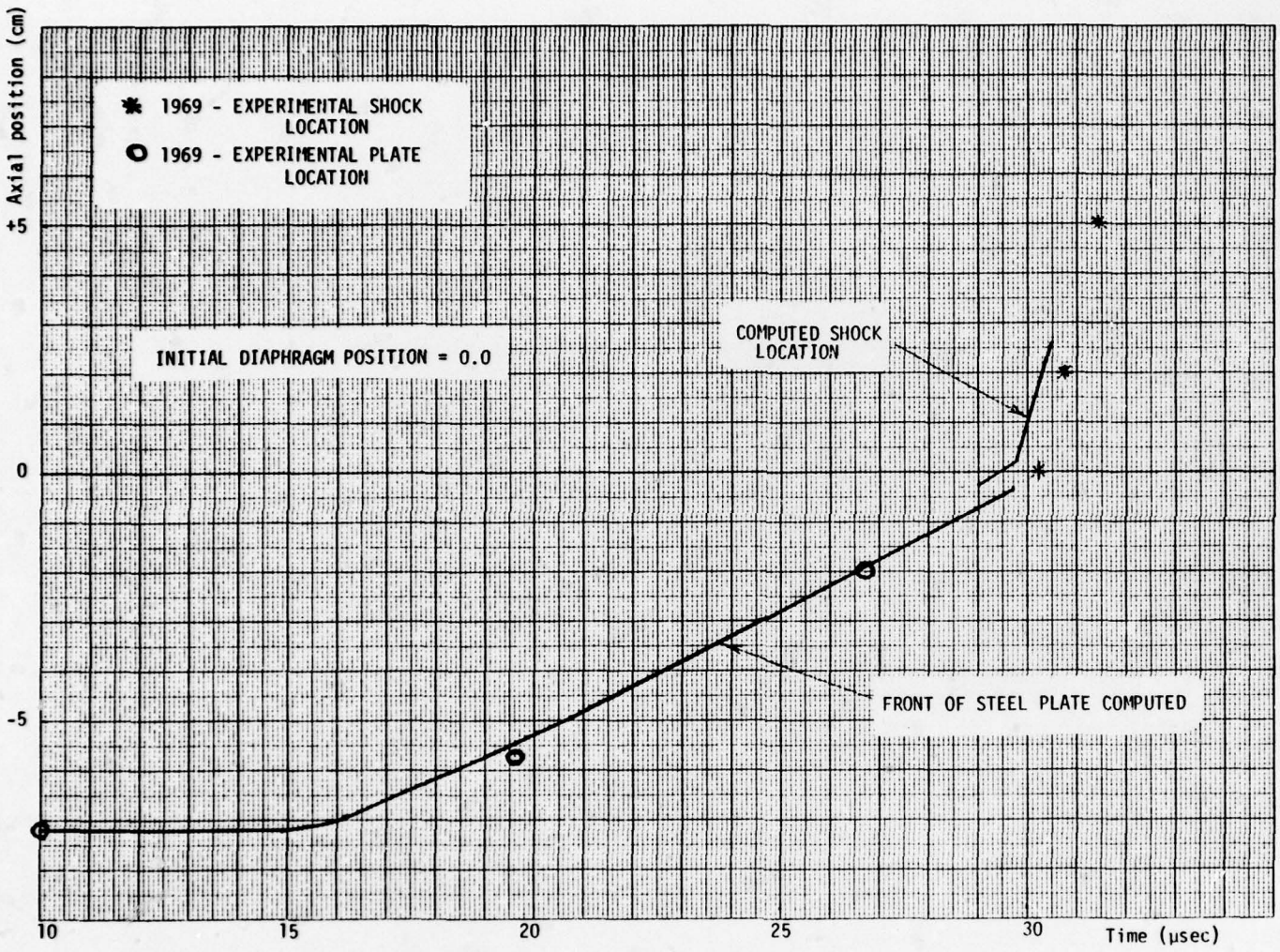

FIGURE 22. Plate and shock trajectories.

ANFO FOR NUCLEAR WEAPONS EFFECTS SIMULATION

by

J. Petes

Naval Surface Weapons Center

ANFO for Nuclear Weapons Effects Simulation

The history of ANFO (ammonium nitrate/fuel oil) as an explosive for use in nuclear weapons blast and shock effects simulation is a short one, hardly twelve years long (reference 1). In the mid-60's, the DNA (Defense Nuclear Agency) was seeking alternative explosion sources for use on its large scale military hardware and structures response operations. TNT (Fig. 1) which had been in use since the nuclear test moratorium had evidenced a number of significant drawbacks. For one, TNT was becoming shorter and shorter in supply because of the military demands brought on by the Vietnam conflict. For another, the cost of preparing large charges such as required for many of the test operations was becoming greater and greater. It was estimated that this total cost for material, preparation, and charge emplacement was one dollar a pound, or $1,000,000 for a 500-ton charge. And on a technical basis, a serious drawback of the block built TNT charges was the unpredictable and severe blast anomalies (reference 2) that were present upon detonation of the charge (Fig. 2). These anomalies, with jetting and ahead running blast waves, extended out to 1,000-ft from GZ and covered as much as 25-30% of the test area. They usually imposed much larger than expected blast forces on the test structures and made analysis of results difficult in some cases and, in others, invalidated expensive and important response studies.

Aware of these problems, in 1966, the Naval Surface Weapons Center (formerly Naval Ordnance Laboratory) suggested the use of ANFO for DNA operations. Enough information about ANFO was available, primarily from the mining industry, to indicate the merits of this explosive. It was readily available; dozens of plants throughout the country made the material in huge quantities-approximately 500 million tons per year. It was cheap; in 1966 the cost of ANFO in 50-lb bags or in tank trucks delivered to a test site was about five cents a pound, (today, it is about ten to fifteen cents a pound). It is safe, relatively insensitive. AN and FO separately are not classed as explosives; mixed as ANFO, it is less sensitive to all the usual tests such as rifle bullet and impact, than TNT. And as deduced from its large use by the mining industry, it is effective, effective in breaking and moving rock and earth. But in 1966 the questions were: Is ANFO effective as an airblast generator? Would it produce anomalies? Could it be made into 500-ton charges? Would the output be predictable and reproducible? These and other questions not faced by the mining industry had to be answered before DNA and the military testing community would accept ANFO as a TNT substitute.

Starting in 1966 with bootleg 8-lb ANFO charges and working up through 1976 with a large multi-agency effort, pre-DICE THROW II, a 120-ton ANFO charge, was fired (Fig. 3); most of the questions posed were satisfactorily answered. So, in October 1976, DICE THROW was conducted - the first full scale DNA sponsored operation using ANFO (Fig. 4). The charge contained 600-tons of ANFO and the results were good - predictable blast and ground shock, and anomalies of less extent and severity than on TNT shots (reference 3). This year in August, ANFO again was the explosive of choice when on operation MISERS BLUFF II six 120-ton charges were fired simultaneously. And on the schedule for 1980, there is planned a 600-ton shot for the

MISTY CASTLE series. ANFO has come of age.

What about the questions asked? And perhaps more important, what are the answers, what are the characteristics of ANFO particularly as it is used in large, multi-ton masses? As indicated previously, much of the early information on ANFO was developed by and for the mining industry for their particular needs. In most mining and earth moving operations, boreholes are drilled into the native rock and earth and the ANFO is poured into the hole. The hole diameters are relatively small, in the neighborhood of 6 to 10 inches and because of the insensitivity of the ANFO, dynamite boosters are used at 10-ft intervals along the length of the boreholes. Hence, much of the information available in 1966 was for small, highly confined charges. For nuclear weapon simulation blast effects tests, large quantities of explosive are required - in the hundreds of tons range - and confinement is to be avoided lest the confining case or structure produce unwanted and deleterious fragments.

The mining industry had shown that unconfined charges had low output as indicated by detonation velocity (Fig. 5). We found similar low output for small charges as measured both in detonation velocity and airblast. But as the charges became larger and larger, apparently self-confinement took place and both detonation velocity and airblast increased. In terms of TNT equivalence (Fig. 6), we found that as the unconfined charge size was increased from 8-lb sizes to 1,000-lbs and larger, the TNT equivalence for airblast increased from 0.47 to 0.82; beyond about 1,000-lbs, the TNT equivalence remains as 0.82. Incidentally, this TNT equivalence is the reason why we now use 120-ton and 600-ton ANFO charges to reproduce the blast effects (beyond a few charge radii) of 100- and 500-ton TNT charges. (Because the detonation velocity and pressures of ANFO are less than those of TNT, we cannot get as high initial airblast pressures as generated by TNT; for most test operations this is of little consequence.)

It is interesting to note that while TNT equivalence of ANFO has stabilized around 0.82 for large charges, the detonation velocity appears to be creeping up as the charges get larger (Fig. 7). Comparing charges with similar geometries, for hemispheres the velocity goes from 4,200 m/s to 4,600 m/s as the charge increases from 1,000-lbs to 100-tons. And for pre-DICE THROW II, a 120-ton capped cylinder, the measured average velocity was 4,790 m/s; for DICE THROW, a charge of similar geometry but weighing 620-tons, the detonation velocity was 5,020 m/s.

Why this continuous increase in average velocity? Again, early data provide a plausible answer. Detonation velocity increases with increases in density (Fig. 8). Translating these data into terms appropriate to the large simulation charges, it seems reasonable to assume that as the charge gets larger, i.e., higher, the prilled ANFO in the lower layers of the charge become more tightly packed, more dense. Hence, it could be expected that higher velocities would be reached in the lower layers. On DICE THROW, where rather extensive detonation velocity measurements were made with rate sticks and by photo interpretation, the detonation velocity, indeed, was found to be a function of the height of the layers (Fig. 9). The lowest layer, which has to be the most densely packed because of all the ANFO

on top of it, had a detonation velocity of 5,600 m/s; the highest layer at which measurements were made - opposite booster #7 - had the lowest detonation velocity (reference 4). It would be nice to make in situ density measurements on future large ANFO shots to check this reasoning.

Now, an obvious question can be asked: how does this changing detonation velocity affect output - airblast, for instance? The evidence is that there is little practical effect. Needham (reference 5) calculated the overpressure and impulse as a function of range for a 600-ton ANFO sphere with two different densities, one with 0.8 grams/cc, and the other with 0.9 grams/cc. For pressure (Fig. 10) and impulse (Fig. 11), you cannot tell the difference. And as shown in the previous figure, the fact that the TNT equivalence for airblast holds steady at 0.82 for charges larger than 1,000-lbs also indicates that output is not affected. It should be noted, however, that airblast is not a particularly sensitive measure of output for any charge - ANFO, TNT, or any other explosive. Ten percent differences in charge weight translate into only 2.1% differences in distances for a given pressure; this difference cannot be ascertained in the field where we are lucky to get ± 10% answers. This is why, incidentally, we use the TNT equivalence of ANFO as 0.8 instead of 0.82 for building large charges; it is easier to multiply by 0.8 and in terms of effects, we cannot tell the difference. The validity of the 0.8 equivalence and the insensitivity of airblast to density variations is summed up in Figure 12 showing the pre-shot predictions and the measured values on DICE THROW; excellent agreement and little scatter (reference 5).

There is at least one other parameter of ANFO that merits attention - the fuel oil content. Commercial ANFO, the kind we use on test operations, is a stoichiometric mixture of ammonium nitrate and diesel fuel oil in a 94.5 to 5.5 weight ratio. This mixture, in which all the reactants are consumed without the need for atmospheric oxygen, gives maximum output as indicated by detonation velocity for a given density and degree of confinement (Fig. 13). Note that quite a spread in FO content can be tolerated - from about 3% to 10% - without severe reduction in detonation velocity. This is fortunate for simulation work because we have found that ANFO manufacturers apparently have some difficulty in maintaining a 5.5% fuel oil content. On DICE THROW the FO averaged about 6% for the whole charge but individual bags ranged between 4.9% to 7%. On MISERS BLUFF II, while the average FO content for all six charges was again 6%, one maverick bag was as low as 2% and another as high as 12.7%.

Apparently these variations in fuel oil content do not affect the overall charge output; as shown before, pressure data fall on prediction curves. But these variations in a given charge do cause concern. On one hand, the FO content influences the sensitivity to initiation of the ANFO; on the other hand, the variations in fuel oil content introduce inhomogeneities in the charge. The lower the FO percentage, the higher the sensitivity (Fig. 14). The material even at 2% FO is still pretty insensitive but we would like to keep it at the 4-6% level where we get the best of everything.

The maverick bags with too high or too low FO percentages invalidate one of the possible and claimed advantages of ANFO charges - homogeneity of charge material throughout the charge. It was

inhomogeneities in TNT block built charges that were considered to be a source of anomalies (Ref. 2). It may be that the few anomalies still witnessed on ANFO shots, while less severe and less extensive than those seen on TNT shots, originate in these FO discrepancies. Better production control at the ANFO plants is called for. This may be nit-picking considering the overall advantages of ANFO over TNT, but if it is easily and cheaply attained, efforts to get uniform fuel oil content would be desirable.

So much for some of the hydro- and thermodynamic properties of ANFO and how they impact on simulation tests where combined airblast and ground shock effects are of concern as on DICE THROW and MISERS BLUFF. ANFO because it comes in convenient 50-lb bags can be used in many configurations other than spheres, hemispheres, and cylinders. A few years back, ANFO was used for simulating craters and direct-induced ground shock from a nuclear weapon surface burst (Ref. 6). In CHEST (Cratering High Explosive Simulation Technique) (Fig. 15), a preformed crater is lined with bags of ANFO and, using multipoint initiation, detonated. The radius of the preformed crater is selected such that the detonation pressure of the ANFO matches some iso-pressure contour of the nuclear burst. The ensuing crater formation and ground shock then is like that from the nuclear burst. This type of arrangement could be used for testing underground structures and facilities - missile silos, command and personnel shelters, utilities, underground stores and other underground structures. Another interesting technical point determined during the CHEST development is that the detonation pressure and velocity could be lowered to meet requirements by adding inert polystyrene beads to the ANFO to lower its density. (And, of course, detonation velocity and pressure can be increased by compacting the ANFO or by using smaller sized or groundup prills thus increasing the bulk density.)

ANFO can be used at sea for testing the vulnerability of Navy ships and their equipment to nuclear weapon proportioned airblast. In one concept (Fig. 16), a large barge loaded with 500-tons, or so, of ANFO can be part of a towed or anchored array with test ships deployed around the charge at predetermined pressure levels. Many ships could participate in a test with realistic, underway conditions.

ANFO could also be used by the Navy to simulate underwater shock waves. A floatable, compliant tank holding up to hundreds of tons of ANFO can be towed to sea, made to flood and sink to some predetermined depth where it would be detonated. Studies (Ref. 7) have shown that a system such as this would work down to a depth of 5,000-ft, that the ANFO, which obviously would be compressed to high density, will reliably detonate. Thus, underwater nuclear weapon bursts could be simulated and with ships underway, realistic operational conditions could be achieved. In sea operations the known hygroscopicity of ANFO can be adequately countered by the use of tarpaulins and waterproof plastic bags.

In summary, ANFO is here for airblast and ground shock use on large target response tests; it can be used to simulate many hydrodynamic effects of military interest in most media*. The properties of the material are as well established as for many other explosives - and probably better established than for most so called "non-ideal" explosives. The material is still relatively cheaper compared to other explosives. It is easily available, easy to handle, and safe. As I once said, only the imagination of military and civilian engineers and scientists can limit the application of large masses of exploding ANFO to its problems; fortunately, this imagination is limitless.

J. Petes
Naval Surface Weapons Center
Silver Spring, Maryland

*Note that ANFO is not the cure-all for all nuclear weapons effects simulation techniques. Its limitations, e.g., large size required to get full output, must be observed. Thus, at present ANFO is eminently suited for large charge configurations; its limitations remain yet to be exploited.

REFERENCES

1. Petes, J., "A History of the Use of ANFO for Nuclear Weapon Blast and Shock Simulation," Proceedings of the Fifth International Symposium on Military Applications of Blast Simulators, 1977.

2. Patterson, A. M., Kingery, C. N., Rowe, R. D., Petes, J., and Dewey, J. M., "Fireball and Shock Wave Anomalies," DASIAC Special Report No. 105, Panel N-2 Report N2-TR 1-70, 1970.

3. Proceedings of the DICE THROW Symposium, 21-23 Jun 1977, DNA Report 4377P-1.

4. Wisotski, J., "Technical Photography from DICE THROW Event," Proceedings of the DICE THROW Symposium 21-23 Jun 1977, DNA Report 4377P-1.

5. Needham, C. E., "DICE THROW Project Officer's Report - Theoretical Air Blast Calculations," Proceedings of the DICE THROW Symposium, 21-23 Jun 1977, DNA Report 4377P-1.

6. Physics International Progress Reports, PIPR 274-1, 1970; PIPR 274-2, 1971; PIPR 274-3, 1971.

7. Kos, DW, Kennedy, J. E., "Development of a System to Deliver and Detonate Large Explosive Charges Undersea," IIT Research Institute Report J6034-25, 1969.

8. Vancik, J. J., "Monsanto Blasting Products ANFO Manual," Monsanto, 1970.

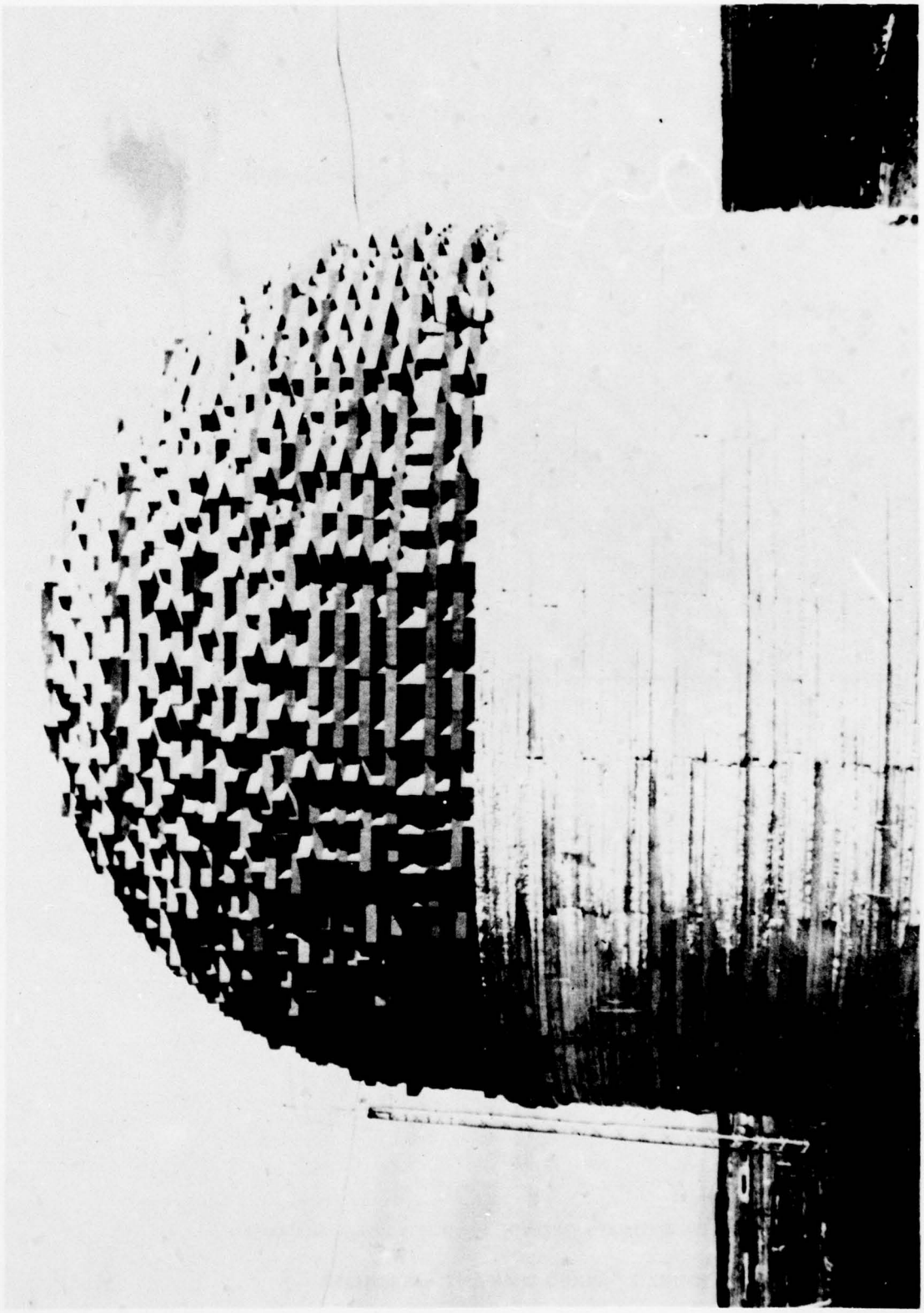

FIGURE 1 MIXED COMPANY – 500-TON TNT CHARGE

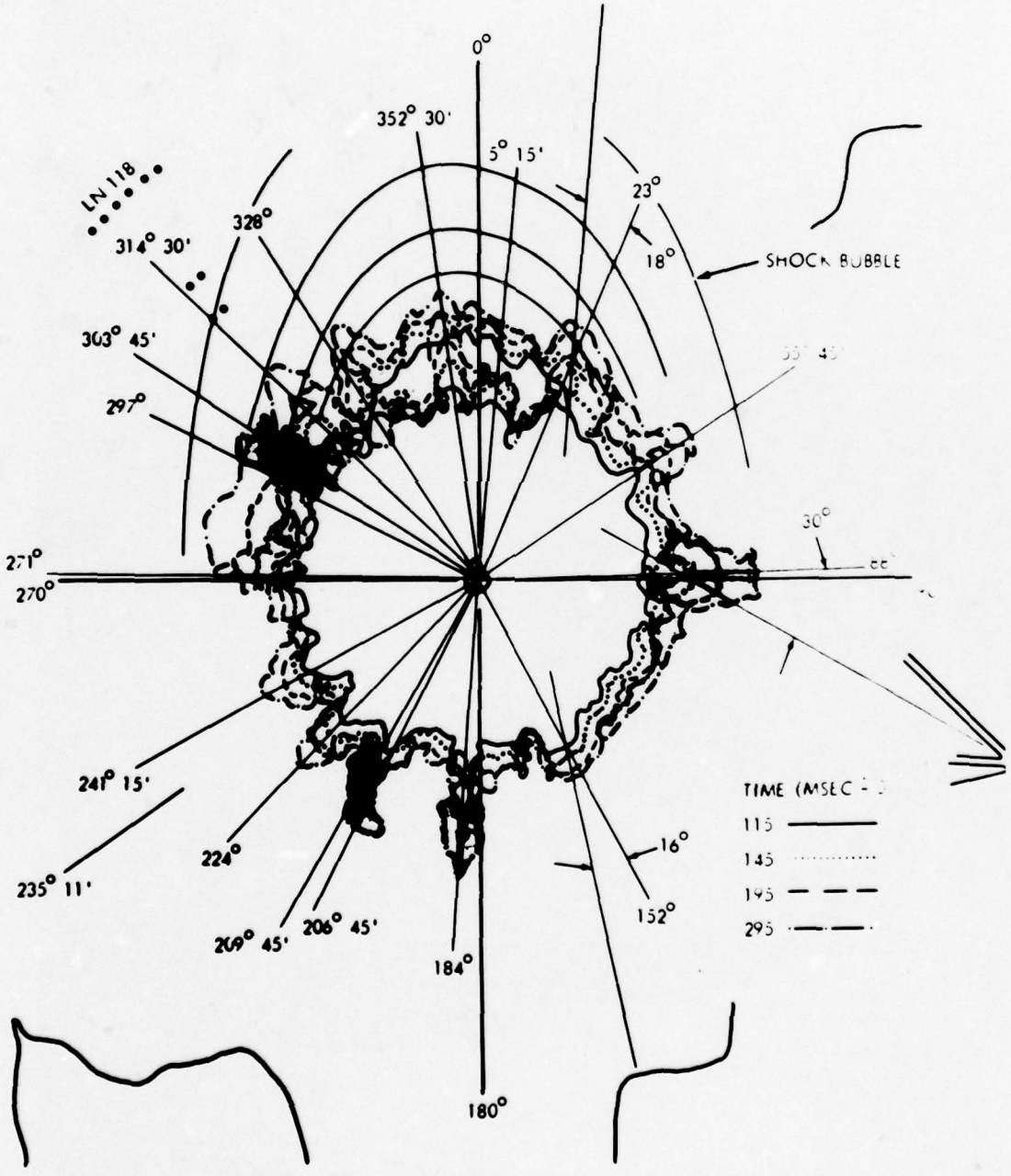

FIREBALL ANOMALY GROWTH AS VIEWED BY AERIAL CAMERA

FIGURE 2 MIXED COMPANY ANOMALIES

FIGURE 3 PRE-DICE THROW II – COMPLETED CHARGE

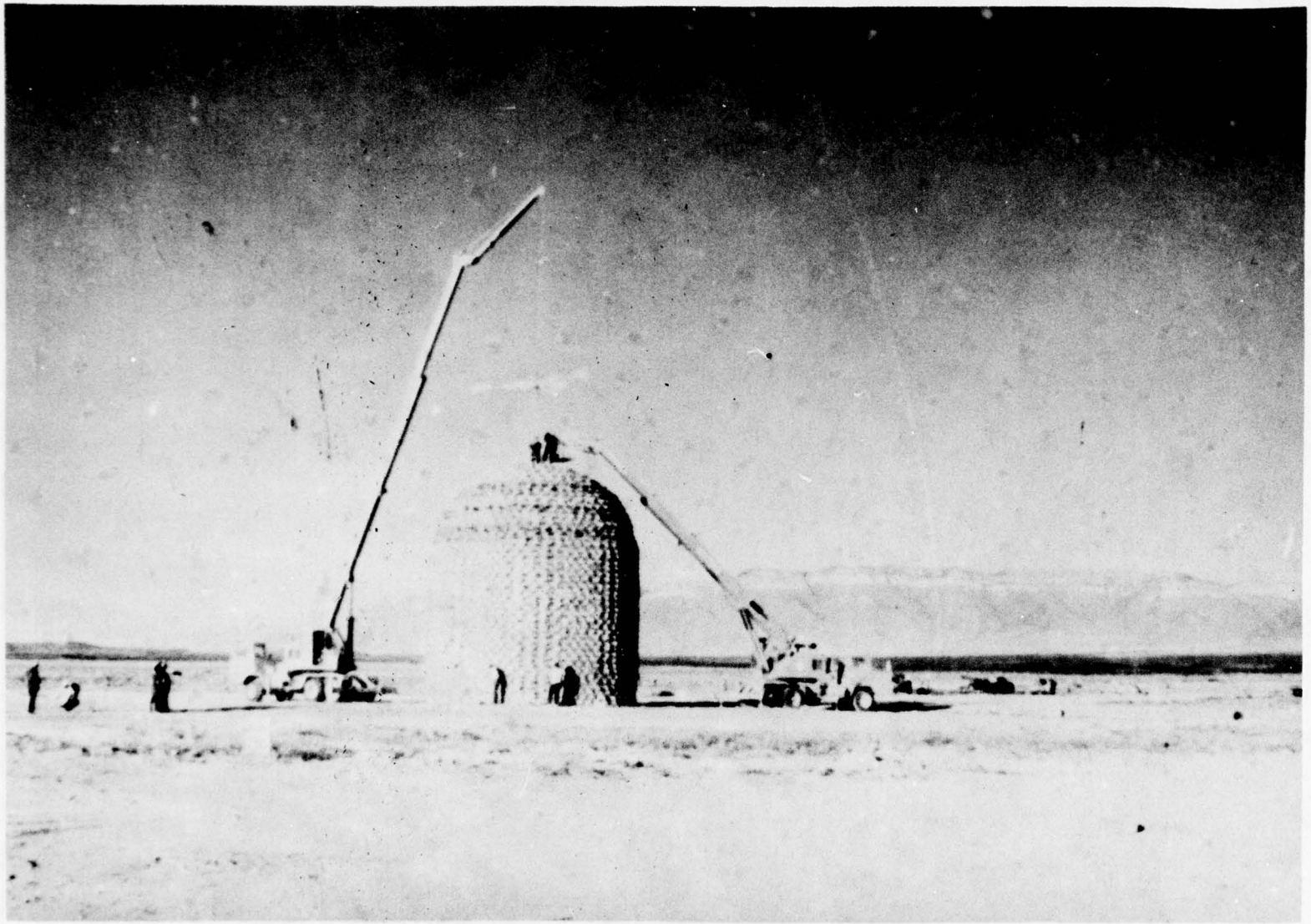

FIGURE 4 DICE THROW – 600-TON ANFO CHARGE

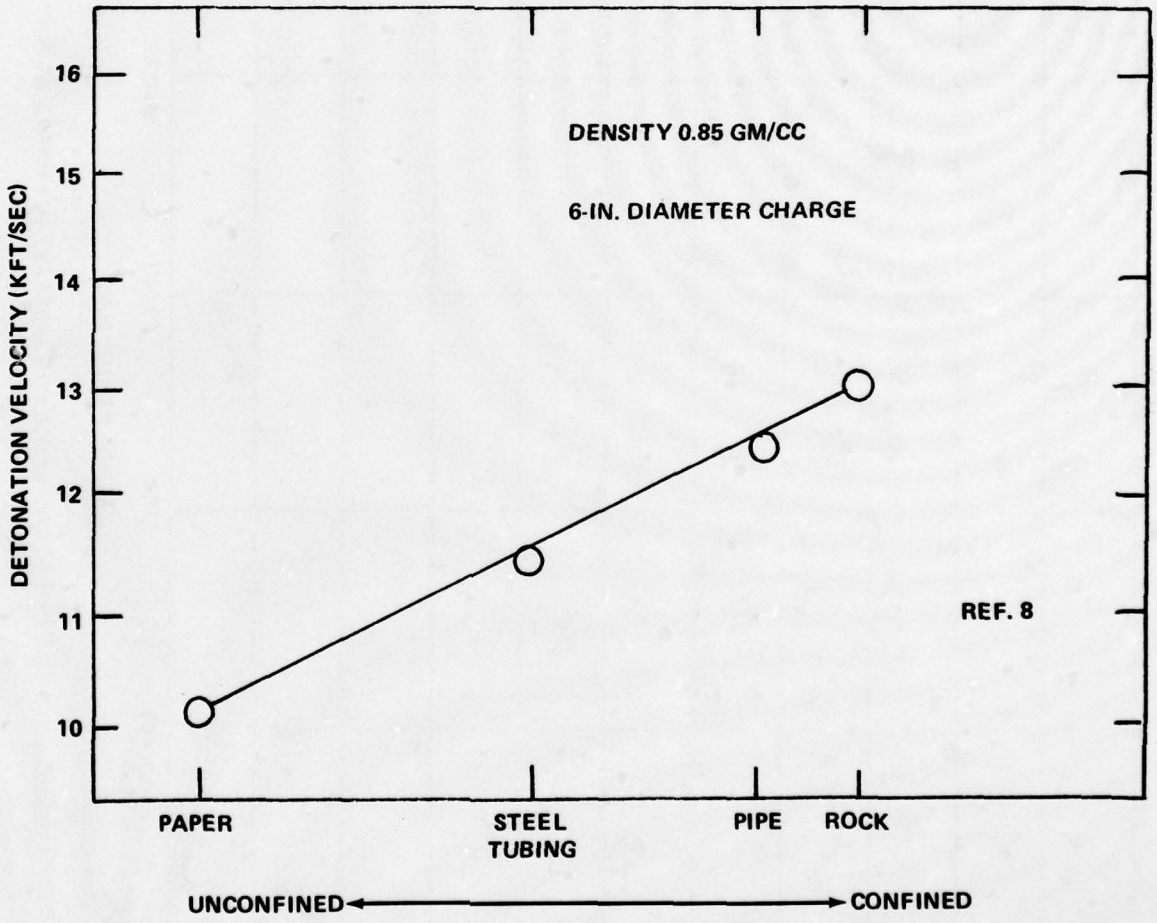

FIGURE 5 CHANGE IN ANFO DETONATION VELOCITY WITH CONFINEMENT

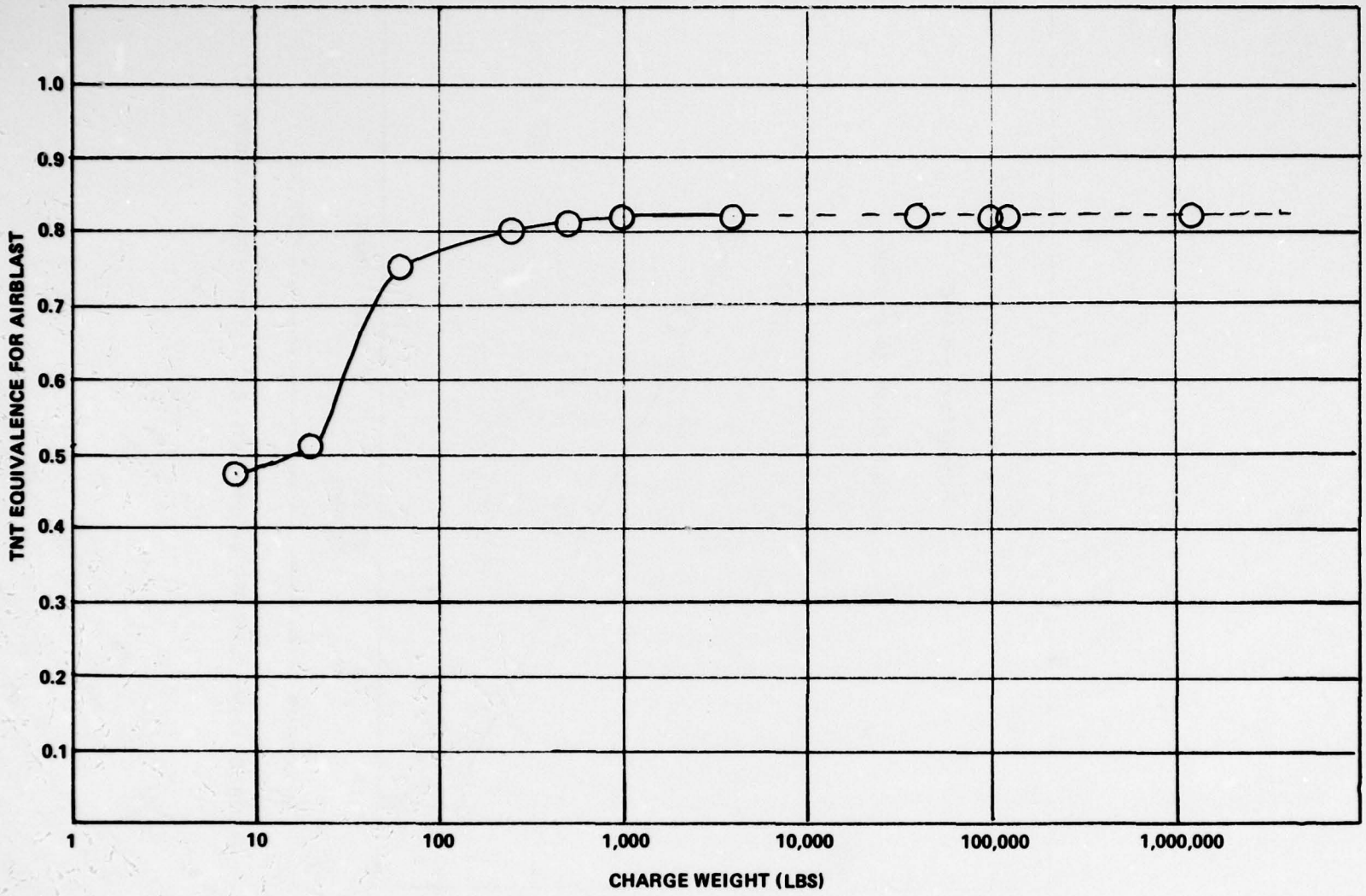

FIGURE 6 ANFO TNT EQUIVALENCE FOR AIRBLAST VS CHARGE WEIGHT

CHARGE WEIGHT	SHAPE	DETONATION VELOCITY (M/SEC)
260–4000 LBS	HEMISPHERE	4200
20-TON	HEMISPHERE	4410
20-TON	SPHERE	4390
100-TON	HEMISPHERE	4600
120-TON	CAPPED CYLINDER	4790
600-TON	CAPPED CYLINDER	5020

FIGURE 7 AVERAGE DETONATION VELOCITIES OF ANFO CHARGES

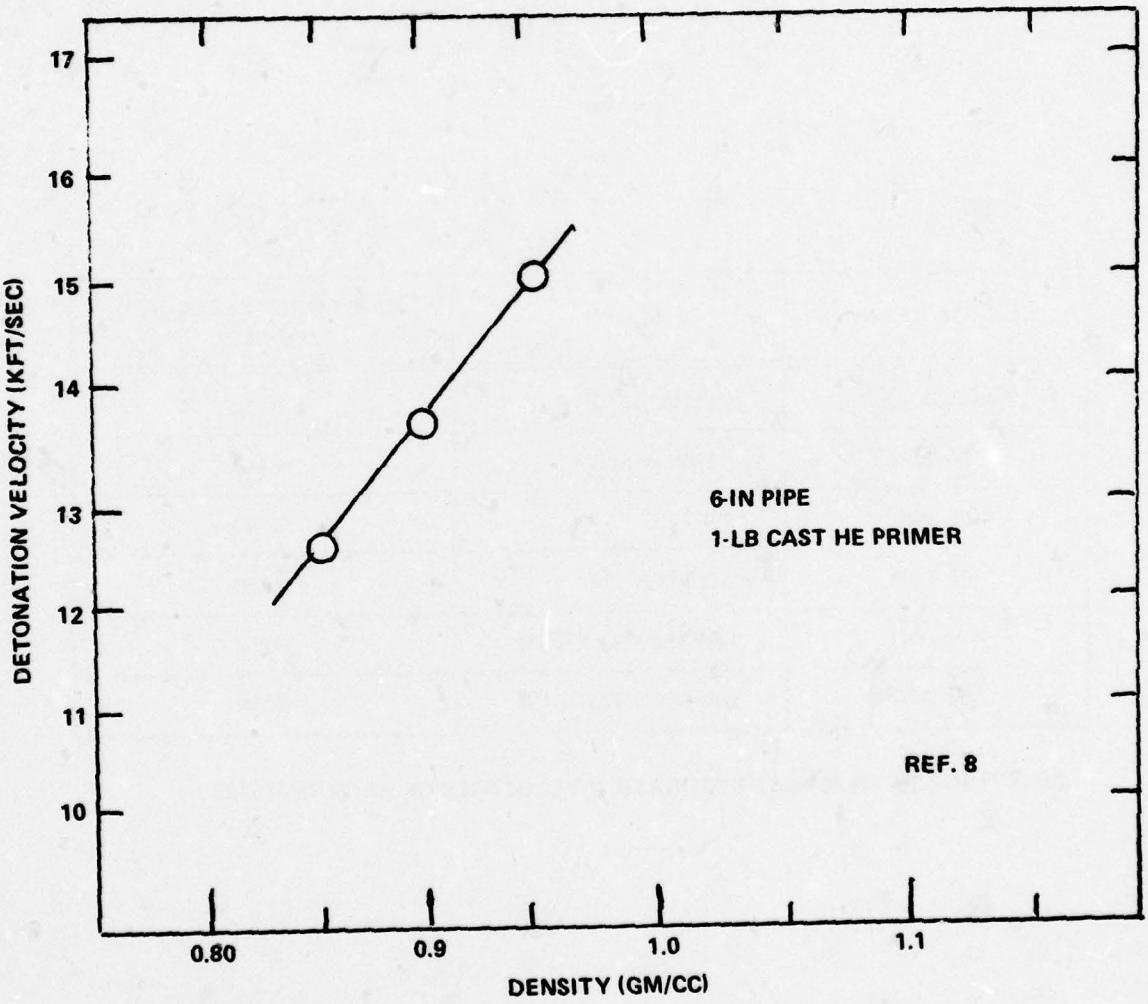

FIGURE 8 CHANGES IN ANFO DETONATION VELOCITY WITH DENSITY

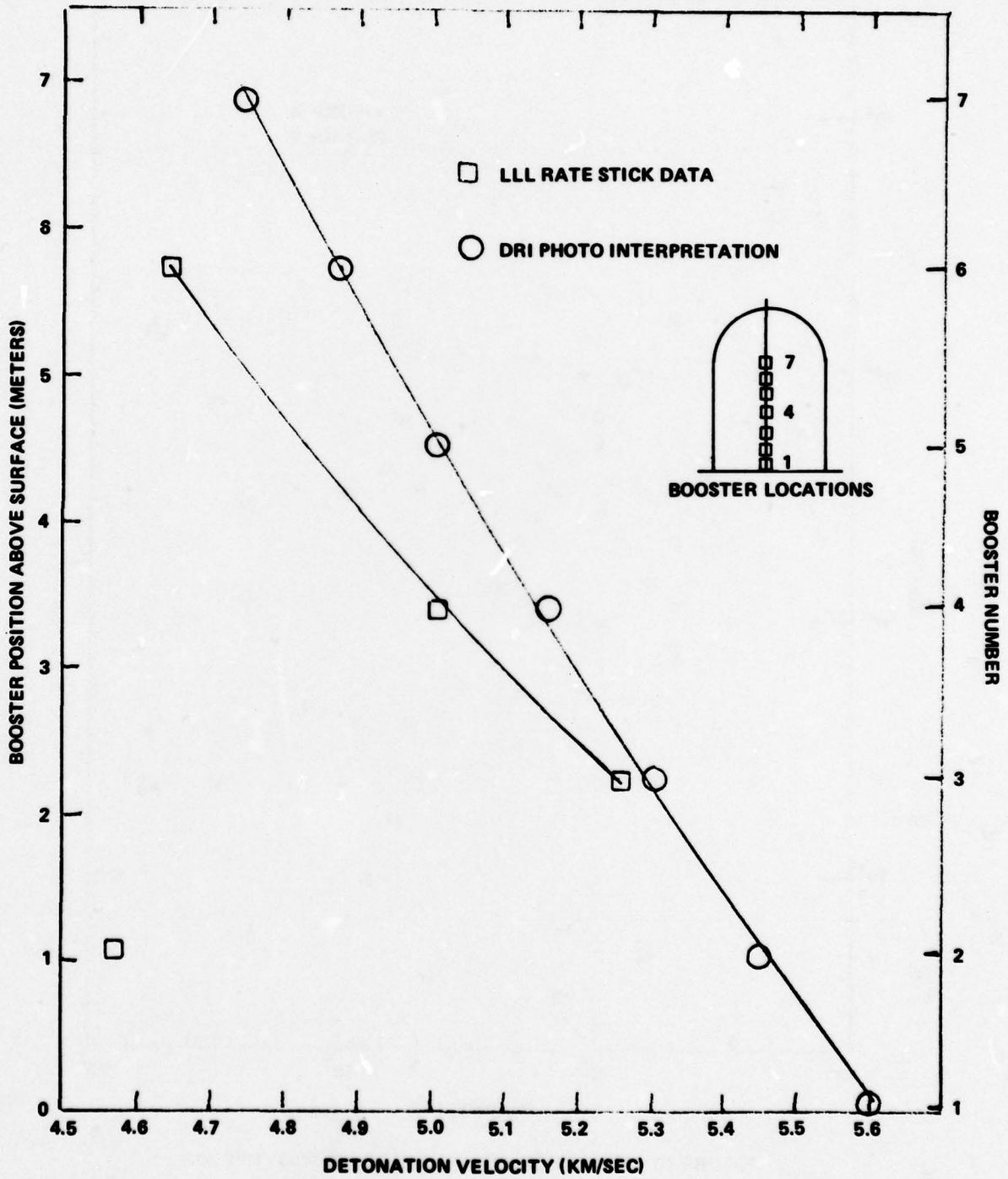

FIGURE 9 ANFO DETONATION VELOCITY AS FUNCTION OF DICE THROW CHARGE HEIGHT

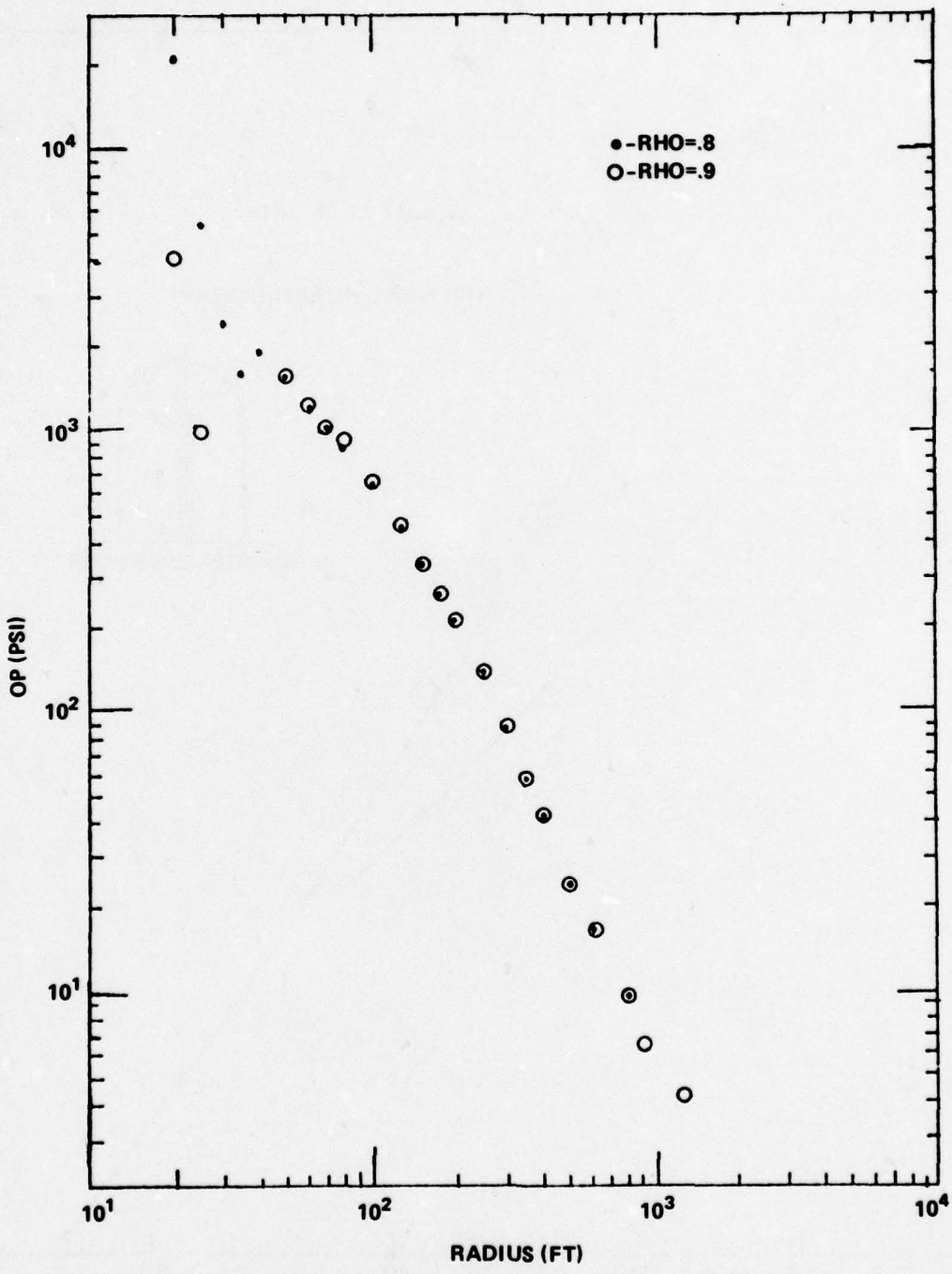

FIGURE 10 OVERPRESSURE VS RANGE 600 TON FREE AIR

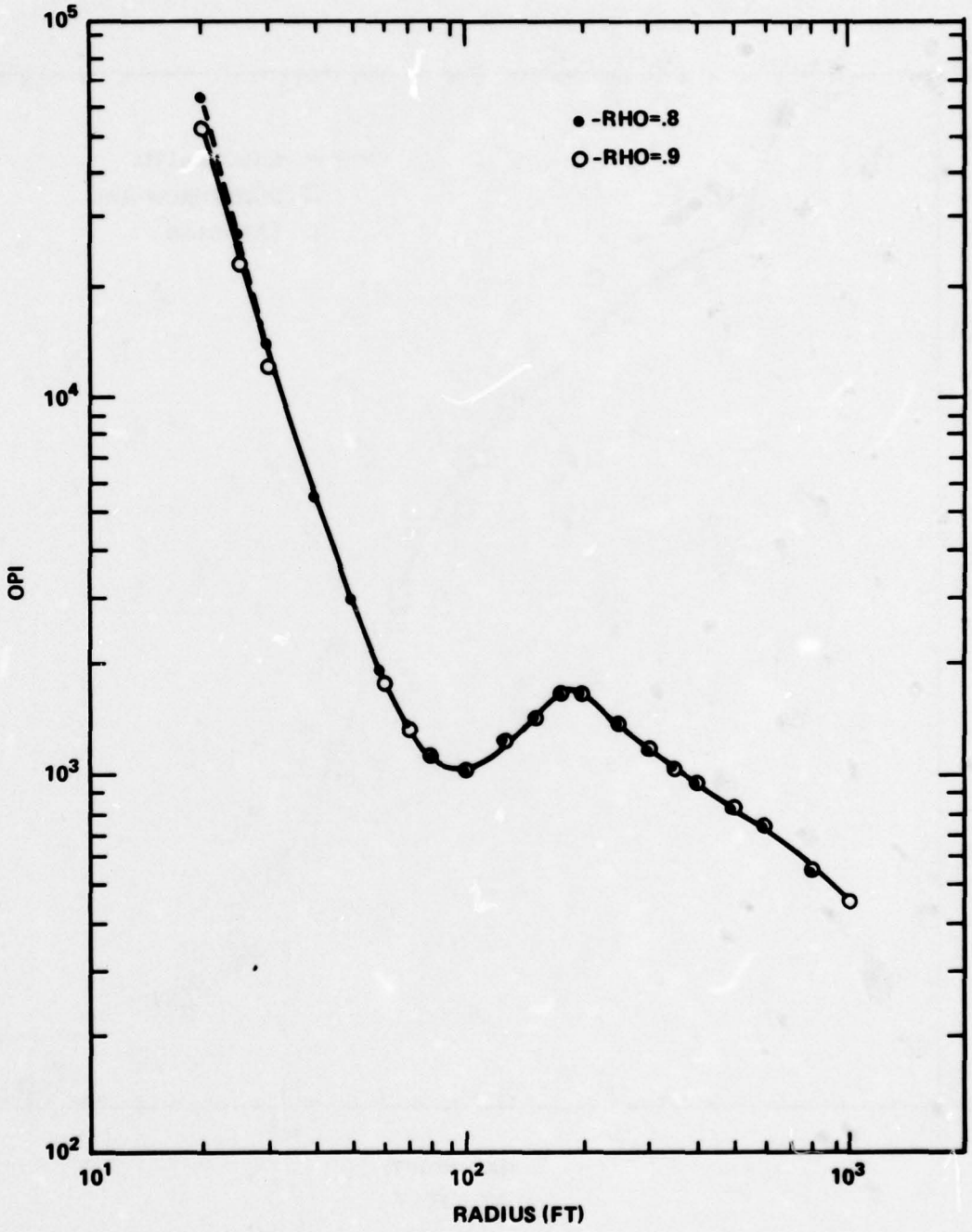

FIGURE 11 OVERPRESSURE IMPULSE VS RANGE 600 TON FREE AIR

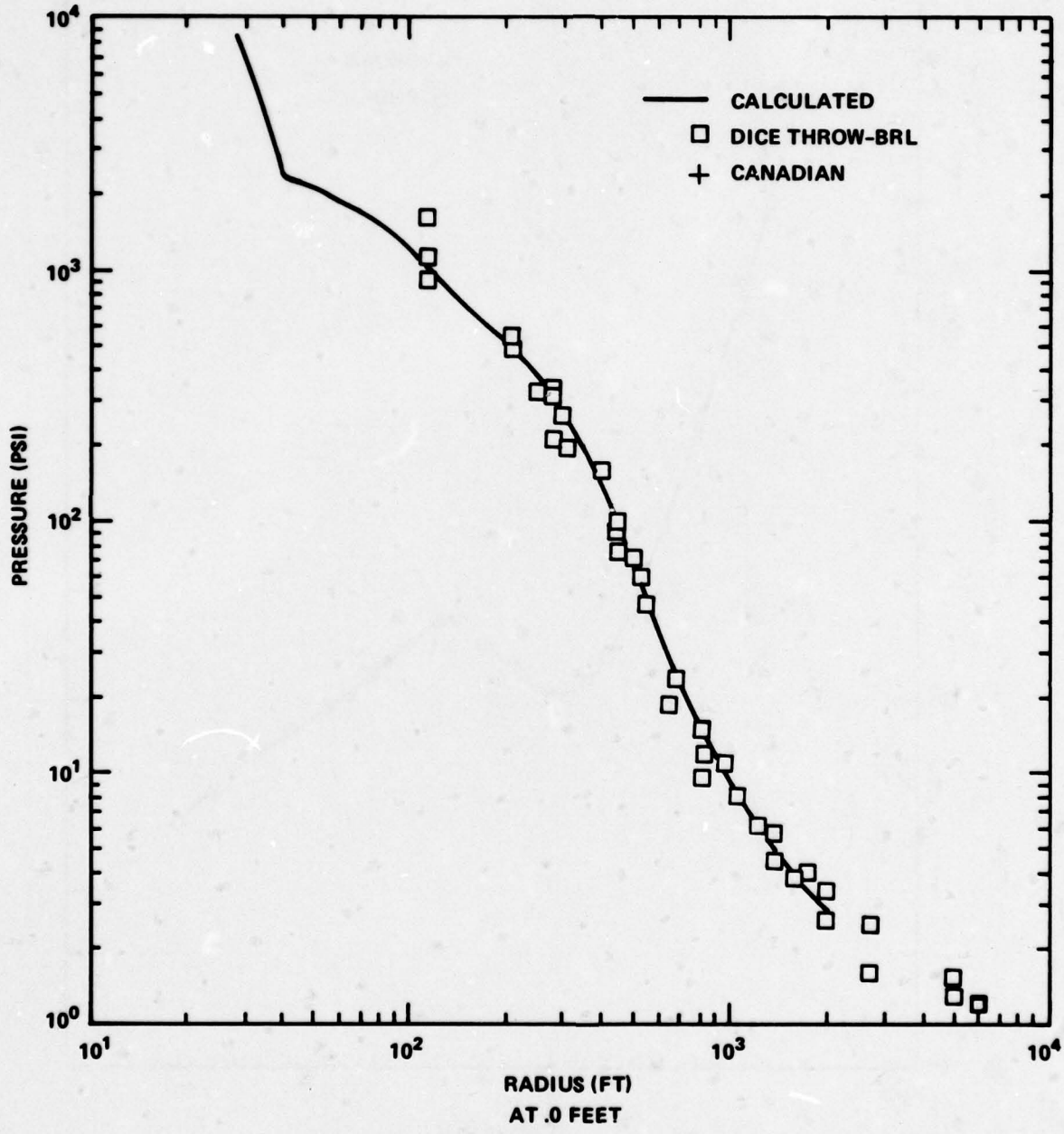

FIGURE 12 AFWL 7 DET 600 TON ANFO PROB = 6001.007 OVERPRESSURE VS RADIUS

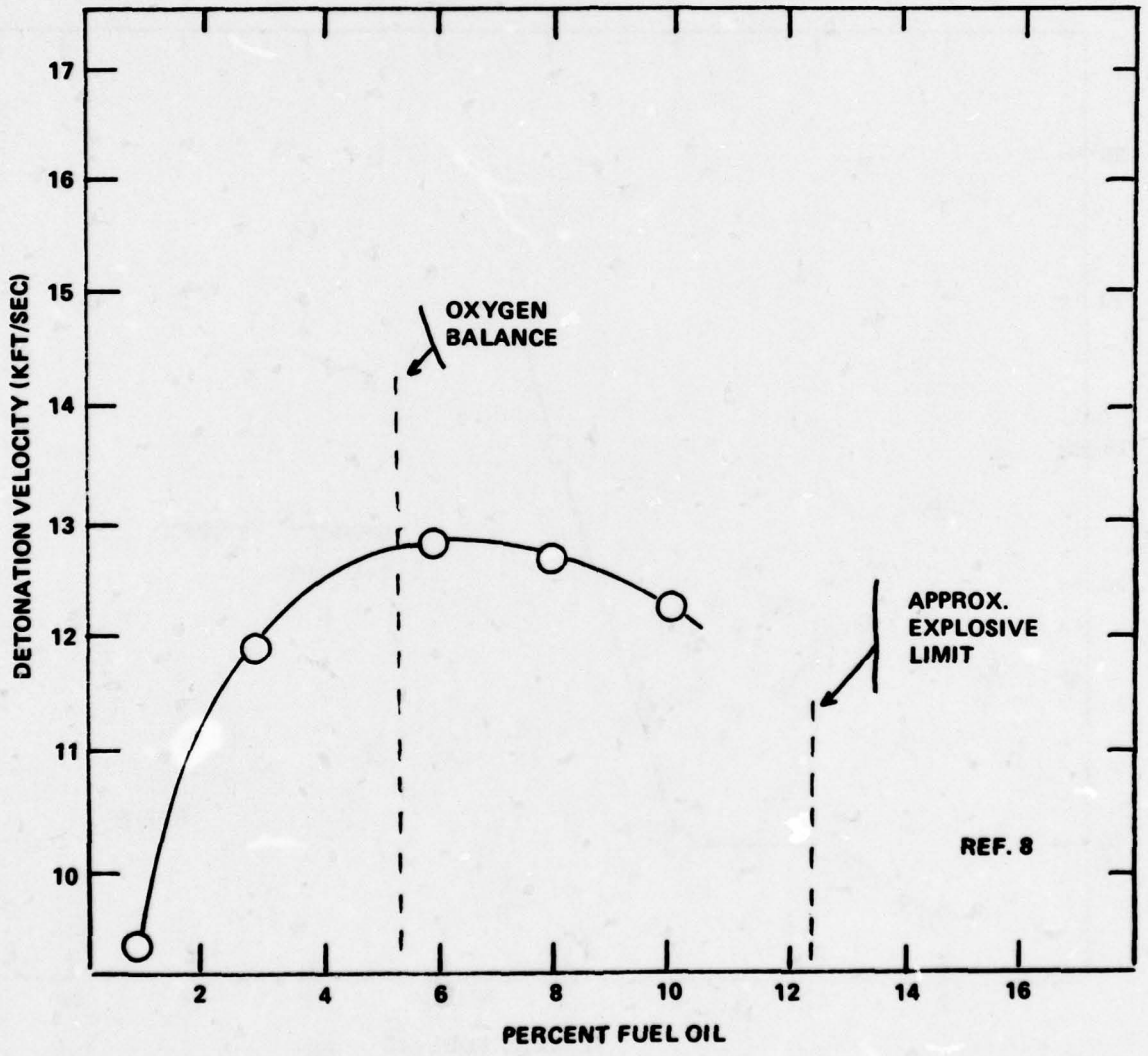

FIGURE 13 CHANGES IN ANFO DETONATION VELOCITY WITH FUEL OIL CONTENT

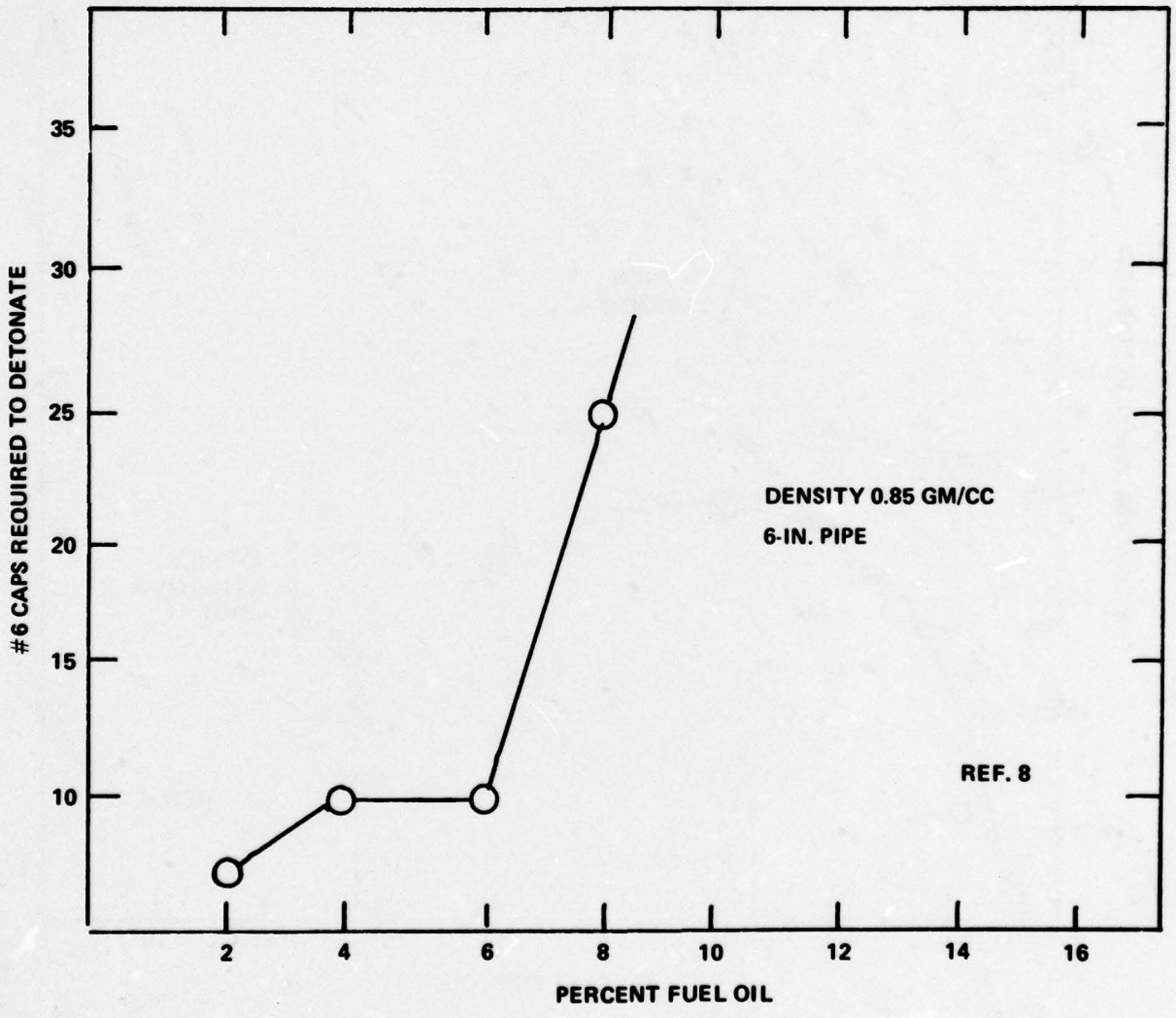

FIGURE 14 CHANGES IN ANFO INITIATION SENSITIVITY WITH FUEL OIL CONTENT

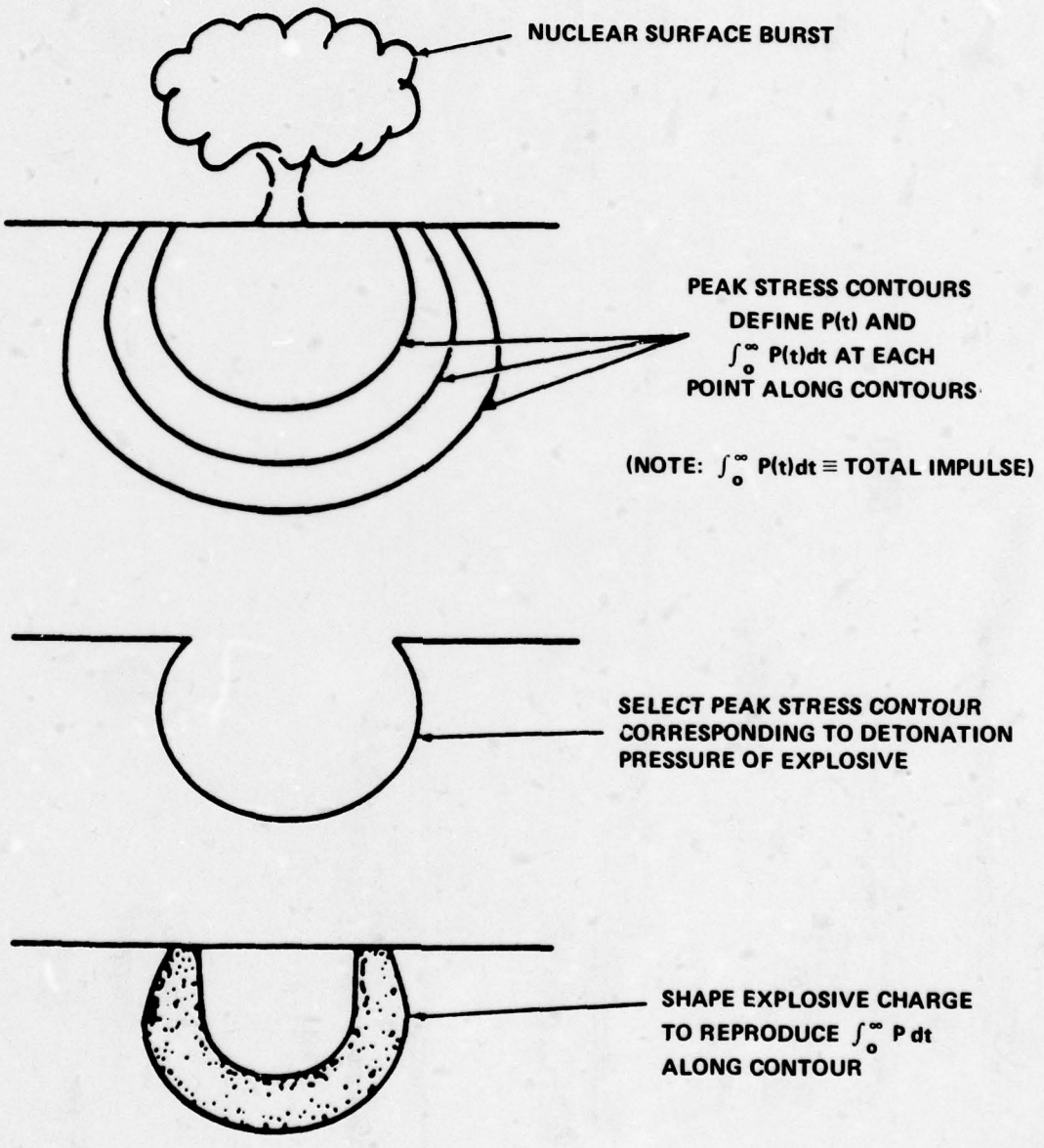

FIGURE 15 CRATERING HIGH EXPLOSIVE SIMULATION TECHNIQUE

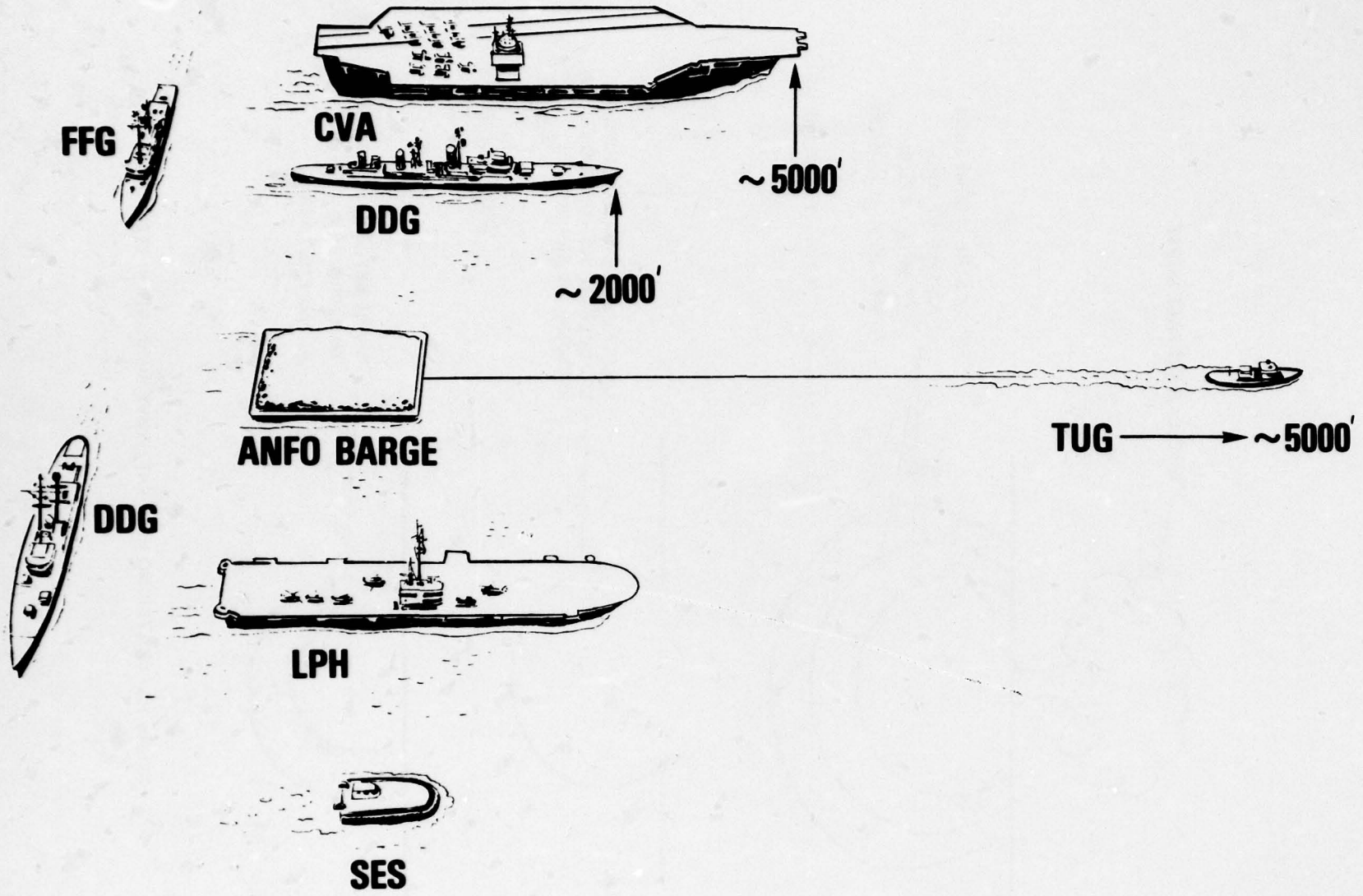

FIGURE 16 SEA TRIAL CONCEPT – AT ANCHOR OR UNDERWAY

CONVENTIONAL HIGH EXPLOSIVES FOR NUCLEAR SIMULATION

by

Gordon F. Lederman, Jr., Capt.,USAF

Air Force Weapons Laboratory

Conventional High Explosives for Nuclear Simulation

Abstract

Conventional high explosives have been used as energy sources for nuclear simulators for quite some time. However, little thought has been given to developing a balanced methodology to address the technical and economic factors involved in optimizing the explosive used for a particular simulation technique. In this paper, an attempt is made to discuss the relevance of technical factors such as the ideality of the explosive, the detonation products, initiation characteristics, detonation velocity, critical or failure diameter, and whether or not the material is characterizable by standard tests. In addition, the often more complex economic factors of availability, production methods, field operations, support facilities, and, of course, cost are also addressed. Many factors for discussion, such as safety and handling, include consideration of both technical and economic data. Specific field examples, as well as suggestions for future work, are discussed and several high explosive systems are detailed. This paper is meant, not as a complete technical evaluation, but rather as a managerial primer to bring forth topics for consideration.

As Mr. J. Petes of the NSWC points out in his paper, the non-ideal explosive, ANFO, has been and will continue to be widely used to simulate nuclear explosions. However, it is quite important to recognize the simulation limitations of ANFO and similar explosives.

ANFO has been widely used as a surface-detonated explosive to simulate a nuclear event. In these experiments, no attempt has been made to significantly enhance the yield of the detonation by confinement or directing of the blast wave. Thus, this may be described as an unsophisticated simulation. That is, the scaled energy input of a nuclear device is input into the environment (ground and air) by producing that energy at ground zero with a non-nuclear (high explosive) energy source (Figure 1). For example, a tenth scale-simulation of a 1 MT nuclear device would require the detonation of 500 tons of TNT or approximately 600 tons of ANFO. The explosive would be detonated at Ground Zero (GZ) and the surrounding environment would interact with the results of the detonation to produce the appropriate shock and other interaction with the test articles.

Obviously, such a simulation can easily escalate greatly in scope and cost, particularly if high yield weapons are being simulated at large scale. For example, a half-scale simulation of a 5 MT weapon would require approximately 375,000 tons of ANFO. At $200.00 per ton, the explosive cost alone would be $75 million. Such a test would require explosive quantities not readily available, a massive construction project, and a test area encompassing several counties. This obviously absurd example is meant only to illustrate the necessity for nuclear simulators which focus energy and shock in order to reduce the amount of explosives and the cost and scope of the project.

There are numerous ways of increasing the sophistication of a simulation and thus decreasing the scope and cost. The most obvious is by limiting the environment "exercised" to that pertinent to the test structure (Figure 2). This limitation, as well as other methods of increasing the sophistication of the simulation, assume some degree of knowledge of the way in which nuclear detonations interact with the environment before the test structure is affected. The Dynamic Airblast Simulator (DABS) (Figure 3) and the High Explosive Simulation Technique (HEST) (Figure 4), discussed elsewhere at this symposium, significantly limit the amount of environment exercised (References 1 and 2). Among other things, they move the energy source explosives closer to the target than the distance to GZ. The energy input is reduced further by confining ("tamping") the explosive in some way and by directing the shock.

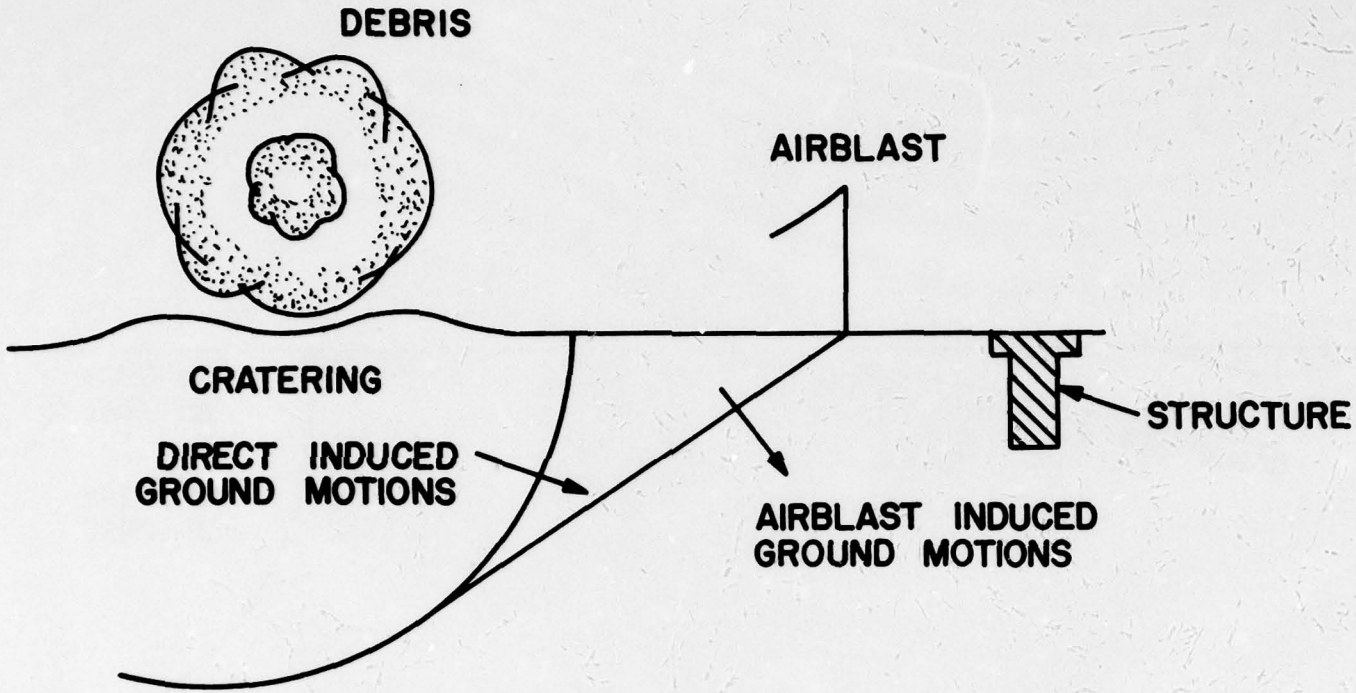

FIGURE 1. NUCLEAR ENVIRONMENT GENERATED BY ENERGY INPUT AT GZ

DYNAMIC AIRBLAST SIMULATION

FIGURE 2. NUCLEAR AIRBLAST ENVIRONMENT LIMITATION OF ENVIRONMENT EXERCISED

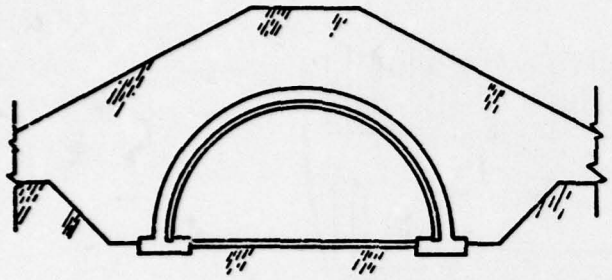

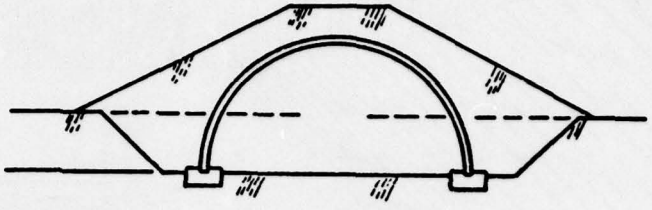

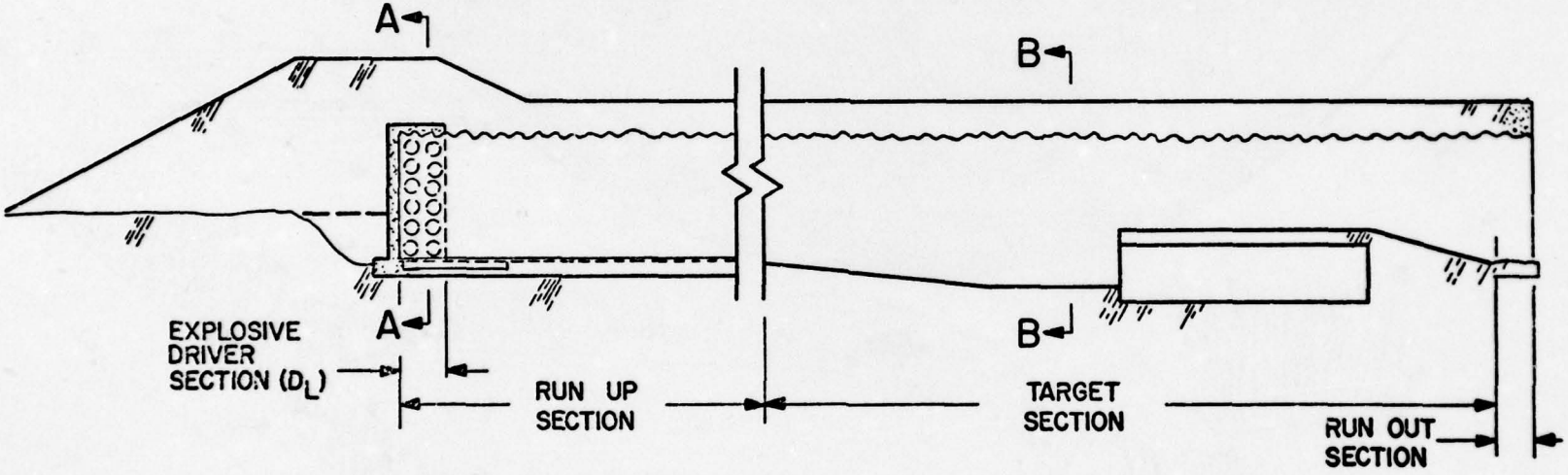

FIGURE 3. ELEMENTS OF A DABS FACILITY

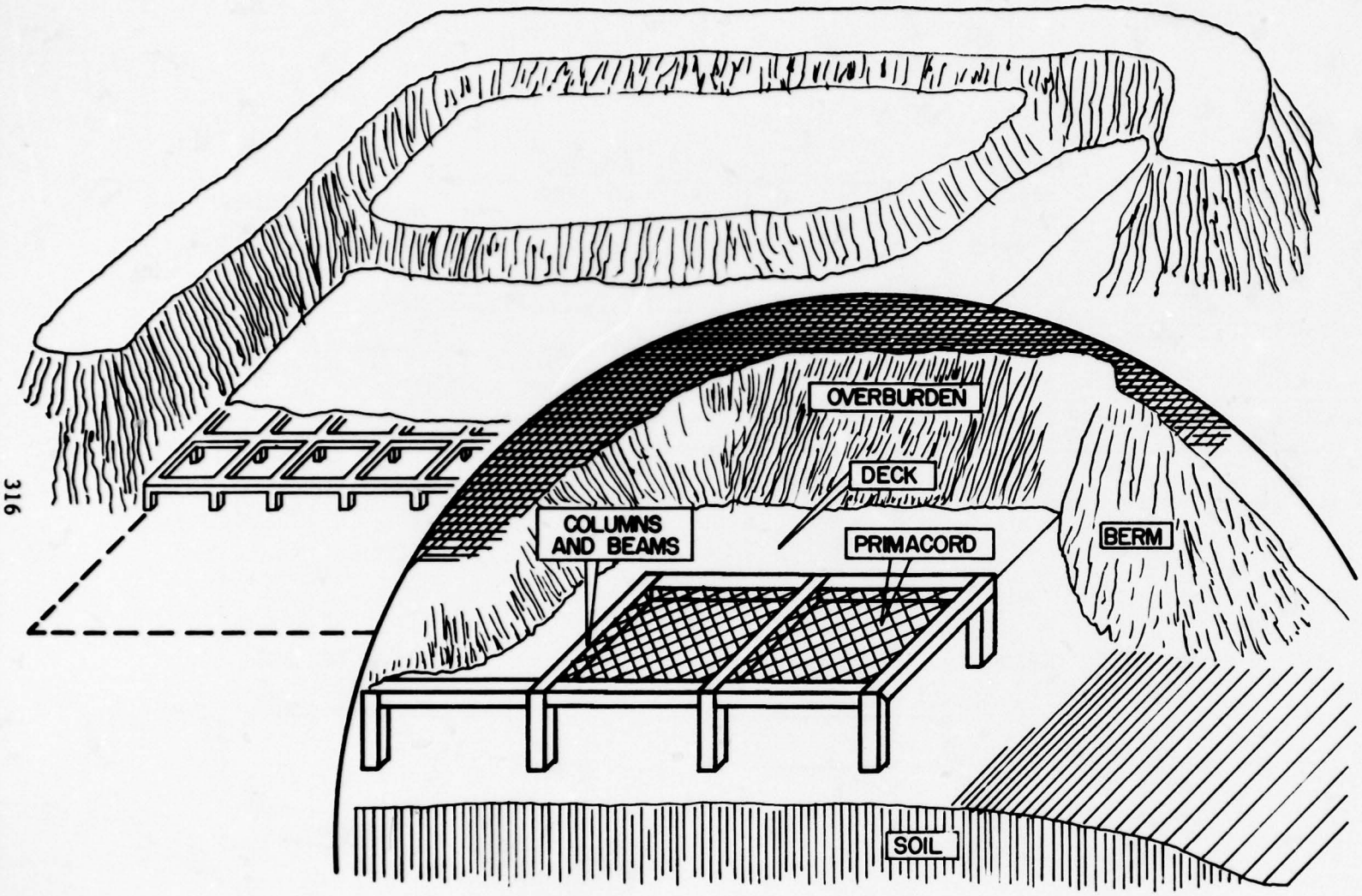

FIGURE 4. SKETCH OF HEST FACILITY

Thus, to reduce the scope and cost of large scale high explosive nuclear simulations, we have developed techniques that require energy sources significantly smaller than multi-ton constructs of bagged ANFO. The larger of these simulators, because of the scale, yield being simulated, duration of simulation, and other factors, may still use many thousands of kilograms of explosives. Thus, budgetary constraints such as constructability of the explosive charge, may require the use of explosives other than the ideal explosives such as TNT.

Non-ideal explosives, such as ANFO, suffer from several drawbacks that must be considered in their use. Ideal explosives have relatively small failure diameters (measured in several millimeters) and properties such as detonation pressures (hundreds of kilobars) and velocities (5-9 mm/μs) that are invariant with charge size above 10-20 mm diameter. These explosives are well characterized and their energy deposition is well characterized and reproducible. Total energy release from the explosive is within a few (less than 5) microseconds after passage of the detonation front. Non-ideal explosives often have failure diameters in the range of several tens to several hundred millimeters and their detonation pressures (usually in the tens of kilobars) and velocities (usually less than 6 mm/μs) vary significantly with charge diameter up to diameters of hundreds of millimeters. These explosives are not well characterized and, unlike ideal explosives, adequate equations of state (E.O.S) do not exist for these explosives except under extremely limited circumstances. Total energy release from these explosives, if it takes place at all, may take up to several hundred microseconds after passage of the detonation front. Figure 5 summarizes these considerations.

Thus, when using non-ideal explosives in simulation applications, a number of considerations must be made that are pertinent to the particular application. These factors are reviewed below. They may be grouped into the following categories: explosive properties, budgetary considerations, constructability, and safety.

Explosive Properties

The important explosive properties may be divided into two groups: detonation properties and physical properties. In the former category, I will discuss the properties important during energy release, such as detonation velocity, detonation pressure,

Figure 5

COMPARISON OF IDEAL & NON-IDEAL EXPLOSIVES

IDEAL	NON-IDEAL
HOMOGENEOUS	INHOMOGENEOUS
SMALL FAILURE DIAMETER	LARGE FAILURE DIAMETER
MINIMAL DIAMETER EFFECTS	DIAMETER EFFECTS
SHORT RUN-UP	LONG RUN-UP
REACTION AT DETONATION FRONT	LENGTHENED REACTION ZONE
STEADY VELOCITY (7 - 9 mm/μs)	VARIABLE VELOCITY (2 - 6 mm/μs)
HIGH ENERGY, PRESSURE	LOWER ENERGY, PRESSURE
KNOWN EQUATION OF STATE, PREDICTABLE	EMPIRICAL EQUATION OF STATE

detonation chemical products, and explosive E.O.S. In the latter category, I will briefly touch on such topics as failure diameter, density, strength, and formulation.

Detonation Properties

Depending on the type of simulation, a precise knowledge of the detonation velocity of the explosive may be important. For example, in the HEST simulations, a cord explosive is normally used as the energy source. To simulate the nuclear shock front propagation velocity, the cord is angled to the direction of propagation. The component of the detonation velocity in the direction of shock front propagation becomes the shock front propagation velocity (Figure 6). In an application such as Dice Throw, a very accurate knowledge of the detonation velocity was neither attainable nor necessary. The detonation pressure refers to the pressure generated at the detonation front by the explosive. This will be reflected in the pressure-time history seen at a later time at a measuring point some distance from the explosive. In some instances, it may be desirable to input a given amount of energy as rapidly as possible--hence, an explosive with a very high detonation pressure may be desired. For purposes of sustaining a load, it may be desirable to avoid a high, initial pressure spike and instead, use an explosive with a lower detonation pressure and longer duration pulse. The chemical products from an explosive may be important for a particular application. In recent DABS work, the production of air-like detonation products was desired. This immediately eliminated from consideration explosives with very negative oxygen balances (high particulate carbon output) and explosives containing metals such as aluminum. All the above properties as well as others may be lumped together by considering the E.O.S. of the explosive. Ideal explosives, as mentioned, have well-defined E.O.S.'s that allow a complete description of the explosive output given certain easily measureable data such as density and chemical composition. Non-ideal explosives may have E.O.S.'s developed for them from experimental data that are applicable within a very narrow range of circumstances. For example, an empirical E.O.S. was developed by Lawr e nce Livermore Laboratory for the ANFO used in Dice Throw. Such E.O.S.'s, however, must be used very cautiously because of their limitations. The E.O.S. for a non-ideal explosive may even vary on a macroscopic scale within a single batch of such an explosive, because of compositional variations in the batch.

Physical Properties

The most important property in this category is the failure diameter and the related topic of the variation of other properties with charge size. The failure diameter may be defined, for cylindrical geometries, as that minimum diameter of explosive

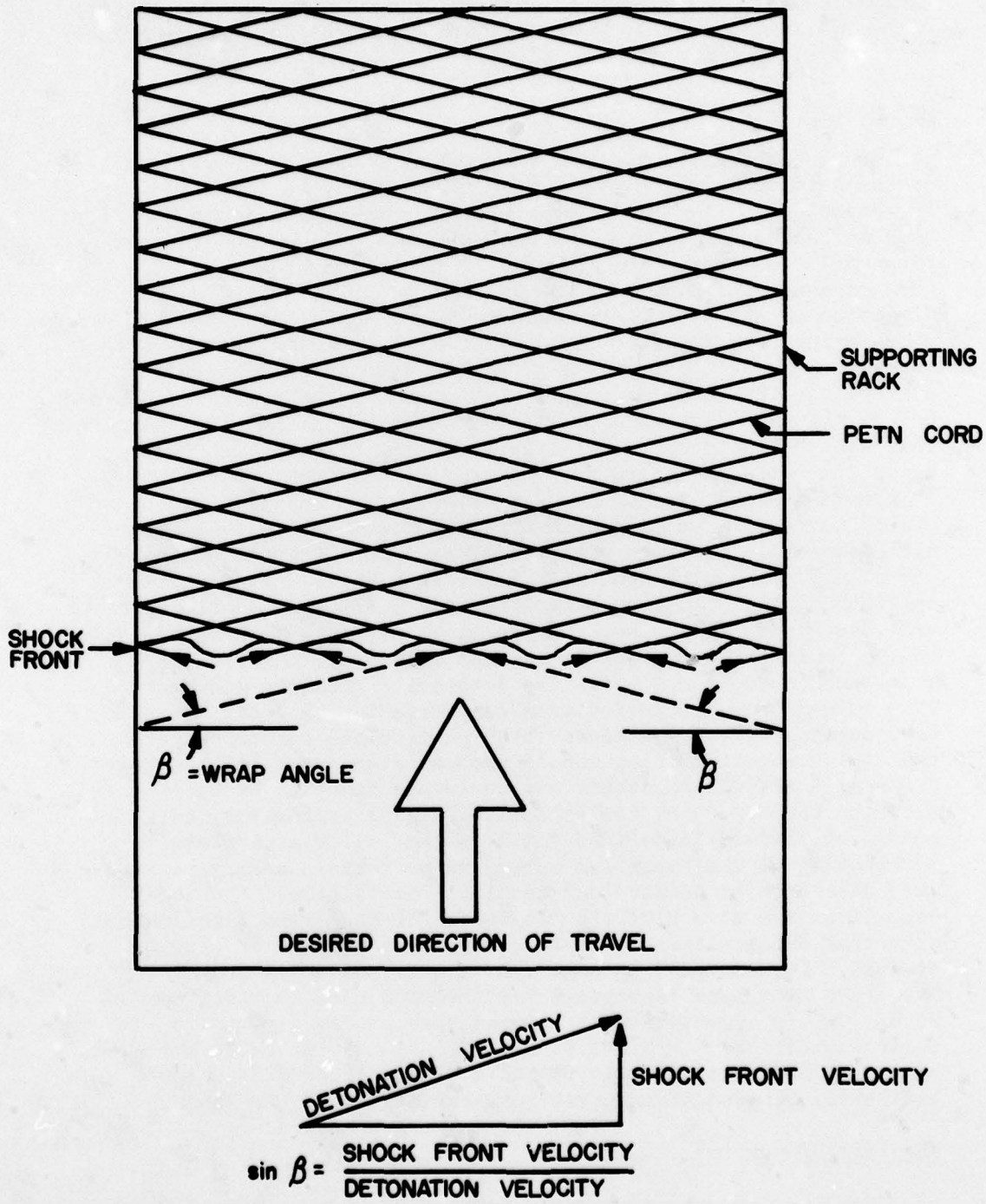

FIGURE 6. CONFIGURATION OF PETN ON RACKS IN A HEST CAVITY

which will sustain a high order detonation. The surface-to-volume ratio and the surface energy losses of an explosive charge determine the failure diameter. This property can become important in two ways. If a charge is small enough in a particular dimension, deflagration or low-order detonation may occur causing the explosive to release only a small fraction of its energy within a useful time period. Further, if a non-ideal charge is within 2 or 3 multiples of its failure diameter, its detonation properties may not be predictable. Thus, its usefulness for predictive models may be limited. ANFO, for example, has an unconfined failure diameter of 100 mm. Further, its detonation properties do not reach equilibrium values even at 300 mm (References 3, 4, and 5). Thus, while it has reliable detonation properties in multi-ton piles, its properties may vary with thickness in many applications. The density of an explosive is an important property for two reasons. First, the density determines many secondary explosive properties, such as detonation velocity. Second, and particularly important if there are volume constraints, a denser material has a higher energy density than the same material in a less dense cast. The physical strength of the material relates primarily to field construction and will be deferred until the section on Constructability.

Budgetary Considerations

The first and foremost budgetary consideration is the availability of the explosive. It does little good to determine that a particular explosive is the best for your simulation purposes if the only way it can be had in quantity is by building your own explosives' plant. A few examples will suffice. Amatol 80/20 is, in terms of detonation velocity and pressure, predictability, physical strength, and detonation products, a very attractive explosive for use in a DABS facility. Because of its viscosity as a melt, however, no manufacturer is remotely interested in producing even small, experimental batches of it--hence, it is not readily available. ANFO, at the other extreme, is the most widely used explosive in the world. It is available from dozens of different manufacturers at prices from 10% down to 1% that of ideal explosives. Related to availability is, of course, cost of the explosive. This consideration is rather obvious and requires no discussion. However, a hidden explosive cost should be mentioned: the manufacturer/customer relationship. If this relationship is friendly, it can mean a willingness on the part of the manufacturer to make slight, but important technical improvements without add-on costs or excessive contractual red tape. A related and often unconsidered cost of the explosive is the cost of the support facilities. These run all the way from cost of transport and cost of storage to the cost of installation and maintenance. Canadian experiments using detonable gas balloons have required

relatively high costs for compressed gas storage tanks, pumping facilities, and maintenance of secure and safe operations (Ref. 6). Liquid or slurry explosives might require on-site mixing, pumping facilities, and appropriate molds.

The bottom line in all discussions of budgetary constraints is the "bang per buck." That is, for the energy delivered to the system desired, what is the total unit cost of the energy. This figure would naturally include all the factors discussed above. For simulations such as DICE THROW, ANFO is not only low in cost, but is also inexpensive to transport in bulk, easy to handle, store, and assemble in 50-lb sacks, and requires no special support facilities--it gives by far the most "bang per buck" for this application.

Constructability

Under the topic Constructability, I first include the manufacturability of the explosive itself. As previously mentioned for Amatol 80/20 and also for some of the Amatex explosives, manufacture may be difficult because of the viscosity of the melt. This and other contributing factors, such as insufficient agitation and too rapid or too slow cooling of the melt may lead to poor quality control of the explosive composition. Hence, an explosive may perform other than expected simply because it literally is not the same explosive as it was thought to be. Additional quality control may be prohibitively expensive.

A second subtopic under Constructability is the actual mounting of the explosive for use. If the explosive is gaseous, liquid, slurry, or a low-strength solid, it will require some sort of form. For a gas or liquid, this form would have to be a high-strength air- or liquid-tight container. In addition to required additional construction and loading equipment, the form material might very well become unwanted high velocity debris. A high-strength solid, such as the Iretol 30T22-C used in DABS facilities may provide their own support if they are suitably designed. Iretol is cast around dowels that are glued into holes drilled in a plywood mount. The mount is then attached directly to the facility wall (Figure 7).

The initiation system must, of course, be an important consideration in the construction of the simulator. The explosive must be able to be initiated in a fairly simple, repeatable manner. That is, the explosive cannot be insensitive to simple initiation, for example, by detonating cord or blasting cap. The initiation must be reliable and must perform in a repeatable, timely manner. For example, in a DABS facility, it is important

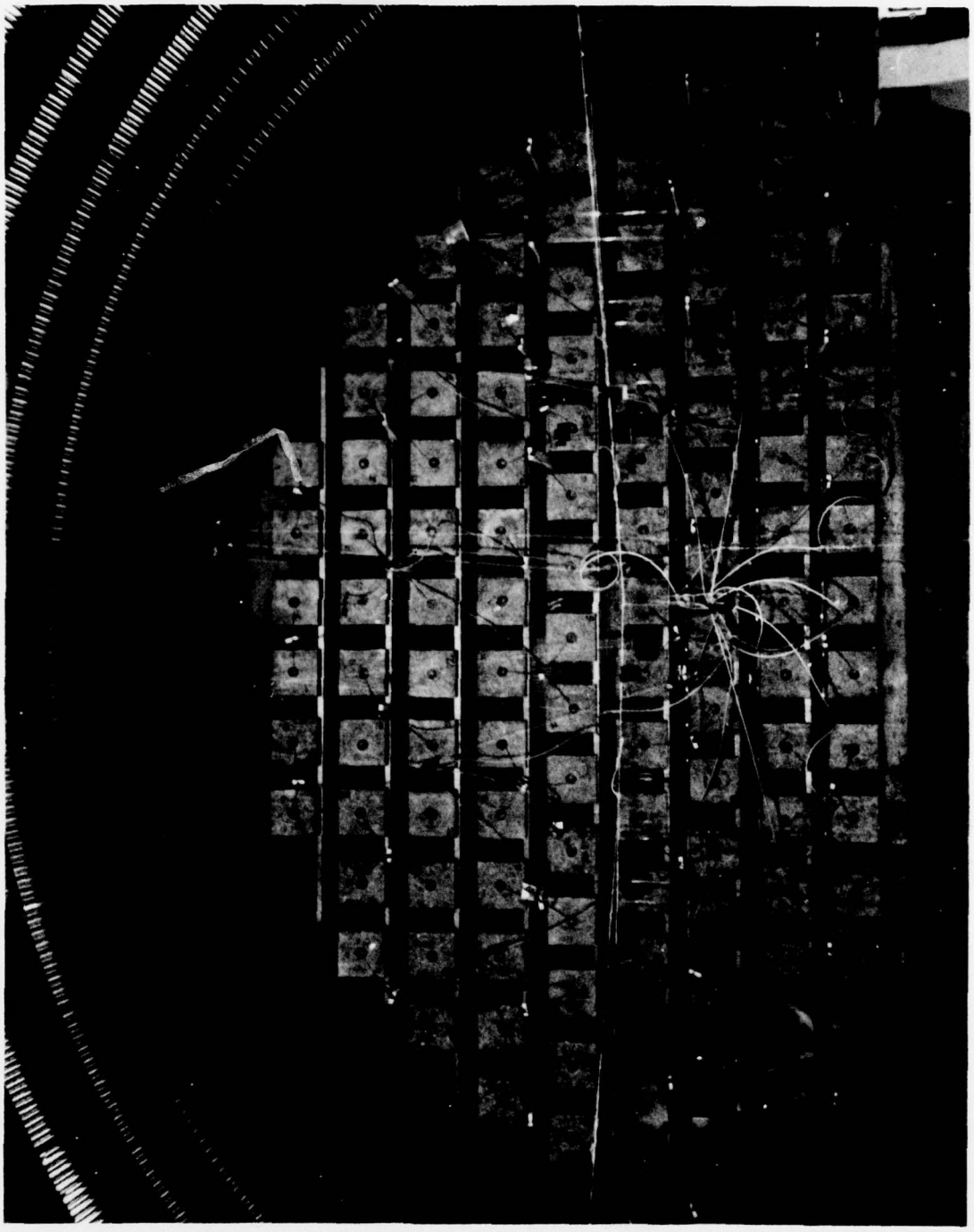

FIGURE 7. PHOTOGRAPH OF THE EXPLOSIVE DRIVER WALL OF A DABS FACILITY

to achieve near simultaneous initiation of the entire explosive wall. To do this, individual 300 mm x 300 mm square blocks of the explosive are all reliably initiated simultaneously with a detonating cord initiation train that is easily constructed beforehand and attached to the driver wall (Figures 8a and 8b).

Safety

I have intentionally left safety for last, not to slight it, but rather to stress its importance. Utilizing a commercially available non-ideal explosive in itself helps to ensure that the explosive has been safely used in numerous, widespread applications. This is not to say that safety can be taken for granted. Rather, especially during transport and storage, well-established safety procedures have been formulated and tested and should be adhered to. However, each new simulator use presents new problems in safety both in the handling of the explosives during mounting and in the mounted explosives themselves. For example, certain explosives, although drop insensitive, may be very highly skid sensitive. Skid sensitivity becomes extremely important where explosives are being moved horizontally over a rough surface. Sensitivity may increase dangerously at elevated temperatures, such as those found in Southern Arizona. Another safety issue that becomes important for larger quantities of explosives is the critical mass--that mass above which an explosive's normal breakdown reactions may generate enough heat to initiate a sustained chain reaction. This mass may decrease at elevated temperatures, under confinement conditions, etc.

Summary

I have attempted to briefly discuss the uses of non-ideal explosives in nuclear weapons' simulation. We in the simulation community have turned to these explosives for numerous reasons. ANFO, which can be used in the larger, inefficient simulations, has several drawbacks for use in the smaller, more sophisticated simulations. In selecting an explosive for simulator use, factors of explosive properties, budgetary restraints, construction considerations, and safety must be addressed. These factors may seem obvious and trivial. If this were so, however, the simulation community would not have the history it has of difficulties with agreeing on the proper use and adequate prediction of the output of explosive drivers. Even at this writing, new explosives are being considered and tested as the energy sources in present simulators and for new simulation systems.

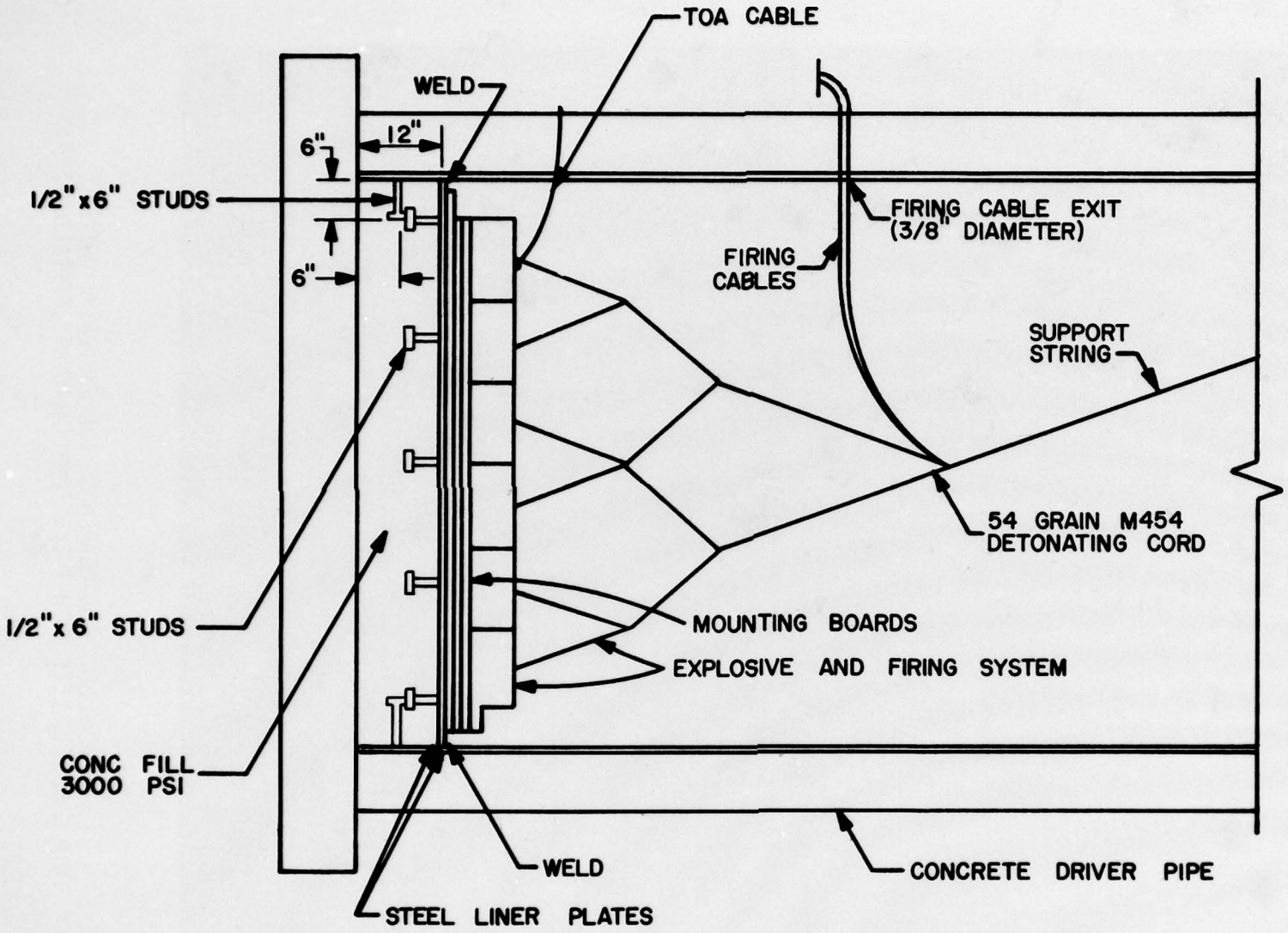

FIGURE 8a. EXPLOSIVE INSTALLATION IN A DABS FACILITY DETAILING INITIATION SYSTEM

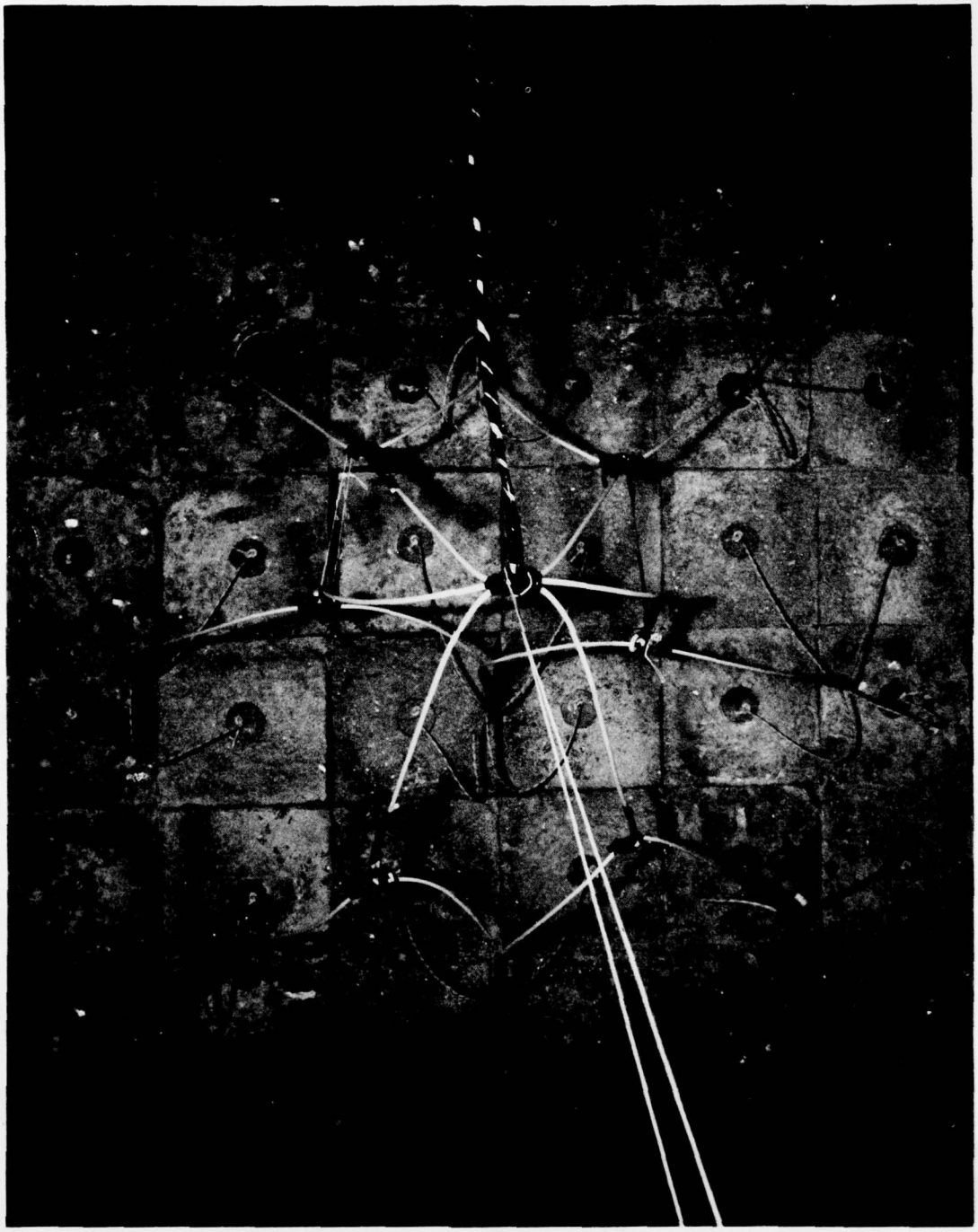

FIGURE 8b. PHOTOGRAPH OF THE EXPLOSIVE DRIVER
IN A DABS FACILITY WITH THE DETONATING CORD INITIATION TRAIN

The list of considerations presented here is far from all-inclusive. To apply these and other criteria properly, a particular simulator application must first be determined. Particularly important are the scale and yield and the sophistication of the simulation. All pertinent considerations must then be listed and weighted appropriately. Then, candidate non-ideal explosives may be compared. Figure 9 shows an evaluation chart used for DABS explosive evaluation. The final test, of course, is when the chosen explosive adequately performs the simulation task. The explosive energy sources for nuclear simulators have, for too long, been taken for granted. The explosive must be investigated early in the simulation design process, not after simulation difficulties begin to appear.

References

1. Martens, D.P. Capt, USAF, and J. D. Renick, AFWL, Kirtland AFB NM, "Development of an Explosively Driven Dynamic Airblast Simulator," Paper presented at Nuclear Blast & Shock Symposium, 28-30Nov78, San Diego CA.

2. Furbee, M. E., Capt, USAF, et al., AFWL, Kirtland AFB NM, "Status & Capability Report on Nuclear Airblast Simulation Using HEST," Pater presented at Nuclear Blast & Shock Symposium, 28-30 Nov 78, San Diego CA.

3. Carter, W. J., Program Manager, LASL NM, "Explosively Produced Fracture of Oil Shale," Apr 1 - Jun 30, 1976, LA-6521-PR.

4. Carter, Program Manager, LASL NM, "Explosively Produced Fracture of Oil Shale," Jul - Sep 76, LA-6594-PR.

5. Carter W. J., Program Manager, LASL NM, "Explosively Produced Fracture of Oil Shale," Oct - Dec 76, LA-6724-PR.

6. "Blast Simulation with Balloons Containing Detonable Gas," General American Research Division, Niles, IL, 30 Sep 74, DNA 3432F.

Figure 9

TYPICAL EXPLOSIVE EVALUATION CHART

CRITERIA	HIGH EXPLOSIVE				
	DETONATING CORD	PETN	TNT	AMATOL 80/20	CASTABLE SLURRY
PERFORMANCE					
ENERGY	X	X	X	X	X
SOLID OUTPUT		X		X	X
CASTABILITY	*NOT* APPLICABLE		X		X
AVAILABILITY	X	X	X		X
SAFETY	X			X	X
CONSTRUCTION SUITABILITY			X	X	X
COST			X		X

X Denotes acceptability

DISTRIBUTION LIST

DEPARTMENT OF DEFENSE

Assistant to the Secretary of Defense
Atomic Energy
ATTN: Executive Assistant

Defense Advanced Rsch. Proj. Agency
ATTN: TIO

Defense Civil Preparedness Agency
ATTN: Hazard Eval. & Vul. Red. Div., G. Sisson

Defense Documentation Center
12 cy ATTN: DD

Defense Intelligence Agency
ATTN: DB-4C, E. O'Farrell
ATTN: DT-1C
ATTN: DT-2

Defense Nuclear Agency
ATTN: DDST
ATTN: SPTD
ATTN: STSP
ATTN: SPAS
4 cy ATTN: TITL
6 cy ATTN: SPSS

Department of Defense Explo. Safety Board
ATTN: Chairman

Field Command
Defense Nuclear Agency
ATTN: FCPR
ATTN: FCTMOF
ATTN: FCT
ATTN: FCTMO, R. Davis
ATTN: FCT, R. Delaar
ATTN: FCTMEI, N. Gantick
ATTN: FCTMEI, J. Holland
ATTN: FCTM, C. Keller
ATTN: FCTMES, D. Martens
ATTN: FCT, F. McMullan
ATTN: FCTMD, D. Shivell
ATTN: FCTMA, L. Stefani
ATTN: FCTMO, J. Strode
ATTN: FCTMO, J. Thomas
ATTN: FCTM, W. Tyler
ATTN: FCTMD, R. Bestgen
ATTN: FCPRK, M. Marlett

Field Command
Defense Nuclear Agency
ATTN: FCPRL
ATTN: FCPRL, W. Beyatte
ATTN: FCPRL, R. Gordon
ATTN: FCPRL, T. Mills

Field Command Test Directorate
Test Construction Division
Defense Nuclear Agency
ATTN: FCTC

NATO School (SHAPE)
ATTN: U.S. Documents Officer

DEPARTMENT OF DEFENSE (Continued)

Under Secy. of Def. for Rsch. & Engrg.
ATTN: Strategic & Space Systems (OS)

DEPARTMENT OF THE ARMY

Chief of Engineers
Department of the Army
ATTN: DAEN-RDM
ATTN: DAEN-MCE-D

Deputy Chief of Staff for Ops. & Plans
Department of the Army
ATTN: MOCA-ADL

Deputy Chief of Staff for Rsch. Dev. & Acq.
Department of the Army
ATTN: DAMA-CSM-N

Harry Diamond Laboratories
Department of the Army
ATTN: DELHD-N-P
ATTN: DELHD-I-TL

U.S. Army Armament Research & Development Command
ATTN: LCWSL, M. Ravotto
ATTN: LCWSL, D. Waxler

U.S. Army Ballistic Research Labs.
ATTN: DRDAR-BLT, W. Taylor
ATTN: DRDAR-BLE, J. Keefer
ATTN: Technical Library
ATTN: DRDAR-BLV
ATTN: DRDAR-BLT, B. Bertrand
ATTN: DRDAR-BLT, N. Ethridge
ATTN: DRDAR-BLT, N. Huffington
ATTN: DRDAR-BLT, C. Kitchens
ATTN: DRDAR-BLV, E. Quigley
ATTN: DRDAR-BLT, G. Teel

U.S. Army Engr. Waterways Exper. Station
ATTN: J. Strange
ATTN: G. Jackson
ATTN: Library
ATTN: W. Flathau

U.S. Army Material & Mechanics Rsch. Center
ATTN: Technical Library

U.S. Army Materiel Dev. & Readiness Cmd.
ATTN: DRXAM-TL

U.S. Army Missile R&D Command
ATTN: RSIC

U.S. Army Mobility Equip. R&D Cmd.
ATTN: DRDME-WC

U.S. Army Natick Rsch. & Dev. Command
ATTN: DRDNA-UST, W. Crenshaw

U.S. Army Nuclear & Chemical Agency
ATTN: Library
ATTN: G. McCall
ATTN: J. Sims

DEPARTMENT OF THE NAVY

David Taylor Naval Ship R & D Ctr.
ATTN: Code 1844
ATTN: Code L42-3
ATTN: Code 17
ATTN: Code 177, E. Palmer
ATTN: Code 1740.1
ATTN: Code 1770.1, V. Bloodgood
ATTN: Code 1740.1, W. Conley
ATTN: Code 1740.4, J. Gordon
ATTN: Code 1770.4, R. Walker
2 cy ATTN: Code 1740.5, B. Whang

Naval Construction Battalion Center
Civil Engineering Laboratory
ATTN: Code L51, R. Odello
ATTN: Code L08A
ATTN: Code L51, W. Armstrong

Naval Electronic Systems Command
ATTN: PME 117-21

Naval Facilities Engineering Command
ATTN: Code 03T
ATTN: Code 04B
ATTN: Code 09M22C

Naval Material Command
ATTN: MAT 08T-22

Naval Ocean Systems Center
ATTN: G. Meyer

Naval Research Laboratory
ATTN: Code 2627
ATTN: Code 8440, G. O'Hara
ATTN: Code 8404, H. Pusey

Naval Sea Systems Command
ATTN: SEA-09G53
ATTN: SEA-0351

Naval Ship Engineering Center
ATTN: Code 09G3
2 cy ATTN: SEC-6105D

Naval Surface Weapons Center
ATTN: Code R14, I. Blatstein
ATTN: Code F31
ATTN: Code R14, M. Giltrud
ATTN: Code R14, D. Nicholson
ATTN: Code R15, J. Petes
ATTN: Code R15, J. Pittman

Naval Surface Weapons Center
ATTN: Tech. Library & Info. Services Branch

Naval Weapons Evaluation Facility
ATTN: R. Friedberg
ATTN: R. Tillery

Office of Naval Research
ATTN: Code 474, N. Perrone
ATTN: Code 715

Office of the Chief of Naval Operations
ATTN: OP 03EG
ATTN: OP 981

DEPARTMENT OF THE NAVY (Continued)

Strategic Systems Project Office
Department of the Navy
ATTN: NSP-272
ATTN: NSP-43

DEPARTMENT OF THE AIR FORCE

Air Force Geophysics Laboratory
ATTN: LWW, K. Thompson

Air Force Institute of Technology
ATTN: Library

Air Force Systems Command
ATTN: DLW
ATTN: IG, J. Neal

Electronics Systems Division
ATTN: TOST, P. Zielie

Air Force Weapons Laboratory, AFSC
ATTN: SUL
ATTN: DE, M. Plamondon
ATTN: DES-C, R. Henny
ATTN: DEX
ATTN: DED, G. Lederman
ATTN: DED, R. Matalucci
ATTN: DED, D. Ray
ATTN: DEX, J. Renick
ATTN: DED, J. Williams

Assistant Chief of Staff
Intelligence
Department of the Air Force
ATTN: INT

Deputy Chief of Staff
Research, Development & Acq.
Department of the Air Force
ATTN: AFRDQSM

Space & Missile Systems Organization
Air Force Systems Command
ATTN: MNNH, T. Edwards
ATTN: MNNH, D. Gale

Strategic Air Command
Department of the Air Force
ATTN: NRI-STINFO Library

Vela Seismological Center
ATTN: G. Ulrrich

DEPARTMENT OF ENERGY

Department of Energy
Albuquerque Operations Office
ATTN: CTID

Department of Energy
ATTN: Doc. Con. for Classified Library

Department of Energy
Nevada Operations Office
ATTN: Mail & Records for Technical Library

Office of Military Application
Department of Energy
ATTN: Doc. Con. for Res., Dev. & Test

DEPARTMENT OF ENERGY CONTRACTORS

Lawrence Livermore Laboratory
ATTN: L-96, L. Woodruff
ATTN: Technical Information Dept. Library
ATTN: P. Brown
ATTN: H. Glenn
ATTN: G. Kramer
ATTN: W. Nok

Los Alamos Scientific Laboratory
ATTN: MS 364
ATTN: B. Craig
ATTN: M. Sanford

Sandia Laboratories
ATTN: 3141

Sandia Laboratories
ATTN: Library & Security Classification Div.

DEPARTMENT OF DEFENSE CONTRACTORS

Acurex Corp.
ATTN: J. Huntington
ATTN: C. Wolf
ATTN: K. Triebes

Aerospace Corp.
ATTN: Technical Information Services
ATTN: D. Holmes
ATTN: R. Mortensen

Agbabian Associates
ATTN: M. Balachandra
ATTN: J. Malthan
ATTN: F. Safford

Boeing Co.
ATTN: Aerospace Library
ATTN: R. Dyrdahl
ATTN: K. Holsapple
ATTN: R. Schmidt

California Research & Technology, Inc.
ATTN: M. Rosenblatt
ATTN: S. Schuster

California Research & Technology, Inc.
ATTN: D. Orphal

Civil Systems, Inc.
ATTN: J. Bratton
ATTN: J. Phillips
ATTN: E. Bultmann
ATTN: L. Melzer

EG&G Washington Analytical Services Center, Inc.
ATTN: Library
ATTN: E. Jaramillo
ATTN: J. Mackey

Electro-Mechanical Systems of New Mexico, Inc.
ATTN: R. Shunk

General Electric Company-TEMPO
Center for Advanced Studies
ATTN: DASIAC
ATTN: R. Rowland
ATTN: J. Kelso

DEPARTMENT OF DEFENSE CONTRACTORS (Continued)

Eric H. Wang
Civil Engineering Rsch. Fac.
The University of New Mexico
ATTN: N. Baum
ATTN: H. Auld
ATTN: K. Bell
ATTN: D. Calhoun
ATTN: G. Leigh
ATTN: H. Wampler

General Electric Company
ATTN: L. Kennedy

Geocenters, Inc.
ATTN: E. Marram

Georgia Institute of Technology
Office of Contract Administration
ATTN: Rsch. Security Coordinator for
S. Hanagud

H-Tech. Labs, Inc.
ATTN: B. Hartenbaum

IIT Research Institute
ATTN: Documents Library

Institute for Defense Analyses
ATTN: Classified Library

Jaycor
ATTN: H. Linnerud

Jaycor
ATTN: P. Nakayama

Kaman Sciences Corp.
ATTN: Library
ATTN: D. Sachs

Lockheed Missiles & Space Co., Inc.
ATTN: TIC-Library

Lockheed Missiles and Space Co., Inc.
ATTN: T. Geers
ATTN: Technical Library

Lovelace Biomedical & Environmental Research
Institute, Inc.
ATTN: D. Richmond
ATTN: R. Fletcher

Martin Marietta Corp.
ATTN: C. Ernst
ATTN: R. Heyman

Merritt CASES, Inc.
ATTN: J. Merritt
ATTN: H. Davis

Pacifica Technology
ATTN: J. Kent
ATTN: R. Allen

Princeton Combustion Research Laboratories, Inc.
ATTN: M. Summerfield

DEPARTMENT OF DEFENSE CONTRACTORS (Continued)

Physics International Co.
ATTN: C. Vincent
ATTN: E. Moore
ATTN: Technical Library
ATTN: F. Sauer
ATTN: J. Thomsen

R & D Associates
ATTN: R. Port
ATTN: C. MacDonald
ATTN: Technical Information Center
ATTN: J. Lewis
ATTN: H. Brode
ATTN: H. Carpenter
ATTN: A. Kuhl
ATTN: J. Whitener

R & D Associates
ATTN: H. Cooper

Radkowski Associates
ATTN: P. Radkowski

Rand Corp.
ATTN: A. Laupa

Science Applications, Inc.
ATTN: Technical Library
ATTN: J. Craig
ATTN: H. Wilson
ATTN: M. McKay
ATTN: R. Schlaug

Science Applications, Inc.
ATTN: J. Dishon

Science Applications, Inc.
ATTN: M. Knasel
ATTN: M. McDonnell
ATTN: B. Chambers

Science Applications, Inc.
ATTN: D. Hove

DEPARTMENT OF DEFENSE CONTRACTORS (Continued)

Southwest Research Institute
ATTN: W. Baker
ATTN: A. Wenzel

SRI International
ATTN: B. Gasten
ATTN: G. Abrahamson
ATTN: A. Florence
ATTN: H. Lindberg
ATTN: P. Senseny

Systems, Science & Software, Inc.
ATTN: Library
ATTN: D. Grine
ATTN: J. Baker
ATTN: J. Barthel
ATTN: P. Coleman
ATTN: E. Demaris
ATTN: H. Kratz
ATTN: C. Peterson
ATTN: T. Pierce
ATTN: K. Pyatt
ATTN: R. Sedgewick

TRW Defense & Space Sys. Group
ATTN: D. Baer
ATTN: Technical Information Center
ATTN: J. Lai
2 cy ATTN: P. Dai

TRW Defense & Space Sys. Group
ATTN: E. Wong
ATTN: N. Lipner
ATTN: T. Schiffman
ATTN: G. Hulcher

Weidlinger Assoc., Consulting Engineers
ATTN: M. Baron
ATTN: D. Ranlet

Weidlinger Assoc., Consulting Engineers
ATTN: J. Isenberg